Modeling and Design of Brushless Doubly-Fed Induction Machines

Wang, Xuezhou

DOI
10.4233/uuid:8feebaa3-3dde-4502-b15d-6057127b0bcd

Publication date
2017

Document Version
Final published version

Citation (APA)
Wang, X. (2017). *Modeling and Design of Brushless Doubly-Fed Induction Machines*. [Dissertation (TU Delft), Delft University of Technology]. https://doi.org/10.4233/uuid:8feebaa3-3dde-4502-b15d-6057127b0bcd

Important note
To cite this publication, please use the final published version (if applicable).
Please check the document version above.

Modeling and Design of Brushless Doubly-Fed Induction Machines

Proefschrift

ter verkrijging van de graad van doctor
aan de Technische Universiteit Delft,
op gezag van de Rector Magnificus prof. ir. K.C.A.M. Luyben;
voorzitter van het College voor Promoties,
in het openbaar te verdedigen op
maandag 19 juni 2017 om 15:00 uur

door

Xuezhou WANG

Master of Engineering in Power Electronics and Electrical Drive,
Northwestern Polytechnical University, Xi'an, China,
geboren te Jiangsu, China

This dissertation has been approved by the

promotor:	Prof. dr. J.A. Ferreira
copromotor:	Dr. ir. D.J.P. Lahaye and Dr. ir. H. Polinder

Composition of the doctoral committee:

Rector magnificus,	chairman
Prof. dr. eng. J.A. Ferreira	Delft University of Technology
Dr. ir. D.J.P. Lahaye	Delft University of Technology
Dr. ir. H. Polinder	Delft University of Technology

Independent members:

Prof. dr. A. Arkkio	Aalto University, Finland
Prof. dr. ir. P. Sergeant	Ghent University, Belgium
Prof. dr. P. Bauer	Delft University of Technology
Prof. dr. ir. C. W. Oosterlee	Delft University of Technology

This research was supported by the China Scholarship Council, and funded by the European Union's Seventh framework Programme (FP7/2007_2013) for the Windrive project under Grant Agreement No. 315485.

Printed by: Ridderprint BV

ISBN: 978-94-6299-625-0

To my beautiful wife Jiehuan Tang, for her love and support,
and to our lovely daughter Heguo Wang.

Contents

Summary

Background and objectives
Renewable energy demand has been growing quickly over the last couple of decades. Wind energy has great potential for large-scale energy production. To further utilize wind energy, wind turbine technology is continuously developing. Among all wind turbine drive-trains currently used in the market, the doubly fed-induction generator (DFIG) with a three-stage gearbox and a partially rated converter is the most employed because it is cost-effective. Unfortunately, the brushes and the slip-rings are prone to failure and need frequent maintenance. However, the reliability and the availability of wind turbines is getting more and more attention, especially in offshore applications. Meanwhile, with the rapid increase of the wind power penetrating the power grid, higher grid connection requirements are required for wind turbines. These increasingly demand reliability and availability which is prompting people to explore alternative wind turbine drive-trains. One potential solution is the brushless doubly-fed induction machine (DFIM) drive-train.

The brushless DFIM has similar operating characteristics to the DFIG in synchronous mode within a limited speed range. They share the same advantage of using a fractionally rated power converter. However, the brushless DFIM also has some additional advantages. The reliability is improved by eliminating the brushes and the slip-rings resulting in a reduction of the regular maintenance. The brushless DFIM is a medium-speed generator. The number of gearbox stages can be reduced, which leads to a further increase in the reliability. It also has a better grid fault ride-through capability. However, the brushless DFIM has not yet been commercialized. The primary objective of this thesis is modeling and design of brushless DFIMs to advance the development of this machine type for wind turbine applications.

The idea of the brushless DFIM came from the self-cascaded induction machine. As the name implies, the brushless DFIM has two stator AC windings with different pole-pair numbers to avoid their direct magnetic coupling. The magnetic coupling is achieved through a special nested-loop rotor. One of the stator windings is referred to as the power winding and is connected to the grid directly. The other one is called the control winding and is connected to the grid through a partially rated converter giving a variable frequency and voltage. The brushless DFIM does not produce a simple rotating magnetic field in the air-gap as conventional electrical machines do. It is a complicated wave with many undesired space-harmonics due to its construction. Surrounding this special feature, the following aspects are discussed in this thesis.

Computationally efficient FE model for optimization
The complicated magnetic field leads to local saturation in the brushless DFIM. This thesis adopts finite element (FE) models to capture this local saturation in order to make efficient use of the material. This thesis presents a computationally efficient FE model based on the magneto-static simulations. The proposed model provides a good trade off regarding computational speed and accuracy. The average torque, losses and efficiency of one candidate design can be evaluated within one to two minutes on a personal workstation. By combining the efficient model with

an optimization algorithm, a fast, flexible and accurate optimization tool is developed for the brushless DFIM. A best design can be found in a large design space within a reasonable time. The FE based optimization tool developed in this thesis has been applied to design a small-scale prototype for experimental studies in this thesis.

Analysis of the effects of skew using a 2D transient multi-slice FE model
Many undesired space-harmonics exist which result in more severe noise, vibrations and lower output power quality in brushless DFIMs. Skewing rotor (or stator) slots is quite practical for overcoming these problems in normal induction machines. This thesis presents a 2D transient multi-slice FE model to investigate the effects of skew on the average torque, the torque ripple, the efficiency and the total harmonic distortion (THD) level of the stator voltages (and/or currents) in the brushless DFIM with a nested-loop rotor. The slices with Gauss distribution are used to reduce the number of slices needed, which helps to reduce the computing time. The 2D transient multi-slice FE model presented is then applied to find out the preferred skew angle considering the above aspects. This thesis proves that, like normal induction machines, skewing the rotor slots over one stator slot pitch is an optimal choice in the brushless DFIM with a nested-loop rotor.

Efficient method to consider the effects of skew in FE post-processing
Considering the large computing time using the 2D multi-slice FE model, this thesis develops a fast semi-numerical method to evaluate the effects of skew on the electromagnetic torque. Meanwhile, the method proposed also provides a validation of the finding which is derived from the 2D multi-slice FE model. The method proposed makes use of normal 2D FE results and applies the well-known skew factors in the post-processing. The appropriate way to apply the skew factors is illustrated based on the analytical derivation of the space- and time-harmonics in the brushless DFIM. The effects of skew on the electromagnetic torque at different skew angles can be predicted while the heavy FE computation does not need to be repeated. It again proves that skewing the rotor slots over one stator slot pitch is an optimal choice to minimize the torque ripple in the brushless DFIM.

Design guidelines for nested-loop rotors
The nested-loop rotor is the key point related to the complicated magnetic field. A better rotor design enhances the main components of the magnetic field and leads to less undesired space-harmonics resulting in a better cross-coupling capability. This thesis evaluates and compares sixteen different nested-loop rotors from four aspects to derive the design guidelines for nested-loop rotors. The four aspects include the torque load-angle characteristics, the torque ripple, the efficiency and the total harmonic distortion (THD) of stator voltages (and/or currents). The results in this thesis indicate that making the loop span bigger and leaving out the loop with a small loop span improves the average torque, the efficiency and the output power quality.

Experimental study on a small-scale prototype
This thesis presents an experimental study on a small-scale prototype to validate the complicated space- and time-harmonics, the influence of rotor skew and the influence of the nested-loop configurations. Unfortunately, the insulation between the rotor bars and the iron core was damaged during the manufacturing processing. The damage of the insulation results in inter-bar

currents which have a significant influence on not only the amplitude but also the distribution of the rotor magnetic field. Therefore, this thesis gives very careful conclusions derived from the measurements. The orders of the space- and time-harmonics predicted analytically are present in the FE results and the measurements. However, the amplitudes of the space- and time-harmonics calculated by the FE model do not agree with the measurements very well. This is because the influence of the inter-bar current is not considered in the FE model. The experimental study in this thesis proves that skewing rotor slots reduces the THD of the stator voltages (and/or currents). Moreover, the experimental study proves that the rotor with large loop span leads to a better cross-coupling between the two stator windings. The 2D FE model and the 2D multi-slice FE model are partially validated in the experimental study.

Analysis of axial flux using a 3D magneto-static FE model
The motivation of a 3D magneto-static FE model is to investigate the validity of the 2D multi-slice FE model. A 3D magneto-static FE model using iterative solvers is implemented. It is then applied to investigate the influence of the axial flux due to the skewed slots on the electromagnetic torque. The results show that iterative solvers significantly reduce the memory required which makes the personal workstation able to deal with a large scale problem with millions of degrees of freedom. Moreover, the results indicate that the 2D multi-slice model is sufficient to capture the effects of skew on the electromagnetic torque.

Improved design for a 3.2MW burshless DFIM
Finally, this thesis brings all the modeling methods and the design guidelines developed together to improve the design of a 3.2MW brushless DFIM. The improved design is based on a case study machine designed by the University of Cambridge. Both the active material cost and the efficiency of the brushless DFIM are considered. The results show that the magnetic loading of the brushless DFIM is increased for a better design by using the FE based multi-objective optimization tool developed. The individual design is selected from the Pareto front for a detailed comparison. The chosen design increases the efficiency and the shear stress, and reduce the torque ripple and the THD level of the stator voltages (and/or currents). However, the chosen design results in a high electric loading which would be a challenge for cooling. Moreover, the results indicate that the optimized brushless DFIM does not show any advantage compared with normal DFIGs and permanent magnet (PM) machines from the efficiency and the shear stress points of view.

In conclusion
This thesis makes efforts towards the modeling and design guidelines of brushless DFIMs. The models and the design guidelines are partially investigated by carrying out measurements on a small-scale prototype with four different nested-loop rotors. All the modeling methods and the design guidelines are brought together to optimize a 3.2MW brushless DFIM based on a case study machine. The results indicate that the modeling methods and the design guidelines developed are useful to improve the design of brushless DFIMs. However, the improved design has not yet shown advantages compared with normal DFIGs and PM generators from the efficiency and the shear stress points of view. Considering the higher reliability and the better grid fault ride-through capability of brushless DFIMs, it makes sense to put efforts into further improving the efficiency and the shear stress for wind turbine applications.

Samenvatting

Achtergrond en Doelstellingen
De vraag naar duurzame energie is de laatste decennia snel toegenomen. Wind energie heeft veel potentie voor grootschalige energie productie. Om wind energie nog meer te benutten is windturbinetechnologie voortdurend in ontwikkeling. Van alle types windturbineaandrijvingen momenteel op de markt, is de Dubbel-Gevoede Inductie Generator (DFIG) met een drie-traps tandwielkast en een gedeeltelijk belaste omvormer het meest toegepast doordat dit type het meest kosten effectief is. Helaas zijn de borstels en sleepringen in de DFIG gevoelig voor storingen en hebben zij regelmatig onderhoud nodig. Daarentegen wordt er steeds meer aandacht besteedt aan betrouwbaarheid en beschikbaarheid van windturbines, vooral in offshore toepassingen. Ondertussen, door de snelle groei van de vraag naar wind energie, worden er steeds strengere net-aansluitingseisen gesteld aan windturbines. De groeiende vraag naar betrouwbaarheid en beschikbaarheid zorgt er voor dat men blijft zoeken naar alternatieve windturbine aandrijvingen. Een mogelijkheid is de borstel-loze Dubbel-Gevoede Inductie Machine (DFIM).

In de synchrone modes en over een gelimiteerde snelheidsrange heeft de borstel-loze DFIM vergelijkbare aansturings-karakteristieken met de DFIG. Ze hebben beiden het voordeel dat ze gebruik maken van een gedeeltelijk belaste omvormer. Daarentegen heeft de borstel-loze DFIM een aantal extra voordelen. De betrouwbaarheid wordt vergroot door het achterwegen laten van borstels en sleepringen, wat ook zorgt voor een vermindering van de onderhoudsbehoefte. Verder is de borstel-loze DFIM een generator die draait met een middelmatige snelheid, waardoor het aantal trappen van de tandwielkast kan worden vermindert. Dit leidt tot een verdere toename in de betrouwbaarheid. Als laatste gedraagt de borstel-loze DFIM zich ook beter tijdens kortstondige spanningsdips in het net. Desondanks is de borstel-loze DFIM nog geen commercieel succes geworden. Het hoofddoel van dit proefschrift is het modeleren en ontwerpen van borstel-loze DFIMs om zo de ontwikkeling van dit type machine voor windturbines te bevorderen.

Het idee voor de borstel-loze DFIM kwam voort uit de ontwikkelingen rond de 'self-cascaded' inductie machine. Zoals de naam al aangeeft heeft de borstel-loze DFIM twee stator AC windingen voor een verschillend aantal poolparen zodat er geen directe magnetische koppeling is tussen beiden. Magnetische koppeling vindt plaats via een speciale rotor constructie met 'nested-loops'. Eén Stator wikkeling, de power-wikkeling, is direct aangesloten aan het net. De andere wikkeling, de control-wikkeling is aangesloten aan het net via een gedeeltelijk belaste omvormer met spanning en frequentie aansturing. The borstel-loze DFIM produceert geen roterend magnetisch veld in de luchtspleet van de machine, zoals gebruikelijk bij conventionele elektrische machines. In plaats daarvan is er een gecompliceerde magnetische golf met veel niet gewenste ruimtelijke harmonische componenten, die ontstaan door de specifieke constructie van deze machine. De volgende aspecten worden besproken in dit proefschrift:

Efficiënte FE computer berekeningen voor optimalisatie
Het gecompliceerde magnetische veld leidt tot lokale verzadiging in de borstel-loze DFIM. Dit

proefschrift behandelt de toepassing van Eindige Elementen (FE) modellen om zo lokale verzadiging aan te pakken en het materiaal waar de borstel-loze DFIM van is gemaakt beter te benutten. Verder behandelt dit proefschrift de ontwikkeling van een rekenkundig efficiënt FE model dat is gebaseerd op magneto-statische simulaties. Het voorgestelde model biedt een goede afweging tussen rekensnelheid en nauwkeurigheid. Het gemiddelde koppel, vermogensverliezen en rendement van een mogelijk ontwerp kunnen met een pc worden geëvalueerd binnen één tot twee minuten. Door dit efficiënte model te combineren met een optimalisatie algoritme is een snelle, flexibele en nauwkeurige borstel-loze DFIM optimalisatie tool ontwikkeld. Een optimaal design kan worden bepaald binnen een grote ruimte aan variabelen en binnen een aanzienlijke tijd. Deze op FE gebaseerde optimalisatie tool is gebruikt voor het ontwerp van een kleinschalig prototype borstel-loze DFIM, die is toegepast voor experimentele studies binnen dit proefschrift.

Het effect van schuine groeven geanalyseerd met een '2D transient multi-slice FE model'
Er bestaan veel ongewenste ruimtelijke harmonische, welke leiden tot meer geluid, trillingen en een lagere vermogens kwaliteit van borstel-loze DFIMs. Het scheef zetten van rotor (of stator) groeven is een praktische manier om deze problemen te verminderen in conventionele inductie machines. Dit proefschrift behandelt de toepassing van een '2D transient multi-slice FE model' om het effect te onderzoeken van schuine groeven op het gemiddelde koppel, het koppelrimpel, het rendement en de Totale Harmonische Vervorming (THD) van de geïnduceerde stator spanningen (en/of stromen) in borstel-loze DFIMs met 'nested-loop' rotoren. Het aantal benodigde plakken in deze methode is verminderd door de plakken een Gauss verdeling te geven. Hierdoor wordt ook de rekentijd verminderd. Het gepresenteerde '2D transient multi-slice FE model' is gebruikt om te onderzoeken onder welke hoek de groeven het beste schuin kunnen worden gezet, rekening houdend met bovenstaande aspecten. Dit proefschrift bewijst dat, net zo als bij conventionele inductie machines, het schuin zetten van de rotor groeven over een hoek gelijk aan de hoek van één stator groef, ook bij de borstel-loze DFIM met 'nested-loop' rotor een optimaal resultaat biedt.

Het effect van schuine groeven in rekening gebracht via een efficiënte methode tijdens FE nabewerking
Gezien de lange benodigde rekentijd bij het toepassen van het '2D transient multi-slice FE model', beschrijft dit proefschrift ook de ontwikkeling van een snellere semi-numerieke methode om het effect van schuine groeven mee te nemen in de berekening van het elektromagnetische koppel. Tegelijkertijd fungeert deze tweede methode als validatie voor de resultaten verkregen met het '2D transient multi-slice FE model'. De nieuw voorgestelde methode maakt gebruik van een enkele 2D FE berekening en maakt tijdens de nabewerking gebruik van de welbekende 'skew factors'. De 'skew factors' kunnen op de juiste manier worden verwerkt in de analytische afleidingen voor de ruimtelijke- en tijd-harmonische componenten van het magnetische veld in de borstel-loze DFIM. Het effect van schuine groeven op het elektromagnetische koppel kan worden voorspeld zonder meerdere zware FE berekeningen uit te voeren. Ook de resultaten verkregen via deze methode tonen aan dat het schuin zetten van de rotor groeven over een hoek gelijk aan één stator groef, zorgt voor een minimaal koppelrimpel in de borstel-loze DFIM.

Ontwerp richtlijnen voor 'nested-loop' rotoren

De 'nested-loop' rotor is het belangrijkste aspect dat zorgt voor het gecompliceerde magnetische veld in de borstel-loze DFIM. Een verbetert rotor ontwerp versterkt de hoofd componenten binnen het magnetische veld en leidt tot minder ongewenste ruimtelijke-harmonische componenten. Dit zorgt voor een betere 'cross-coupling'. Dit proefschrift evalueert en vergelijkt zestien verschillende 'nested-loop' rotoren op vier verschillende aspecten. Hieruit is een set van ontwerprichtlijnen opgesteld voor 'nested-loop' rotoren. De vier verschillende aspecten omvatten de koppel-belasting karakteristiek, koppelrimpel, rendement en de THD van de statorspanningen (en/of stromen). De behaalde resultaten duiden erop dat wijdere loops en het verwijderen van de binnenste (smalle) loops uit de nesten zorgt voor een hoger gemiddeld koppel, rendement en vermogenskwaliteit.

Experimentele studie uitgevoerd op een kleinschalig prototype
Dit proefschrift presenteert een experimentele studie uitgevoerd op een kleinschalig prototype voor de validatie van de gecompliceerde en aanwezige ruimtelijke- en tijd-harmonische componenten, de invloed van schuine rotorgroeven en de invloed van de 'nested-loop' rotor configuraties. Helaas was de isolatie tussen de koperen rotorbars en het rotor blikpakket beschadigd geraakt tijdens het productie proces. Dit heeft ertoe geleidt dat er elektrische stromen kunnen lopen tussen de verschillende rotorbars door het blikpakket heen. Dit heeft weer een aanzienlijke invloed op de amplitude en verdeling van het magnetische veld component van de rotor. Daarom worden slechts voorzichtige conclusies getrokken uit de behaalde meetresultaten. De analytisch voorspelde ruimtelijke- en tijd-harmonische componenten kwamen zowel naar voren in de FE simulaties als in de metingen. Echter de berekende amplitudes van de ruimtelijke- en tijd-harmonische uit het FE model correleren niet goed met de meetresultaten. Dit komt doordat het FE model de elektrische stromen tussen rotorbars, door de beschadigde isolatie, niet goed meeneemt. De experimentele studie toont wel aan dat schuine rotor groeven de THD van stator spanningen (en/of stromen) vermindert. Verder is aangetoond dat een rotor met een wijde loop-span lijdt tot een betere 'cross-coupling' tussen de twee statorwindingen. Het 2D FE model en het '2D transient multi-slice FE model' zijn deels gevalideerd tijdens de experimentele studie.

Axiale flux analyse met behulp van een 3D magneto-statisch FE model
De reden voor een 3D magneto-statisch FE model is het valideren van het het '2D transient multi-slice FE model'. Een 3D magneto-statisch FE model dat gebruik maakt van iteratieve 'solvers' is ontwikkeld. Dit model is toegepast om de invloed van axiale flux, door schuine rotor groeven, op het elektromagnetische koppel te onderzoeken. De resultaten tonen aan dat iteratieve 'solvers' de benodigde dataopslag significant verminderen, waardoor een normale pc kan worden gebruikt voor het oplossen van grootschalige problemen met miljoenen vrije dimensies. De resultaten tonen ook aan dat het '2D transient multi-slice FE model' het effect van schuine groeven op het elektromagnetische koppel voldoende nauwkeurig berekent.

Een verbetert ontwerp voor een 3.2MW borstel-loze DFIM
Als laatste worden in dit proefschrift de ontwikkelde ontwerp methodes en ontwerp richtlijnen verenigt om te zorgen voor een verbetert ontwerp van een 3.2MW brushless DFIM. Het verbeterde ontwerp is gebaseerd op een casusstudie machine eerder ontworpen door de universiteit van Cambridge. Zowel de kosten van het (actieve) materiaal als het rendement van de borstel-loze

DFIM zijn in beschouwing genomen. De resultaten laten zien dat de magnetische belasting van het verbeterde ontwerp voor de borstel-loze DFIM is toegenomen door het toepassen van de ontwikkelde op FE gebaseerde optimalisatie tool. Het uiteindelijke ontwerp is geselecteerd uit een 'Pareto front'. Het geselecteerde ontwerp heeft een hoger rendement en krachtbelasting in de luchtspleet en een kleiner koppelrimpel en THD van de statorspanningen (en/of stromen). Het gekozen ontwerp leidt echter wel tot een hoge elektrische belasting wat een uitdaging vormt voor de koeling van de machine. De resultaten lijken erop te duiden dat de geoptimaliseerde borstel-loze DFIM geen voordeel biedt ten opzichte van de normale DFIG of een generator met permanente magneten wanneer wordt gekeken naar efficiëntie en krachtbelasting in de luchtspleet.

Conclusies

Dit proefschrift doet een poging om modellen en ontwerprichtlijnen voor bostel-loze DFIMs op te stellen. De modellen en ontwerprichtlijnen zijn deels onderzocht door het verrichten van metingen op een kleinschalig prototype met vier verschillende 'nested-loop' rotoren. Alle modeleringsmethoden en ontwerp richtlijnen zijn verenigd voor de optimalisatie van een 3.2MW borstel-loze DFIM gebaseerd op een machine uit een casusstudie. De behaalde resultaten tonen aan dat de ontwikkelde modeleringsmethoden en opgestelde ontwerprichtlijnen nuttig zijn voor het verbeteren van borstel-loze DFIM ontwerpen. De gegenereerde verbeterde ontwerpen vormen echter geen aantoonbare verbetering op het gebied van rendement en krachtbelasting in de luchtspleet ten opzichte van normale DFIGs of generatoren met permanente magneten. Gezien de grotere betrouwbaarheid en een beter vermogen om om te gaan met kortstondige spanningsdips in het net, is het aan te raden om het rendement en de krachtbelasting in de luchtspleet nog verder te verbeteren voor borstel-loze DFIMs voor windturbine toepassingen.

Glossary

CG conjugate gradients
CW control winding
DFIG doubly-fed induction generator
DFIM doubly-fed induction machine
DFRM doubly-fed reluctance machine
DoF degree of freedom
EESG electrically excited synchronous generator
EMF electromotive force
FE(M) finite element (method/model)
GA genetic algorithm
GMRES generalized minimum residual
IM induction machine
MMF magnetomotive force
MVP magnetic vector potential
PE power electronic
PM permanent magnet
PMSG permanent magnet synchronous generator
POF Pareto optimal front
PW power winding
RMS root mean square
SG synchronous generator
SCIG squirrel-cage induction generator
STFT short-time Fourier transform
THD total harmonic distortion
WRIG wound rotor induction generator

λ linked flux (Wb)
μ_r relative permeability
σ conductivity (S/m)
ω electrical angular frequency (rad/s)
Ω mechanical angular frequency (rad/s)

CHAPTER 1

Introduction

1.1 Background

Renewable energy demand has been growing quickly over the last decades as shown in Figure 1.1. At present, most of the energy is generated from fossil fuel. This leads to huge CO_2 emissions and hence global warming. However, the reserves of fossil sources are limited. This prompts people to harvest renewable energy. Therefore, the use of renewable energy sources such as, wind, solar, hydro, etc. has been increasing. Wind is available almost everywhere on earth, although wind strengths varies with locations. The total wind resource is roughly estimated to be a million GW for all land coverage [1], therefore, wind energy has great potential for large-scale energy production. In 2015, the global cumulative installed wind capacity reached 433 GW, which is ninety times more than the installed capacity of 4.8 GW in 1995. By the end of 2020, it is expected

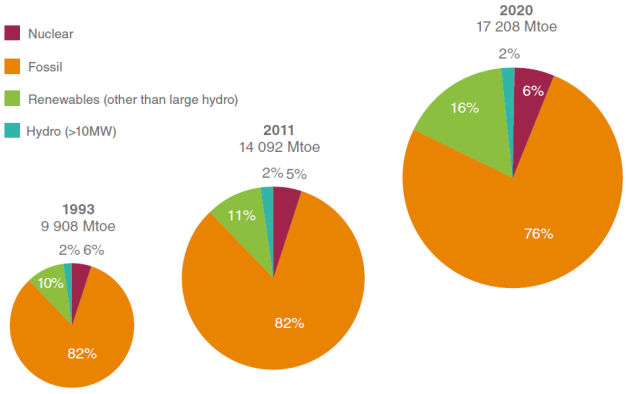

Figure 1.1 Total primary energy supply in Mtoe (Million tonnes of oil equivalent) [1]

that the global cumulative wind power capacity will increase to 792 GW [2]. The average annual growth rate of cumulative wind power capacity has been around 20% since 2006 as illustrated in Figure 1.2.

In order to further utilize wind energy, wind turbine technologies have been being developed further over the past few decades. The size and the power rating of wind turbines has increased considerably, as is evident in Figure 1.3. The up-scaling of the size and the power rating benefits to reduce the cost of energy because of the economy of scale. Many wind turbines are placed offshore to reduce their influence on local residents. Besides the above developments, several topologies of wind turbine drive-train have been developed which will be briefly introduced in Chapter 2. Nowadays, the doubly-fed induction generator (DFIG) drive-train with a gearbox and a partially rated power electronic (PE) converter is the most applied in commercial wind turbines [14].

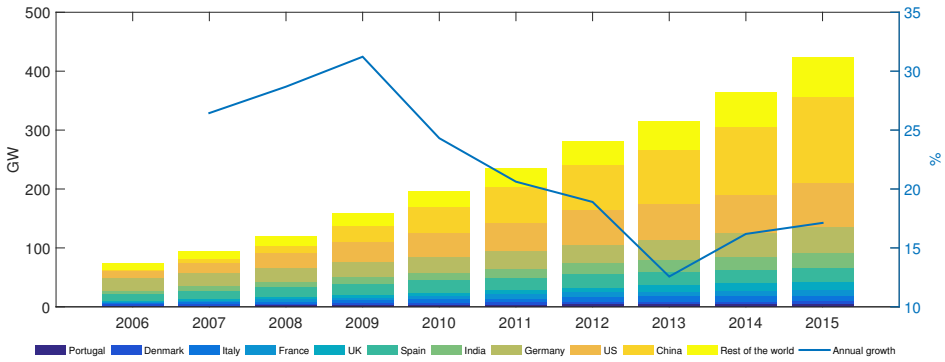

Figure 1.2 Global cumulative growth of wind power capacity (Data from [2–12])

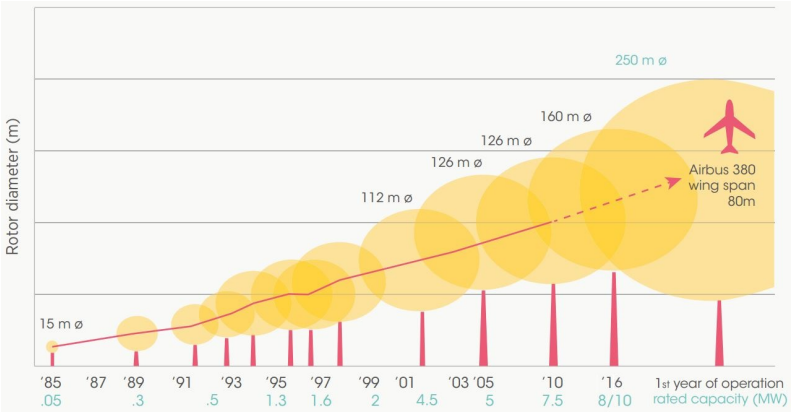

Figure 1.3 Growth in the size of wind turbines since 1985 [13]

With the rapid development of wind turbines, the penetration of wind power into the power grid continues to increase. This results in strict grid connection requirements for wind turbines which mainly concerns the power control capability and the grid fault ride-through capability. The reliability and availability of wind turbines become increasingly important, especially in offshore applications [15]. In the DFIG drive-train, which is currently the most applied, brushes and slip-rings are prone to failure and need frequent maintenance [16]. Although gearboxes do not have the highest failure rate compared with the other assemblies in wind turbines, their failures lead to the highest downtime [15]. These increasing demands of grid code requirements, reliability and availability prompt people to explore alternative wind turbine drive-trains. One of them is the brushless doubly-fed induction machine (DFIM) drive-train. This chapter will not discuss the existing wind generators and the brushless DFIM in detail. They will be further discussed in Chapter 2.

1.2 Motivation

This thesis is ultimately driven by exploring the brushless DFIM drive-train for wind turbine applications. The existing DFIG drive-train with a three-stage gearbox and a partially rated converter is so widely employed because it is cost-effective. The proposed brushless DFIM drive-train shares the same advantages of the DFIG drive-train, but also improves the intrinsic reliability due to the absence of brushes and slip-rings. The brushless DFIM is a medium speed generator and the high-speed gear stage of the gearbox is avoided. This increases the reliability and the efficiency of the system. Moreover, the brushless DFIM has a significantly improved low-voltage ride-through capability compared with a normal DFIG. The brushless DFIM has a great potential to be an industrial generator for multi-MW wind turbine applications because of these promising benefits.

1.3 Objectives

The electromagnetic coupling in the brushless DFIM is complicated resulting in complicated operating principles. This is mainly because the brushless DFIM has two stator windings with different pole-pair numbers and is supplied with different frequencies. These two stator magnetic fields are not coupled directly, but are cross-coupled through a special rotor. It is not straightforward to apply the classic design theory for normal induction machines (IMs) to design the brushless DFIMs. Chapter 2 will discuss the complicated operating principle and the existing modeling technologies in detail. Until now, the brushless DFIM has never been commercialized in wind turbine drive-trains since its performance has not yet been optimized to the industrial levels based on the current modeling technologies and design guidelines. The primary objective of this thesis can, therefore, be formulated as:

Modeling and design of brushless doubly-fed induction machines, to advance the development of this machine type for wind turbine applications.

To achieve the primary objective, this thesis makes efforts towards the following sub-objectives:

- *Apply and develop finite element models to constitute accurate and efficient design & optimization tools for brushless DFIMs.*
- *Investigate design guidelines for brushless DFIMs.*

1.4 Outline and approach

This thesis is organized as shown in Fig. 1.4. Most chapters cover both the modeling technique aspect and the design aspect, corresponding to the above two sub-objectives. Each chapter has its own focus and contributions, either on the modeling technique aspect or the machine design aspect. Chapters are mostly self-contained, having a separate introduction, method, results, and conclusions. Consequently, each chapter can be regarded as a separate topic related to the primary objective, and can be read largely independent of the other chapters. The detailed objective of each chapter is explained as follows:

Chapter 2 - Overview of brushless doubly-fed induction machines
Advantages and disadvantages of current wind generator systems and brushless DFIM based systems are briefly discussed. The operating principles of brushless DFIMs are introduced. A review study discussing the modeling and design is presented to highlight the need for FE models and the topics studied in the following chapters. The transient 2D FE model is illustrated as the basic approach throughout the thesis.

Chapter 3 - Computationally efficient 2D finite element model
The aim of this chapter is to develop a computationally efficient 2D FE model for the purpose of design & optimization. An FE based multi-objective optimization method is useful, which is also a trend in the design procedure of electrical machines. The normal transient 2D FE model presented in the previous chapter is time-consuming. It is not suitable for optimization purposes in which many candidate designs would be evaluated. This chapter proposes a fast FE model to predict the average torque, losses, and efficiency of brushless DFIMs using magneto-static FE solutions. To demonstrate its effectiveness, a purely FE based optimization approach combining the presented method and a genetic algorithm (NSGA-II) is applied to design a small-scale prototype. The influence of two construction variables, namely, pole-pair combinations and the number of loops per nest, on the steady-state performance is studied.

Chapter 4 - Analysis of the effects of skew using 2D transient multi-slice FE model
The aim of this chapter is to apply a 2D transient multi-slice FE model to investigate the effects of rotor skew on the performance of brushless DFIMs. A special nested-loop rotor is designed to couple both stator windings in brushless DFIMs. This leads to more undesired space harmonics in the air-gap magnetic field compared with conventional induction machines. This results

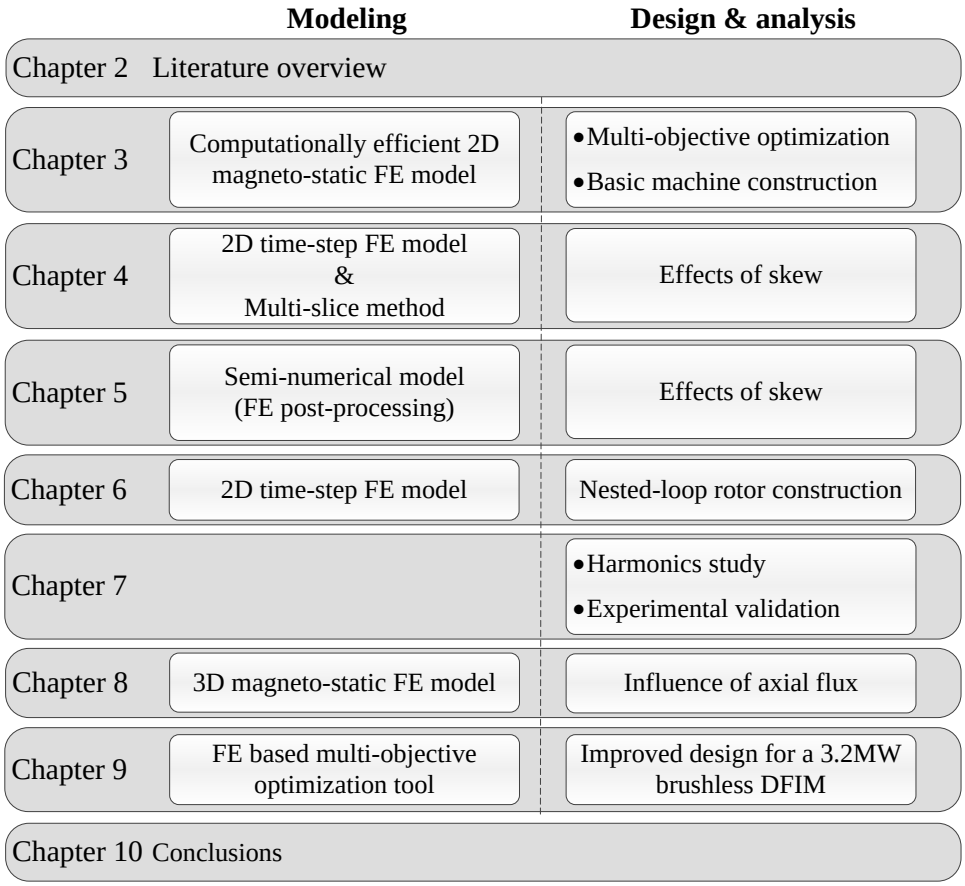

Figure 1.4 Thesis layout

in a concern about noise and vibration due to torque ripple, and a reduction of power quality because of increased total harmonic distortion (THD). Applying rotor skew is a benefit towards overcoming these natural drawbacks in brushless DFIMs. Additionally, this chapter can be regarded as a complement to the previous chapter since the torque ripple is not evaluated by the fast model in chapter 3.

Chapter 5 - FE post-processing for skew effects based on analytical harmonic analysis
The aim of this chapter is to develop a fast semi-numerical method to evaluate the effects of skew on the torque response. Chapter 4 presents a 2D multi-slice FE model to evaluate the skew effects on torque response. However, the conclusion cannot be easily be validated by taking measurements on the torque ripple or by 3D transient FE models which have not yet been well developed. Therefore, the initial purpose of this chapter is to look for an alternative method to support the effectiveness of the results obtained from 2D multi-slice FE models. Additionally, the multi-slice model is time-consuming which makes it inefficient at the stage of initial design. Therefore, the alternative method should be computationally efficient. This chapter presents a method applying well-known skew factors in the post-processing of a transient 2D FE model to evaluate the effects of skew on the torque response. An analytical harmonic analysis is also included in this chapter. It helps to understand the procedures of the presented semi-numerical method. This does not conflict with the primary objective of this thesis. On the other hand, the analytical derivation precisely promotes FE models in the design of brushless DFIMs.

Chapter 6 - Comparison of nested-loop rotors using 2D transient FE model
The aim of this chapter is to derive some design guidelines for nested-loop rotors by applying 2D transient FE models. The special nested-loop rotor is the key point to achieve cross-coupling between the two stator windings. However, there are not many design guidelines for a better nested-loop rotor. This chapter applies 2D FE models to evaluate the torque load-angle characteristics, the torque ripple, the efficiency and the grid THD of brushless DFIMs with sixteen different nested-loop rotors. The differences among them are the number of loops per nest and the position of an individual loop. The criteria of a better nested-loop rotor defined in this chapter are higher average torque and efficiency, but lower torque ripple and grid THD.

Chapter 7 - Experimental study of a brushless DFIM prototype
The aims of this chapter are to validate the harmonic analysis and study the influence of rotor skew and nested-loop configurations. However, the insulation between the rotor bars and the iron core is damaged which makes the experimental study not so perfect. The harmonic analysis in Chapter 5 is applied to derive the appropriate skew factors. The effectiveness of the presented semi-numerical method depends on the correctness of the harmonic analysis. In this chapter, space and time harmonics are validated by 2D FE simulations and by taking measurements on a prototype in simple induction operation mode. The measurements are carried out on nested-loop rotors without/with skewed slots to illustrate the effects of skew which is studied in Chapter 4. The measurements are also carried out on nested-loop rotors with different configurations to study the influence of different rotor configurations on the harmonics, as well as on the machine performance. Moreover, the 2D FE model and the 2D multi-slice FE model applied throughout this thesis are partially validated by the experimental study.

Chapter 8 - Analysis of axial flux due to skewed slots using 3D magneto-static FE model
The motivation of this chapter is to develop 3D FE models to investigate some 3D effects in brushless DFIMs. 3D FE models provide the possibilities to investigate the effects of end-windings, laminated iron cores, and eddy-current fields, etc., which are not taken into account in 2D FE models. In this thesis, studying the effects of skew is essentially a 3D problem as well. Therefore, the aim of this chapter is to implement a 3D magneto-static FE model with iterative solvers to study the influence of the axial flux due to skewed slots. Some comments are then given on the validity of the 2D multi-slice FE model that is presented in chapter 4.

Chapter 9 - Improved design for a 3.2MW brushless DFIM
The aim of this chapter is to bring together all the modeling methods and the design guidelines presented in the previous chapters for an improved design of a 3.2MW brushless DFIM. The FE based multi-objective optimization tool developed in this thesis is applied to optimize the active material costs and the efficiency of the case study machine.

Chapter 10 - Conclusions
Important conclusions are drawn in this chapter. The chapter lists the main contributions of this thesis and gives recommendations for future research.

CHAPTER 2

Overview of Brushless Doubly-Fed Induction Machines

The aim of this chapter is to give an overview of brushless doubly-fed induction machines (DFIMs). The advantages and disadvantages of current wind generators are discussed. The doubly-fed induction generator (DFIG) drive-train employs a fractionally rated power converter resulting in an advantage from an economic point of view. The brushless DFIM shares the same advantages of a DFIG. Moreover, the brushless DFIM has higher reliability and availability because it eliminates the need for brushes and slip rings. It also has a better grid fault ride-through capability. The brushless DFIM has two stator AC windings with different pole-pairs to avoid their direct magnetic coupling. The magnetic coupling is achieved through a unique rotor. This results in a complicated magnetic field with many undesirable space harmonics. A literature survey of modeling techniques and design related problems is presented. To study this complex machine, compared with analytical models, FE models have the advantages of taking into account not only saturation but also detailed geometries. A 2D transient FE model including rotor motion is then presented as the basic approach in this thesis.

2.1 Introduction

As mentioned in Chapter 1, the development of wind energy has progressed rapidly over the last decades. Various wind turbine concepts and wind generators have already been developed. However, the increasing demands of grid code requirements, reliability and availability prompt people to explore better wind turbine drive-train systems. The brushless DFIM based drive-train shows a great potential to be a variable speed generator for wind turbine applications.

The brushless DFIM is not a new electrical machine, but a special and complicated machine. This chapter gives a background overview to provide a basic understanding of brushless DFIMs. The questions to be answered in this chapter are as follows:

- Why are the brushless DFIMs attractive?
- What are the brushless DFIMs?
- How do the brushless DFIMs operate?
- What is the state of art on modeling and design of the brushless DFIMs?

This chapter starts with a brief introduction of common wind turbine generators which are currently used in the market. Their advantages and disadvantages are discussed to highlight the potential advantages of the brushless DFIM based wind turbine systems. Next, the stator and rotor constructions of the brushless DFIMs are introduced. Subsequently, the basic operating principles of the brushless DFIMs are explained. A literature survey is presented to provide an overview of modeling and design related problems of the brushless DFIMs. Finally, the 2D transient FE model including rotor motion for brushless DFIMs is illustrated as the basic approach throughout this thesis. Conclusions are drawn at the end.

2.2 Current wind turbine generators

Wind turbine concepts can be classified according to the rotation speed, the rating of the power converter related to the generator capacity and the drive-train construction. Considering the rotation speed, wind turbine concepts can be classified into fixed speed, limited variable speed and variable speed. Referring to the rating of the power converter related to the generator capacity, wind turbine concepts can be classified into generator systems with a partially-scale and a full-scale power converter. Considering the drive-train construction, wind turbine concepts can be classified into direct-drive and geared-drive wind turbines. The features, the advantages and the disadvantages of different wind turbine concepts are discussed in [14, 16, 17]. Not all of the existing wind turbine concepts will be mentioned in this section. The main aim of this section is to provide an overview of common wind generator systems which are currently used in wind turbine applications.

2.2.1 Synchronous generator

Electrically excited synchronous generator (EESG)

Fig. 2.1 shows the scheme of a variable speed direct-drive EESG system with a full-scale power converter. There is no gearbox in this concept. The generator rotor is directly connected to the hub of the turbine rotor so that the generator rotates at a low speed. This low speed makes it necessary to produce a high torque, leading to a generator with a large size. The stator has a normal three-phase winding while the rotor carries a field system provided with a DC excitation. This means brushes and slip rings are necessary to excite the rotor winding with DC. The EESG can control the flux to minimize the losses in different power ranges. The full-scale power converter can fully control the amplitude and frequency of the voltage at the generator side.Therefore, the generator speed can be controlled over a wide speed range. However, the full-scale power converter has a high cost and high power losses since all the generated power have to go through the converter. It was the most commonly used direct-drive generator around ten years ago [18] although Enercon still uses this concept in the market. The largest direct-drive EESD built by Enercon is E-126 with a rated power of 7.5MW [19].

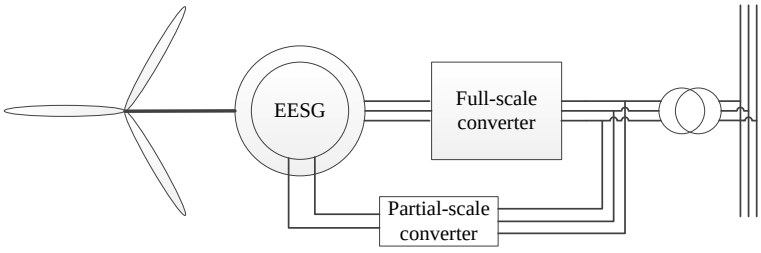

Figure 2.1 Scheme of a direct-drive EESG concept

Permanent magnet synchronous generator (PMSG)

Fig. 2.2 and Fig. 2.3 show the schemes of a variable speed PMSG system without and with a gearbox, respectively. Compared with the direct-drive system, the geared-drive system reduces the size of PMSGs at the expense of reliability. A full-scale power converter is necessary for both situations like the one in the EESG system. Compared with EESGs, the cost of PMs could be a big part of the total generator costs and an additional protection is needed against the demagnetization of PMs. However, PMSGs offer higher efficiency due to the absence of excitation losses. This leads to a higher power density. Moreover, reliability is improved due to the absence of brushes and slip rings. The regular maintenance cost will also decrease. PMSG is promising regarding

efficiency and reliability, especially for off-shore applications. Wind turbine manufacturers such as Goldwind and Mitsubishi have products using the direct-drive PMSG concept [20]. Manufacturers such as Areva Wind (formerly Multibrid GmbH) and WinWind use the geared-drive PMSG concept [16].

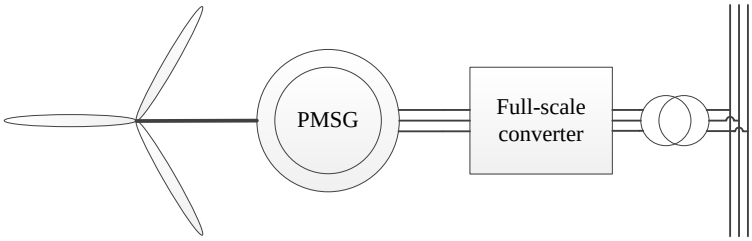

Figure 2.2 Scheme of a direct-drive PMSG concept

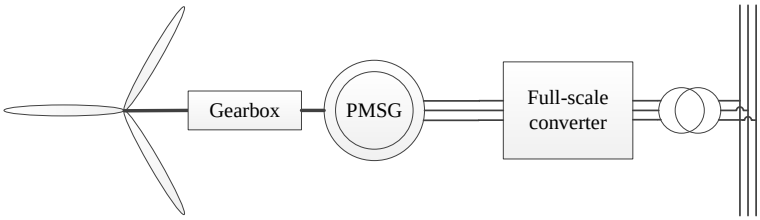

Figure 2.3 Scheme of a geared-drive PMSG concept

2.2.2 Induction generator

Squirrel-cage induction generator (SCIG)

Fig. 2.4 shows the scheme of a variable speed geared-drive SCIG system with a full-scale power converter. A SCIG is rugged and relatively cheap for mass production. However, the full-scale power converter leads to a high cost and high power losses as mentioned before. Siemens used this concept for some products in the market [20], however, this concept is not popular in the current market.

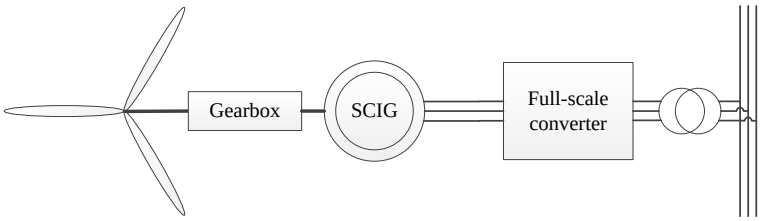

Figure 2.4 Scheme of a geared-drive SCIG concept

Wound rotor induction generator (WRIG)

Fig. 2.5 shows the scheme of a variable speed geared-drive WRIG system with a partially-scaled power converter. This configuration is well-known as the doubly-fed induction generator (DFIG) concept. The stator is directly connected to the grid while the rotor is connected through a power converter. The power converter can control the rotor frequency to control the rotation speed of the rotor. Typically, the rating of the converter is chosen as about 30% of the generator capacity that allows a speed variation of about ±30% around the synchronous speed [14, 16, 17]. The fractionally rated power converter makes this concept attractive from an economic point of view. However, the DFIG concept has some disadvantages of regular maintenance of brushes and slip-rings and complicated control strategies for grid fault ride-through capability. There are many wind turbine manufacturers, such as Vestas, Gamesa, Nordex, using this DFIG concept.

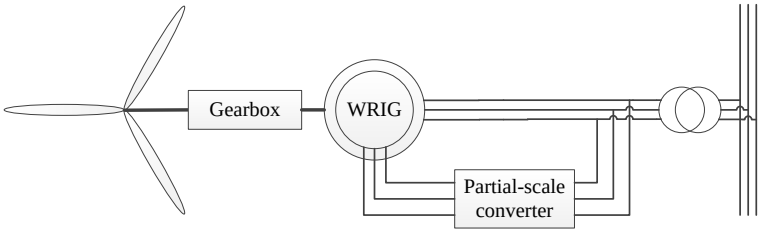

Figure 2.5 Scheme of a geared-drive WRIG (DFIG) concept

2.2.3 Potential advantages of brushless DFIMs

There are two ways of looking at everything. It is difficult to decide which wind turbine concept is the best one. Considering the market share's point of view, the DFIG system with a three-stage

gearbox and a partially-scale power converter is the most popular type in the current wind turbine market. This configuration is cost-effective because it makes use of widely available industrial components and adopts a low-cost partially rated power converter.

This thesis makes efforts to improve the reliability of this existing DFIG concept by using brushless doubly-fed induction machines (DFIMs). Fig. 2.6 shows the scheme of a variable speed geared-drive brushless DFIM system with a partially-scaled power converter. The brushless DFIM shares the same advantages as the commonly applied DFIG, but has some additional advantages:

- The reliability is improved by eliminating brushes and slip rings. The regular maintenance cost will decrease.
- The brushless DFIM is a medium-speed generator so that a two-stage gearbox can be used. The capital cost will reduce, and a higher reliability can be achieved.
- The brushless DFIM has a better grid fault ride-through capability [21, 22].

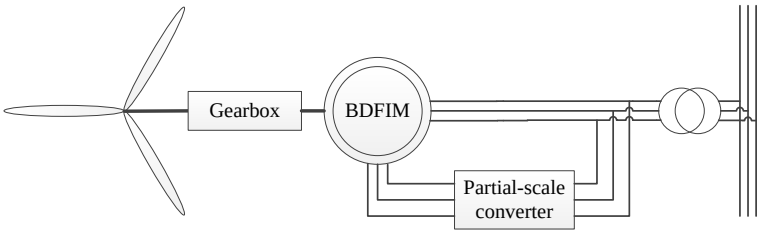

Figure 2.6 Scheme of a geared-drive brushless DFIM concept

2.3 Concept of brushless DFIMs

The idea of a brushless DFIM came from the self-cascaded machine. The concept of the modern brushless DFIM is essentially the same as that proposed by Burbridge and Broadway [23]. Fig. 2.7 shows a typical structure of a brushless DFIM. Both the stator and the rotor are different from normal induction machines.

2.3.1 Stator construction

A brushless DFIM has two stator three-phase AC windings. One of the stator windings is referred to as the power winding (PW), with p_p pole-pairs and is connected directly to the grid. The other one is called the control winding (CW), with p_c pole-pairs, and is connected to the grid through a partially rated power converter giving a variable frequency and voltage.

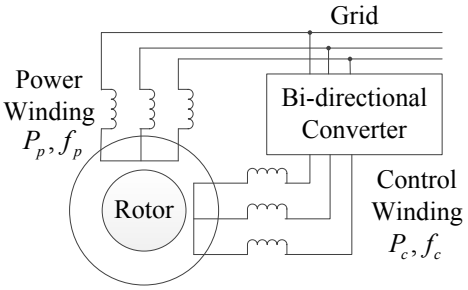

Figure 2.7 The concept of a brushless DFIM

One basic requirement for choosing the stator pole-pair combinations is to avoid the direct magnetic coupling between the PW and the CW. This can be guaranteed if and only if $p_p \neq p_c$. Moreover, if p_p, p_c are both even, $\max(\frac{p_p}{p_c}, \frac{p_c}{p_p})$ should not be odd to prevent higher space-harmonics of one stator field coupling to the other stator field [24]. For large-scale electrical machines, there is a further requirement for choosing the appropriate pole-pair combinations to avoid the unbalanced magnetic pull (UMP) on the rotor. p_p and p_c must be chosen so that $|p_p - p_c| \neq 1$ [24]. The stator pole-pair combination has a big influence on the performance of brushless DFIMs. It not only determines the operating speed, but also affects the level of harmonic distortions.

Besides the pole-pair selections, another issue can be considered on the stator side. Magnetic wedges can be applied to open slots in large-scale brushless DFIMs to lower magnetizing currents and improve the power factor [25]. However, magnetic wedges may result in an issue of unreliability.

2.3.2 Rotor construction

The PW and the CW have no direct magnetic coupling. The magnetic coupling is achieved through a special rotor. More precisely, each stator winding is directly coupled to the rotor and 'cross-coupled' via the rotor to the other stator winding. Several different rotor constructions have been proposed to provide the magnetic cross-coupling. Normally, three different kinds of rotors are under investigation, reluctance rotors, wound rotors and cage rotors.

Reluctance rotor

Compared to brushless doubly-fed machines with wound rotors and cage rotors, brushless doubly-fed reluctance machines (DFRMs) have slightly different operating principles. The reluctance rotors change the distribution of the air-gap permeance to achieve the magnetic cross-coupling between the PW and the CW. There are three types of reluctance rotors: the reluctance rotor with

simple salient poles, the segment reluctance rotor with magnetic barriers and the axially laminated anisotropic (ALA) reluctance rotor. Fig. 2.8 shows a segment reluctance rotor. Compared with the cage rotors, the reluctance rotors give a more effective capability of cross-coupling [26]. It can also be seen that the ALA reluctance rotor has a better synchronous operation and doubly-fed adjustable speed performance while the cage rotor gives better starting and asynchronous characteristics [27]. Moreover, recent advances have shown that brushless DFRMs with better designs can operate at high torque density and efficiency [28,29]. Therefore, brushless DFRMs can be potential alternatives to brushless DFIMs for wind turbine applications [30,31]. The Windrive project only focuses on the type of induction machines. Therefore, this thesis will not go further into brushless DFRMs. The comparison between brushless DFRMs and brushless DFIMs is open to be investigated.

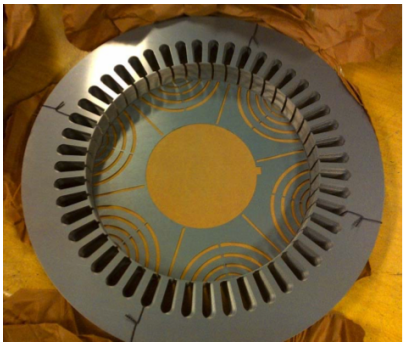

Figure 2.8 Reluctance rotor of brushless DFRM [28]

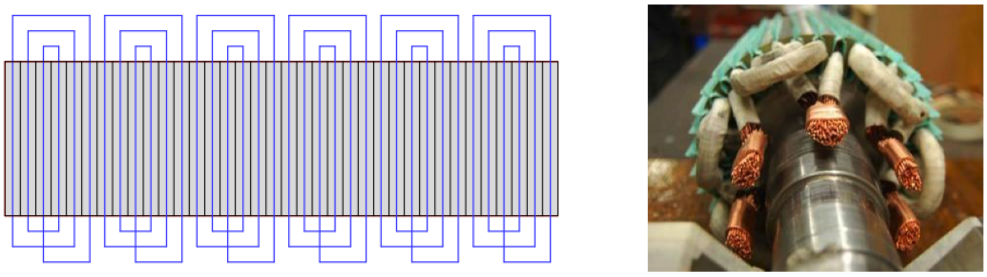

(a) Rotor winding diagrams **(b)** Prototype

Figure 2.9 Wound-loop rotor [32]

Wound rotor

Compared with the reluctance and cage rotors, wound rotors offer more flexible connections. Fig. 2.9 shows a simple series-wound rotor. It shows that the torque produced by this wound-loop rotor is not as big as the equivalent nested-loop rotor (shown in Fig. 2.10) [33]. However, to large-scale wind generators, a concern may arise about skin effects raising rotor resistance. In this situation, the wound rotors with multiple conductors in one slot or with multilayer windings may be attractive [34]. A more complicated double-Sine wound rotor is proposed for brushless DFIMs to reduce the space harmonics of the rotor winding. It is designed to be constructed double-layer unequal-turn coils based on the principles of tooth harmonic and sinusoidal winding [35, 36] and validated by a 60kW prototype [37]. However, it is not straightforward to manufacture such complicated wound rotors.

Cage rotor

Compared with wound rotors, cage rotors have the advantages of higher fill factors and lower impedance [26]. Several different cage rotors have been built and studied [24]. The standard squirrel cage rotor gives a weak cross-coupling capability as can be expected. Among the rotors which show a strong cross-coupling capability, the nested-loop rotor construction is considered favorable because of its simplicity. This construction is proposed and investigated by Broadway and Burbridge [23]. Fig. 2.10 shows a typical structure of the nested-loop rotor. This type of rotor is comprised of nested loops terminated with a common end ring at one end only. The nested-loop construction makes it possible to cast a cheap rotor using aluminum or copper. However, special steps must be taken to achieve bar-to-stack insulation since the performance of brushless DFIMs is significantly degraded due to inter-bar currents [38]. [39] presents methods to provide this insulation. Overall, the nested-loop rotor constructions are robust and cost effective to manufacture. This thesis will mainly focus on this type.

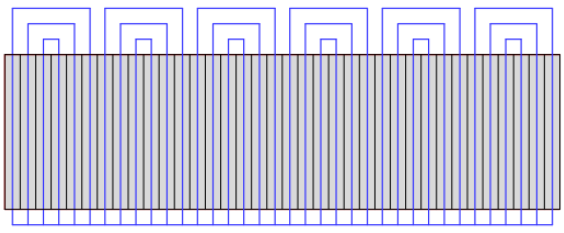

(a) Rotor winding diagrams

(b) Prototype

Figure 2.10 Nested-loop rotor [32]

2.4 Operating principles of brushless DFIMs

The brushless DFIM can be thought of as two induction machines which have different pole-pair numbers, with their rotors connected together both physically and electrically. Theoretically, it belongs to induction machines. However, it can operate like a synchronous machine with the use of a power converter connected to the CW.

2.4.1 Simple induction mode

The brushless DFIM can operate as an induction machine with p_p pole-pairs if the PW is supplied and the CW is open-circuited. On the other hand, it can also run as an induction machine with p_c pole-pairs when the CW is supplied, and the PW is open-circuited. This operation mode is referred to as simple induction mode.

2.4.2 Cascade induction mode

If the open-circuited stator winding is short-circuited, the brushless DFIM can operate like a cascade induction machine. This mode is referred to as cascade induction mode. These two modes are both asynchronous operation modes. They are not the operation modes desired for variable-speed wind generators. However, they are often applied in experimental measurements to evaluate rotor constructions [40, 41].

2.4.3 Synchronous operating mode

The brushless DFIM can also operate in synchronous mode, which is the desirable operating mode, and the one in which this kind of machines is typically analyzed. The synchronous operation mode depends on the cross-coupling of the fields produced by the PW and the CW. As mentioned previously, the magnetic coupling does not occur directly between two stator fields since they have different numbers of pole-pairs. It happens through a special nested-loop rotor. The PW has p_p pole-pairs and frequencyf_p. And the CW has p_c pole-pairs and frequency f_c. For ease of derivation, the magnetic flux density B_g in the air-gap produced by the stator windings can be expressed as follows:

$$B_{gp}(t,\theta_s) = \hat{B}_{gp}\cos(\omega_p t - p_p\theta_s + \varphi_p), \tag{2.1}$$

$$B_{gc}(t,\theta_s) = \hat{B}_{gc}\cos(\omega_c t + p_c\theta_s + \varphi_c), \tag{2.2}$$

where θ_s is the angle along the stator circumference, ω_p and ω_c are the angular frequencies of PW and CW which equal $2\pi f_p$ and $2\pi f_c$, and φ_p and φ_c are the initial phase angles of the PW and

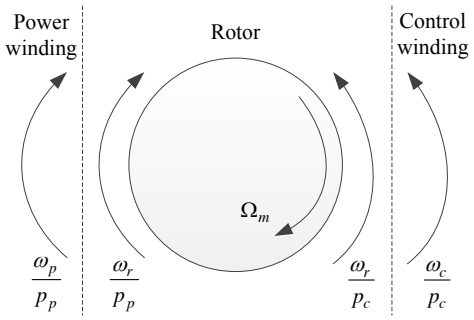

Figure 2.11 Rotating speed of fundamental magnetic fields in brushless DFIMs seen from the rotor

the CW, respectively. According to Fig. 2.11, considering the rotor mechanical angular velocity Ω_m, (2.1) and (2.2) can be expressed in a coordinate reference frame fixed to the rotor by using:

$$\theta_s = \theta_r + \Omega_m t, \tag{2.3}$$

where θ_r is the angle along the rotor circumference.

$$B_{gp}(t,\theta_r) = \hat{B}_{gp}\cos((\omega_p - p_p\Omega_m)t - p_p\theta_r + \varphi_p), \tag{2.4}$$

$$B_{gc}(t,\theta_r) = \hat{B}_{gc}\cos((\omega_c + p_c\Omega_m)t + p_c\theta_r + \varphi_c), \tag{2.5}$$

Therefore, the frequencies of the rotor currents ω_r induced by the PW and CW are:

$$\omega_{rp} = \omega_p - p_p\Omega_m, \tag{2.6}$$

$$\omega_{rc} = \omega_c + p_c\Omega_m. \tag{2.7}$$

The cross-coupling requires that the frequencies of rotor currents induced by the PW and CW should be the same. Considering $\cos(X) = \cos(-X)$, we have:

$$\omega_p - p_p\Omega_m = \pm(\omega_c + p_c\Omega_m). \tag{2.8}$$

Therefore, the synchronous angular speed can be derived as:

$$\Omega_m = \frac{\omega_p - \omega_c}{p_p + p_c} \quad (or \quad \Omega_m = \frac{\omega_p + \omega_c}{p_p - p_c}). \tag{2.9}$$

(2.9) gives the requirement on rotor speed for cross-coupling to occur. When $\omega_c = 0$, it is referred to as the 'natural synchronous speed'. The first condition is preferred in wind turbines applications, because it leads to a lower natural synchronous speed. In this way, a two-stage gearbox can be used which further improves the reliability.

As a wind turbine generator, the operating speed range of a brushless DFIM depends on the rating of the power converter. Similar to DFIMs, the rating of the converter is chosen as about 30% of the

total capacity to provide a speed variation of about 30% around the natural synchronous speed. Fig. 2.12 gives the relationship of the power of the PW and the CW at different speeds. When the brushless DFIM is at its natural speed, the CW neither supplies or generates power. When ω_c is positive, the sequence of the three-phase supply for the CW is opposite to the PW. The brushless DFIM is in the sub-synchronous operation mode in which the PW generates power, and the CW supplies power. When ω_c is negative, the brushless DFIM is in the super-synchronous operation mode in which both stator windings generator power.

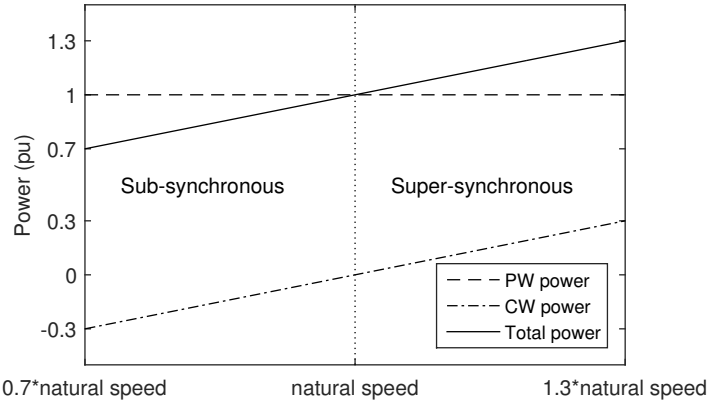

Figure 2.12 Sub- and super-synchronous ranges

Furthermore, there should be spatial compatibility for cross-coupling to happen. [42] provides a good understanding of the cross-coupling which is actually the interaction of the stator magnetic field with the rotor. In the rotor reference frame, the total stator magnetic field has many characteristics of a standing wave. It is a stationary pulsating wave with $(p_p + p_c)$ poles. This stator magnetic field is optimally coupled to a rotor that has the same number of poles. Therefore, for the nested-loop rotor construction, the number of rotor nests N_{nest} should equal $(p_p + p_c)$. Each loop within any nest can be seen as a short-circuited coil (shown in Fig. 2.10) and has a linkage with a pulsating magnetic field. Currents are induced in the loops to produce a rotor magnetic field which opposes the stator magnetic field. An electromagnetic torque is produced to force the rotor in the direction of minimum flux-linkage of nested loops.

When the previous requirements are met, the brushless DFIM produces a torque controlled by the relative position angle between the rotor and the stator magnetic field. This angle is referred to as load-angle. Fig. 2.13 gives the typical torque load-angle characteristic of a brushless DFIM. It indicates that the brushless DFIM can operate like a synchronous machine. The load-angle is controlled with respect to the applied shaft torque by changing the phase angle between the PW and CW currents. However, if the applied torque increases too much, the brushless DFIM cannot produce enough electromagnetic torque to operate in the stable range. The brushless DFIM will

then lose synchronism.

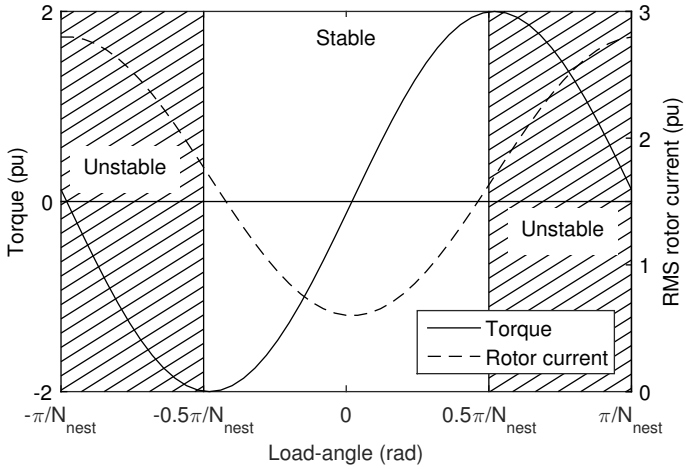

Figure 2.13 Torque load-angle characteristic

2.5 Overview of modeling and design of brushless DFIMs

Different kinds of models have been developed for brushless DFIMs. Generally, analytical models give more insight into the operating principles. However, finite element (FE) models have the advantage of high accuracy. Both methods are applied to investigate the machine operating characteristics or used for design and optimization purposes. This section presents a brief overview of modeling techniques, as well as design considerations, for modern brushless DFIMs.

2.5.1 Coupled-circuit model

The coupled-circuit model is also known as a coupled-coil model. It has been well applied to the modeling of electrical machines. The basic idea of the couple-circuit model essentially relates the currents and voltages of the stator and rotor as:

$$v = iR + \frac{d\phi}{dt}, \tag{2.10}$$

where v is the terminal voltage of a circuit, i is the current flowing in the circuit, R is the resistance of the circuit and ϕ is the flux linked by the circuit. The coupled-circuit model for the brushless

DFIM was first presented in [43] as:

$$\begin{bmatrix} v_p \\ v_c \\ 0 \end{bmatrix} = \left(\begin{bmatrix} R_p & 0 & 0 \\ 0 & R_c & 0 \\ 0 & 0 & R_r \end{bmatrix} + \omega_r \begin{bmatrix} 0 & 0 & \frac{dM_{pr}}{d\theta_r} \\ 0 & 0 & \frac{dM_{cr}}{d\theta_r} \\ \frac{dM_{pr}^T}{d\theta_r} & \frac{dM_{cr}^T}{d\theta_r} & 0 \end{bmatrix} \right) \begin{bmatrix} i_p \\ i_c \\ i_r \end{bmatrix} + \begin{bmatrix} M_p & 0 & M_{pr} \\ 0 & M_c & M_{cr} \\ M_{pr} & M_{cr} & M_r \end{bmatrix} \frac{d}{dt} \begin{bmatrix} i_p \\ i_c \\ i_r \end{bmatrix}, \tag{2.11}$$

where v_p, v_c and i_p, i_c are the voltages and currents of the PW and the CW, respectively. i_r is the rotor currents. R_p, R_c, R_r and M_p, M_c, M_r are the resistance and self inductance of the PW, CW and rotor loops, respectively. M_{pr} and M_{cr} are the PW-rotor and the CW-rotor mutual inductance. θ_r and ω_r are the rotor position and speed, respectively. (2.11) indicates that the mutual inductance between the PW and the CW is assumed to be zero for a well-designed brushless DFIM.

The coupled-circuit model has been applied to study the steady-state and dynamic characteristics of some certain specific brushless DFIM configurations [44,45]. However, the effects of the leakage inductance has not been addressed in their model. A *dq* transformation could be applied to the coupled-circuit model to reduce the model complexity [46, 47]. However, in fact, the *dq* model is more suitable for control and stability studies. These models do not have sufficient generality to provide design guidelines. A more generalized coupled-circuit model is presented in [48] and verified by measurements on a prototype in [49]. This model is then applied to study the influence of inter-bar currents on the performance of brushless DFIMs [38]. The coupled-circuit model has been further generalized for arbitrary winding connections [24, 50].

2.5.2 Electrical equivalent circuit (EEC) model

A *dq* model for a certain brushless DFIM construction is used to derive an equivalent circuit representation [46]. It is then applied to study power flows in that machine [51]. However, it is not a generalized derivation for a wide class of brushless DFIMs. [48] gives a generalized coupled-circuit model based on harmonic analysis, but this is not developed to an EEC model. The *dq* model has been transformed into complex symmetrical components which could be viewed as an EEC model [52]. The EEC model gains much interest because it is simple and its parameters have clear physical interpretations. It has been developed to take core losses into account [53, 54]. The EEC model can be combined with an MEC model to take saturation into account [55] and can be coupled with a lumped parameter thermal model to investigate the thermal limitation [56]. Recent research shows that the EEC model can be more simplified in synchronous mode, which makes it similar to conventional DFIMs [57]. The identification of the EEC parameters is not easy. Fig. 2.14 gives a simplified per-phase EEC in which the parameters can be identified by the measurements [58]. The parameters in Fig. 2.14 are obtained based on fitting to measured torque-speed curves [58]. Another method, using a range of different supply frequencies, has been proposed for the parameter identification [59].

The EEC model shown in Fig. 2.14 constitutes a useful tool to determine basic operating characteristics of the brushless DFIMs [60–62]. This EEC model provides a quantitative method to

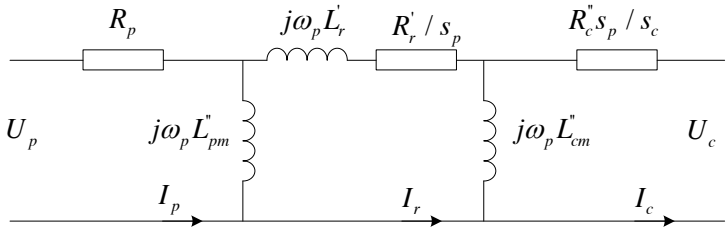

Figure 2.14 Simplified referred per-phase electric equivalent circuit

optimize the stator design [63, 64]. The machine dimensions are fixed while the slot areas of the PW and the CW and their numbers of turns per coil are to be optimized. The parameters of the original design are firstly extracted experimentally from the prototype. The EEC parameters of each prospective design are calculated based on the constant machine dimensions and the EEC parameters of the original design. The optimization is to find the maximum output power. The EEC parameters can be calculated or measured with different rotors. The rotor designs can be evaluated by comparing the steady-state performance predicted by the EEC model [32, 33, 65, 66]. Moreover, it can be applied to study the inverter rating [67]. It can even be used to investigate the effects of magnetic wedges in stator slots [68]. The EEC model has been applied to analyze the performance of a 250kW brushless DFIMs and validated by carrying out tests on the prototype [69]. This EEC model is then applied to design a 6MW medium-speed brushless DFIM for wind turbine applications [70].

However, the EEC model is not accurate enough for detailed design. Saturation is normally not taken into account in the calculation of EEC parameters [71]. Saturation effects can be considered in EEC parameters by combining the EEC model with an MEC model [55]. However, the modeling procedure is not straightforward.

2.5.3 Analytical magnetic field model

The stator and rotor currents can be calculated using the coupled-circuit model. Ampere's law is then applied to calculate the air-gap magnetic field analytically. Analytical magnetic field models provide more understanding in the machine operating mechanisms from the electromagnetic coupling point of view. A rigorous analytical magnetic field model considering the main magnetic field components, is presented in [48]. This has already been developed and takes slotting effects into account [42, 72]. Space- and time-harmonics can be then studied to gain a better understanding of the magnetic cross-coupling [73, 74]. The effects of these harmonics on the torque-speed characteristic are studied using a basic EEC model [75, 76]. The analytical magnetic field model can also be used to investigate the torque ripple [77, 78], as well as the noise and vibration in brushless DFIMs [79]. All these research studies show that the motion of the magnetic field in brushless DFIMs is not a simple rotation as in normal IMs. The complicated magnetic

field can be expected to have a significant harmonics due to special operating principles. This may lead to severe issues of harmonic distortions, torque ripple and core losses in brushless DFIMs.

2.5.4 Magnetic equivalent circuit (MEC) model

An MEC model is a compromise method between the analytical magnetic field model and the FE model. It has been successfully used to design studies of brushless DFIMs [80–82]. It is time efficient to predict the flux density, taking saturation effects into account at the initial design stage, compared with the much more accurate FE models.

2.5.5 Finite element modeling

The above analytical models have been widely applied to model and design brushless DFIMs. These analytical models make many contributions to providing a good insight into the operating principles and characteristics of this special machine. Previously, most research studies have regarded FE models as validation tools for their analytical models [54–56, 68, 83]. However, with the development of computer hardware and software technologies, FE models have been more and more applied to the design of electrical machines [84]. A 2D transient FE model has been built to study the core losses and saturation effects in brushless DFIMs [85]. A 2D FE model coupling the magnetic field, the electric circuit and the movement equations is presented to predict the performance of brushless DFIMs [37, 86]. It has been used to study the comparison between reluctance rotors and cage rotors [26, 87]. It has also been used to design wound rotors [35, 36, 88]. The FE model is the main tool to model and design brushless DFIMs in this thesis. The advantages of the FE model on the topics covered in this thesis are considered as follows.

FE model for optimization
Generally speaking, FE models have the advantages of accurately taking detailed physical dimensions and material properties into account. These features are needed more for brushless DFIMs. As mentioned before, brushless DFIMs have two stator magnetic fields with different pole-pair numbers. A special rotor is designed to couple both stator fields. This special construction leads to a complicated magnetic field. The two stator magnetic fields are added at some positions and subtracted at some other positions and results in the local saturation in brushless DFIMs. It is not straightforward to take the saturation in the normal analytical models into account for brushless DFIMs. The analytical models are generally accurate when the machine does not operate in the high saturation region. Therefore, the magnetic loading of the brushless DFIMs designed by the analytical models is relatively low to prevent the brushless DFIM operating in the high saturation region. FE models help to capture the local saturation and make best use of the material.

The effects of skew
Skewing rotor slots is proposed to deal with the concern of severe noise, vibrations and low output power quality in brushless DFIMs. These drawbacks are mainly because of the undesired

space-harmonics. Several aspects such as the stator winding distribution, the rotor construction, the slotting and the saturation make contribution to the space-harmonics. It is critical to consider all of these aspects to fully understand the influence of the space-harmonics on the torque and the stator voltages (and/or currents). One analytical model has been presented to study the effects of skew in brushless DFIMs [89]. However, it is assumed that the slotting effects of stator slots are negligible, the nested-loop rotor has one loop per nest, the rotor slots are rectangular shaped and saturation is ignored. Obviously, this analytical model is not accurate enough to investigate the effects of skew in detail. A 2D transient multi-slice FE model is applied to study the effects of skew in this thesis.

An FE post-processing method is also presented to study the effects of skew. The well-known skew factors are applied with the post-processing method based on the analytical derivation. This method keeps the accuracy of FE models while the analytical derivation helps to speed up the calculation.

Comparison of nested-loop rotors
As mentioned before, different rotors have been evaluated and compared using the EEC model. The EEC parameters are identified either by calculations or measurements. The accuracy of the EEC model depends on the accuracy of the parameters. The calculation of the EEC parameters is not accurate because saturation is hardly considered in the parameters. Moreover, the leakage inductance depends on the geometry which is not accurately considered in the analytical calculation. On the other hand, measurements results in more accurate EEC parameters. However, it is not practical to built all of the rotors for comparison. FE models take advantages of capturing the detailed configurations of nested-loop rotors. Moreover, it is flexible to be able to change the number of loops per nest and the distribution of loops in the FE model.

3D FE model
Most analytical and 2D FE models are assumed that the magnetic field does not vary along the axial direction. Some practical features such as end effects of eddy currents and end-windings, anisotropy of material properties, skewed slots, etc. are impossible or not straightforward to be modeled using analytical or 2D FE models. For instance, the effects of skew discussed in this thesis is essentially a 3D problem. The classic analytical models apply skew factors to approximately consider the effects of skew on the air-gap magnetic field. However, the analytical models do not take into account the variety of the air-gap permeance due to the shifting between the stator and the rotor. A set of normal 2D FE models taken at different positions along the axial direction can be applied to consider the variety of the air-gap permeance. However, the induced rotor currents are assumed to flow in the axial direction even if the rotor slots are actually skewed over a certain pitch. Axial flux due to skewed slots is ignored in 2D multi-slice FE models. The 3D FE model takes the advantage of looking into the influence of the axial flux.

Overall, FE models are especially suited to model the special brushless DFIM. Using FE analysis may lose some insights into the operating principles and possibly leads to very long calculation times. However, it actually shifts the required time from humans to computer for the purpose of improving the accuracy.

2.6 2D transient finite element model for brushless DFIMs

The 2D transient FE model is utilized as the basic approach throughout this thesis. Fig. 2.15 gives the general procedure for building a 2D FE model [90]. In this thesis, the FE analysis is performed by a combination of MATLAB to create and post-process the FE models and COMSOL Multiphysics to solve the FE models.

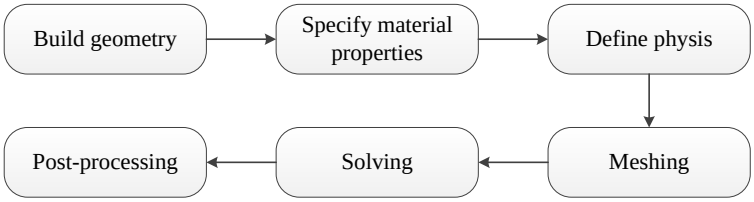

Figure 2.15 Steps of FE modeling

2.6.1 Assumptions

Several assumptions are made to simplify the 2D transient FE model:

- Neglect of eddy-current field: This assumption is guaranteed because the eddy currents are reduced significantly due to the laminated structure in the stator and rotor cores. In fact, it is not straightforward to determine the correct electric conductivity for the laminated core which is not in the scope of this thesis.
- Neglect of skin effects and proximity effects: This assumption is reasonable since the frequencies of the currents are not so high. It is useful to avoid too dense meshes in the domains of stator windings and rotor bars.

2.6.2 Physical model

Electromagnetic field equation

In two-dimensional Cartesian coordinates, the problem is posed on a domain Ω in the xy-plane and all field quantities are assumed to be z-independent. For machine modeling, Ω can be the cross-section perpendicular to the axial of the machine. Then the current density is assumed to

be perpendicular to Ω and only has J_z component. The electromagnetic field equation for the brushless DFIMs is formulated as (2.12) in terms of the magnetic vector potential [91, 92].

$$\frac{\partial}{\partial x}(\frac{1}{\mu}\frac{\partial A_z}{\partial x})+\frac{\partial}{\partial y}(\frac{1}{\mu}\frac{\partial A_z}{\partial y})+\sigma\frac{\partial A_z}{\partial t}=J_z(t), \tag{2.12}$$

where μ is the magnetic permeability of the material, σ is the electric conductivity of the material, A_z is the z component of the magnetic vector potential.

Calculation of induced rotor currents

Based on previous assumptions, the electric conductivity σ is set as zero in all domains. A field-circuit coupled model is then applied to calculate the unknown rotor currents [86]. Each loop of any nest can be considered as a short-circuited coil. The current depends on the flux linkage of that loop. Meanwhile, this rotor current affects the total flux. Fig. 2.16 gives the principle of a field-circuit coupled model.

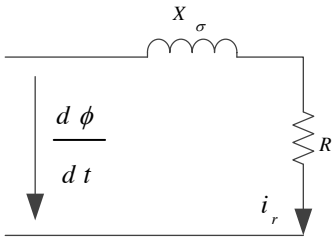

Figure 2.16 Field-circuit coupled model

The induced rotor current i_r can be related to the magnetic field as:

$$i_r=\frac{1}{R+X_\sigma}\frac{d\phi}{dt}, \tag{2.13}$$

in which R is the resistance of a rotor loop, X_σ is the leakage inductance of the end part and ϕ is the flux linkage of that loop.

$$\phi=\frac{L}{S}(\iint A_z dS_+-\iint A_z dS_-), \tag{2.14}$$

in which L is the axial length of the machine, S is the cross-sectional area of the rotor bar, S_+ and S_- are the integration areas corresponding to the go and return conductors, respectively [91]. (2.12) relates the unknown rotor currents with the resultant magnetic field. It is not calculated separately, but simultaneously with (2.12).

Modeling of motion

The algorithms of continuum mechanics usually makes use of two classical descriptions of motion: the Lagrangian description and the Eulerian description. In Lagrangian algorithms, each individual node of the computational mesh follows the associated material particle during motion while the computational mesh is fixed and the continuum moves with respect to the grid in Eulerian algorithms. A more flexible approach is the Arbitrary Lagrangian-Eulerian (ALE) description in which the nodes of computational mesh may be moved with the continuum in normal Lagrangian fashion, be held in a fixed Eulerian manner, or be moved in some arbitrarily specified way to give a continuous rezoning capability [93].

A reduced ALE method is applied to the rotating machines. Eulerian algorithms are applied to the stationary part (stator) with the stationary coordinate system represented by $x_j(x, y, z)$. Lagrangian algorithms are applied to the motion part (rotor) with the motion coordinate system represented by $X_i(X, Y, Z)$. As an example, we evaluate the magnetic vector potential A at particle X_i which locates x_j in stationary coordinate system. This can be described in the motion coordinate system and the stationary coordinate system respectively:

$$\begin{cases} A = A_X(X_i, t), & \text{in the motion coordinate system} \\ A = A_x(x_j, t), & \text{in the stationary coordinate system.} \end{cases} \tag{2.15}$$

Although two coordinate systems are used, the total time derivative of the quantity A should be equal:

$$\frac{DA_X}{Dt} = \frac{DA_x}{Dt}, \tag{2.16}$$

and therefore

$$\frac{\partial A_X}{\partial t}|_{X_i} + \frac{dX_i}{dt}\frac{\partial A_X}{\partial X_i}|_t = \frac{\partial A_x}{\partial t}|_{x_j} + \frac{dx_j}{dt}\frac{\partial A_x}{\partial x_j}|_t. \tag{2.17}$$

We already know that $\frac{dX_i}{dt} = 0$ in a motion coordinate system while $\frac{dx_j}{dt} = v_j$ in a stationary coordinate system. We therefore have that:

$$\frac{\partial A_X}{\partial t}|_{X_i} = \frac{\partial A_x}{\partial t}|_{x_j} + v_j\frac{\partial A_x}{\partial x_j}|_t. \tag{2.18}$$

The rotor seems stand still if we give the same rotational speed to the calculating mesh nodes. However, according to the Equation (2.18), the motion has, essentially, been taken into account.

Boundary condition

Generally, there are two boundary conditions applied in the machine modeling. They are magnetic insulation conditions applied to the most outer boundary of the machine and continuity conditions applied to the moving boundary between the stator and rotor. To most conventional electrical machines, periodic or anti-periodic boundary conditions are normally used to reduce

the computing time. However, it is not always straightforward to find continuity-periodic boundary conditions in brushless DFIMs since two stator windings have different pole-pairs and are fed with different frequencies. A 2D FE model with full geometry is built in this thesis. This is applicable to any stator pole-pair combination.

2.6.3 Meshing

Triangular elements are applied in this thesis. Fig. 2.17 shows triangular elements with different orders [94]. Second-order elements and higher-order elements lead to additional degrees of freedom on midpoint and interior nodes in the mesh elements. These additional degrees of freedom normally result in a more accurate solution at the expense of more memory being required. The 6-node quadratic elements are used in this thesis.

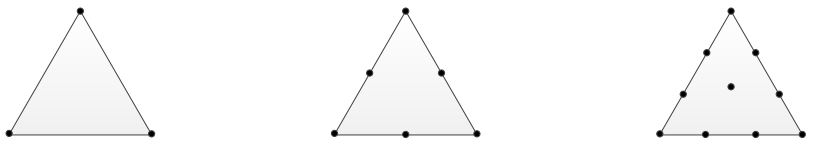

(a) 3-node linear **(b)** 6-node quadratic **(c)** 10-node cubic

Figure 2.17 Triangular elements

2.6.4 Adaptive time-step solver

In COMSOL Multiphysics, the default solver for the time-dependent study is an adaptive time-step solver. Users have to specify the tolerance (an absolute tolerance and a relative tolerance). COMSOL automatically adjusts the size of the time-step to the local variation in the computed solution to meet a certain local error criterion. This approach results in a smaller size of time-step in regions of rapid variation. It also leads to a larger size of time-step in regions of slow variation. Normally, the adaptive time-step solver leads to more efficient calculation [95].

2.6.5 Post-processing

Electromagnetic torque

The Maxwell's stress tensor method is applied to calculate the electromagnetic torque [90, 91]. The torque depends on the radial component B_r and the tangential component B_t of the air-gap

flux density and can be formulated as:

$$T = \frac{L}{\mu_0} \int_0^{2\pi} r^2 B_r B_t d\theta, \tag{2.19}$$

where μ_0 is the magnetic permeability of air, r is the radius of any contour circle in the air gap and θ is the angular position along the circumference of the contour circle.

If the first-order triangular elements are used, the solution for the magnetic vector potential A is relatively accurate. However, the flux density B and the magnetic field strength H are one order less accurate. Therefore, some modified Maxwell's stress tensor methods have been developed to increase the accuracy [96, 97]. Since the triangular element used in this thesis is second-order, those modified methods do not show the advantage of increasing accuracy. However, in this thesis, they are applied to predict the torque produced by the fundamental components of the magnetic field.

Core losses

The effects of eddy currents are not taken into account during the FE calculation while the core losses are calculated in the post-processing. The Modified Steinmetz Equation (MSE) is widely applied to evaluate core losses [98–101]. Hysteresis losses and eddy-current losses can be calculated as:

$$P_{hys} = k_h f^{\alpha} B^{\beta} v, \tag{2.20}$$

$$P_{ec} = k_e f^2 B^2 v, \tag{2.21}$$

where f is the frequency and B is the peak flux density, v is the volume, and k_h, k_e, α and β are material dependent constants provided by the material manufacturer.

2.7 Conclusion

With the rapid development of wind power conversion technology, various wind turbine concepts have been developed, and different wind generators have been built for the market. Each concept has its advantages and disadvantages. However, the trends towards increasing demands of grid code requirements, higher reliability and availability are the same for each concept. The brushless DFIM has advantages on these aspects compared with the current commonly applied DFIG. It has a great potential to be a variable speed wind generator. Although brushless DFIMs belong to induction machines, they could provide similar torque load-angle characteristics to normal synchronous machines. Analytical models are well developed in the literature. They have the advantages to provide more insight into the complicated operating principles of brushless DFIMs. They have been applied to analyze the steady state performance and investigate some design

problems, for example, noises and vibration, harmonic distortion and rotor designs etc. However, saturation is normally neglected in the analytical models when considering the complicated magnetic field in brushless DFIMs. The FE model has the advantage of taking into account not only saturation but also detailed geometries. FE models serve as the main tool in this thesis. The 2D transient FE model including rotor motion for brushless DFIMs is presented. The induced rotor currents are calculated by coupling a circuit equation to the field equations. The methods to calculate electromagnetic torques and core losses are given, and are implemented in post-processing.

CHAPTER 3

Computationally Efficient 2D Finite Element Model

The aim of this chapter is to develop a computationally efficient 2D finite element (FE) model for the purpose of design & optimization. The air-gap magnetic fields of brushless doubly-fed induction machines (DFIMs) are complicated because of the cross-coupling between two stator fields via a special nested-loop rotor. Compared with classical analytical models, transient FE modeling is easier for evaluating the machine performance taking saturation into account. However, it is not efficient to evaluate many candidates in a large design space using transient FE models considering the time cost. In transient simulation, the induced rotor currents are calculated by solving several time differential equations using backward differentiation formula (BDF). This chapter presents a computationally efficient FE analysis for brushless DFIMs based on the magneto-static solution. The induced rotor currents can be calculated based on a space-time relationship of the rotor currents derived analytically. The average torque, losses, and efficiency can also be predicted using magneto-static solutions. Each possible design can be evaluated within one to two minutes on a personal workstation. The efficient analysis is validated by the transient FE results. The presented model is applied to the optimization of a small-scale prototype. The influence of two construction variables, namely, pole-pair combinations and the number of loops per nest, is studied. One pole-pair combination is selected to manufacture the prototype used in the experiments in this thesis.

Most parts of this chapter have been published in

- X. Wang, T. D. Strous, D. Lahaye, H. Polinder, and J. A. Ferreira, "Finite Element Modeling of Brushless Doubly-Fed Induction Machine Based on Magneto-Static Simulation," in *IEEE Int. Electric Machines Drives Conf. (IEMDC)*, Coeur d'Alene, USA, May 2015.
- X. Wang, T. D. Strous, D. Lahaye, H. Polinder, and J. A. Ferreira, "Modeling and Optimization of Brushless Doubly-Fed Induction Machines Using Computationally Efficient Finite-Element Analysis," *IEEE Trans. on Industry Applications*, vol.52, no.6, 2016.

3.1 Introduction

The brushless DFIM is a potentially attractive choice for a variable-speed wind generator because of its additional advantages compared with the DFIM. However, the brushless DFIM also has some disadvantages such as higher manufacturing cost, slightly larger dimensions, and lower efficiency compared with a DFIM with the same rating [61]. The brushless DFIM has never been commercialized because its performance has not yet been created to the desired industrial levels. Therefore, it is important to improve the design for the brushless DFIM to make it commercially viable.

Chapter 2 reviewed the existing modeling techniques for brushless DFIMs including analytical modeling and FE modeling. The air-gap of a brushless DFIM contains two main magnetic fields with different pole-pair numbers and different frequencies resulting in a complex distribution of the magnetic field. Therefore, analytical models are not straightforward to take saturation effects into account, while the machine is typically designed to work in the saturation region to make efficient use of the materials. FE modeling has the advantages of considering the complex geometry and saturation effects. A normal transient FE model is presented in Chapter 2 and applied to analyze the performance of brushless DFIMs. However, the adaptive solver of transient simulation results in a small time step to solve the electromagnetic diffusion equations and the time differential equations for induced rotor currents. A certain period of tens or hundreds of time-step is simulated to predict the machine performance. It is not efficient to evaluate many design candidates by combining a transient FE model with some optimization algorithms. Several methods are proposed for a fast FE calculation and have been applied to analyze the PM machines [102], [103]. However, it is more complicated to analyze induction machines. This is because the induced rotor currents are calculated by simultaneously coupling several circuit equations together with the resultant magnetic field. These coupled equations are solved using the backward differentiation formula (BDF) in COMSOL Multiphysics used in this thesis. Several simulations (depending on the BDF order) at adjacent time moments are needed to solve the time differential equations for the induced rotor currents.

This chapter presents a novel method to calculate the induced rotor currents in brushless DFIMs. The features at two positions in one magneto-static can be transformed to those at two moments based on a special space-time relationship of the induced rotor currents. Then the currents can be calculated using a single static simulation. The average torque, losses, and efficiency can also be predicted using one static solution. Compared with the transient simulation, the presented model can predict the machine performance accurately but reduce the simulation time significantly.

In this chapter, the space-time relationship of the magnetic field in the rotor reference is derived considering the symmetry of the magnetic circuit and the periodicity of the electromagnetic field. Next, the methods to calculate the rotor currents, electromagnetic torque and losses using magneto-static FE solution are described. The simulation results are then validated by the transient results. Subsequently, the model presented is applied to the optimization of a prototype. The influence of pole-pair combinations and the number of loops per nest is studied. Finally,

conclusions are drawn. Table 3.1 gives the main specifications of the brushless DFIM studied. The rated operating point is studied in this chapter.

Table 3.1 Main specifications of the brushless DFIM studied

Description	Machine parameter	Value
Axial length [m]	l_{stk}	1.60
Air-gap length [mm]	l_g	1.5
Stator outer radius [m]	r_{so}	0.83
Stator inner radius [m]	r_{si}	0.67
Rotor inner radius [m]	r_{ri}	0.58
Number of phases	N_{ph}	3
Number of pole-pairs	p_p, p_c	4, 6
Rated frequency [Hz]	f_p, f_c	50, -10
Number of stator slots	N_{ss}	72
Number of rotor nests	N_{nest}	10
Number of loops per nest	q_r	3
Rotational speed [rad/s]	Ω_m	37.7
Slot current density [A/mm^2]	J	4
Rated power [MW]	P	3.2

3.2 Space-time transformation

By being rewritten in the rotor reference frame, one space-time relationship of the stator magnetic field can be obtained. The angular frequency of the electric quantities in the rotor can be defined by:

$$\omega_r = \omega_p - p_p\Omega_m = \frac{p_c\omega_p + p_p\omega_c}{p_p + p_c}. \tag{3.1}$$

Then the flux density created by stator winding in the rotor reference frame (2.4), (2.5) can be rewritten as:

$$B_{gp}(t,\theta_r) = \hat{B}_{gp}\cos(\omega_r t - p_p\theta_r + \varphi_p), \tag{3.2}$$

$$B_{gc}(t,\theta_r) = \hat{B}_{gc}\cos(\omega_r t + p_c\theta_r + \varphi_c). \tag{3.3}$$

The total flux density B_{gs} can be written as:

$$B_{gs}(t,\theta_r) = \hat{B}_{gp}\cos(\omega_r t - p_p\theta_r + \varphi_p) + \hat{B}_{gc}\cos(\omega_r t + p_c\theta_r + \varphi_c). \tag{3.4}$$

Van der Blij *et al.* [104] indicates that, in the rotor reference frame, the flux density created by stator windings has frequency ω_r and $(p_p + p_c)$ poles. It is optimally coupled to a rotor which has the same number of poles. Therefore, for a commonly used nested-loop rotor structure, the number of nests N_{nest} equals to $(p_p + p_c)$. Furthermore,

$$B_{gs}(t,\theta_r - 2\tau) = \hat{B}_{gp}\cos(\omega_r t - p_p\theta_r + p_p 2\tau + \varphi_p) + \hat{B}_{gc}\cos(\omega_r t + p_c\theta_r - p_c 2\tau + \varphi_c), \tag{3.5}$$

where

$$\tau = \frac{2\pi}{p_p + p_c}. \tag{3.6}$$

Then

$$\begin{aligned} &B_{gs}(t,\theta_r - 2\tau) \\ &= \hat{B}_{gp}\cos(\omega_r t - p_p\theta_r + p_p 2\tau + \varphi_p - 2\pi) + \hat{B}_{gc}\cos(\omega_r t + p_c\theta_r - p_c 2\tau + \varphi_c + 2\pi) \\ &= \hat{B}_{gp}\cos(\omega_r t - p_p\theta_r + \varphi_p + (p_p - p_c)\tau) + \hat{B}_{gc}\cos(\omega_r t + p_c\theta_r + \varphi_c + (p_p - p_c)\tau). \end{aligned} \tag{3.7}$$

$$\begin{aligned} &B_{gs}\left(t + \frac{p_p - p_c}{\omega_r}\tau, \theta_r\right) \\ &= \hat{B}_{gp}\cos(\omega_r t + (p_p - p_c)\tau - p_p\theta_r + \varphi_p) + \hat{B}_{gc}\cos(\omega_r t + (p_p - p_c)\tau + p_c\theta_r + \varphi_c). \end{aligned} \tag{3.8}$$

We can see:

$$B_{gs}(t,\theta_r - 2\tau) = B_{gs}\left(t + \frac{p_p - p_c}{\omega_r}\tau, \theta_r\right). \tag{3.9}$$

Then the induced rotor current due to B_{gs} will also follow the similar relationship:

$$I_r(t,\theta_r - 2\tau) = I_r\left(t + \frac{p_p - p_c}{\omega_r}\tau, \theta_r\right). \tag{3.10}$$

Equations (3.9) and (3.10) mean, in the rotor reference frame, that the flux density and its induced rotor current at position $(\theta_r - 2\tau)$ which is 2τ behind the position θ and the instant t time is equal to that at the position θ_r and the instant $\left(t + \frac{p_p - p_c}{\omega_r}\tau\right)$ time which is $\left(\frac{p_p - p_c}{\omega_r}\tau\right)$ time before t moment. This relationship gives the ideas of the rotor current calculation and an approximate way for the rotor core losses calculation in the FE modeling section.

3.3 Computationally efficient FE analysis

3.3.1 Assumptions

We have two assumptions throughout the modeling for the purpose of simplification:

1. The field produced by eddy currents in the stator and rotor core has little influence on the main field. These eddy currents are ignored during the calculation while the core losses are computed in post-processing. This assumption is met because the eddy currents are reduced significantly due to the lamination structure in the core.

2. The skin-effect and the proximity-effect are ignored for the stator windings and solid rotor bars. This assumption will be briefly discussed in subsection 3.4.4.

These two assumptions lead to the electric conductivity being zero in the computing domains. For saving simulation time, they are also useful for avoiding too dense meshes.

3.3.2 Induced rotor currents

Transient FE model

The main magnetic fields are created by the stator and rotor currents flowing in the axial direction. In this case, the problem can be written in a domain in the xy-plane which could be the cross-section perpendicular to the axial direction and all field quantities are assumed to be z-independent. In the case when the electric conductivity σ is set as zero, the two-dimensional electromagnetic field equation is:

$$\frac{\partial}{\partial x}\left(\frac{1}{\mu}\frac{\partial A_z}{\partial x}\right)+\frac{\partial}{\partial y}\left(\frac{1}{\mu}\frac{\partial A_z}{\partial y}\right)=J_z(t). \tag{3.11}$$

where μ is the magnetic permeability of the material, A_z is the z component of the magnetic vector potential and J_z is the externally applied current density.

In the air-gap and the iron domains J_z is zero. In the stator conductor domains, the stator currents are known as inputs:

$$J_{p(c)}(t)=\hat{J}_{p(c)}\sin\left(\omega_{p(c)}t+\phi_{p(c)}\right). \tag{3.12}$$

In the rotor conductor domains, the rotor currents are unknown. According to Fig. 3.1, each closed loop has an independent circuit equation as:

$$e_r^{nx}+I_r^{nx}R_{bar}^{nx}=0, \tag{3.13}$$

where I_r^{nx} and R_{bar}^{nx} are the instant rotor current and the resistance of the n^{th} loop in the x^{th} nest (shown in Fig. 3.1). The resistance of the end part is taken into account in R_{bar}^{nx}. e_r^{nx} is the back electromotive force (EMF) of the n^{th} loop in the x^{th} nest, which can be calculated as [91]:

$$e_r^{nx}=-\frac{d\phi^{nx}}{dt}=-\frac{l_{stk}}{S_{bar}^{nx}}\frac{d\left(\iint A_z dS_+^{nx}-\iint A_z dS_-^{nx}\right)}{dt}, \tag{3.14}$$

where ϕ^{nx} is the flux linkage, l_{stk} is the machine axial length, S_{bar}^{nx} is the cross-sectional area of the rotor bar, S_+^{nx} and S_-^{nx} are the surface of the go and return conductors, respectively. By substituting (3.14) into (3.13), the J_z applied in the domain of rotor conductor of the n^{th} loop in the x^{th} nest is:

$$J_r^{nx}=\frac{I_r^{nx}}{S_{bar}^{nx}}=\frac{l_{stk}}{R_{bar}^{nx}\left(S_{bar}^{nx}\right)^2}\frac{d\left(\iint A_z dS_+^{nx}-\iint A_z dS_-^{nx}\right)}{dt}. \tag{3.15}$$

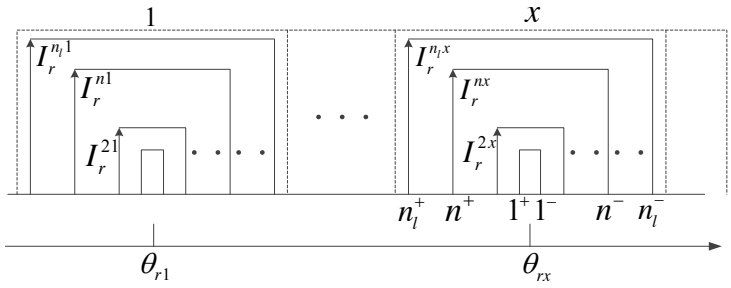

Figure 3.1 Nested-loop rotor structure

(3.15) is applicable to all loops of all nests. It actually relates the unknown rotor currents with the total resultant magnetic field in which both stator and rotor currents are taken into account.

COMSOL Multiphysics, a commercial FE software is utilized to solve the partial differential equation (3.11). The rotor rotation is modeled by using Arbitrary Lagrangian-Eulerian (ALE) formulation in the transient model. BDF is applied to solve the coupled time differential equations. It needs several solutions (depending on the BDF order taken by the solver) at several adjacent time moments with small time steps. The time-step is adaptive depending on the error tolerance and the convergence in COMSOL Multiphysics. The size of the time-step can be increased with increasing the error tolerance. This leads to a fast calculation but at the expense of accuracy. However, using a big time-step is a risk since the FE calculation sometimes does not converge at all.

Magneto-static FE model

The static electromagnetic field equation has the same form as (3.11) while J_z is no longer a function of time t. Any instantaneous time moment t_s in the previous transient model can be achieved by rotating the rotor geometry manually with a mechanical angle $\Omega_m t_s$ in the magneto-static model.

In the air-gap and the iron domains J_z is still zero. In the stator conductor domains

$$J_{p(c)} = \hat{J}_{p(c)} \sin\left(\omega_{p(c)} t_s + \phi_{p(c)}\right). \tag{3.16}$$

In the rotor conductor domains, it is not possible to carry out the time derivative of (3.14), (3.15) in a magneto-static simulation. However, if the fundamental angular frequency ω_r of rotor currents dominates, compared with the higher frequencies, one fictitious rotor current density could be obtained from the flux linkage multiplied by ω_r. In a magneto-static model at t_s moment, the instantaneous fictitious current density in a loop belonging to the nest at θ_{r1} position, as well as

the $\theta_{r2} = \theta_{r1} - 2\tau$ position, can be obtained as:

$$J_{rf}^{n}(t_s, \theta_{r1}) = \frac{l_{stk} \cdot \omega_r}{R_{bar}^{n\theta_{r1}} \left(S_{bar}^{n\theta_{r1}}\right)^2} \left(\iint A_z dS_{+}^{n\theta_{r1}} - \iint A_z dS_{-}^{n\theta_{r1}} \right), \tag{3.17}$$

$$J_{rf}^{n}(t_s, \theta_{r2}) = \frac{l_{stk} \cdot \omega_r}{R_{bar}^{n\theta_{r2}} \left(S_{bar}^{n\theta_{r2}}\right)^2} \left(\iint A_z dS_{+}^{n\theta_{r2}} - \iint A_z dS_{-}^{n\theta_{r2}} \right). \tag{3.18}$$

It is obvious that the fictitious current densities are not real physical ones. They are not equal to those given by (3.15) in the transient model at t_s moment. However, the space-time transformation presented in section 3.2 gives an idea as to how to obtain the real physical rotor current density from (3.17) and (3.18). Actually, the key idea is that the need of solutions at different time moments can be substituted by the solutions in different positions at one time moment. The detailed explanations are as follows.

It is assumed that the fundamental frequency ω_r of rotor currents dominates compared with the higher frequencies. Then it is reasonable to formulate the flux linkage of the n^{th} loop in the x^{th} nest as:

$$\phi^{nx}(t) = \hat{\phi}^{nx} \sin\left(\omega_r t + \varphi_0^{nx}\right). \tag{3.19}$$

By substituting (3.19) into (3.14), the rotor current density of (3.15) could be expressed as:

$$J_r^{nx}(t) = \frac{1}{R_{bar}^{nx} S_{bar}^{nx}} \frac{d\phi^{nx}(t)}{dt} = \hat{J}_r^{nx} \cos\left(\omega_r t + \varphi_0^{nx}\right). \tag{3.20}$$

Without calculating the time derivative, one fictitious rotor current density could be defined by considering (3.15) and (3.19).

$$J_{rf}^{nx}(t) = \frac{1}{R_{bar}^{nx} S_{bar}^{nx}} \phi^{nx}(t) \cdot \omega_r = \hat{J}_{rf}^{nx} \sin\left(\omega_r t + \varphi_0^{nx}\right). \tag{3.21}$$

The fictitious rotor current density $J_{rf}^{nx}(t)$ has the same amplitude and frequency as the real physical rotor current density $J_r^{nx}(t)$, but with a 90 degree phase shift. Then (3.17) and (3.18) can be formulated as (3.22) and (3.23) by considering (3.10) as follows

$$J_{rf}^{n}(t_s, \theta_{r1}) = \hat{J}_{rf}^{n\theta_{r1}} \sin\left(\omega_r t_s + \varphi_0^{n\theta_{r1}}\right), \tag{3.22}$$

$$J_{rf}^{n}(t_s, \theta_{r2}) = J_{rf}^{n}\left(t_s + \frac{p_p - p_c}{\omega_r}\tau, \theta_{r1}\right) = \hat{J}_{rf}^{n\theta_{r1}} \sin\left(\omega_r \left(t_s + \frac{p_p - p_c}{\omega_r}\tau\right) + \varphi_0^{n\theta_{r1}}\right). \tag{3.23}$$

Therefore, two unknowns $\varphi_0^{n\theta_{r1}}$ and $\hat{J}_{rf}^{n\theta_{r1}}$ can be solved by (3.22) and (3.23).

$$\varphi_0^{n\theta_{r1}} = \arctan\left\{ \frac{\sin[(p_p - p_c)\tau]}{\frac{J_{rf}^{n}(t_s, \theta_{r2})}{J_{rf}^{n}(t_s, \theta_{r1})} - \cos[(p_p - p_c)\tau]} \right\}, \tag{3.24}$$

$$\hat{J}_{rf}^{n\theta_{r1}} = \frac{J_{rf}^{n}(t_s, \theta_{r1})}{\sin\left(\omega_r t_s + \varphi_0^{n\theta_{r1}}\right)}. \tag{3.25}$$

Then, the J_r finally applied in the domain of the rotor conductor of the n^{th} loop in the nest locating θ_{r1} position at t_s moment is reconstructed as:

$$J_r^{n\theta_{r1}} = \hat{J}_{rf}^{n\theta_{r1}} \cos\left(\omega_r t_s + \varphi_0^{n\theta_{r1}}\right). \tag{3.26}$$

Similarly to the transient model, the unknown rotor currents are not calculated separately from the field equation. They are formulated as functions of A_z and calculated together with the field equation. In most commercial FE packages, the initial value for A_z is zero in magneto-static simulations. In this paper, one magneto-static simulation is first performed, in which J_z set as zero in all rotor conductor domains. Its solution is then specified as the initial value for A_z in the complete magneto-static model in which J_r is specified as (3.26). Numerical results show that this approach accelerates the convergence of the computations.

3.3.3 Electromagnetic torque and power

Maxwell's stress tensor method indicated by (3.27) is used for the torque calculation.

$$T_e = \frac{l_{stk}}{\mu_0} \int_0^{2\pi} r^2 B_r B_t d\theta, \tag{3.27}$$

where μ_0 is the magnetic permeability of the vacuum, r is the radius of the air-gap, B_r and B_t are the radial and tangential components of the flux density in the air-gap. The average torque is considered the torque produced due to p_p and p_c pole-pair fields. The torque ripple is not considered in the study. The Maxwell stress harmonic filter method presented in [96,97]is applied to calculate the torque due to p_p and p_c pole-pair fields only. The flux density can be analytically expressed in Fourier series:

$$B_r(\theta) = B_{r0} + \sum_{n=1}^{\infty} [a_{rn}\cos(n\theta) + b_{rn}\sin(n\theta)], \tag{3.28}$$

$$B_t(\theta) = B_{t0} + \sum_{n=1}^{\infty} [a_{tn}\cos(n\theta) + b_{tn}\sin(n\theta)]. \tag{3.29}$$

The torque due to the n^{th} component can be calculated as:

$$T_n = \frac{\pi r^2 l_{stk}}{\mu_0}(a_{rn}a_{tn} + b_{rn}b_{tn}). \tag{3.30}$$

Then the main torque can be calculated as:

$$T_{main} = T_{p_p} + T_{p_c}. \tag{3.31}$$

Finally, the calculation of the main electromagnetic power is straightforward:

$$P_{main} = T_{main} \cdot \Omega_m. \tag{3.32}$$

3.3.4 Losses and efficiency

For the core losses calculation, only the radial component of flux density is considered in the teeth part and only the tangential component is considered in the yoke part. There are two rotating fields, due to the power winding and the control winding, without direct magnetic coupling in the stator. The stator magnetic field has two fundamental frequencies (i.e. f_p, f_c). Generally speaking, f_c is smaller than f_p which means that the time oscillation of the p_p pole-pair component is superimposed on that of p_c pole-pair component. Therefore, the eddy-current losses include two components due to p_p and p_c pole-pair fields. The hysteresis loss is considered by approximately assuming the magnetic field in the stator core as a pure sinusoidal waveform with amplitude B_{eq} and frequency f_p [101]. The stator core losses can be evaluated by the Modified Steinmetz Equation (MSE) as:

$$P^s_{core} = k_e(f_p^2 B^2_{p,max} + f_c^2 B^2_{c,max})\upsilon_s + k_h f_p^\alpha B^\beta_{eq}\upsilon_s, \tag{3.33}$$

where,

$$B_{eq} = \sqrt{B^2_{p,max} + B^2_{c,max}}, \tag{3.34}$$

υ_s is the volume of the stator core in units of m^3, α and β are material-dependent constant exponents, k_e and k_h are the eddy current loss factor and the hysteresis loss factor, respectively. The amplitude of the flux densities in the stator core due to p_p and p_c pole-pair fields (i.e. $B_{p,max}$, $B_{c,max}$) can be obtained by performing space FFT to the flux densities of all teeth and their corresponding yoke part.

In the rotor reference frame, the variation of the magnetic field has characteristics of a standing wave. The variations of the flux density of different parts in the rotor yoke and teeth have the same fundamental frequency (i.e. f_r), but with different amplitudes. According to (3.9), the distribution and variation of the flux density in each nest are approximately equal but with some time delay. If only the fundamental component is considered, the rotor core losses can be calculated as:

$$P^r_{core} = k_e f_r^2 B^2_{rotor,max}\upsilon_r + k_h f_r^\alpha B^\beta_{rotor,max}\upsilon_r, \tag{3.35}$$

Table 3.2 Specifications of laminated core(M800-65A) [101]

Description	Parameter	Value
Hysteresis loss factor	k_h	273.2
Eddy current loss factor	k_e	0.4786
Lamination thickness [mm]	d_t	0.65
Resistivity [nΩm]	ρ	390
MSE constant	α	1.2558
MSE constant	β	1.685

where v_r is the volume of the rotor core in units of m^3. One static simulation can give $(p_p + p_c)/2$ points along the rotor circumference with same space interval 2τ. According to the space-time relationship given by equation(3.9), these $(p_p + p_c)/2$ points are with same time interval $\tau(p_p - p_c)/\omega_r$ in one rotor electrical cycle $1/f_r$. This means that one magneto-static solution is enough to approximately estimate the amplitude of the flux density $B_{rotor,max}$. Table 3.2 gives all the specifications of electric steel used in the stator and rotor core.

The copper losses calculation is straightforward as:

$$P_{copper}^{s(r)} = I_{s(r)}^2 R_{s(r)}. \tag{3.36}$$

Then the efficiency is calculated as:

$$\eta = \frac{P_{main}}{P_{main} + P_{core}^s + P_{core}^r + P_{copper}^s + P_{copper}^r}. \tag{3.37}$$

3.4 Simulation results and discussions

3.4.1 Induced rotor currents

Fig. 3.2 shows the waveform of the rotor current obtained from the transient simulation and the instant rotor current calculated with one magneto-static solution at one time moment. The instant current is close to that at the corresponding time moment in the transient results. The dashed lines give the waveform of the rotor current predicted by one magneto-static solution. The dashed lines are computed by only taking the fundamental frequency into account. The currents in the first and third nest have some phase shift which is theoretically expressed by (3.10). The method proposed can predict the rotor current accurately at the corresponding time moment. The magneto-static and transient simulations however differ at other time instances. It is because we know the exact magnetic field at one time moment with its corresponding magneto-static simulation, but it is hard to know the exact magnetic field at other moments with that magneto-static solution. The accurate rotor currents at any other moment can be calculated by rotating the rotor to the corresponding position manually and using another magneto-static simulation. Fig. 3.2 also gives the enlarged views of the currents. At the corresponding time moment, the static model presented still leads to some small errors compared with the transient results due to the assumption of the fundamental frequency.

According to the time FFT results of the rotor currents shown in Fig. 3.3, the current with the fundamental frequency dominates in each loop which ensures that the assumption will be valid for the calculation. In addition, Fig. 3.3 (a) and (b) again prove that the currents flowing in the first and third nests are with similar amplitude, as well as the time-harmonic orders. Furthermore, the outer loop flows with much higher current than the inner one which means that the outer loop makes more contribution to the torque.

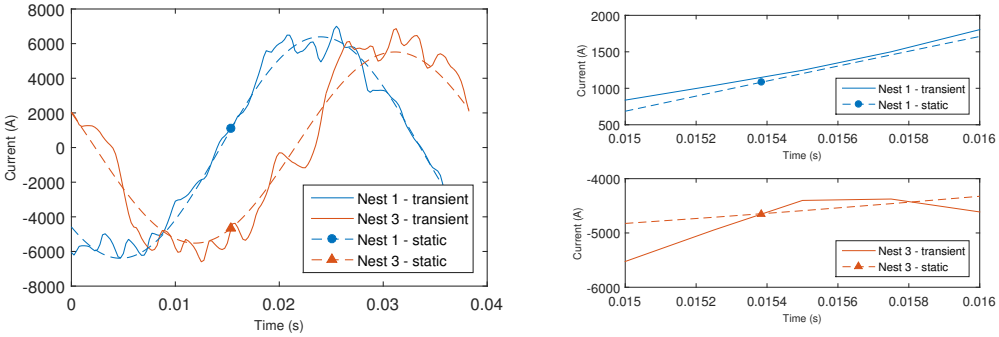

(a) Outer loop of nest 1 & 3

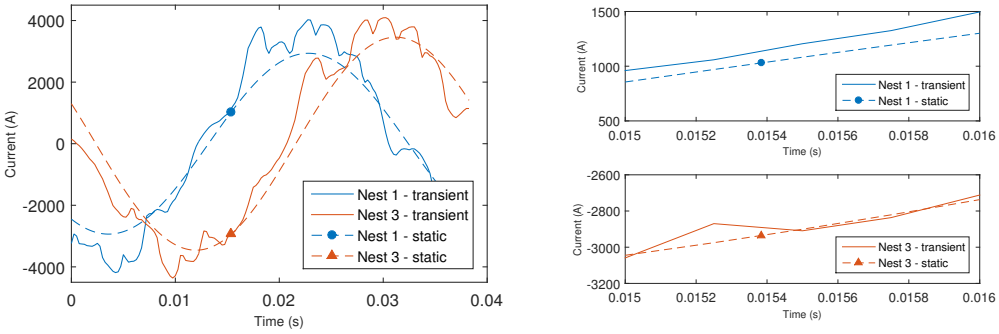

(b) Middle loop of nest 1 & 3

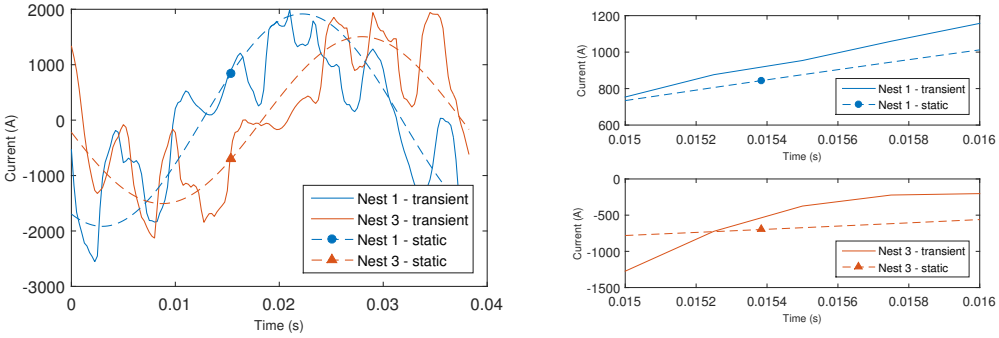

(c) Inner loop of nest 1 & 3

Figure 3.2 Rotor currents calculated in transient and magneto-static simulations

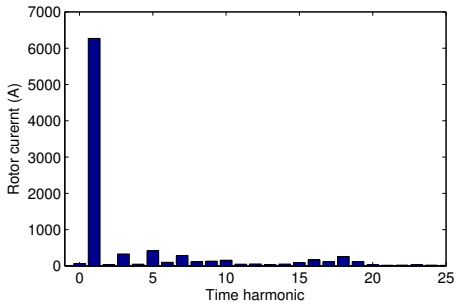

(a) Outer loop of nest 1

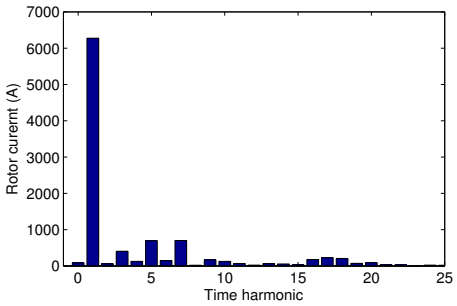

(b) Outer loop of nest 3

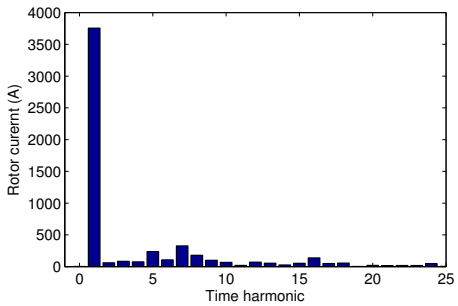

(c) Middle loop of nest 1

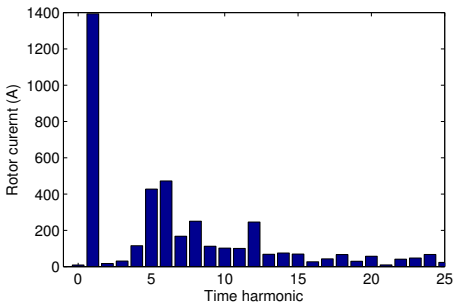

(d) Inner loop of nest 1

Figure 3.3 Time FFT of rotor currents

3.4.2 Air-gap magnetic field

Fig. 3.4 gives the 2D distributions of magnetic fields and flux lines calculated by the transient model and the proposed magneto-static model at 0.0155s. Fig. 3.5 gives the comparison of the total flux density in the radial direction between the transient simulation and the proposed alternative way at one time point. It is not difficult to understand the agreement between them since the applied stator currents are the same and the calculated rotor currents are so close to each other (show in Fig. 3.2). However, some little difference is still there because the calculated rotor currents are not exactly the same in these two models.

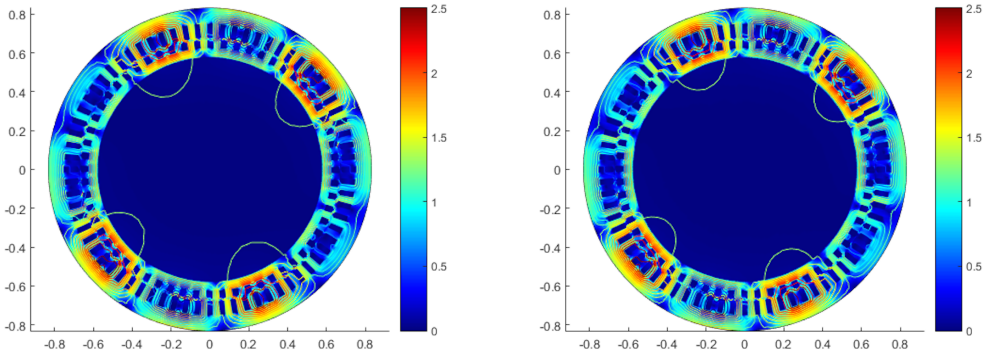

(a) Transient result at $0.0155s$ **(b)** Magneto-static result $t_s = 0.0155s$

Figure 3.4 Magnetic fields and flux lines

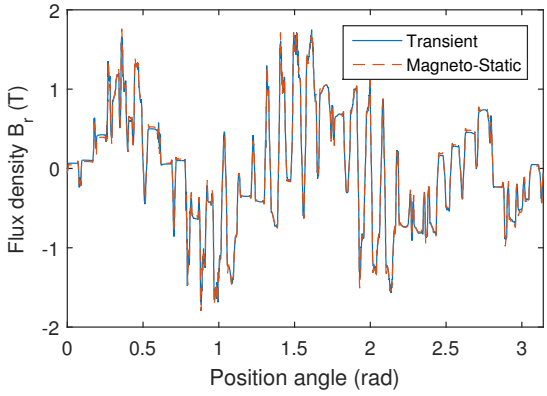

Figure 3.5 Total air-gap flux density in the radial direction

3.4.3 Machine performance

The brushless DFIM performance estimated by the transient simulations and the magneto-static simulations are listed in Table 3.3. The proposed FE model based on the magneto-static simulation provides the predictions at the same accurate level as the transient simulation. But it reduces the computing time dramatically which makes it possible for it to be combined with the optimization progress. The meshes in the transient model and the static model are almost the same so we can minimize the influence of the mesh level on the computing time.

Table 3.3 Brushless DFIM performance prediction ($q_r = 3$)

Performance	**Transient model**	**Static model**	**Error**
Torque [kN·m]	85.20	84.79	0.5%
Power [MW]	3.21	3.20	0.5%
Stator core losses [kW]	68.96	65.48	5.0%
Rotor core losses [kW]	18.54	16.28	12.2%
Stator copper losses [kW]	79.56	79.56	-
Rotor copper losses [kW]	32.31	30.29	6.3%
Efficiency [%]	94.16	94.35	-0.2%
Time cost [s]	≈8257	≈55	

3.4.4 Limitation of the model proposed

The computing time is saved at the expense of several limitations of the magneto-static model.

1. The accuracy of the average torque predicted by the magneto-static model depends on the rotor position. Fig. 3.6(a) gives the electromagnetic torque obtained from the transient FE model. The variation of the main torque (given by (3.31) due to p_p and p_c pole-pair fields is much smaller than that of the total torque response. Fig. 3.6(b) shows the difference between the main torque and the average torque. The accuracy of using the main torque as the average torque depends on the rotor position. It can be expected that average torque predicted by the magneto-static model at a random position results in an error up to about 5%. However, at most positions, the error is lower than 2.5%.
2. The rotor core losses are calculated only with respect to the fundamental frequency f_r because the main components of the rotor currents are assumed to be with fundamental frequency f_r. This is acceptable in the previous case study as mentioned in section 3.4.1.
3. The presented fast model cannot take into account the skin-effect and the proximity-effect because the magneto-static requires that the electric conductivity is set as zero. However, a concern may arise about the skin-effect in solid rotor bars, especially in large-scale

machines (e.g. the 3.2MW case study machine given in Table. 3.1). The case study machine has also been evaluated by taking the skin-effect into account. The results indicate that the rotor copper losses are about 8 times larger than that without considering the skin-effect, while the other performance (i.e. the average torque, stator/rotor core losses, stator copper losses) varies within around 4%. Therefore, it needs careful consideration for the skin-effect in the final design of brushless DFIMs.

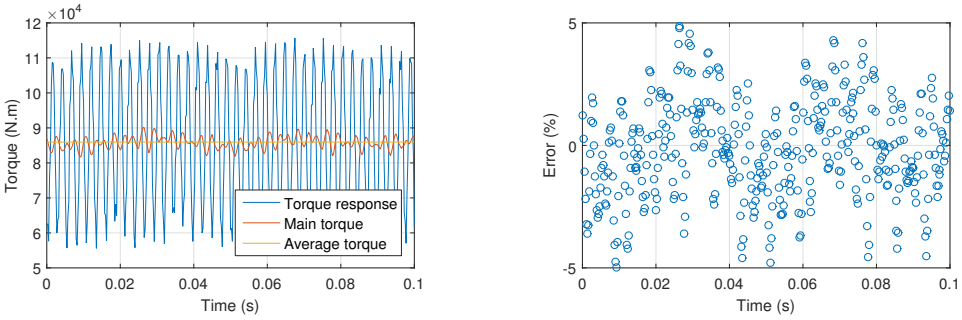

(a) Torque waveform **(b)** Error using the main torque

Figure 3.6 Electromagnetic torque obtained from the transient FE model

3.5 Application example: multi-objective optimization

In order to show the usefulness of the computationally efficient FE analysis presented, it is utilized to optimize a brushless DFIM in larger design spaces for a better prototype design.

3.5.1 Optimization procedure

Fig. 3.7 gives the optimization procedure. Based on the input parameters, the machine geometry is calculated using a geometric model developed in MATLAB. Using a MATLAB-COMSOL interface, the machine geometry is loaded into the magneto-static brushless DFIM model presented. For optimization, the NSGA-II (non-dominated sorting genetic algorithm II) is applied [105]. This well-known evolutionary based algorithm can determine Pareto optimal solutions to multi-objective problems. The first population of N machine designs is generated and evaluated by the magneto-static brushless DFIM FE model. Each design varies based on a set of provided geometric input variables. All N machine designs are evaluated according the optimization objectives, and a new generation of N machine designs is generated from the best (fittest) individuals of the previous generation. In this study, the population sizes N and the generations are chosen as 30 and 40, respectively.

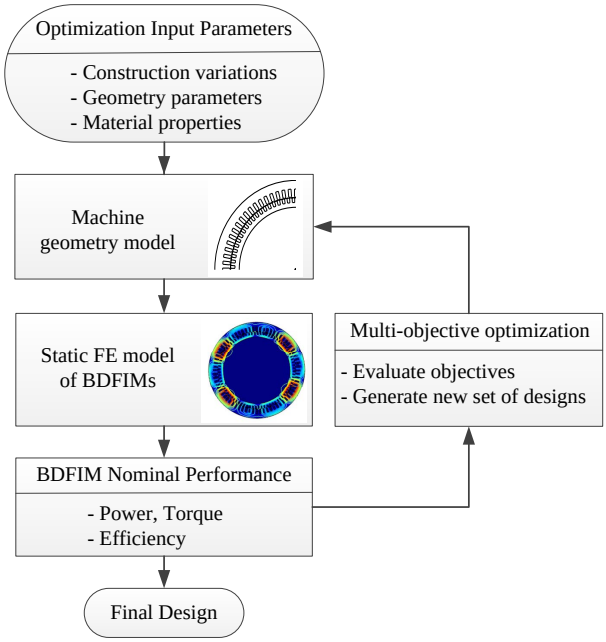

Figure 3.7 Optimization of procedure of a brushless DFIM

Table 3.4 Fixed parameters of the brushless DFIM studied

Description	**Machine parameter**	**Value**
Axial length [mm]	l_{stk}	240.0
Air-gap length [mm]	l_g	1.0
Stator outer radius [mm]	r_{so}	135.0
Rotor inner radius [mm]	r_{ri}	35.0
Number of phases	N_{ph}	3
PW/CW stator slot area ratio		50%/50%
Stator/rotor tooth tip height		$1/16^{th}$ tooth height
Stator/rotor tooth tip width		50% closed
Rated frequency [Hz]	f_p, f_c	50, -10
Slot current density [A/mm^2]	J	1

3.5.2 Optimization objectives and variables

The objectives of this study are to optimize both the torque and efficiency of a potential prototype that fits a frame size D180 in which the stator outer radius is fixed as 135mm. The machine is optimized at its nominal operating point where the maximum torque is produced [72]. Table 3.4 gives an overview of fixed design parameters. The objective functions of this study are:

$$OF_1(\mathbf{V}) = -T_{main}(r_{si}, \alpha_{s,y}, \alpha_{r,y}, \alpha_{s,sw}, \alpha_{r,sw}), \tag{3.38}$$

$$OF_2(\mathbf{V}) = -\eta(r_{si}, \alpha_{s,y}, \alpha_{r,y}, \alpha_{s,sw}, \alpha_{r,sw}), \tag{3.39}$$

in which T_{main} is the average torque given by (3.31), η is the efficiency give by (3.37) and $\mathbf{V} = (r_{si}, \alpha_{s,y}, \alpha_{r,y}, \alpha_{s,sw}, \alpha_{r,sw})$ is the vector of optimization variables. These optimization variables, as well as their constraints, are listed in Table 3.5. The optimizations are performed for different brushless DFIM constructions given in Table 3.6.

Table 3.5 Geometry variables of the brushless DFIM studied

Description	**Variables**	**Value**	
		min	**max**
Stator inner radius [m]	r_{si}	0.05	0.11
Ratio stator slot/yoke height	$\alpha_{s,y}$	0.2	0.8
Ration rotor slot/yoke height	$\alpha_{r,y}$	0.2	0.8
Ratio stator inner/max slot width	$\alpha_{s,sw}$	0.2	0.8
Ratio rotor inner/max slot width	$\alpha_{r,sw}$	0.2	0.8

Table 3.6 Construction variations of the brushless DFIM studied

	p_p	p_c	N_{ss}	q_r
Construction 1.1	1	3	54	4
Construction 1.2	1	3	54	5
Construction 1.3	1	3	72	5
Construction 2	2	3	72	5
Construction 3.1	2	4	72	4
Construction 3.2	2	4	72	5
Construction 4	4	6	72	3

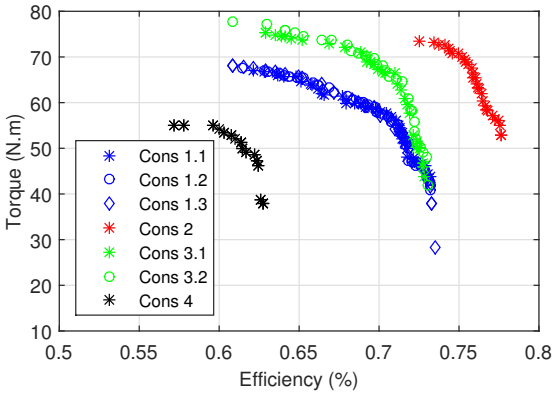

Figure 3.8 Optimization results for different construction variations

3.5.3 Optimization results and discussions

It takes approximately 38 minutes to evaluate each generation with the efficient model proposed. Fig. 3.8 shows the optimization results with respect to different constructions given in Table 3.6. It is expected that the efficiency is low in a small-scale machine. This efficiency level coincides with the measurements that have been carried out by the project partner on a brushless DFIM with a similar size in Cambridge [62]. There is a trade-off between electromagnetic torque and efficiency. Furthermore, within this fixed frame size, the design with pole-pair combination $p_p = 2, p_c = 3$ gives the best performance considering both efficiency and electromagnetic torque. However, it has been proven that, to avoid unbalanced magnetic pull (UMP) on the rotor, the pole pairs must be chosen so that $|p_p - p_c| \neq 1$ [24]. This brushless DFIM with $p_p = 2, p_c = 3$ is subject to UMP. Considering the fact that UMP is limited in a small-scale prototype (e.g. D180 frame size), the pole-pair combination with $p_p = 2, p_c = 3$ is finally selected for our prototype. In addition, the number of loops per nest q_r and the number of stator slots N_{ss} have little influence on the nominal performance. But they do have effects on torque ripple, as well as harmonic pollution.

3.6 Conclusion

The adaptive time-step solver is usually used for the transient model in some commercial software FE packages (e.g. COMSOL Multiphysics) . It results in a small size of the time-step to capture higher time-harmonics in the magnetic fields, as well as in the currents. It is not time efficient to evaluate many design candidates using transient FE models which contain tens or hundreds of time steps. According to a special space-time relationship of the induced rotor currents in the brushless DFIMs, this chapter gives an approximate way to calculate the rotor currents which is not restricted by the time-step. The induced rotor current can be predicted using one

magneto-static simulation. And some of the brushless DFIM performance (e.g. average torque, core losses, etc.) can be estimated using one magneto-static solution. Compared with the results obtained from the transient simulation, it indicates that the model presented can estimate the brushless DFIM performance at an acceptable accurate level while the computing time is reduced significantly. It is then possible to combine the efficient model proposed with some optimization programs. The model presented has been applied to the optimization of a prototype. Several pole-pair combinations and the number of loops per nest are studied using the method presented. It shows that $p_p = 2, p_c = 3$ can be a good pole-pair combination although it may suffer the problem of UMP in large scale wind generators. It also shows the number of loops per nest has little influence on the nominal performance. Therefore, the presented FE analysis using a magneto-static solution constitutes a valuable tool for the design and optimization of brushless DFIMs.

CHAPTER 4

Analysis of the Effects of Skew Using 2D Transient Multi-Slice FE Model

The aim of this chapter is to investigate the effects of skewing nested-loop rotors on the performance of brushless DFIMs. Many undesired space harmonics exist because the special rotor is designed to couple to two stator windings with different pole-pair numbers and different frequencies. These undesired space harmonics lead to more severe noise, vibrations and lower power quality compared with normal induction machines. Skewing slots is practical to overcome these drawbacks in normal induction machines. This chapter applies 2D transient multi-slice FE models to study the effects of skew in brushless DFIMs. Slices with Gauss distribution are used to reduce the computing time. Several aspects of the performance are evaluated including induced rotor currents, air-gap magnetic fields, induced stator voltages, electromagnetic torque, torque ripple and core losses. The results indicate that skewing rotor slots reduces the harmonics in the induced rotor currents, the induced stator voltages and air-gap magnetic fields. The torque ripple is reduced significantly at the expense of a slightly lower average torque and efficiency. It also indicates that skewing the rotor slot over one stator slot pitch is a good choice in brushless DFIMs with nested-loop rotors.

Most parts of this chapter have been published in

- X. Wang, T. D. Strous, D. Lahaye, H. Polinder, and J. A. Ferreira, "Effects of Rotor Skew on the Performance of Brushless Doubly-Fed Induction Machine," in *IEEE Int. Electric Machines Drives Conf. (IEMDC)*, Coeur d'Alene, USA, May 2015.

4.1 Introduction

Compared with normal induction machines, brushless DFIMs have two stator magnetic fields. These are created by the power winding (PW) and the control winding (CW). There is no direct magnetic coupling between them since they have different pole-pair numbers and different frequencies. A special nested-loop rotor is designed to couple with both main harmonic fields resulting in a complicated distribution of the air-gap magnetic field in this special electrical machine. One of the negative consequences is that many undesirable space harmonics appear in the air-gap field.

Fig. 4.1 shows the relationships of space- and time-harmonics in brushless DFIMs. The fundamental components of PW and CW currents produce the stator fundamental magnetic fields with p_p and p_c pole-pairs, respectively. These two components induce the rotor currents with the same fundamental frequency f_r. It then produces a magnetic field with two main components, as well as many undesirable space harmonics. The main electromagnetic torque is produced due to the coupling between stator and rotor main components. Moreover, the winding distribution, the slotting and the saturation contribute to space-harmonics in stator magnetic fields. These stator space harmonics induce time harmonics in the rotor currents, which also contribute to the unwanted rotor space harmonics. All these undesirable space harmonics then induce additional time harmonics in the stator currents. Torque ripple arises when both stator and rotor magnetic fields contain space harmonics of the same pole-pitch but with different rotational frequencies.

Space and time harmonics lead to a concern about noise and vibrations due to torque ripple, which has harmful influences on the lifetime of the generator and other components (e.g. gearboxes) of the drive-train system. They also lead to lower efficiency compared with normal DFIMs. Furthermore, they result in a reduction of power quality because of increased total harmonic distortion (THD) in output currents. These shortcomings prevent brushless DFIMs from being commercialized for wind turbine applications. Chapter 3 has indicated that the pole-pair combination of stator windings has a big influence on the main torque and efficiency. This chapter will further look into the torque ripple and the THD of stator induced voltages. The effects of rotor skew will be studied in this chapter.

In normal induction machines, skewing rotor (or stator) slots is quite practical to reduce the torque ripple [106]. It will also result in lower time-harmonics in induced rotor currents [107], which reduce the THD of the output currents. It has been proven analytically that the torque ripple of brushless DFIMs decreases by applying rotor skew [89]. Slotting and saturation are ignored in that analytical model whist they may also have some influence on the torque ripple. Moreover, it is also assumed that the nested-loop rotor has only one loop per nest and its slot is rectangular shaped. However, it has been already shown that the number of loops per nest has an effect on the torque ripple [104]. The finite element (FE) model can overcome these assumptions since it can easily take into account exact geometries and saturation effects. It has been applied to the brushless doubly-fed reluctance machines [108], but not yet to the brushless DFIMs.

The aim of this chapter is to apply 2D transient FE models with a multi-slice method to investigate

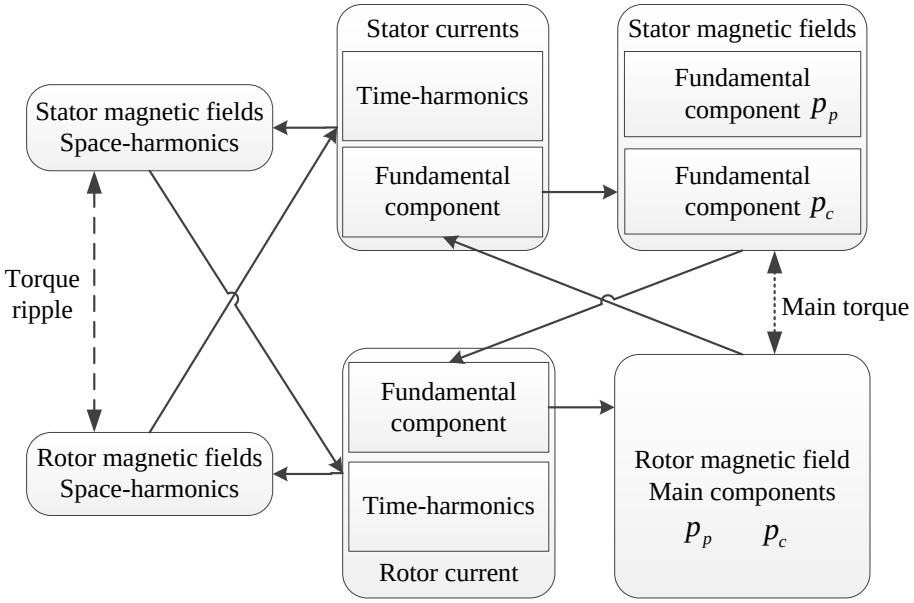

Figure 4.1 Space- and time-harmonic relations

the effects of rotor skew on the performance of brushless DFIMs. This chapter starts with the modeling of rotor skew. Next, the methods to calculate the induced rotor currents, electromagnetic torque and losses are introduced. Subsequently, the selection of slices is explained. Then, the simulation results without skewing and with skewing at different skew angles are given, followed by discussions. Finally, conclusions are drawn.

4.2 Modeling of skew effects

4.2.1 Assumptions

The following assumptions are made:

1. The eddy-currents in the iron cores are neglected during the FE calculation while the core losses are computed in the post-processing.
2. The skin-effect and the proximity-effect are ignored.
3. The resistances of the end parts of the rotor bar are taken into account by coupling the electrical circuits with the field equations while the magnetic field due to the end part is neglected.

These assumptions are the same as those made for the 2D transient FE models in section 2.6.1.

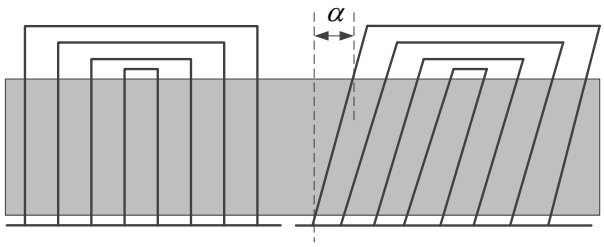

Figure 4.2 Nested-loop rotor without & with skew

4.2.2 Transient 2D FEM with multi-slice method

The rotor bars are no longer parallel to the axial direction since the bar is skewed with an angle. Therefore, rotor skew is essentially a 3D problem due to the fact that the induced rotor currents do not flow only along the axial direction. However, one approximate way is to represent a skewed

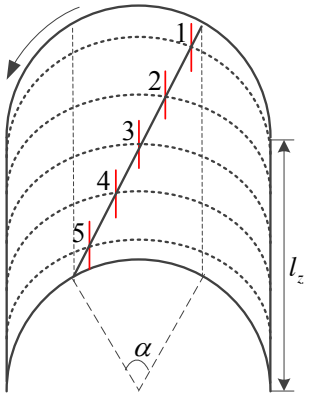

Figure 4.3 Multi-slice representation of the rotor skew

machine with a 2D FE model with the multi-slice method [107], [108]. The nested-loop rotor with skew angle α is shown in Fig. 4.2 and Fig. 4.3 gives the representation of the skew by using the multi-slice method. The currents in each slice are assumed to flow only in the axial direction. Therefore, a set of normal 2D models is used to model the skewed rotor. Each slice corresponds to a section with $w_n l_z$ length which is taken at different positions along the axial direction, where w_n is the weight of the n^{th} slice. This can be achieved by making the relative position between the stator and the rotor of the middle slice (e.g. No. 3 in Fig. 4.3) correspond to that of the machine without a skewed rotor. The other slices are then shifted with $\varepsilon_n \alpha$ angle one by one, where ε_n is the position of the n^{th} slice. w_n and ε_n depend on the number of slices and the distribution of slices. w_n and ε_n of N slices with uniform distribution are:

$$w_n = \frac{1}{N}, \tag{4.1}$$

$$\varepsilon_n = \frac{2n - N - 1}{2N}. \tag{4.2}$$

The w_n and ε_n for another distribution will be explained in section 4.3. The 2D electromagnetic field equation in each slice is solved simultaneously as:

$$\frac{\partial}{\partial x}\left(\frac{1}{\mu}\frac{\partial A_z^n}{\partial x}\right) + \frac{\partial}{\partial y}\left(\frac{1}{\mu}\frac{\partial A_z^n}{\partial y}\right) = J_z^n(t), \tag{4.3}$$

where n represents the label number of the slice ($n = 1, 2, .., N$), μ is the permeability of the material, A_z is the z component of the magnetic vector potential and J_z is the externally applied current density.

1. In the air-gap and iron domains

$$J_z^n = 0. \tag{4.4}$$

2. In the stator conductor domains, the stator currents are known as inputs

$$J^n_{p(c)}(t) = \hat{J}_{p(c)} \sin(\omega_{p(c)} t + \phi_{p(c)}). \tag{4.5}$$

3. In the rotor conductor domains, each loop can be regarded as an independent short-circuited loop. One constraint is enforced to obtain the same current in the corresponding rotor bar of each slice. The applied rotor current density of a certain loop can be formulated as

$$J_r = \frac{w_n l_z}{RS^2} \sum_{n=1}^{n=N} \frac{d(\iint A^n_z dS_+ - \iint A^n_z dS_-)}{dt}, \tag{4.6}$$

where l_z is the axial length, S is the cross-sectional area of the rotor bar, S_+ and S_- are the surface of the go and return conductors, R is the resistance of one rotor loop including the resistance of the end parts of the bar. The detailed derivation of (4.6) follows that of (3.15) in section 3.3.2.

The skew angle α is relatively small in practical applications. The components of the rotor currents in the axial direction dominate in total. Therefore, the flux in the axial direction is neglected in our model. Table 4.1 gives the main specifications of the brushless DFIM studied in this chapter.

Table 4.1 Main specifications of the brushless DFIM studied

Description	**Machine parameter**	**Value**
Axial length [m]	l_{stk}	1.60
Air-gap length [mm]	l_g	1.5
Stator outer radius [m]	r_{so}	0.83
Stator inner radius [m]	r_{si}	0.67
Rotor inner radius [m]	r_{ri}	0.58
Number of phases	N_{ph}	3
Number of pole-pairs	p_p, p_c	4, 6
Rated frequency [Hz]	f_p, f_c	50, -10
Number of stator slots	N_{ss}	72
Number of rotor nests	N_{nest}	10
Number of loops per nest	q_r	4
Rotational speed [rad/s]	Ω_m	37.7
Slot current density [A/mm^2]	J	4
Rated power [MW]	P	3.2

Maxwell's stress tensor method given by (3.27) is applied to calculate the torque in each slice. The effective torque response with a skewed rotor can be calculated as:

$$T_e^{skew} = \sum_{n=1}^{n=N} \frac{w_n l_z}{\mu_0} \int_0^{2\pi} r^2 B_r B_t d\theta, \tag{4.7}$$

where μ_0 is the magnetic permeability of the vacuum, r is the radius of the air-gap, B_r and B_t are the radial and tangential components of the flux density in the air-gap. The torque ripple is defined as:

$$ripple = \frac{max(T_e^{skew}) - min(T_e^{skew})}{mean(T_e^{skew})} \times 100\%. \tag{4.8}$$

The core losses can be evaluated by the Modified Steinmetz Equation (MSE) given by (3.33) and (3.35). The amplitude of the flux densities in the stator and rotor core can be obtained by performing time FFT on the flux densities.

THD is a way to evaluate the harmonic distortions of the induced rotor currents, the air-gap magnetic field and the induced stator voltages. The general calculation of THD is as follows [69]:

$$THD = \frac{\sqrt{\sum_{h=2}^{\infty} H_h^2}}{H_1} \times 100\%, \tag{4.9}$$

where H_h is the amplitude of the h^{th} harmonic component and $h = 1$ is the fundamental component.

4.3 Selection of slices

Essentially, the multi-slice method is a discretization of a continuous physical problem. The criterion for selecting the slices is to minimize the discretization error. Firstly, the number of slices has an influence on the accuracy. The approximation is closer to the real physics if more slices are used. However, on the other hand, this leads to more degrees of freedom and more computing time. Table 4.2 gives a case study result to indicate the influence of the number of slices on the number of degree of freedom (DoF) and time cost. The number of DoF, as well as the time cost, is approximately proportional to the number of slices.

Secondly, the distribution of the slices also has influence on the accuracy. A Gauss distribution of slices (shown in Fig. 4.4) has been proposed to reduce the discretization error of the multi-slice method [109]. The Gauss distribution of slices will be further studied and finally applied to the multi-slice method in this chapter.

The influence of these two aspects on the accuracy can be studied by evaluating skew factors which are normally applied in the classical analytical rotating field theory. The fundamental

Table 4.2 Influence of the number of slices on DoF and time cost

Number of slices	Degrees of freedom	Time cost
1 (nonskew)	261253	3h 59min
3	783679	11h 56min
5	1306105	17h 19min
7	1828531	27h 49min
9	2350957	41h 16min

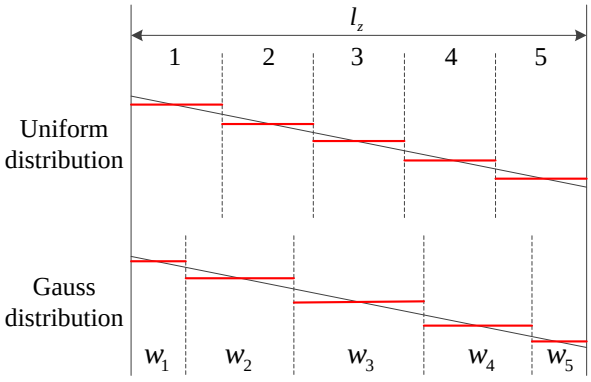

Figure 4.4 Uniform and Gauss distributions of slices (N=5)

magnetic field due to the PW given by (2.1) can be written as (4.10), if seen by the skewed rotor conductor.

$$B_{gp}^{skew}(t,\theta_s) = \frac{1}{\alpha}\int_{-\frac{\alpha}{2}}^{\frac{\alpha}{2}} \hat{B}_{gp}\cos[\omega_p t - p_p(\theta_s+\theta)+\varphi_p]d\theta = \hat{B}_{gp}\cos(\omega_p t - p_p\theta_s+\varphi_p)F_s, \quad (4.10)$$

where F_s is the well-known skew factor depending on the space-harmonic order p_p and the skew angle α:

$$F_s = \frac{1}{\alpha}\int_{-\frac{\alpha}{2}}^{\frac{\alpha}{2}} \cos(p_p\theta)d\theta = \frac{\sin(p_p\frac{\alpha}{2})}{p_p\frac{\alpha}{2}}. \quad (4.11)$$

The resultant field in the multi-slice model can be calculated as:

$$\begin{aligned} B_{gp}^{skew} &= \sum_{n=1}^{n=N} w_n \hat{B}_{gp}\cos[\omega_p t - p_p(\theta_s+\varepsilon_n\alpha)+\varphi_p] \\ &= \hat{B}_{gp}\cos(\omega_p t - p_p\theta_s+\varphi_p)\sum_{n=1}^{n=N} w_n\cos\left(p_p\varepsilon_n\alpha\right), \end{aligned} \quad (4.12)$$

Therefore, the effective discrete skew factor is:

$$F_{s,N} = \sum_{n=1}^{n=N} w_n\cos(p_p\varepsilon_n\alpha). \quad (4.13)$$

To the Gauss distribution, w_n and ε_n can be found in [110], [111]. Table 4.3 lists some common weight and position of individual slice with Gauss distribution.

Table 4.3 Weight and position of individual slice with Gauss distribution

Number	**Weights**								
of slices	w_1	w_2	w_3	w_4	w_5	w_6	w_7	w_8	w_9
3	27.78%	44.44%	27.78%	-	-	-	-	-	-
5	11.85%	23.93%	28.44%	23.93%	11.85%	-	-	-	-
7	6.47%	13.99%	19.09%	20.90%	19.09%	13.99%	6.47%	-	-
9	4.06%	9.03%	13.03%	15.62%	16.51%	15.62%	13.03%	9.03%	4.06%
	Positions								
	ε_1	ε_2	ε_3	ε_4	ε_5	ε_6	ε_7	ε_8	ε_9
3	-0.3873	0	0.3873	-	-	-	-	-	-
5	-0.4531	-0.2692	0	0.2692	0.4531	-	-	-	-
7	-0.4746	-0.3708	-0.2029	0	0.2029	0.3708	0.4746	-	-
9	-0.4841	-0.4180	-0.3067	-0.1621	0	0.1621	0.3067	0.4180	0.4841

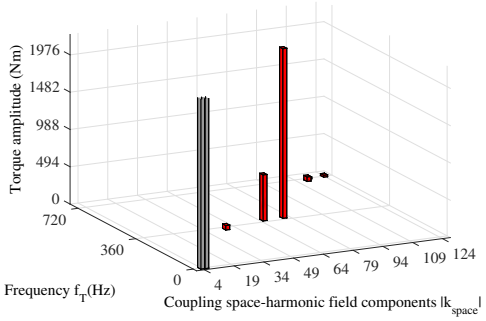

(a) Due to winding distribution

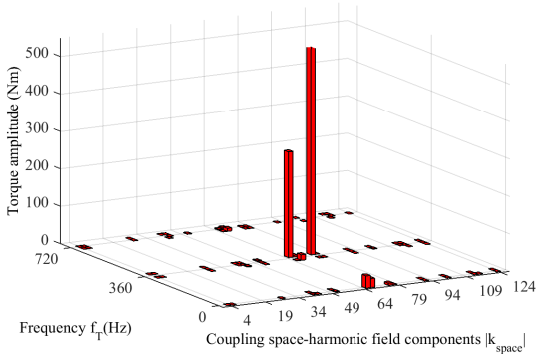

(b) Due to slotting

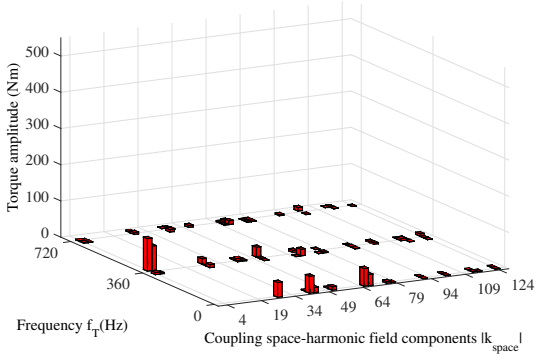

(c) Due to time harmonics in rotor currents

Figure 4.5 Torque ripple components

(4.11) and (4.13) are given based on the fundamental component of the PW field. However, they are also valid for the higher space-harmonic components when p_p is replaced by the corresponding space harmonic order. Moreover, for the magnetic field due to the CW, they are still applicable. In the related paper, Strous *et al.* [78] has concluded that the 66$^{\text{th}}$ and 76$^{\text{th}}$ space-harmonic field components made the largest contribution to the torque ripple, which is shown in Fig. 4.5. This is because the distributions of PW and CW, as well as the slotting harmonics, all contribute to the 66$^{\text{th}}$ and 76$^{\text{th}}$ space harmonics. (4.11) and (4.13) are then applied to calculate the skew factors of the 66$^{\text{th}}$ and 76$^{\text{th}}$ components, as well as the fundamental 4$^{\text{th}}$ and 6$^{\text{th}}$ components. The relative discretization errors, given by

$$\frac{F_{s,N} - F_s}{F_s} \times 100\%, \tag{4.14}$$

are presented in Fig. 4.6. The number of slices depends on the highest space-harmonic order which plays a big role. For the higher space-harmonic components, more slices are needed to achieve more accurate prediction. Overall, the Gauss discretization results in a smaller error compared with the uniform discretization, although it does not provide a good accuracy to the higher space-harmonic components in the case of three slices. Five slices with Gauss distribution might be a compromise choice considering both accuracy and time cost.

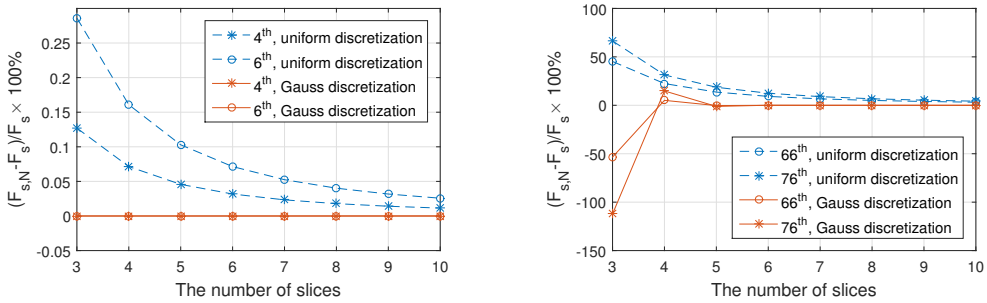

(a) Fundamental field components **(b)** Space-harmonic field component

Figure 4.6 The discretization error of skew factors ($\alpha = 2\pi/72$)

Fig. 4.7 gives the average torque and ripple predicted by the presented FE models using different numbers of slices with uniform and Gauss distributions. Both distributions give a stable estimation of the average torque from using five slices. However, for the torque ripple, the Gauss discretization gives a more stable prediction. Therefore, five slices with Gauss distribution are applied to the case study brushless DFIM in this chapter.

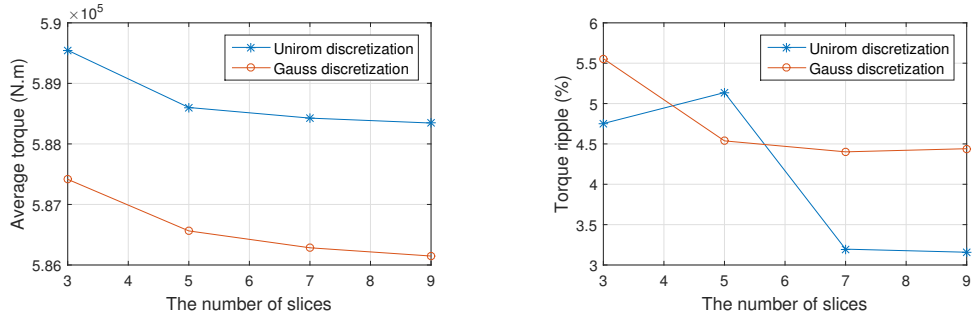

(a) Average torque **(b)** Torque ripple

Figure 4.7 Torque response using different number of slices ($\alpha = 2\pi/72$)

4.4 Skew effects on machine performance

4.4.1 Induced rotor currents

Fig. 4.8 shows the induced rotor currents and their time FFT results in most outer loop in the cases without skewing and with skewing over one stator slot pitch τ_s. The time-harmonics are reduced in the rotor currents by skewing the rotor slots. This can also help to reduce the torque ripple although Fig. 4.5 has indicated that the effect of induced time-harmonic rotor currents on the torque ripple is much smaller compared to the winding distribution space-harmonics and the slotting space-harmonics [78].

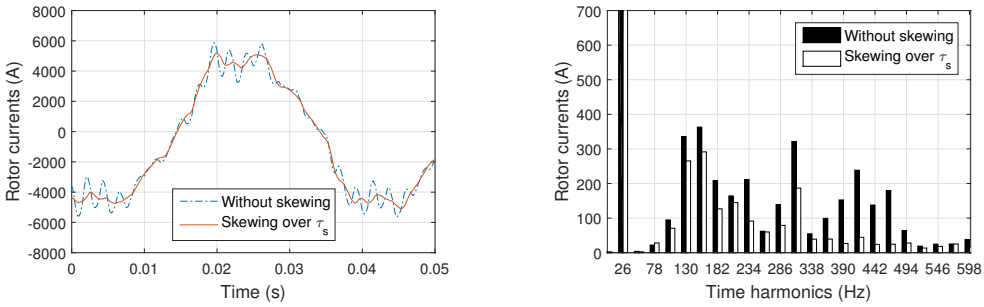

(a) Waveforms **(b)** Time FFT results

Figure 4.8 Induced rotor currents in the most outer loop

Fig. 4.9 gives the THD of the induced rotor currents. More time-harmonics are induced in the inner loop than the outer ones, which has also been observed in Fig. 3.2. With the skew angle increasing, the THD of each rotor current decreases. The THDs of the currents in the outer three loops can be reduced to a similar level by skewing the slots while the current flowing in the most inner loop (Loop 1) always contains many time-harmonics. In addition, considering the fact that Loop 1 flows a much smaller current than the outer loops, it is reasonable to consider leaving out the most inner loop entirely.

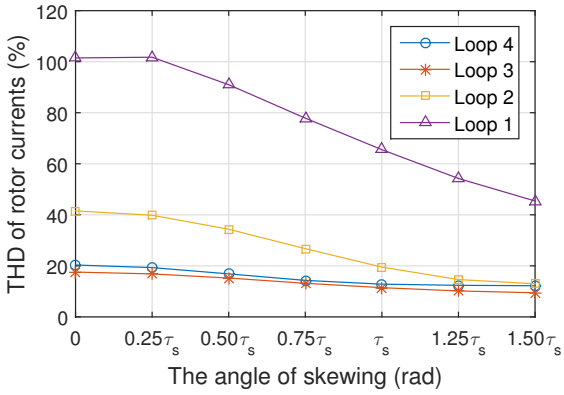

Figure 4.9 THD of induced rotor currents

4.4.2 Air-gap magnetic field

Fig. 4.10 shows the total air-gap flux density in radial direction. It indicates that skewing rotor slots reduces the space-harmonics in the total air-gap magnetic field. Fig. 4.11 gives the 2D-FFT results of the total air-gap magnetic field with and without skewing. The components whose amplitudes are lower than 0.01T are not shown for clarity. As mentioned before, there are two main components instead of one fundamental component in the air-gap field. They are the 4^{th} space-harmonic rotating at 50Hz and the 6^{th} space-harmonic rotating at 10Hz. Some of the other undesired components are clearly reduced because of skewing. For instance, the stator slotting harmonics 76^{th} rotating at 50Hz and 78^{th} rotating at 10Hz are reduced by skewing rotor slots.

Fig. 4.12 gives the THD of the air-gap magnetic field in the radial direction. Two main components are both considered as the fundamental ones in (4.9). This will result in fewer harmonics in the air-gap field with the skew angle increasing.

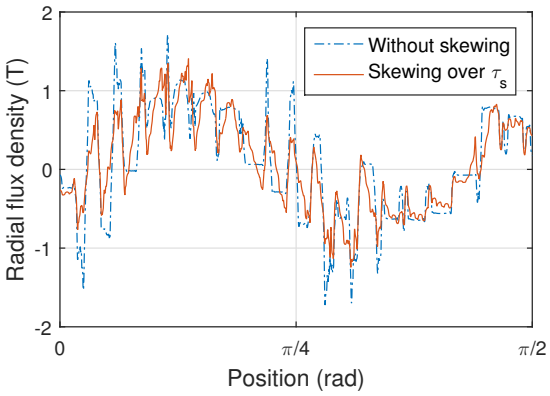

Figure 4.10 Total air-gap flux density in the radial direction

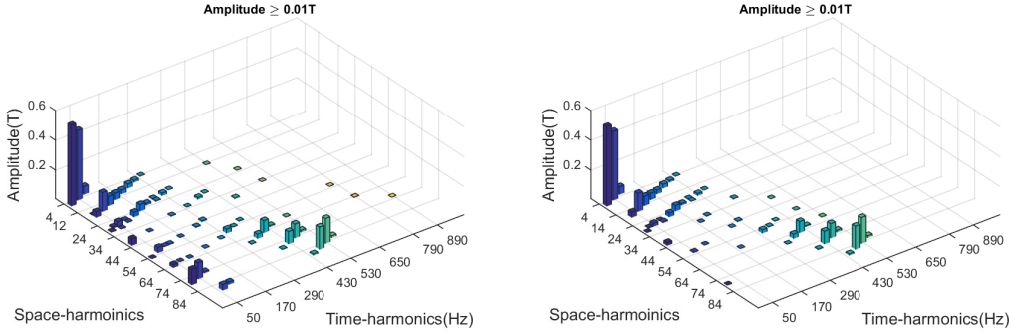

(a) Without skewing **(b)** Skewing over τ_s

Figure 4.11 Space and time harmonics of the air-gap magnetic field in a brushless DFIM

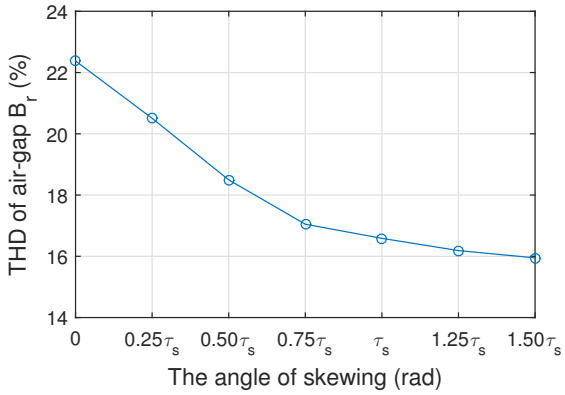

Figure 4.12 THD of air-gap flux density in radial direction

4.4.3 Induced stator voltages

Fig. 4.13 and 4.14 show the waveforms of the induced stator voltages and their time-FFT results, respectively. It can be expected that less time-harmonics will be induced in the stator voltages since there are less harmonics in the air-gap magnetic field because of skewing.

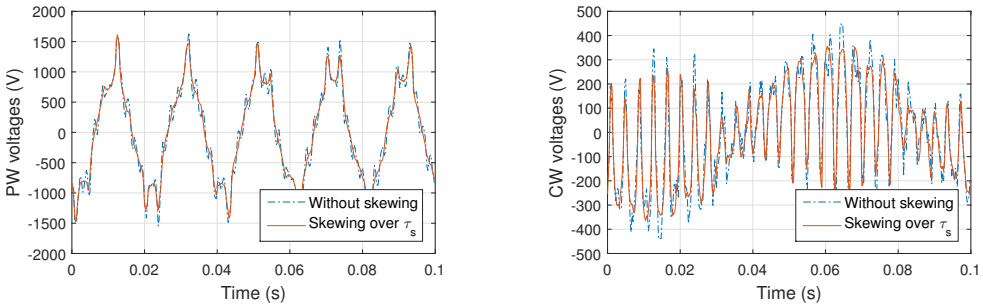

(a) Power winding **(b)** Control winding

Figure 4.13 Induced stator voltages

Fig. 4.15 gives the THD of induced stator voltages. To both induced voltages, the THD decreases when the skew angle goes up. However, the improvement is not significant. This is because the pole-pair combination of $p_p = 4, p_c = 6$ is already a good choice. This pole-pair combination leads to less coupling of higher space-harmonics between the stator and the rotor.

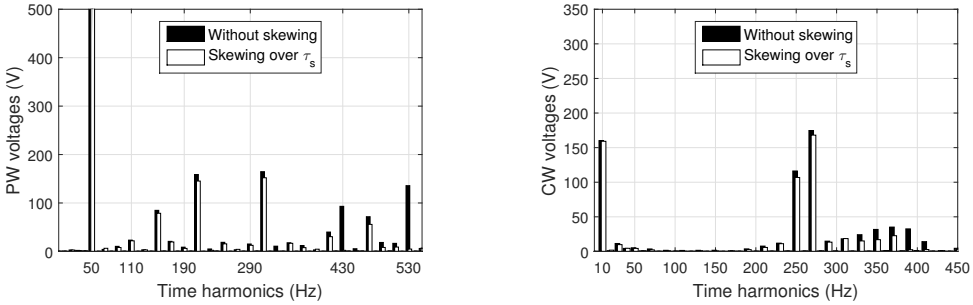

(a) Power winding **(b)** Control winding

Figure 4.14 Time-FFT results of induced stator voltages

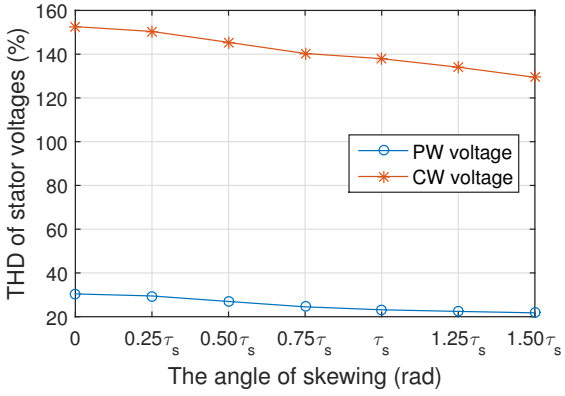

Figure 4.15 THD of induced stator voltages

4.4.4 Electromagnetic torque and torque ripple

Fig. 4.16 shows the waveforms of electromagnetic torque, as well as their time-FFT results. The second largest component in the spectrum is at 380Hz. This component is caused by the winding distribution and the slotting harmonics [78]. They are reduced effectively by skewing the rotor slots.

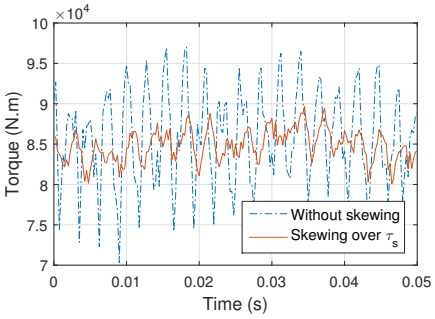

(a) Waveforms

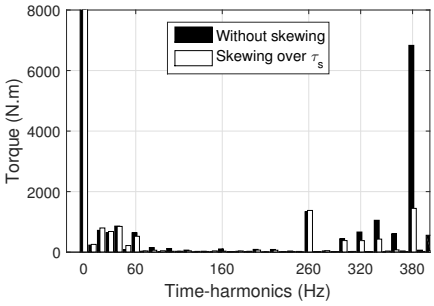

(b) Time-FFT results

Figure 4.16 Electromagnetic torque with saturation

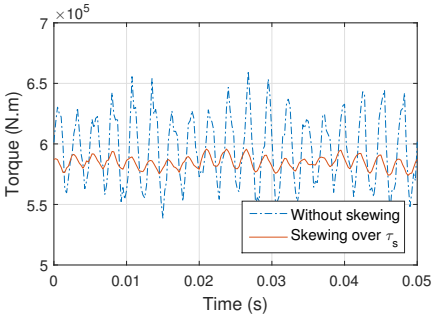

(a) Waveforms

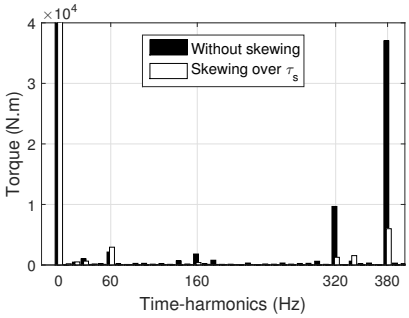

(b) Time-FFT results

Figure 4.17 Electromagnetic torque without saturation

Fig. 4.17 gives the torque waveforms and their time-FFT results in the case without saturation. The torque is extremely high which means that the air-gap flux density has already achieved an unrealistic value. The purpose of showing this figure is to look into the time-harmonics due to the saturation in the torque waveforms. Comparing Fig. 4.16(b) with Fig. 4.17(b), some components

(e.g. between 0 and 60Hz, at 260Hz, etc.) appear because of the saturation. It is not difficult to see that these components are hardly influenced by skewing the rotor slots.

Fig. 4.18 summarizes the average torque and the torque ripple with respect to different skew angles. The average torque decreases with the skew angle increasing while the torque ripple achieves a minimal value at the skew angle of one stator slot pitch τ_s.

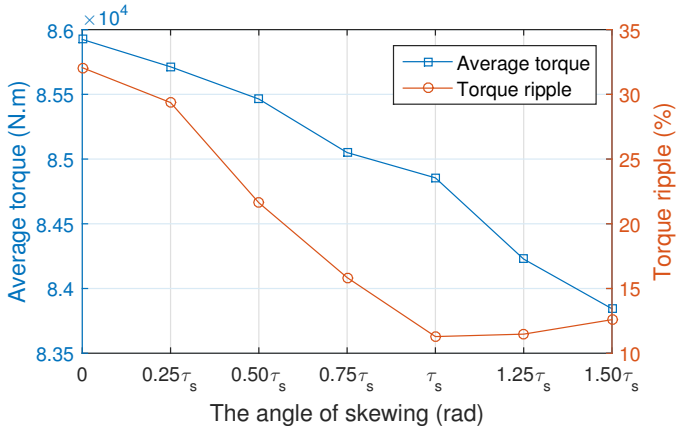

Figure 4.18 Average torque and torque ripple at different skew angles

4.4.5 Losses and efficiency

Fig. 4.19 gives the losses and efficiency at different skew angles. The stator copper losses keep the same because fixed current sources are applied to the stator windings in the 2D FE multi-slice model. The rotor copper losses decrease with the skew angle increasing and achieve minimal value at a skew angle of around τ_s and $1.25\tau_s$. The stator and rotor core losses increase as the skew angle goes up. These core losses are underestimated because the axial flux due to skewing is neglected in the model. Overall, the efficiency decreases as the skew angle increases. Again, the efficiency should be lower if the additional core losses caused by the axial flux are taken into account. A 3D FE model might be necessary to investigate how much the additional core losses would be.

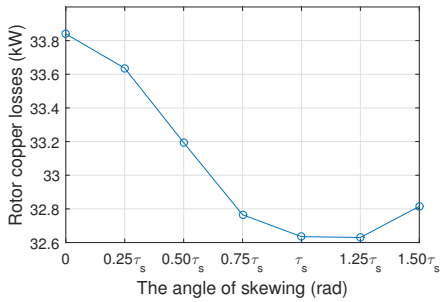

(a) Rotor copper losses

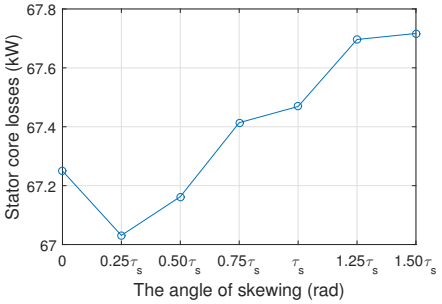

(b) Stator core losses

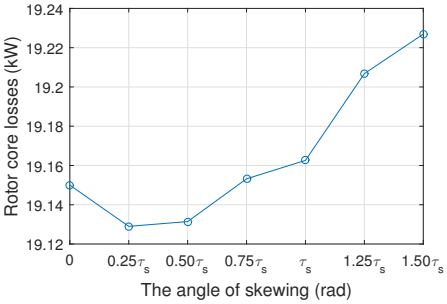

(c) Rotor core losses

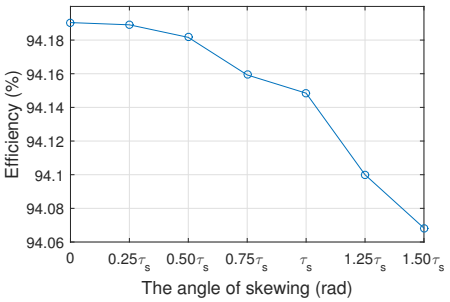

(d) Efficiency

Figure 4.19 Losses and efficiency

4.5 Conclusion

This chapter applies a 2D multi-slice FE model to study the influence of skewing rotor slots on the performance of a brushless DFIM. Slices with Gauss distribution are recommended to reduce the computing time. The results indicate that skewing the rotor slots leads to lower harmonics in the induced rotor currents, the air-gap magnetic field and the induced stator voltages. The largest component of torque ripple due to the harmonics caused by the winding distribution and the slotting is reduced significantly by skewing rotor slots. However, this is at the expense of a slightly lower average torque and a slightly lower efficiency. In addition, skewing slots has negligible influence on the harmonics due to saturation. Furthermore, it is proved that skewing one stator slot pitch is a compromise choice to minimize torque ripple while the average torque and efficiency do not decrease too much in the brushless DFIM, which is common in normal induction machines. However, it might be good to validate this conclusion by measurements or an alternative modeling method in the future. Moreover, it would also be good to use a 3D FE model to investigate the additional core losses due to the axial flux which was not considered in this chapter.

CHAPTER 5

FE Post-Processing for Skew Effects Based on Analytical Harmonic Analysis

The aim of this chapter is to develop a fast semi-numerical method to evaluate the effects of skew on the torque response. Previously, a 2D multi-slice finite element (FE) method has been applied to study the effects of skew which is time consuming. In the point of initial design, it is not efficient to use such a model to predict how much the average torque and the torque ripple will be reduced by skewing slots. This chapter makes use of normal 2D FE results and applies skew factors in post-processing to investigate the influence of rotor skew. It proves that to apply skew factors appropriately, not only the space-harmonic order needs to be considered, but also the time-harmonic order. The proposed method can give an approximate prediction of skew effects with limited computing time. The results also prove one conclusion of Chapter 4 that skewing the rotor slot over one stator slot pitch is a good choice to minimize the torque ripple in the brushless doubly-fed induction machine (DFIM).

Most parts of this chapter have been published in

- X. Wang, T. D. Strous, D. Lahaye, H. Polinder, and J. A. Ferreira, "A Finite Element Post-Processing for Skew Effect in Brushless Doubly-Fed Induction Machines," in *22th Int. Conf. Elec. Machines (ICEM)*, Lausanne, Switzerland, Sept. 2016.
- X. Wang, T. D. Strous, D. Lahaye, H. Polinder, and J. A. Ferreira, "Computationally Efficient Calculation of Skew Effects in Brushless Doubly-Fed Induction Machines," *IET Electric Power Applications*, vol.11, no.3, 2017.

5.1 Introduction

Chapter 4 applies a 2D transient FE model with the multi-slice method to investigate the effects of skew on performance in brushless DFIMs. The performance, including the induced rotor currents, the total air-gap magnetic field, the induced stator voltages, the electromagnetic torque, the torque ripple and core losses has been evaluated appropriately using the 2D transient multi-slice FE model. One of the conclusions of Chapter 4 is that skewing the rotor slot over one stator slot pitch is a good choice for minimizing the torque ripple in the brushless DFIM with a nested-loop rotor. However, that conclusion has not yet been validated by any measurements or any other modeling method. Therefore, one motivation of this chapter is to develop an alternative model to evaluate the effects of skew on the electromagnetic torque.

An analytical model has been applied to study the effects of skew in brushless DFIMs in [89]. However, it is not straightforward to take the exact construction and geometry into account. In [89], it is assumed that the nested-loop rotor has only one loop per nest and its slots are rectangular in shape. However, it has been already shown that the number of loops per nest has an effect on torque ripple [104]. FE models can overcome these assumptions. A 3D FE model is most accurate for studying the effects of skew, since the skew is essentially a 3D problem. However, it is expensive to build a 3D FE model, both from human effort and numerical perspectives. A 2D FE model with a multi-slice method is a compromise to take the effects of skew into account at the expense of slightly lower accuracy. This has been applied to permanent magnet (PM) synchronous machines [112] and normal induction machines [113], [114], as well as brushless doubly-fed reluctance machines (DFRMs) [108]. In Chapter 4, the 2D transient multi-slice FE model has also been applied to the brushless DFIMs and successfully predicts the electromagnetic torques at different skew angles. However, the computing time cost is still high because several slices are coupled and simulated simultaneously. The time spent is approximately equal to the time for a normal 2D FE model multiplied by the number of slices.

A rough approximation method is to make use of normal 2D FE results and apply well-known skew factors in post-processing to study the effects of skew. The air-gap field is extracted from a 2D FE model. Space-FFT is applied to that air-gap field at each moment in time. Skew factors are then applied to the corresponding components. The effective air-gap field considering skew effects can be reconstructed by performing an inverse FFT. This approximation method has been implemented to a synchronous reluctance machine [115] and gives an accurate estimation of skew effects compared with a 3D FE model. This is not so complicated because the air-gap field consists only of a stator field in the reluctance machine. However, this becomes complicated in an induction machine since the air-gap fields consist of not only a stator field, but also an induced rotor field. It is even more complicated in the brushless DFIMs because there are two stator fields. The procedures will be even more complex if the space harmonics due to slotting are also considered.

The contribution of this chapter is to present a computationally efficient method combining skew factors with normal 2D FE results to study the effects of skew in the brushless DFIMs. The

presented method is valuable to predict how much electromagnetic torque and torque ripple will be reduced by applying skewed slots in the stage of initial design, before building heavy 3D FE models or 2D FE multi-slice models. The well-known skew factor is a function of the space-harmonic order and the skew angle. However, the appropriate way to apply skew factors is to not only consider the space-harmonic order, but also the time-harmonic order. This will be explained in this chapter.

This chapter starts with an analytical derivation of space and time harmonics in brushless DFIMs. Next, the appropriate skew factors are analytically derived to take into account the effects of skew on the air-gap magnetic field. Then the method to apply these factors to the air-gap field, obtained from the 2D FE model, is illustrated. Subsequently, the effective magnetic field and the electromagnetic torque are calculated using the method proposed to take the effects of skew into account. The results are validated by a time-step 2D FE multi-slice model. Finally, conclusions are drawn.

Table 5.1 Main specifications of the brushless DFIM studied

Description	Machine parameter	Value
Axial length [m]	L	1.60
Air-gap length [mm]	g	1.5
Stator outer radius [m]	r_{so}	0.83
Stator inner radius [m]	r_{si}	0.67
Rotor inner radius [m]	r_{ri}	0.58
Number of phases	N_{ph}	3
Number of pole-pairs	p_p, p_c	4, 6
Rated frequency [Hz]	f_p, f_c	50, 10
Number of stator slots	N_{ss}	72
Number of rotor nests	p_r	10
Number of loops per nest	q_r	4
Rotational speed [Hz]	f_m	6
Rated power [MW]	P	3.2

5.2 Analytical derivation of harmonics

The original magnetic fields without skewed rotor slots in brushless DFIMs are derived analytically, and their harmonics are analyzed in this section. Saturation is not taken into account. The analytical expressions for the magnetic fields in this section are only used to analyze the harmonics and further derive the appropriate skew factors in section 5.3. The magnetic fields of the brushless

DFIMs are obtained from 2D transient FE models. For ease of reading, the main specifications of the case study brushless DFIM given in the previous chapters are again shown in Table 5.1. It is an initial design of a 3.2MW generator for wind turbine applications. This initial design was provided by the project partner based on their design experiences on 20kW [116] and 250kW prototypes [69] in Cambridge.

5.2.1 Stator space-harmonics and time-harmonics

In order to reduce the complexity of the analytical derivation, the following assumptions are made:

- Conductors are assumed as infinitely small conductors in the air-gap with an effective air-gap length.
- The magnetic permeability of the iron is considered infinite.
- The magnetic flux crosses the air-gap in radial direction.

Under the given set of assumptions, the air-gap flux density $B_s(\theta_s, t)$ produced by the stator windings can be calculated from the magnetomotive force (MMF) $\mathscr{F}(\theta_s, t)$ and the permeance of the air-gap $\Lambda_g(\theta_s, t)$ as:

$$B_s(\theta_s, t) = \mathscr{F}_s(\theta_s, t)\Lambda_g(\theta_s, t), \tag{5.1}$$

where θ_s is the angle along the stator circumference. The MMF $\mathscr{F}_s(\theta_s, t)$ of a three-phase symmetrical stator winding fed with a balanced current is a function of space and time [117]:

$$\begin{aligned} \mathscr{F}_s(\theta_s, t) &= \sum_{\nu=1}^{\infty} \hat{\mathscr{F}}_{s\nu} \cos(\nu p\theta_s \mp \omega t), \\ \nu &= 1, 5, 7, ..., 6m \pm 1, \forall m \in \mathbb{N}^+, \end{aligned} \tag{5.2}$$

$$\hat{\mathscr{F}}_{s\nu} = \frac{3\sqrt{2}}{\pi} \frac{N_s k_{w\nu}}{\nu p} I_s, \tag{5.3}$$

where ν is the space-harmonic order, p is the number of the pole-pairs, N_s is the number of turns in series per phase, $k_{w\nu}$ is the winding factor for the ν-th harmonic, I_s is the RMS value of the input current, $\omega = 2\pi f$ is the stator current angular frequency and f is the input frequency of the sinusoidal current. The sign before ω is negative when $\nu = 1$. Otherwise, it corresponds to the sign in $\nu = 6m \pm 1$ when $\nu > 1$.

Neglect slotting effect

In the case when the air-gap is uniform, the permeance of the air-gap without slotting being considered is:

$$\Lambda_{g0} = \frac{\mu_0}{k_C g}, \tag{5.4}$$

where μ_0 is the permeability of the vacuum, g is the air-gap length and k_C is the Carter's factor. By putting (5.2) and (5.4) into (5.1), the stator magnetic field can be calculated as:

$$B_{s0}(\theta_s, t) = \sum_{\nu=1}^{\infty} \hat{B}_{s0}^{\nu} \cos(\nu p\theta_s \mp \omega t), \tag{5.5}$$

where

$$\hat{B}_{s0}^{\nu} = \frac{\mu_0}{k_C g} \frac{3\sqrt{2}}{\pi} \frac{N_s k_{w\nu}}{\nu p} I_s. \tag{5.6}$$

Consider slotting effect

The permeance of the air-gap with slotting being considered is:

$$\Lambda_g(\theta_s, t) = \Lambda_{g0} \lambda_{g1}(\theta_s) \lambda_{g2}(\theta_s, t), \tag{5.7}$$

where λ_{g1} and λ_{g2} are relative specific permeances of the air-gap when the stator and rotor are slotted, respectively. These can be calculated by (5.8) and (5.9) [117].

$$\lambda_{g1}(\theta_s) = 1 + \sum_{k=1}^{\infty} A_k \cos(k s_1 \theta_s), \tag{5.8}$$

$$\lambda_{g2}(\theta_s, t) = 1 + \sum_{l=1}^{\infty} A_l \cos[l s_2(\theta_s - \Omega_m t + \delta_{12})], \tag{5.9}$$

where k and l are the harmonic orders due to the stator slots and the rotor slots, s_1 and s_2 are the number of stator slots and rotor slots, $\Omega_m (= 2\pi f_m)$ is the mechanical rotating speed of the rotor in rad/s. δ_{12} is the angle between the center axes of the stator tooth and the rotor tooth at the origin of coordinate system when $t = 0$. The formulas for calculating coefficients A_k and A_l can be found in [117], which depend on the geometry of the slots. The complete stator flux density in the air-gap can be formulated as (5.10) by putting (5.7) and (5.4) into (5.1) in the case when $\delta_{12} = 0$,

$$B_s(\theta_s, t) = \sum_{\nu=1}^{\infty} \hat{B}_{s0}^{\nu} \cos(\nu p\theta_s \mp \omega t) \cdot \left\{ 1 + \sum_{k=1}^{\infty} A_k \cos(k s_1 \theta_s) + \sum_{l=1}^{\infty} A_l \cos[l s_2(\theta_s - \Omega_m t)] + \frac{1}{2} \sum_{k=1}^{\infty} \sum_{l=1}^{\infty} A_k A_l \right.$$
$$\left. \cdot \{\cos[(l s_2 + k s_1)\theta_s - l s_2 \Omega_m t] + \cos[(l s_2 - k s_1)\theta_s - l s_2 \Omega_m t]\} \right\}. \tag{5.10}$$

The first term represents the winding distribution harmonics while the other three terms indicate the slotting harmonics. Then the space-harmonics and the corresponding time-harmonics due to the power winding (PW) and the control winding (CW) can be summarized in the left two columns of Table. 5.2. The meaning of the right hand two columns will be explained in 5.2.2.

Table 5.2 Space and time harmonics of stator field and induced rotor field

Stator magnetic field		**Induced rotor magnetic field**	
Space harmonics	**Time harmonics**	**Space harmonics**	**Time harmonics**
vp	$\mp f$	$vp+Kp_r$	$\mp f-Kp_r f_m$
		$-vp+Kp_r$	$\mp f+Kp_r f_m$
$vp+ls_2$	$\mp f-ls_2 f_m$	$vp+ls_2+Kp_r$	$\mp f-Kp_r f_m-ls_2 f_m$
		$-(vp+ls_2)+Kp_r$	$\mp f+Kp_r f_m-ls_2 f_m$
$vp-ls_2$	$\mp f+ls_2 f_m$	$vp-ls_2+Kp_r$	$\mp f-Kp_r f_m+ls_2 f_m$
		$-(vp-ls_2)+Kp_r$	$\mp f+Kp_r f_m+ls_2 f_m$
$vp+ks_1$	$\mp f$	$vp+ks_1+Kp_r$	$\mp f-Kp_r f_m$
		$-(vp+ks_1)+Kp_r$	$\mp f+Kp_r f_m$
$vp+ks_1+ls_2$	$\mp f-ls_2 f_m$	$vp+ks_1+ls_2+Kp_r$	$\mp f-Kp_r f_m-ls_2 f_m$
		$-(vp+ks_1+ls_2)+Kp_r$	$\mp f+Kp_r f_m-ls_2 f_m$
$vp+ks_1-ls_2$	$\mp f+ls_2 f_m$	$vp+ks_1-ls_2+Kp_r$	$\mp f-Kp_r f_m+ls_2 f_m$
		$-(vp+ks_1-ls_2)+Kp_r$	$\mp f+Kp_r f_m+ls_2 f_m$
$vp-ks_1$	$\mp f$	$vp-ks_1+Kp_r$	$\mp f-Kp_r f_m$
		$-(vp-ks_1)+Kp_r$	$\mp f+Kp_r f_m$
$vp-ks_1+ls_2$	$\mp f-ls_2 f_m$	$vp-ks_1+ls_2+Kp_r$	$\mp f-Kp_r f_m-ls_2 f_m$
		$-(vp-ks_1+ls_2)+Kp_r$	$\mp f+Kp_r f_m-ls_2 f_m$
$vp-ks_1-ls_2$	$\mp f+ls_2 f_m$	$vp-ks_1-ls_2+Kp_r$	$\mp f-Kp_r f_m+ls_2 f_m$
		$-(vp-ks_1-ls_2)+Kp_r$	$\mp f+Kp_r f_m+ls_2 f_m$

* p is p_p or p_c corresponding to the power winding or the control winding.
* f is f_p or f_c corresponding to the power winding or the control winding.

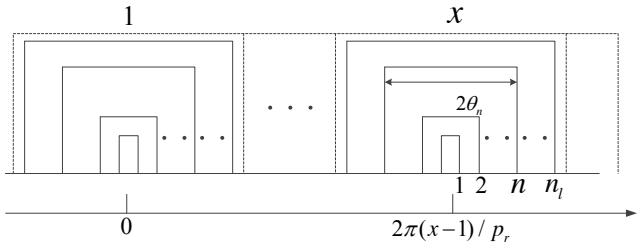

Figure 5.1 The configuration of the nested-loop rotor structure

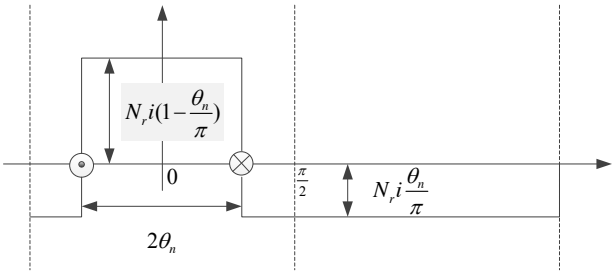

Figure 5.2 The MMF waveform due to the current in one short-circuit loop

5.2.2 Induced rotor space-harmonics and time-harmonics

Considering the mechanical rotational speed Ω_m, the relationship between the stator reference frame (θ_s) and the rotor reference frame (θ_r) is:

$$\theta_s = \theta_r + \Omega_m t. \tag{5.11}$$

To calculate the flux linkage and the induced EMF of the rotor, the air-gap flux densities produced by the power winding or the control winding are firstly expressed in the rotor reference frame as (5.12). Here, the first component of (5.10) is used as an example for the derivation and the derivations are similar for the other three terms.

$$B_s(\theta_r, t) = \sum_{\nu=1}^{\infty} \hat{B_{s0}^{\nu}} \cos[\nu p\theta_r + (\mp\omega + \nu p\Omega_m)t]. \tag{5.12}$$

There are p_r nests in the rotor. To achieve the magnetic cross-coupling, p_r is designed to equal $(p_p + p_c)$. The reason has been well explained by Williamson *et al.* in [48]. The flux linkage in the n^{th} loop of the x^{th} nest (shown in Fig. 5.1) is calculated as (5.13):

$$\begin{aligned}\phi(t,n,x) &= Lr\int_{-\theta_n+(x-1)\frac{2\pi}{p_r}}^{\theta_n+(x-1)\frac{2\pi}{p_r}} B_s(\theta_r,t)d\theta_r \\ &= \sum_{\nu=1}^{\infty}\frac{2Lr}{\nu p}\hat{B}_{s0}^{\nu}\sin(\nu p\theta_n)\cos\left[\nu p\frac{2\pi(x-1)}{p_r} + (\mp\omega+\nu p\Omega_m)t\right],\end{aligned} \tag{5.13}$$

in which L is the axial length of the machine and r is the radius of the air-gap. The induced rotor current is shown as (5.14) by assuming the impedance of the n^{th} loop of the x^{th} nest is $Z_r(x,n)$. A detailed calculation of $Z_r(x,n)$ can be found in [48], [42].

$$\begin{aligned}i_r(t,x,n) &= -\frac{1}{Z_r}\frac{d\phi}{dt} \\ &= \sum_{\nu=1}^{\infty}\frac{2Lr}{Z_r\nu p}\hat{B}_{s0}^{\nu}\sin(\nu p\theta_n)(\mp\omega+\nu p\Omega_m)\cdot\sin\left[\nu p\frac{2\pi(x-1)}{p_r} + (\mp\omega+\nu p\Omega_m)t\right].\end{aligned} \tag{5.14}$$

Fig. 5.2 shows the MMF waveform produced by the rotor current in one short-circuited loop. Because the nested-loops are constructed with solid bars to maximize slot fill factor, the number of turns of a single loop N_r equals one. The induced rotor MMF can be expressed by the Fourier series as:

$$\mathscr{F}_r(\theta_r, t, x, n) = \sum_{u=1}^{\infty} \hat{\mathscr{F}}_{ru} \cos\left[u\left(\theta_r - (x-1)\frac{2\pi}{p_r}\right)\right], \tag{5.15}$$

in which u indicates the space-harmonic order and $\hat{\mathscr{F}}_{ru}$ is given by (5.16):

$$\begin{aligned}\hat{\mathscr{F}}_{ru} =& \frac{2}{\pi}\left\{\int_{(x-1)\frac{2\pi}{p_r}}^{\theta_n+(x-1)\frac{2\pi}{p_r}} \left(1-\frac{\theta_n}{\pi}\right) N_r i_r \cos\left[u\left(\theta_r-(x-1)\frac{2\pi}{p_r}\right)\right] d\theta_r \right.\\ &\left. + \int_{\theta_n+(x-1)\frac{2\pi}{p_r}}^{\pi+(x-1)\frac{2\pi}{p_r}} \left(-\frac{\theta_n}{\pi}\right) N_r i_r \cos\left[u\left(\theta_r-(x-1)\frac{2\pi}{p_r}\right)\right] d\theta_r \right\}\\ =& \sum_{v=1}^{\infty} \frac{4N_r Lr}{Z_r vpu\pi} \hat{B}_{s0}^{v} \sin(vp\theta_n)(\mp\omega + vp\Omega_m)\cdot\sin(u\theta_n)\sin\left[vp\frac{2\pi(x-1)}{p_r} + (\mp\omega+vp\Omega_m)t\right].\end{aligned} \tag{5.16}$$

For ease of illustration, (5.4) is taken as the permeance of the air-gap for the calculation of the induced magnetic field. Therefore, the induced rotor magnetic field due to the power winding (or the control winding) can be formulated as (5.17).

$$\begin{aligned}B_r(\theta_r, t) =& \sum_{n=1}^{n_l}\sum_{x=1}^{p_r}\sum_{u=1}^{\infty}\sum_{v=1}^{\infty} \frac{2N_r Lr\Lambda_{g0}}{Z_r vpu\pi}\hat{B}_{s0}^{v}\cdot\sin(vp\theta_n)(\mp\omega+vp\Omega_m)\sin(u\theta_n)\\ &\cdot\left\{\sin\left[(\mp\omega+vp\Omega_m)t + u\theta_r + (vp-u)(x-1)\frac{2\pi}{p_r}\right] + \sin\left[(\mp\omega+vp\Omega_m)t - u\theta_r + (vp+u)(x-1)\frac{2\pi}{p_r}\right]\right\}.\end{aligned} \tag{5.17}$$

The induced B_r will not be equal to zero when $u = vp + Kp_r (\forall K \in N)$ or $u = -vp + Kp_r (\forall K \in N^+)$. When p equals to p_p, (5.17) represents the induced rotor magnetic field due to the PW. The induced rotor field has two main components p_p and $(-p_p + p_r) = p_c$. The second one would couple with the CW field. This actually means that the PW field cross-couples with the CW through the nested-loop rotor. The situation is similar when p equals to p_c. The space-harmonics and time-harmonics of induced rotor magnetic fields are given in the right two columns of Table 5.2 in which p could be p_p or p_c corresponding to the situation due to the power winding or the control winding.

According to (5.14), the frequencies of the induced currents due to the power winding and the control winding are $\mp f_p + vp_p f_m$ and $\mp f_c + vp_c f_m$, respectively. This indicates that the cross-coupling occurs when the current induced by the fundamental component of the power winding magnetic field ($v = 1$) has the same frequency as the current induced by the fundamental component of the control winding magnetic field ($v = 1$) [118]. Then the synchronous mechanical

speed f_m can be derived as:

$$\begin{aligned} -f_p + p_p f_m &= -(f_c + p_c f_m), \\ \Rightarrow f_m &= \frac{f_p + f_c}{p_p + p_c}. \end{aligned} \tag{5.18}$$

The stator magnetic fields and the induced rotor fields have been analytically derived in this section. The influence of skew effects on the fields are further discussed in the following section.

5.3 Incorporation of skew factors

In the case without skewed rotor slots, the air-gap magnetic fields do not vary along the axial direction. The air-gap magnetic fields will vary along the axial direction if skewed slots are applied. This section attempts to define an effective field taking the effects of skew into account. Then, the skew factor for each space- and time-harmonic of the magnetic field can be derived by comparing the effective field with the original one.

5.3.1 Skew factors for stator fields

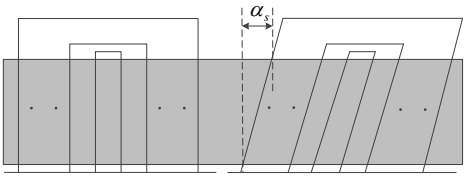

Figure 5.3 Nested-loop rotor with & without skewed slots

If the rotor slots are skewed with an angle α_s (shown in Fig. 5.3), the flux linkage in the n^{th} loop of the x^{th} nest due to the stator field given by (5.10) can be calculated as:

$$\phi_{skew}(t,n,x) = Lr \int_{-\theta_n+2\pi(x-1)/p_r}^{\theta_n+2\pi(x-1)/p_r} \frac{1}{\alpha_s} \int_{-\frac{\alpha_s}{2}}^{\frac{\alpha_s}{2}} B_s(\theta_s+\alpha,t)\,d\alpha\,d\theta_s. \tag{5.19}$$

The effective stator magnetic field is defined as:

$$B_{eff}(\theta_s,t) = \frac{1}{\alpha_s}\int_{-\frac{\alpha_s}{2}}^{\frac{\alpha_s}{2}} B_s(\theta_s+\alpha,t)\,d\alpha = \frac{1}{\alpha_s}\int_{-\frac{\alpha_s}{2}}^{\frac{\alpha_s}{2}} \mathscr{F}_s(\theta_s+\alpha,t)\Lambda_{g0}\lambda_{g1}(\theta_s+\alpha)\lambda_{g2}(\theta_s,t)\,d\alpha. \tag{5.20}$$

By putting (5.2), (5.8) and (5.9) into (5.20), the complete effective stator magnetic field includes four components given by (5.21a), (5.21b), (5.21c) and (5.21d).

$$B_{eff}^{cons}(\theta_s,t) = \sum_{\nu=1}^{\infty} \hat{B}_{s0}^{\nu} \frac{\sin(\nu p\alpha_s/2)}{\nu p\alpha_s/2} \cos(\nu p\theta_s \mp \omega t), \tag{5.21a}$$

$$B^{s}_{eff}(\theta_s,t)=\sum_{\nu=1}^{\infty}\sum_{k=1}^{\infty}\frac{1}{2}\hat{B}^{\nu}_{s0}A_k\cdot\left\{\frac{\sin[(\nu p+ks_1)\alpha_s/2]}{(\nu p+ks_1)\alpha_s/2}\cos[(\nu p+ks_1)\theta_s\mp\omega t]\right.$$
$$\left.+\frac{\sin[(\nu p-ks_1)\alpha_s/2]}{(\nu p-ks_1)\alpha_s/2}\cos[(\nu p-ks_1)\theta_s\mp\omega t]\right\}, \tag{5.21b}$$

$$B^{r}_{eff}(\theta_s,t)=\sum_{\nu=1}^{\infty}\sum_{l=1}^{\infty}\frac{1}{2}\hat{B}^{\nu}_{s0}A_l\cdot\left\{\frac{\sin(\nu p\alpha_s/2)}{\nu p\alpha_s/2}\cos[(\nu p+ls_2)\theta_s+(\mp\omega-ls_2\Omega_m)t]\right.$$
$$\left.+\frac{\sin(\nu p\alpha_s/2)}{\nu p\alpha_s/2}\cos[(\nu p-ls_2)\theta_s+(\mp\omega+ls_2\Omega_m)t]\right\}, \tag{5.21c}$$

$$\begin{aligned}B^{sr}_{eff}(\theta_s,t)=\sum_{\nu=1}^{\infty}\sum_{k=1}^{\infty}\sum_{l=1}^{\infty}\frac{1}{4}\hat{B}^{\nu}_{s0}A_kA_l\left\{\right.&\frac{\sin[(\nu p+ks_1)\alpha_s/2]}{(\nu p+ks_1)\alpha_s/2}\cos[(\nu p+ks_1+ls_2)\theta_s+(\mp\omega-ls_2\Omega_m)t]\\&+\frac{\sin[(\nu p+ks_1)\alpha_s/2]}{(\nu p+ks_1)\alpha_s/2}\cos[(\nu p+ks_1-ls_2)\theta_s+(\mp\omega+ls_2\Omega_m)t]\\&+\frac{\sin[(\nu p-ks_1)\alpha_s/2]}{(\nu p-ks_1)\alpha_s/2}\cos[(\nu p-ks_1+ls_2)\theta_s+(\mp\omega-ls_2\Omega_m)t]\\&\left.+\frac{\sin[(\nu p-ks_1)\alpha_s/2]}{(\nu p-ks_1)\alpha_s/2}\cos[(\nu p-ks_1-ls_2)\theta_s+(\mp\omega+ls_2\Omega_m)t]\right\}.\end{aligned} \tag{5.21d}$$

Compared with the original stator magnetic field (5.10), the amplitude of corresponding component is scaled by a factor due to skewing. Each component of the original stator field can be recognized according to its space-harmonic order and time-harmonic order since it is a function of space and time. Table 5.3 summaries the factors applied to all the components (including the fundamental one and the harmonics) of the stator magnetic field.

Table 5.3 Skew factors for stator magnetic field

Space harmonics	Time harmonics	Skew factor
νp	$\mp f$	$\frac{\sin(\nu p\alpha_s/2)}{\nu p\alpha_s/2}$
$\nu p+ls_2$	$\mp f-ls_2f_m$	
$\nu p-ls_2$	$\mp f+ls_2f_m$	
$\nu p+ks_1$	$\mp f$	$\frac{\sin[(\nu p+ks_1)\alpha_s/2]}{(\nu p+ks_1)\alpha_s/2}$
$\nu p+ks_1+ls_2$	$\mp f-ls_2f_m$	
$\nu p+ks_1-ls_2$	$\mp f+ls_2f_m$	
$\nu p-ks_1$	$\mp f$	$\frac{\sin[(\nu p-ks_1)\alpha_s/2]}{(\nu p-ks_1)\alpha_s/2}$
$\nu p-ks_1+ls_2$	$\mp f-ls_2f_m$	
$\nu p-ks_1-ls_2$	$\mp f+ls_2f_m$	

5.3.2 Skew factors for induced rotor fields

The induced rotor magnetic field given by (5.17) is derived using the first term of the total stator field given by (5.10), which is scaled by a factor because of the skewing indicated by (5.21a). Therefore, that induced rotor field is also scaled by the same factor due to skewing. Furthermore, the other three components of the total stator field follow a similar procedure. The factors applied to the induced rotor field are given in Table. 5.4.

Table 5.4 Skew factors for induced rotor magnetic field

Space harmonics	Time harmonics	Skew factor
$vp + Kp_r$	$\mp f - Kp_r f_m$	
$-vp + Kp_r$	$\mp f + Kp_r f_m$	
$vp + ls_2 + Kp_r$	$\mp f - Kp_r f_m - ls_2 f_m$	$\frac{\sin(vp\alpha_s/2)}{vp\alpha_s/2}$
$-(vp + ls_2) + Kp_r$	$\mp f + Kp_r f_m - ls_2 f_m$	
$vp - ls_2 + Kp_r$	$\mp f - Kp_r f_m + ls_2 f_m$	
$-(vp - ls_2) + Kp_r$	$\mp f + Kp_r f_m + ls_2 f_m$	
$vp + ks_1 + Kp_r$	$\mp f - Kp_r f_m$	
$-(vp + ks_1) + Kp_r$	$\mp f + Kp_r f_m$	
$vp + ks_1 + ls_2 + Kp_r$	$\mp f - Kp_r f_m - ls_2 f_m$	$\frac{\sin[(vp+ks_1)\alpha_s/2]}{(vp+ks_1)\alpha_s/2}$
$-(vp + ks_1 + ls_2) + Kp_r$	$\mp f + Kp_r f_m - ls_2 f_m$	
$vp + ks_1 - ls_2 + Kp_r$	$\mp f - Kp_r f_m + ls_2 f_m$	
$-(vp + ks_1 - ls_2) + Kp_r$	$\mp f + Kp_r f_m + ls_2 f_m$	
$vp - ks_1 + Kp_r$	$\mp f - Kp_r f_m$	
$-(vp - ks_1) + Kp_r$	$\mp f + Kp_r f_m$	
$vp - ks_1 + ls_2 + Kp_r$	$\mp f - Kp_r f_m - ls_2 f_m$	$\frac{\sin[(vp-ks_1)\alpha_s/2]}{(vp-ks_1)\alpha_s/2}$
$-(vp - ks_1 + ls_2) + Kp_r$	$\mp f + Kp_r f_m - ls_2 f_m$	
$vp - ks_1 - ls_2 + Kp_r$	$\mp f - Kp_r f_m + ls_2 f_m$	
$-(vp - ks_1 - ls_2) + Kp_r$	$\mp f + Kp_r f_m + ls_2 f_m$	

* p is p_p or p_c corresponding to the PW or the CW.
* f is f_p or f_c corresponding to the PW or the CW.

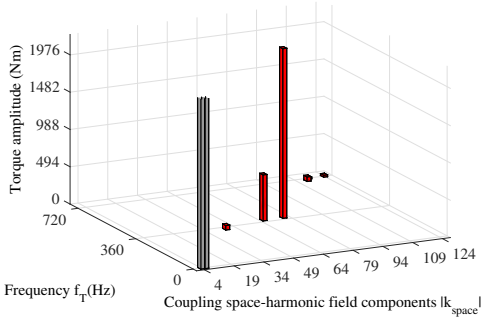

(a) Due to winding distribution

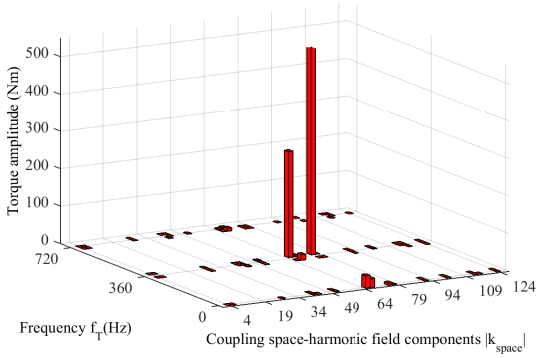

(b) Due to slotting

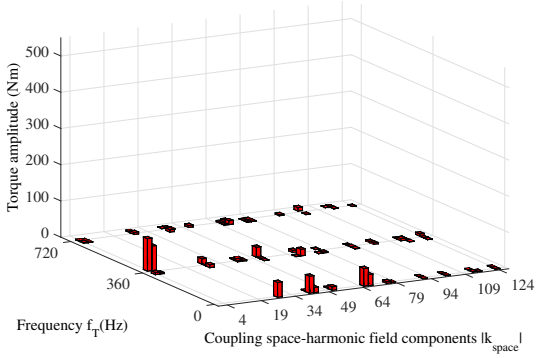

(c) Due to time harmonics in rotor currents

Figure 5.4 Torque ripple components [78]

5.3.3 Discussion on the skew factors

Skew factor is a well-known variable which is a function of the space-harmonic order and the skew angle. Therefore, it is necessary to figure out the corresponding space-harmonic order and the angle when we apply the skew factor to a certain space-harmonic component. This is sufficient in the case where slotting is not taken into account. According to Table 5.3, the factors applied to the space harmonics νp due to the winding distribution exactly depend on their corresponding space-harmonic orders. It is still valid if we look at the factors applied to the space harmonics $\nu p \pm k s_1$ due to stator slots. However, the factors applied to the space harmonics $\nu p \pm l s_2$, $\nu p \pm k s_1 \pm l s_2$ due to the rotor slots do not depend on their corresponding space harmonic orders. These components can be recognized by not only considering their space-harmonic orders, but also the corresponding time-harmonic orders. Previously, we studied the cause of the torque ripple (shown in Fig. 5.4) in the case study brushless DFIM [78]. It indicates that the slotting space harmonics have some contribution to the torque ripple and cannot be ignored. Therefore, both space-harmonic order and time-harmonic order need to be considered when we apply a skew factor to a certain space harmonic component in the case study machine.

5.3.4 Approach to take into account the effects of skew

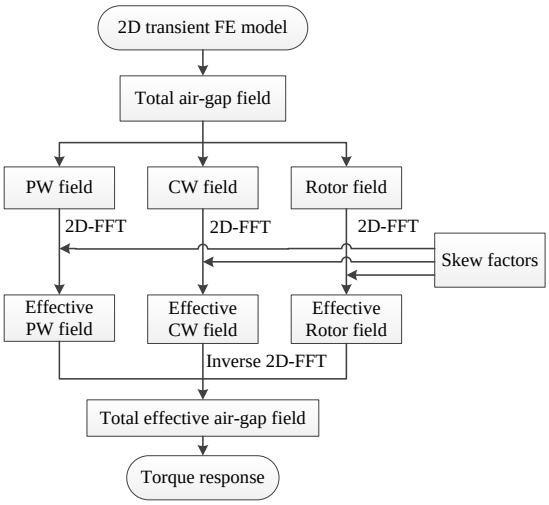

Figure 5.5 Procedures to take into account the skew effect in the post-processing

Fig. 5.5 gives the steps to apply skew factors in post-processing. Saturation is not considered in this chapter. Firstly, the PW field is obtained by performing a 2D transient FE simulation in

which the PW is supplied and the CW and the rotor are not supplied. Secondly, another 2D transient FE simulation is performed in which the PW and the rotor are supplied while the CW is open-circuited. By subtraction of these two simulation results, the rotor field due to the PW is obtained. The same steps are repeated for the CW to obtain the CW field and the rotor field due to the CW. A 2D-FFT is applied to the fields, and we get a spectrum with respect to space-harmonic and time-harmonic order. Next, the skew factors (given in Table. 5.3 and 5.4) are applied to the components according to their corresponding space-harmonic and time-harmonic orders. Afterwards, an inverse 2D-FFT is performed to calculate the effective air-gap field in which skew effects are approximately being taken into account. Finally, the electromagnetic torque is calculated using the normal Maxwell stress tensor method. We can do the calculation at different skew angles by applying corresponding skew factors in the post-processing while the heavy FE computation no longer needs to be repeated.

5.4 Results and discussions

5.4.1 Harmonic analysis based on FEM results

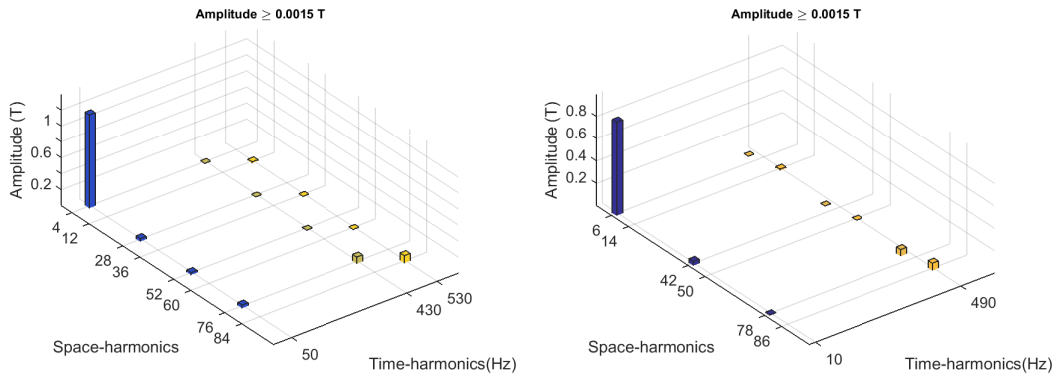

(a) Due to power winding **(b)** Due to control winding

Figure 5.6 Space and time harmonics of the stator fields

Fig. 5.6 gives the space and time harmonics of the stator magnetic fields obtained from the 2D FE model. The components having amplitudes are lower than 0.0015T are not shown for clarity. Table 5.2 has indicated that the frequencies of the components due to the winding distribution (νp) and the stator slots ($\nu p \pm k s_1$) are same as the frequency f of the stator input currents. These components correspond to the blue bars in Fig. 5.6. They rotate at 50Hz to the PW field while they rotate at 10Hz to the CW field. Table 5.2 also shows the frequencies of the components due to the

rotor slots do not equal $\mp f$, but $(\mp f) \pm ls_2 f_m$ in which the mechanical rotational speed is taken into account as well. These components correspond to the yellow bars in Fig. 5.6. For instance, two space harmonics due to the rotor slots are -76 and 84 calculated by $(p_p \pm ls_2)$. The minus sign indicates the rotating direction of the harmonic field. However, the minus sign is not given in the 2D-FFT results shown in Fig. 5.6. According to Table 5.2, their corresponding time harmonics are 430Hz and -530Hz, respectively. These two components are clearly present in Fig. 5.6(a) while the minus sign is not shown in the 2D-FFT results.

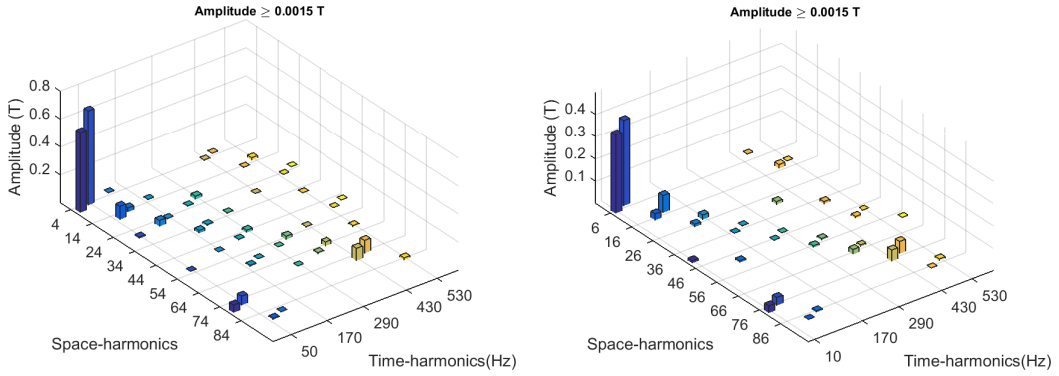

(a) Induced by power winding **(b)** Induced by control winding

Figure 5.7 Space and time harmonics of the induced rotor fields

Fig. 5.7 shows the space and time harmonics of the induced rotor magnetic fields. Table 5.2 has already shown that one space harmonic in the stator magnetic field (e.g. vp) would induce two space-harmonic components in the rotor magnetic field (e.g. $vp + Kp_r$ and $-vp + Kp_r$). Therefore, the fundamental component of the PW field (i.e. $p_p = 4$) could be expected to induce two main components, 4^{th} and 6^{th}, according to Table 5.2. The 6^{th} component will couple with the CW field, which essentially shows the cross-coupling between the PW and the CW through the nested-loop rotor. These two components can be seen in the left corner of Fig. 5.7(a). Moreover, not only the 4^{th} and 6^{th} components, but also some other undesired higher space harmonics will be produced with the K (in $vp + Kp_r$ and $-vp + Kp_r$) increasing according to Table 5.2. They are 14^{th}, 16^{th}, 24^{th}, 26^{th}, etc. rotating in -110Hz, 70Hz, -170Hz, 130Hz, etc. respectively. They all appear in Fig. 5.7(a). For the induced rotor magnetic fields due to the CW shown in Fig. 5.7(b), the explanations are similar to those shown in Fig. 5.7(a).

The harmonic analysis presented in Table 5.2 of Section 5.2 is validated by the FEM results shown in Fig. 5.6 and 5.7. This validation is a guarantee of the derivation of incorporating skew factors in Section 5.3.

5.4.2 Comparison of air-gap magnetic field

The time-step 2D FEM combined with the multi-slice method is applied to investigate the influence of skew effects in the case study machine [119]. We extend the previous simulation with nine slices and make its result a reference for the method presented in this paper. In the multi-slice model, the effective air-gap field is calculated by taking the average of the fields along the skewed rotor bar. Fig. 5.8 shows the comparison between the total effective air-gap fields obtained from the multi-slice model and the one calculated by applying the skew factors to the original fields in the post-processing. The proposed method gives a comparable accurate estimation of the resultant air-gap fields compared with the multi-slice method. A small difference can be expected because of the natural limitation of the proposed method. Skew effects are taken into account in the iterative calculation of induced rotor currents and the resultant magnetic fields in 2D FE multi-slice models, but not in the presented model.

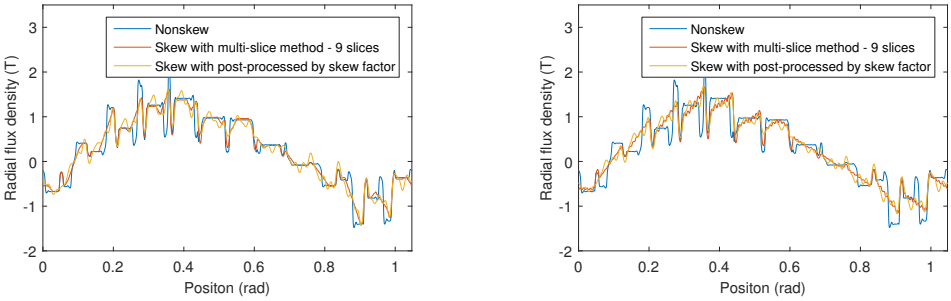

(a) Skewed with 0.5 stator slot pitch **(b)** Skewed with 1 stator slot pitch

Figure 5.8 Total air-gap field considering skew effect with different methods

5.4.3 Comparison of torque response

Fig. 5.9 gives the electromagnetic torques with 0.5 and 1 stator slot pitch skewed, which is calculated by the multi-slice model and the method presented. Although there is a difference, the method proposed can still capture the influence of skew effects on the electromagnetic torque. Electromagnetic torques are related to both radial and tangential flux densities. Therefore, it is not difficult to understand that the errors in torques are bigger than those in flux densities.

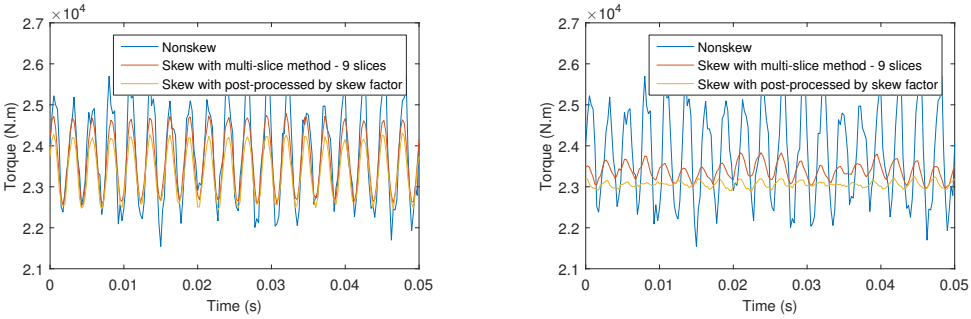

(a) Skewed with 0.5 stator slot pitch **(b)** Skewed with 1 stator slot pitch

Figure 5.9 Torque response considering skew effect with different methods

5.4.4 Torque response and ripple at different skew angles

Torque ripple is defined as:

$$Ripple = \frac{max(T) - min(T)}{mean(T)} \times 100\%. \tag{5.22}$$

Fig. 5.10 shows the average torque and torque ripple at different skew angles calculated using the multi-slice model and the proposed method. Both Fig. 5.9 and Fig. 5.10 indicate that the presented method has a reasonable capability for estimating the average torque while it slightly underestimates the amount of torque ripple. The average torque calculated by the presented method is around 1.5% lower than that predicted by the multi-slice model. For the torque ripple, the presented method gives around 2 percent lower compared with the multi-slice model. During the stage of initial design, the proposed method can be applied to predict how much the average torque and torque ripple would be reduced due to skewing, before building heavy 3D FE models or 2D FE multi-slice models. The average torque decreases when the skew angle increases. The torque ripple achieves a minimal value at 0.087rad in this case study machine. This is approximately equal to one stator slot pitch which is consistent with common sense. This further indicates the proposed method captures the trend accurately.

For the computing time, the multi-slice model with nine slices takes around 41 hours at one skew angle. It still takes around 17 hours at one skew angle for five slices with Gauss distribution which helps to reduce the number of slices [109]. The numerical results show that five slices with Gauss distribution is minimal to capture skew effects sufficiently in this case study. However, the presented method takes approximately 13 hours in total for four FE simulations to separate the total magnetic fields. Corresponding skew factors are applied in the post-processing at different skew angles while the FE simulations do not need to be repeated. Although the computing time for the post-processing is not recorded, it could reasonably be expected to be much cheaper compared with the numerical simulation.

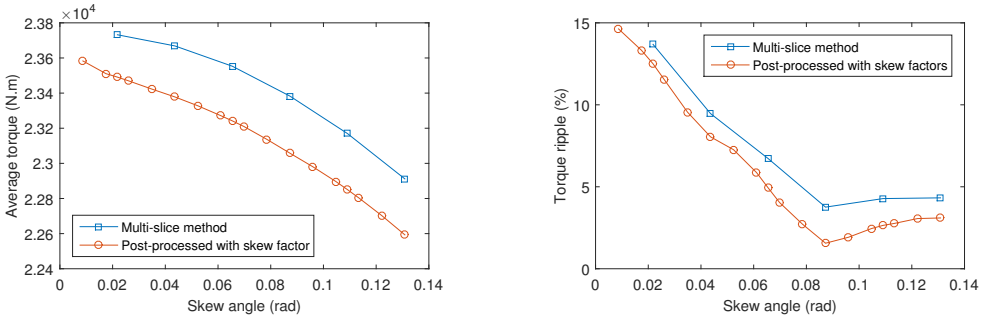

(a) Average torque **(b)** Torque ripple

Figure 5.10 Average torque and ripple with respect to different skew angles

5.5 Conclusion

This chapter presents a computationally efficient method to study the effects of skew in brushless DFIMs. Time-step 2D FE models are computed initially and the air-gap fields are extracted in the post-processing. Based on the 2D-FFT results of the fields, the appropriate skew factors can be applied to each component according to the space-harmonic and the time-harmonic order. The electromagnetic torque can be calculated based on the effective magnetic field in which the effects of skew have been approximately considered. Compared with the 2D multi-slice FE method or the 3D FE model, the proposed method reduces the computing time significantly. The trend of the average torque and the ripple with respect to different skew angles can be predicted with a level of accuracy comparable to the multi-slice model. Therefore, this method constitutes a valuable tool to approximately estimate how much the average torque and the torque ripple will be reduced by applying skewed slots during the initial design stage. Moreover, the results indicate that applying skewed slots is useful to reduce the torque ripple in the brushless DFIMs, although it may lead to a lower average torque, higher core losses and additional manufacturing costs. It also shows that skewing one stator slot pitch is a good choice to minimize the torque ripple. This is consistent with the conclusion of Chapter 4. In other words, to a certain extent, the method presented in this chapter and the 2D transient multi-slice FE model are validated with each other. Furthermore, the presented method can also be applied to normal induction machines following the derivation in this paper. Saturation is not considered in this chapter which may also have an influence on the magnetic field, as well as the electromagnetic torque. They could be investigated separately in the future.

CHAPTER 6

Comparison of Nested-Loop Rotors Using 2D Transient FE Model

The aim of this chapter is to derive design guidelines for nested-loop rotors. The nested-loop rotor is preferred in a brushless doubly-fed induction machine (DFIM) because it has the advantages of ruggedness, a lower impedance and a higher slot fill factor. However, there are few papers giving the design guidelines for nested-loop rotors. This chapter applies 2D transient finite element (FE) models to evaluate sixteen nested-loop rotor constructions from four aspects of output characteristics. The effects of the number of loops per nest and the position for each individual loop on the torque load-angle characteristics, torque ripple, efficiency and total harmonic distortion (THD) of the stator voltages are studied. The results indicate that the number of loops per nest and their position have a systematic influence on the torque load-angle characteristics and the efficiency, but not such a systematic effect on the torque ripple and the THD of stator voltages.

Most parts of this chapter have been published in

- X. Wang, D. Liu, H. Polinder, D. Lahaye, and J. A. Ferreira, "Comparison of Nested-Loop Rotors in Brushless Doubly-Fed Induction Machines," in *19th Int. Conf. Elec. Machines Systems (ICEMS)*, Chiba, Japan, Nov. 2016.

6.1 Introduction

There are generally two kinds of rotors investigated for the brushless DFIMs. They are wound rotors and cage rotors. Wound rotors offer more flexible connections. For example, a complicated doubly-sine wound rotor has been proposed to reduce the space harmonics of the rotor winding [36]. It is designed to be constituted by doubly-layer unequal-turn coils based on the principles of tooth harmonic and sinusoidal winding. However, it is not straightforward to manufacture such complicated wound rotors. Compared with wound rotors, cage rotors have the advantages of ruggedness, a lower impedance [26] and a higher fill factor [33]. Moreover, it is cheaper to cast a cage rotor using aluminum or copper. However, special measures must be taken to achieve bar-to-stack insulation since the performance of the brushless DFIM is significantly degraded due to inter-bar currents [38]. The standard squirrel cage rotor gives a weak cross-coupling capability as can be expected. Among the rotors which show a strong cross-coupling capability, the nested-loop rotor construction is considered favorable because of its simplicity. Fig. 6.1 shows a typical construction of nested-loop rotors. This type of rotor comprises of nested loops terminated with a common end ring at one end only. The number of rotor nests should equal $(p_p + p_c)$ to provide spatial compatibility for cross-couplings [42].

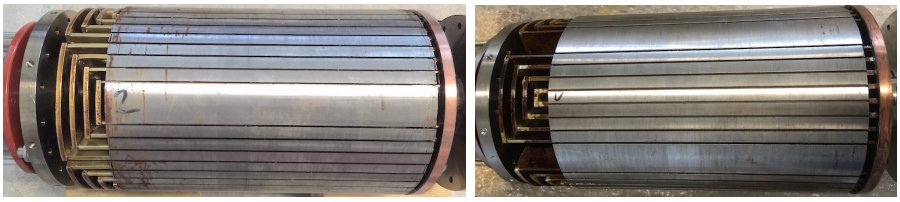

(a) **(b)**

Figure 6.1 Nested-loop rotor constructions

Only a limited number of references have studied the design of nested-loop rotors. Several different nested-loop rotors have been built and evaluated by measuring the torque-speed characteristics [24]. However, a higher average torque is not the only criterion for a better rotor design. Moreover, it is not straightforward to vary some configurations on a prototype in the measurements. Equivalent circuit models (ECMs) have been applied to study the design of nested-loop rotors [65], [66]. The influence of the loop span and the number of loops per nest on the ECM parameters has been studied in [66]. However, the influence of different nested-loop rotors on torque ripples and harmonic distortions is not discussed. It has also been proposed that the rotor loops be connected in series to improve the spatial distribution of the rotor magneto-motive force (MMF) [65]. This leads to a more complicated nested-loop rotor rather than giving a better design for the conventional nested-loop rotor shown in Fig. 6.1.

FE models have the advantages of taking into account saturation and detailed geometry constructions. They have been applied to study the influence of the number of loops per nest on the

machine performance [104]. However, it is assumed that the rotor slots are distributed evenly along the rotor circumference. In this thesis, the influence of the number of loops per nest on the average torque was studied in Chapter 3. This indicated that the outer most loop makes the biggest contribution to the average torque and that the number of loops per nest has little influence on the average torque. However, the rotor slots are also distributed evenly along the rotor circumference.

The aim of this chapter is to derive some design guidelines for nested-loop rotors by investigating the performance of different nested-loop rotor constructions. 2D transient FE models will be applied to predict the torque load-angle characteristics, the torque ripple, the efficiency and the THD of induced stator voltages. The influence of the number of loops per nest and the position for each individual loop on these output performance will be compared and discussed. Some design guidelines are drawn at the end of this chapter.

6.2 Nested-loop rotor constructions studied

Table 6.1 gives the main specifications of the brushless DFIM studied. Fig. 6.2 shows all of the constructions studied in this paper. The stator construction is fixed for all rotor constructions. Construction *a* is the reference designated one. It has five loops per nest and the rotor slots are distributed evenly along the rotor circumference. All the other constructions are developed from construction *a*. For ease of discussion, the inner most loop of construction *a* is designated loop 1 and the outer most loop is designated loop 5. In construction *b*, the loops from inner to outer are loop 2 to loop 5.

Table 6.1 Main specifications of the brushless DFIM studied

Description	**Machine parameter**	**Value**
Axial length [mm]	L	240.0
Air-gap length [mm]	g	1.0
Stator outer radius [mm]	r_{so}	135.0
Stator inner radius [mm]	r_{si}	85.0
Rotor inner radius [mm]	r_{ri}	35.0
Number of phases	N_{ph}	3
Number of pole-pairs	p_p, p_c	2, 3
Rated frequency [Hz]	f_p, f_c	50, -10
Number of stator slots	N_{ss}	72
Number of rotor nests	p_r	5
Number of loops per nest	q_r	5, 4, 3
Rotor slot pitch in Fig. 6.2(a) [rad]		$\pi/25$

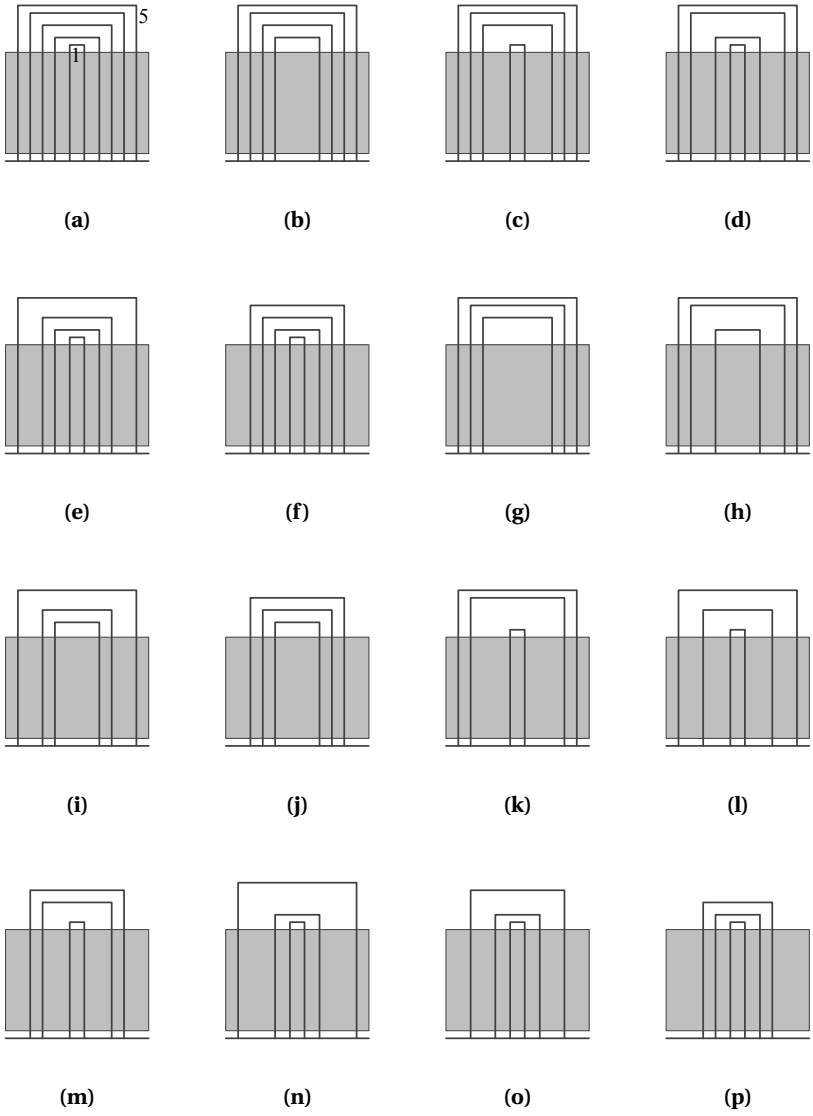

Figure 6.2 Nested-loop rotor constructions

6.3 Simulation results and discussions

The rated operating point will be evaluated in which the mechanical speed is 75.40rad/s according to Table. 6.1. Fig. 6.3 gives a typical 2D-FFT result of the total air-gap magnetic field in a brushless DFIM with rotor *a*. The components whose amplitudes lower than 0.01T are not shown for clarity. There are two main components in the air-gap field. In this case study machine, they are 2^{nd} space-harmonic rotating at 50Hz and 3^{rd} space-harmonic rotating at -10Hz. The minus sign is not given in the 2D-FFT result shown in Fig. 6.3. Many undesired harmonic components also appear in the spectrum due to the special operating mechanism that the induced rotor magnetic field needs to couple both stator magnetic fields. The detailed explanation for these harmonics can refer to the analysis of Fig. 5.6 and 5.7.These undesired harmonics may lead to issues of higher torque ripple, higher THD of induced stator voltages and lower efficiency. This section will present comparative results of different nested-loop rotors on the aspects of torque load-angle characteristics, torque ripple, efficiency and THD of induced stator voltages.

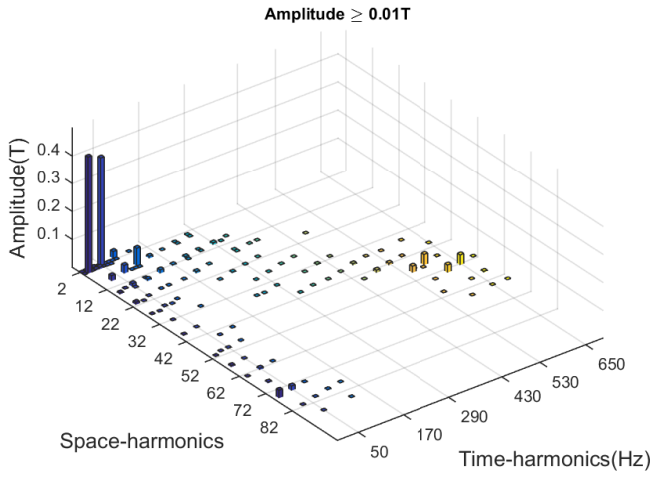

Figure 6.3 Space and time harmonics of the air-gap magnetic field in a brushless DFIM (rotor *a*)

6.3.1 Torque load-angle characteristics

Typical torque load-angle characteristics of the brushless DFIM is shown in Fig. 6.4. The brushless DFIM can operate like a synchronous machine. The load-angle is controlled by changing the phase angle between power winding (PW) and control winding (CW) currents. However, if the applied torque increases too much, the brushless DFIM cannot produce enough electromagnetic torque to operate in the stable range. It will then lose synchronism. Fig. 6.4 indicates the

influences of the outer most loop on the torque load-angle characteristics. To rotor a and p, the outer most loops are loop 5 and loop 3, respectively. To rotor f, j, m, o, the outer most loops are loop 4. The outer most loop determines the average torque level. The brushless DFIM produces a bigger torque if the outer most loop of a nested-loop rotor has a bigger loop span. This is consistent with the conclusion of [66]. The extreme case with the biggest loop span is that the rotor has $(p_p + p_c)$ bars with several loops being located between adjacent bars as shown in Fig. 6.5. This rotor can be expected to produce a bigger average torque.

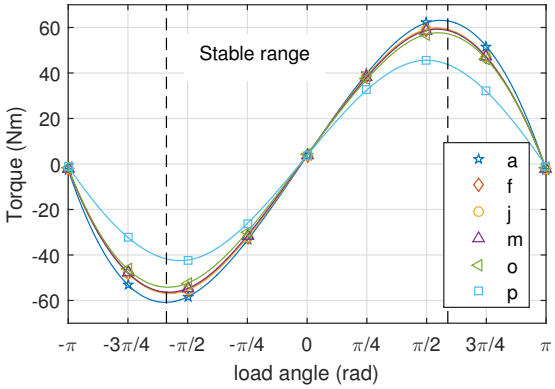

Figure 6.4 Torque load-angle curves - influence of outer most loop

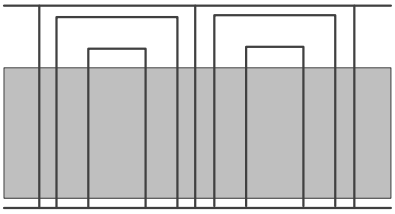

Figure 6.5 Nested-loop rotor construction with common bars

Fig. 6.6 gives the torque load-angle curves of rotors whose outer most loop is loop 5. Overall, they produce torques at the same level except for rotor n. Besides loop 5, rotor n contains loops 1 and 2. It means that the inner loop makes less contribution to the torque. Fig. 6.6(b) gives the enlarged view of the curves. The torques produced in the sequence from big to small are: $b > g > a > c > h > d > i > e > l > k > n$.

Fig. 6.7 indicates the influence of the inner most loop. The difference between a and b, c and g, d

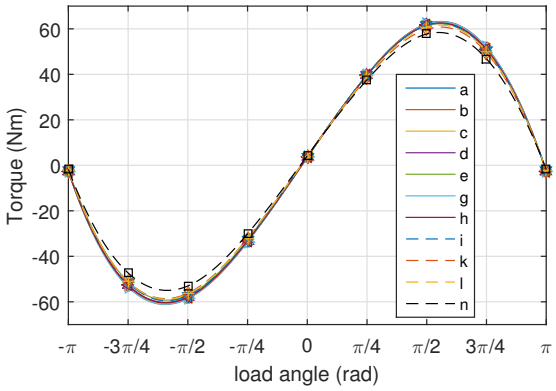

(a) All view

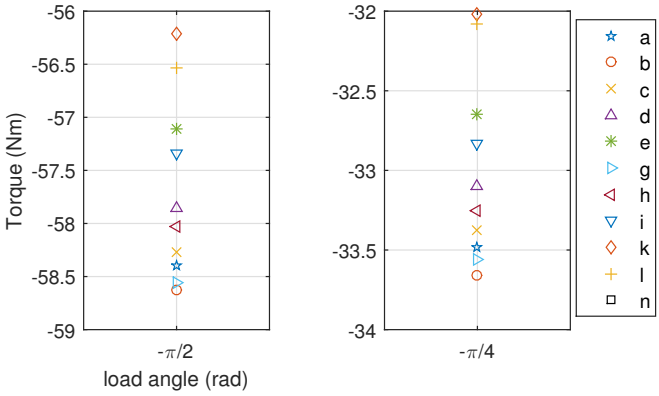

(b) Enlarge view

Figure 6.6 Torque load-angle curves - rotors with loop 5

and h, e and i, f and j is loop 1. Loop 1 makes a negative contribution to the torque. From the average torque point of view, it is better to leave out the inner most loop. It is loop 1 in this case study machine. However, it needs further investigation to determine the exact loop span of the inner loop which could be left out.

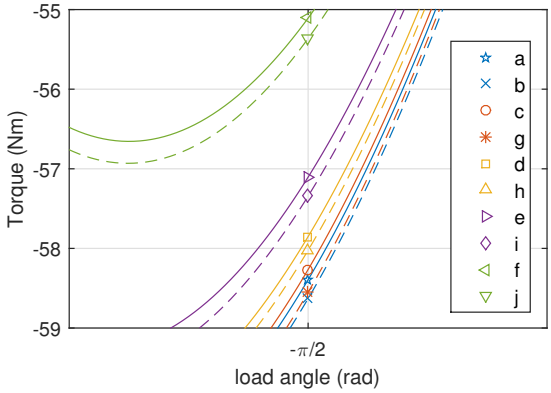

Figure 6.7 Torque load-angle curves - influence of the inner most loop

Fig. 6.8 shows the torque load-angle curves of rotor b, c, d, e, f. It once again indicates that the importance of an individual loop exactly depends on its loop span.

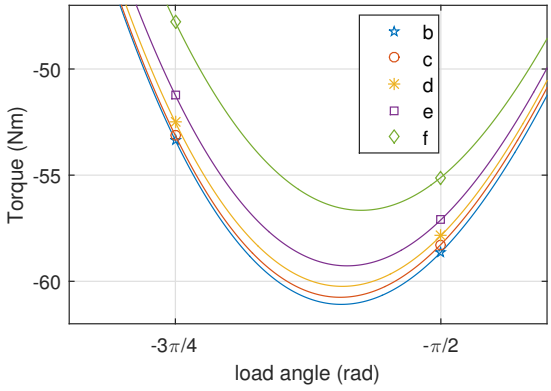

Figure 6.8 Torque load-angle curves - influence of the individual loop

6.3.2 Torque ripple

The torque ripple is defined as:

$$ripple = \frac{max(T) - min(T)}{mean(T)} \times 100\%. \tag{6.1}$$

The average torque at zero load angle is around zero. Therefore, the relative ripple defined by (6.1) is extremely high. It does not make sense to show the torque ripple at zero load angle in the figure. Fig. 6.9 shows the torque ripple corresponding to Fig. 6.4. Unlike the average torque aspect, rotor a does not always have the advantage from the torque ripple point of view. Meanwhile, rotor p is again the worst on the aspect of torque ripple.

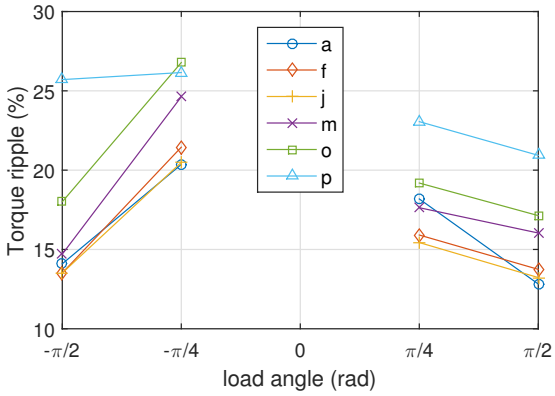

Figure 6.9 Torque ripple - influence of the outer most loop

Fig. 6.10 gives the torque ripple corresponding to Fig. 6.6. Once again, it is not straightforward to see a sequence for the torque ripple produced. Overall, rotor b has the smallest torque ripple. One interesting thing which can be observed is that rotor a leads to a smaller torque ripple while it results in a lower average torque compared with rotor g.

Fig. 6.11 shows the influence of the inner most loop on the torque ripple. In each case, leaving out the inner most loop (loop 1 in this case study) is useful in order to reduce the torque ripple.

Fig. 6.12 gives the torque ripple corresponding to Fig. 6.8. Unlike that in the average torque, it is hard to evaluate the influence of an individual loop on the torque ripple.

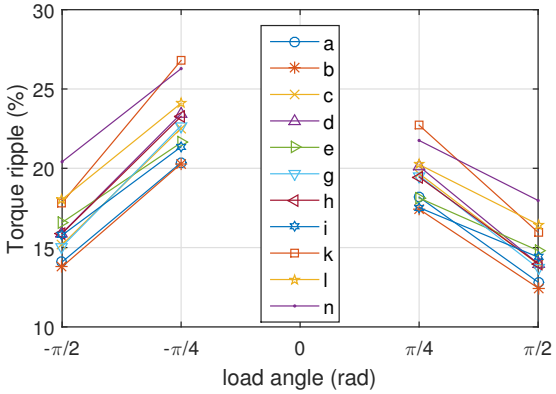

Figure 6.10 Torque ripple - rotors with loop 5

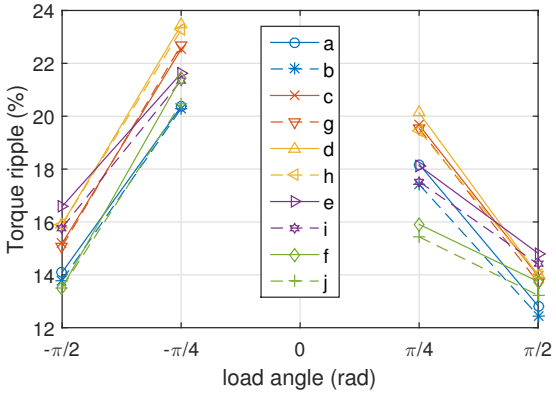

Figure 6.11 Torque ripple - influence of the inner most loop

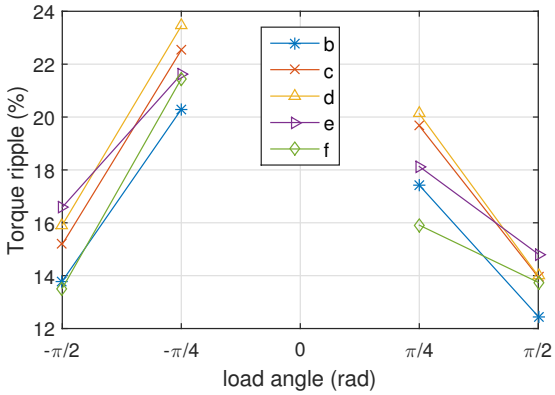

Figure 6.12 Torque ripple - influence of the individual loop

6.3.3 Efficiency

Fig. 6.13 indicates that rotor a whose outer most loop is loop 5 leads to a higher efficiency compared with the rotors whose outer most loop is loops 4 or 3. However, this is not always true. Fig. 6.14 gives the efficiency when the outer most loop is loop 5. Rotor i, e, k, l, n does not show too many advantages compared with the rotors whose outer most loop is loop 4. The efficiency in descending sequence is: $b > a > g > c > h > d > i > e > k > l > n$.

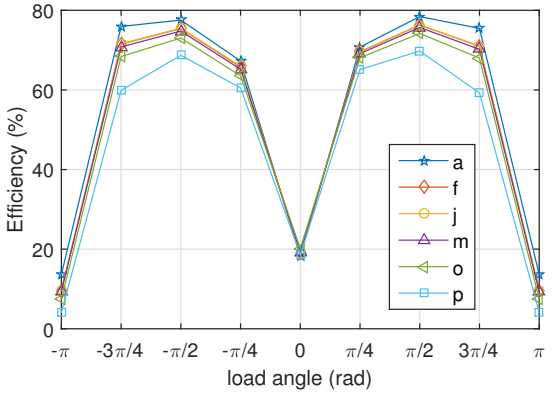

Figure 6.13 Efficiency - influence of the outer most loop

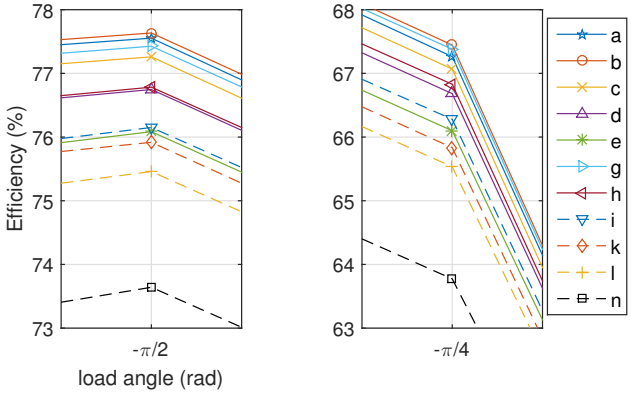

Figure 6.14 Efficiency - rotors with loop 5

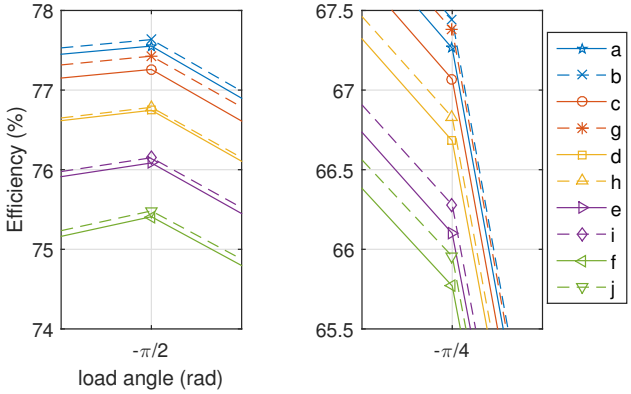

Figure 6.15 Efficiency - influence of the inner most loop

Fig. 6.15 shows the influence of the inner most loop on the efficiency. Leaving out the inner most loop (loop 1 in this case study) slightly improves the machine's efficiency.

Fig. 6.16 gives the efficiency in the case where the rotors have four loops per nest. It shows that putting the loops close to the outer most loop (loop 5 in this study) leads to higher efficiency.

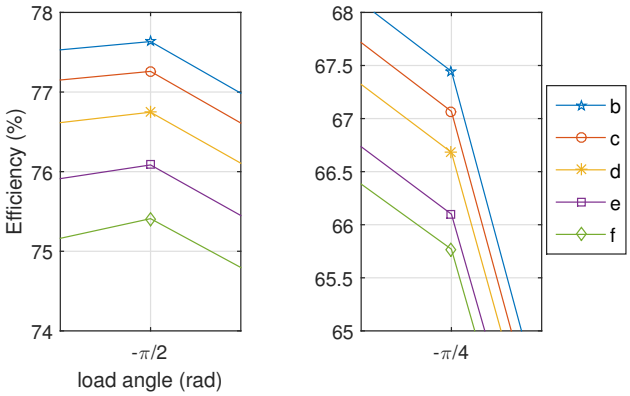

Figure 6.16 Efficiency - influence of an individual loop

6.3.4 THD of induced stator voltages

Fig. 6.17 gives the THD of e_p and e_c. Similar to the torque load-angle curves, it shows that THDs have three levels with respect to different outer most loops. Rotor a with loop 5 leads to a lower THD than rotor p in which the outer most loop is loop 3. Rotors f, j, m and o, whose outer most loops are all loop 4, result in the THD at a similar level. It can be concluded that the loop span of the outer most loop determines the overall THD level.

Fig. 6.18 shows the THD due to the rotors whose outer most loop is loop 5.This results in a similar THD level. Overall, rotors a, b lead to a relative lower THD level while rotors k, n lead to a higher THD level. Rotor g has the advantage of producing higher torques, however, it does not show the benefit on the THD. It can be concluded that more outer loops would result in a lower THD.

Fig. 6.19 shows the effects of loop 1. It is not straightforward to see whether it is of benefit to leave out loop 1 for a lower THD. Fig. 6.20 gives the influence of an individual loop on the THD. Rotors f and e lead to a higher THD of e_p and e_c, respectively. Rotor d leads to a lower THD of e_p while rotor c leads to a lower THD of e_c.

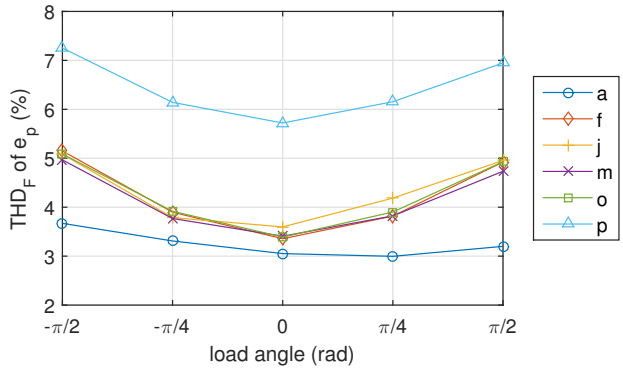

(a) THD_F of e_p

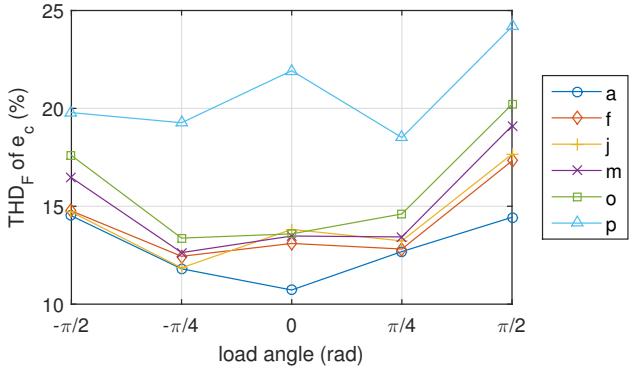

(b) THD_F of e_c

Figure 6.17 Total harmonic distortion - influence of outer most loop

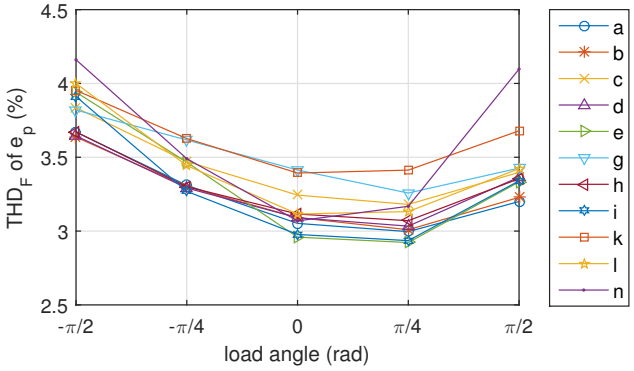

(a) THD_F of e_p

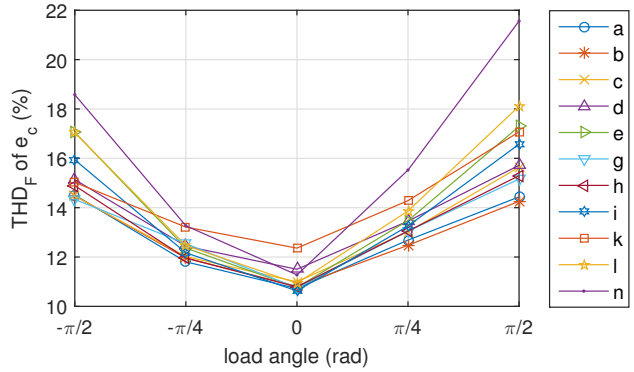

(b) THD_F of e_c

Figure 6.18 Total harmonic distortion - rotors with loop 5

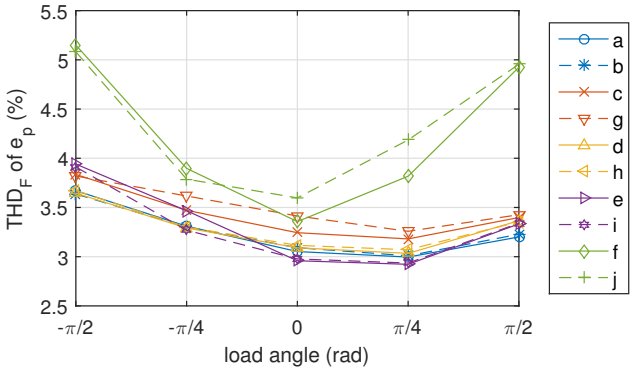

(a) THD_F of e_p

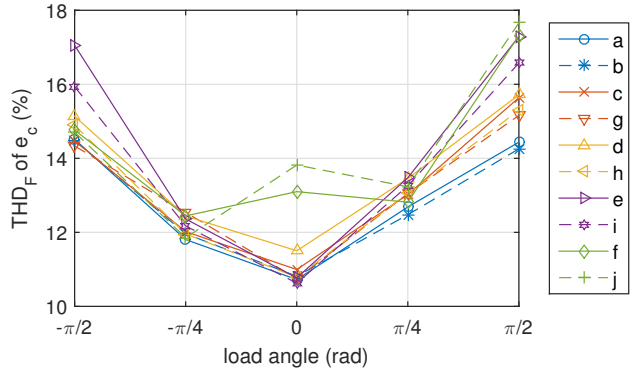

(b) THD_F of e_c

Figure 6.19 Total harmonic distortion - influence of inner most loop

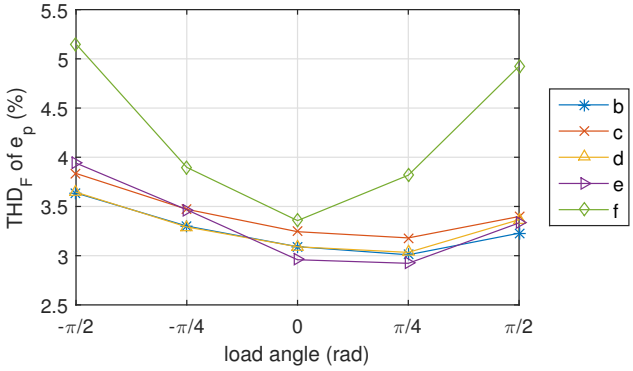

(a) THD_F of e_p

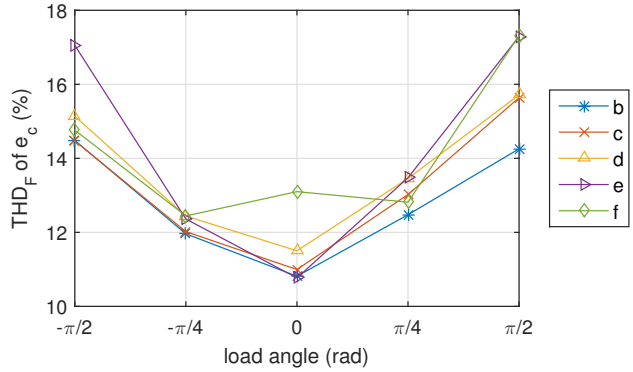

(b) THD_F of e_c

Figure 6.20 Total harmonic distortion - influence of individual loop

6.4 Conclusion

This chapter presents a comparison of nested-loop rotors. 2D transient FE models are applied to predict the torque load-angle characteristics, the torque ripple, the efficiency and the THD of induced stator voltages at different load-angles. Some design guidelines can be concluded as:

1. The number of loops per nest and their position have a systematic influence on the average torque and the machine efficiency, but not such a systematic effect on the torque ripple and the THD of induced stator voltages.
2. For the average torque, the contribution made by an individual loop strongly depends on its loop span. The loop span of the outer most loop should be as big as possible in order to achieve a bigger average torque. The biggest three torques are produced by rotors b, g and a.
3. There are no explicit rules for relating the number of loops per nest and their position to the torque ripple. Rotors b, g and a produce the biggest average torque and rotors b and a show a relatively lower torque ripple compared with the other rotors. However, rotor g is not so attractive from the torque ripple point of view like that from the average torque point of view.
4. Similar to the average torque, making the loop with a bigger span can lead to higher efficiency. In this case study, rotor b, a and g give the highest three efficiencies.
5. The THD level of stator voltages is reduced by making the loop span of the outer most loop as big as possible. It is not straightforward to derive an explicit rule for lowering the overall THD since the results do not show a clear influence of an individual loop located in the middle on the THD. However, one possible way to reduce the THD might be to increase the number of outer loops. In this case study, rotor a and b lead to a relatively low THD of stator voltages.
6. The results indicate that leaving out the inner most loop (loop 1 in this case study) can slightly increase the average torque and efficiency and slightly reduce the torque ripple. However, it does not show clear benefits on the THD of the stator voltages. Furthermore, further investigation is needed on how big the loop span of the inner most loop should be.
7. Considering all of those four output characteristics, rotor b might be the best one in this case study. A better one might exist, which is not listed in Fig. 6.2, by designing the middle loops better. However, how to better design the middle loops is open for further investigation.

CHAPTER 7

Experimental Study of a Brushless DFIM Prototype

The aim of this chapter is to validate the space- and time-harmonics, the influence of the rotor skew and the influence of the nested-loop configurations which have been presented in the previous chapters. A DC motor drives the brushless doubly-fed induction machine (DFIM) to operate in simple induction mode. One of the stator windings is supplied while the other is open-circuited. The induced voltages of the open-circuited winding can be measured at a fixed and variable speed. The space- and time-harmonics are validated by the frequency spectrogram of the induced voltages. The influence of the rotor skew is studied by comparing the measurements on rotors with and without skewed slots. The influence of the nested-loop constructions is studied by comparing the measurements on rotors with a large and small loop span. The insulation between the rotor bars and the iron core is damaged. This makes the validation less successful than expected. The results indicate that the orders of the space- and time-harmonics predicted analytically agree with the measurements and the FE results. However, the amplitudes of the harmonics calculated by the FE models are not close to the measurements since the inter-bar currents are not expected at the outset. The FE models are partially validated. The measurements also prove that skewing rotor slots reduces the total harmonic distortion (THD) of the stator voltages. Moreover, the measurements prove that the rotor with large loop span leads to a better cross-coupling between two stator windings.

Most parts of this chapter have been published in

- X. Wang, T. D. Strous, D. Lahaye, H. Polinder, and J. A. Ferreira, "Harmonics Study of Nested-Loop Rotors in Brushless Doubly-Fed Induction Machines," in *22th Int. Conf. Elec. Machines (ICEM)*, Lausanne, Switzerland, Sept. 2016.

7.1 Introduction

Unlike normal induction machines, the brushless doubly-fed induction machines (DFIMs) have two stator magnetic fields. These are produced by the power winding (PW) and control winding (CW). They have different pole-pair numbers and are fed with different frequencies. There is no direct magnetic coupling between the PW and the CW. A special nested-loop rotor is designed to couple with both stator windings.This cross-coupling leads to a very complicated distribution of the air-gap magnetic field in this special machine. This complicated magnetic field has two main components, as well as many undesirable space-harmonics.

Previously, the 2D finite element (FE) model has been used to model this complicated magnetic field and predict the performance of the brushless DFIM. The undesirable space-harmonics lead to more severe noise, vibrations and lower power quality compared with normal induction machines. Skewing rotor slots is proposed to reduce the negative consequences caused by the undesirable space-harmonics. Moreover, some design guidelines for the nested-loop rotor have been derived from the FE results. All previous chapters are based on these simulations. The aim of this chapter is to present the experimental study on a small-scale brushless DFIM prototype.

A better understanding of the space- and time-harmonics of the complicated magnetic field is critical and helpful for the understanding of the operating principle of the brushless DFIMs. Moreover, the analysis of the space- and time-harmonics is the foundation for the efficient method developed in Chapter 5. The appropriate skew factors are derived, based on the analytical derivation of the space- and time-harmonics. The analytical derivation is only applied to work out the order of the space- and time-harmonics while the related amplitude is not calculated analytically. The order of the space- and time-harmonics has been validated by the FE simulations in Chapter 5. Then it is worth studying and validating the space- and time-harmonics by carrying out measurements on the prototype. The effects of skew have been investigated by using the 2D multi-slice FE model and a fast semi-numerical method. In this chapter, the effects of skew are studied by carrying out measurements on rotors with/without skewing. Sixteen different configurations of nested-loop rotors have been simulated and investigated to derive the design guidelines for nested-loop rotors. The influence of nested-loop configurations is studied by carrying out measurements on nested-loop rotors with a large and small loop span. The detailed measurements will be explained in section 7.3. Unfortunately, the nested-loop rotors were not manufactured as required. The insulation between the rotor bars and the iron core was completely damaged during the manufacturing processing. The influence of the damaged insulation will be explained in section 7.2.2.

The following aspects are covered in this chapter.

1. The space- and time-harmonics:
   The order of the space- and time-harmonics is derived analytically. Saturation is not taken into account in the analytical derivation. Therefore, the space- and time-harmonics due to saturation are not discussed in detail. The voltage supplied in measurements is not high in order to avoid the machine being too saturated. The order of the space- and time-harmonics

derived will be validated by FE simulations and the measurements. The amplitude of the space- and time-harmonics will be calculated by the 2D FE model and compared to the measurements. It is not straightforward to measure the rotor currents, therefore, the order of the time-harmonics in the rotor currents predicted by the analytical derivation are only validated by the 2D FE results.

2. The influence of rotor skew:
   Measurements will be carried out on nested-loop rotors with/without skewing in simple induction mode. The amplitude of the induced voltage of the open-circuited stator winding, as well as the total harmonic distortion (THD) of the stator voltages, will be compared to show the influence of the rotor skew. However, the conclusion that skewing rotor slots over one stator slot pitch is a good choice cannot be validated since the rotors were only skewed over one stator slot pitch.

3. The influence of nested-loop configurations:
   Measurements will be carried out on nested-loop rotors with big and small loop spans in simple induction mode. The amplitude of the induced voltage of the open-circuited stator winding, as well as the total harmonic distortion (THD) of the stator voltages, will be compared to show the influence of nested-loop configurations.

This chapter starts with an introduction of the prototype. The damage of the insulation in the rotors is discussed. The set-up and the detailed steps of the measurements are then illustrated. Next, the order of the space- and time-harmonics is briefly explained. Subsequently, the measurements and the FE results are presented together with some discussions. Finally, conclusions are drawn.

7.2 Description of the prototype

7.2.1 Main specifications

The brushless DFIM used in the experimental set-up is a small-scale prototype fitted in a D180 frame-size housing and designed based on an early prototype developed by the University of Cambridge [41]. Its main specifications are provided in Table 7.1.

Fig. 7.1 shows the stator of the prototype. Fig. 7.2 gives the four rotors of the prototype. Each rotor has four loops per nest. Rotors 1 and 3 correspond to rotors f and b in Chapter 6, respectively. The loop span of each individual loop in rotor 3 is larger than that in rotor 1. The individual loop in rotor 2 and rotor 4 have the same loop span as rotors 1 and 3, respectively. The only difference between rotors 1 and 2 (rotors 3 and 4) is the rotor slots of rotor 2 (rotor 4) are skewed over one stator slot pitch. Fig. 7.3 gives the 2D schematic diagrams of four rotors.

Table 7.1 Main specifications of the brushless DFIM prototype

Description	Machine parameter	Value
Axial length [mm]	L	240.0
Air-gap length [mm]	g	1.0
Stator outer radius [mm]	r_{so}	135.0
Stator inner radius [mm]	r_{si}	85.0
Rotor inner radius [mm]	r_{ri}	35.0
Number of phases	N_{ph}	3
Number of pole-pairs	p_p, p_c	2, 3
Rated frequency [Hz]	f_p, f_c	50, 10
Number of stator slots	N_{ss}	72
Number of rotor nests	p_r	5
Number of loops per nest	q_r	4

Figure 7.1 The stator of the brushless DFIM prototype

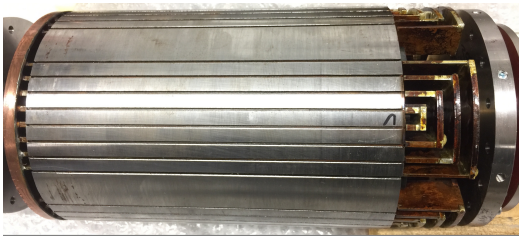

(a) Rotor 1 (small loop span, non-skewed)

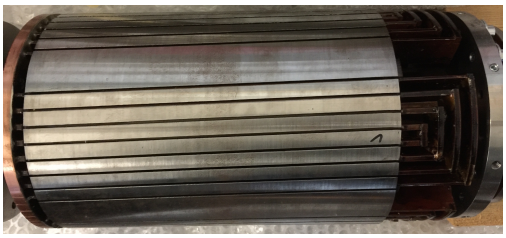

(b) Rotor 2 (small loop span, skewed)

(c) Rotor 3 (big loop span, non-skewed)

(d) Rotor 4 (big loop span, skewed)

Figure 7.2 The nested-loop rotors of the brushless DFIM prototype

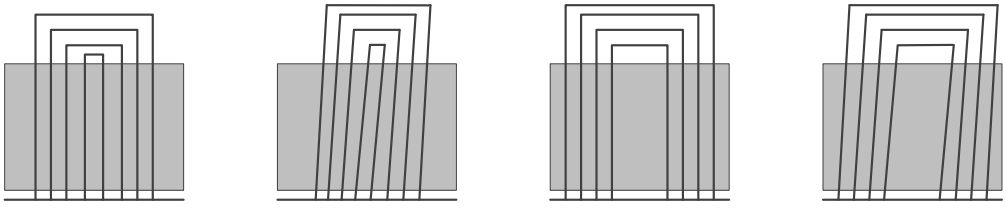

(a) Rotor 1 **(b)** Rotor 2 **(c)** Rotor 3 **(d)** Rotor 4

Figure 7.3 Nested-loop rotor constructions studied

7.2.2 Inter-bar currents in the prototype

As mentioned in Chapter 2, special steps should be taken to achieve bar-to-bar insulation because the performance of the brushless DFIMs is significantly degraded due to inter-bar currents [38]. Initially, the rotor bars of the prototype were planned to be insulated with Kapton tape. However, the tape was completely damaged during the manufacture processing.

The insulation between the rotor bars and the core is not so critical in normal squirrel-cage induction machines. The rotor bars of a squirrel-cage rotor are short-circuited at the end on both sides. The electric potential of each bar is approximately equal. Therefore, there are almost no currents flowing through the rotor core.

However, the insulation between the rotor bars and the core can be critical in brushless DFIMs with nested-loop rotors. Fig. 7.4 gives a circuit example of a nested-loop rotor without the insulation between the bars and the core. The bar impedances are shown in white and the inter-bar impedances are shown in black. To the inner most loop (loop 1 in this example), two adjacent rotor bars are short-circuited at the end on both sides. Similar to the squirrel-cage rotor, there are almost no inter-bar currents through the core. For the other rotor bars, the outer most loops for instance, the electric potential of loop 3 in Nests 1 and 2 can be quite different. Then there exist large inter-bar currents flowing through the iron core. Therefore, the nested-loop rotor without insulation will lead to a higher input stator current than the rotor with insulation if the same stator voltages are applied. This increase has been observed by carrying out measurements on nested-loop rotors with and without insulation [38]. The nested-loop rotor forces the currents to flow in certain loops. However, the damaged insulation makes the nested-loop rotor act similarly to a squirrel-cage rotor. Therefore, this damaged insulation has an influence not only on the amplitude of the induced rotor magnetic field, but also on the distribution of the rotor magnetic field.

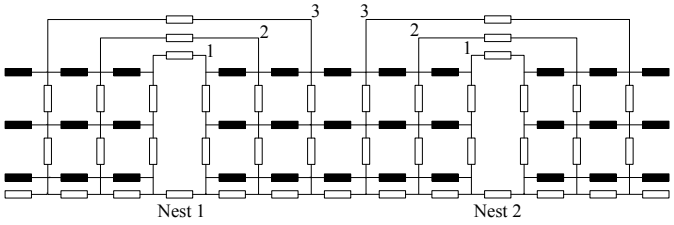

Figure 7.4 Rotor circuit configuration of a nested-loop rotor without insulation (The bar impedances are shown in white and the inter-bar impedances are shown in black.)

For a first impression on the influence of the inter-bar currents, a simple test can be performed. The PW is supplied with several different voltages by using a voltage source. Then the PW currents are measured when the rotor is blocked. Fig. 7.5 gives the RMS values of the input three-phase PW currents with different nested-loop rotors. Firstly, it can be observed that rotor 2 leads to the highest PW currents. Rotor 3 results in slightly lower currents than rotor 2. Rotor 1 and rotor

4 lead to approximately the same PW currents which are the lowest among the four rotors. As mentioned before, the stator input currents increase due to the presence of the inter-bar currents. Therefore, it can be expected that the influence of the inter-bar currents is highest in rotors 2 and 3. Secondly, the three-phase PW currents are not balanced, mostly in rotors 2 and 3. This unbalance could be due to manufacturing error. However, the influence of the manufacturing error should not be that big since the three-phase currents of rotors 1 and 4 were almost balanced. Again, the unbalanced three-phase PW currents indicate that rotors 2 and 3 have more severe inter-bar currents. The same conclusion can be derived by supplying the CW shown in Fig. 7.6.

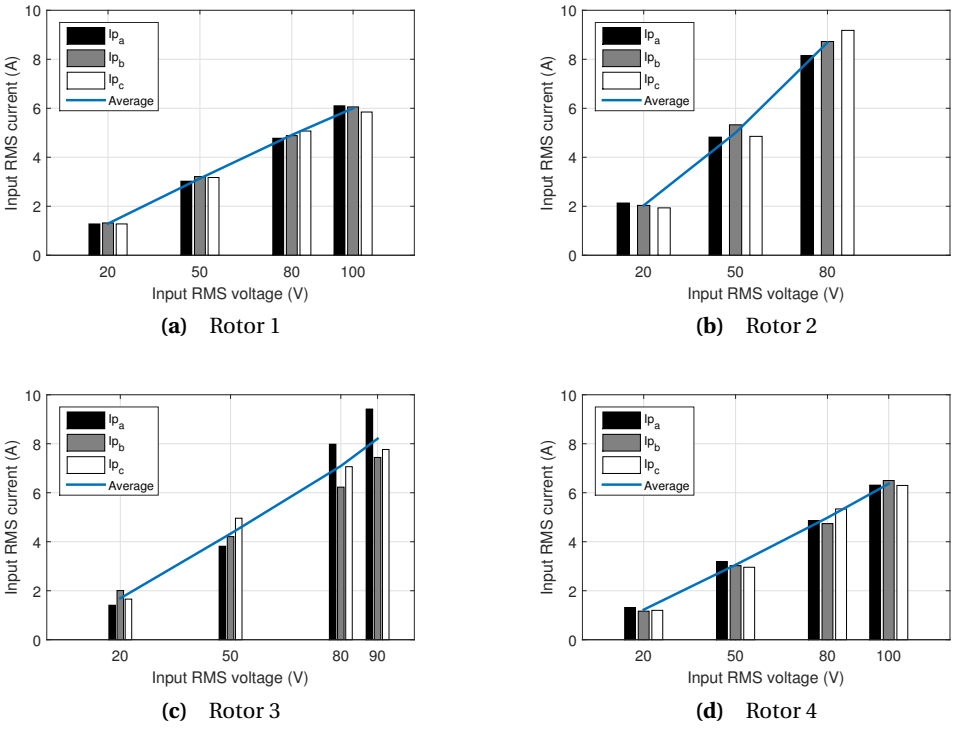

(a) Rotor 1 **(b)** Rotor 2

(c) Rotor 3 **(d)** Rotor 4

Figure 7.5 RMS value of three-phase input PW currents at 0rpm

The damaged insulation makes the nested-loop close to a squirrel-cage rotor. However, it is not possible to manufacture new nested-loop rotors with insulation due to the limited time for this thesis. It can be expected that most rotor currents should still flow in the rotor bars since the resistivity of the copper is over ten times smaller than that of the iron. These four rotors partially have the characteristics of a perfect nested-loop rotor. Therefore, it makes sense to carry out measurements on these four rotors for some validation in this thesis. However, the results measured may not agree with the expectation derived from previous chapters.

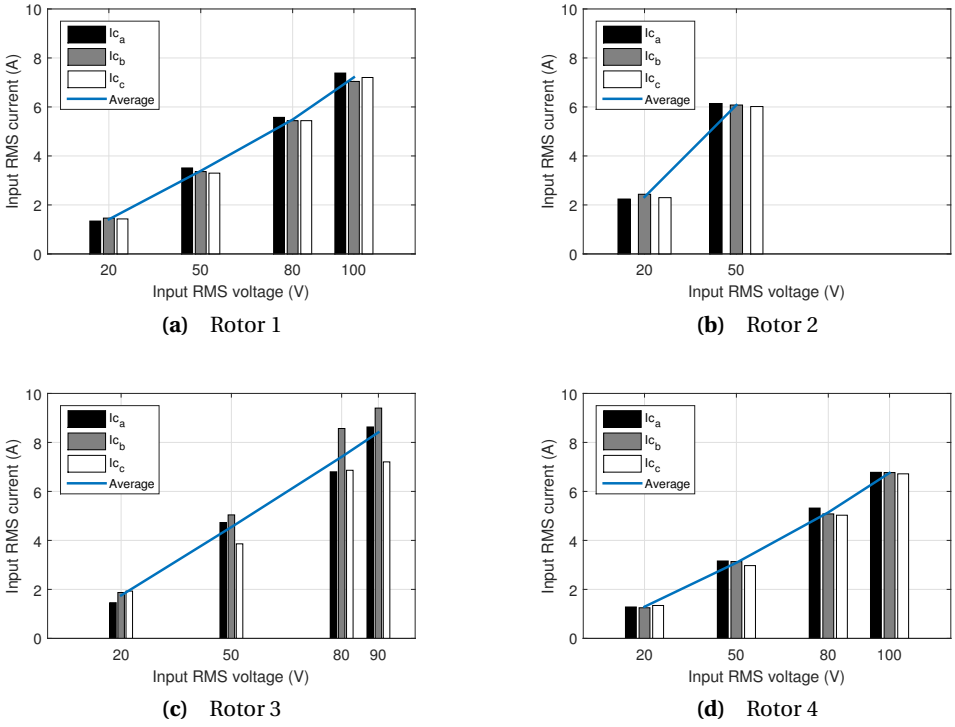

(a) Rotor 1

(b) Rotor 2

(c) Rotor 3

(d) Rotor 4

Figure 7.6 RMS value of three-phase input CW currents at 0rpm

7.3 Description of experiments

As mentioned in Chapter 2, the brushless DFIM can operate in synchronous mode. The synchronous mode is the desirable operating mode for wind turbine applications. The PW is directly connected to the grid. The frequency of the CW can be controlled according to the wind speed, while the torque produced can be controlled by a load-angle. This means that a controller is necessary to achieve the synchronous operating mode. However, it would be better if the experimental validation could be carried out using simpler tests. The brushless DFIM can also operate in simple and cascade induction modes, although these two modes do not appear in wind turbine applications. Actually, these two modes are often applied to study and evaluate the performance of brushless DFIMs [40, 41], because they are simple to carry out and no controller is needed.

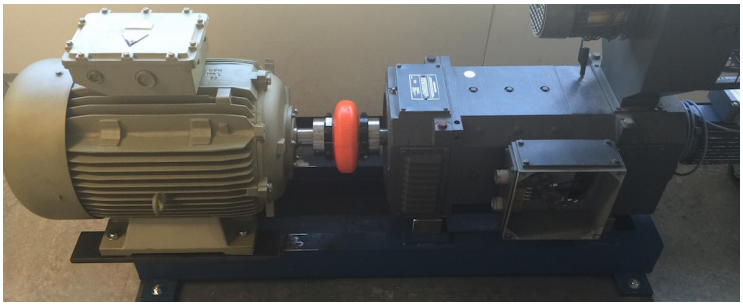

Figure 7.7 Experimental platform

The simple induction mode will be adopted in this chapter. One of the stator windings will be supplied while the other will be open-circuited. Fig. 7.7 shows the platform for the tests. A DC motor (on the right side) is used to drive the brushless DFIM prototype (on the left side) to any desirable rotating speed. Detailed descriptions of the measurements are as follows.

1. Space- and time-harmonics:
   The first test is the speed-up test in simple induction mode. The PW is supplied with a three-phase voltage of 80V (RMS value of phase voltage), 50Hz. The supplied voltage is not high due to the limitation of the power source. On the other hand, it prevents the prototype operating in the high saturation region. It is because the harmonics due to saturation are not taken into account in the analytical predictions. The DC motor drives the brushless DFIM from 0rpm to over 1000rpm. In this speed-up test, the induced CW voltage waveforms are measured and recorded. This test is carried on all rotors. The frequencies of the induced CW voltages can be analyzed using a short-time Fourier transform. Then the spectrum of the induced CW voltage gives a validation of the space- and time-harmonics, which will be presented in subsection7.5.1. These measurements and the spectrum analysis are then carried out on when the CW is supplied with the same three-phase voltage source. The results will be presented in subsection 7.5.2.
   For detailed comparison, the brushless DFIM prototype is driven to a fixed speed (e.g.

480rpm in our tests). The PW is supplied with a three-phase voltage of 80V (RMS value of phase voltage), 50Hz. The PW current waveforms and the induced CW voltage waveforms are measured and recorded. In the 2D FE model, the PW is supplied with a three-phase current which is obtained from the measurement results while the rotor speed is set the same as in the test. The induced CW voltage is calculated based on the transient simulation and compared with the measurements in subsection 7.5.3. This simulation and comparison are relatively straightforward. It is not necessary to repeat them when the CW is supplied and the PW is open-circuited since it does not provide more information.

2. The influence of rotor skew:
   The results measured on rotors 1 and 3 in the first test can be compared to the results on rotors 2 and 4, respectively, to show the influence of rotor skew. The results will be presented in subsection 7.5.5.
3. The influence of nested-loop configurations:
   The results measured on rotors 1 and 3 in the first test can be compared to indicate the influence of nested-loop configurations. The results will be presented in subsection 7.5.6.

All the analytical predictions and 2D FE models have been well explained in the previous chapters. It is not necessary to introduce them again in this chapter. However, the space- and time-harmonics in the brushless DFIM are complicated and critical to machine operation. To facilitate reading, it is helpful to explain them briefly in this chapter. The detailed derivation of the space- and time-harmonics can be found in Chapter 5 in which they are explained in a way to incorporate skew factors.

7.4 Harmonic analysis in a brushless DFIM

This section firstly explains the space-harmonics of the stator magnetic field due to the winding distribution and slotting effect. Then the space-harmonics of the induced rotor magnetic field are derived analytically. Subsequently, the time-harmonic frequencies of rotor currents, induced by the stator fields, are given. Finally, the time-harmonic frequencies of the voltages (and currents) of the PW and the CW due to the space-harmonics of the rotor magnetic field are derived. The assumptions are the same as those in Chapter 5.

7.4.1 Space-harmonics

The stator winding magnetic field in the air-gap can be expressed as:

$$B_s(\theta_s, t) = \sum_{k_s}^{\infty} \hat{B}_s^{(k_s)} \cos(k_s\theta_s - \omega t), \tag{7.1}$$

$$\hat{B}_s^{(k_s)} = \frac{\mu_0}{k_C g} \frac{3\sqrt{2}}{\pi} \frac{N_s k_{w(k_s)}}{k_s} I_s, \tag{7.2}$$

where μ_0 is the permeability of the vacuum, g is the air-gap length, k_C is the Carter's factor, N_s is the number of turns in series per phase, $k_{w(k_s)}$ is the winding factor for the k_s^{th} harmonic, I_s is the RMS value of the input current, $\omega = 2\pi f$ is the stator current angular frequency, f is the input frequency of the sinusoidal current and θ_s is the angle along the stator circumference.

The stator winding space-harmonic component k_s is an element of (7.3) when considering the PW magnetic field and an element of (7.4) when considering the CW magnetic field.

$$k_s \in k_p = p_p(1-6m), \forall m \in \mathbb{Z}, \tag{7.3}$$

$$k_s \in k_c = p_c(6m-1), \forall m \in \mathbb{Z}. \tag{7.4}$$

The slotting space-harmonics k_s due to the stator slots and the rotor slots is an element of (7.5) and (7.6), respectively.

$$k_s \in (k_p \cup k_c) \pm mN_{ss}, \forall m \in \mathbb{Z}_0^+, \tag{7.5}$$

$$k_s \in (k_p \cup k_c) \pm mN_{rs}, \forall m \in \mathbb{Z}_0^+, \tag{7.6}$$

in which N_{ss} and N_{rs} are the number of stator slots and rotor slots, respectively. The positive space-harmonic orders indicate that the magnetic field is moving in a positive direction while the negative ones indicate the magnetic field is moving in a negative direction.

Considering the mechanical rotational speed Ω_m, the relationship between the stator reference frame (θ_s) and the rotor reference frame (θ_r) is:

$$\theta_s = \theta_r + \Omega_m t. \tag{7.7}$$

To calculate the flux linkage and the induced EMF of the rotor, the air-gap flux densities produced by the PW or the CW are firstly expressed in the rotor reference frame as:

$$B_s(\theta_r, t) = \sum_{k_s}^{\infty} \hat{B}_s^{(k_s)} \cos[k_s\theta_r + (-\omega + k_s\Omega_m)t]. \tag{7.8}$$

The flux linkage in the n$^{\text{th}}$ loop of the x$^{\text{th}}$ nest (shown in Fig. 7.8) is calculated as (7.9):

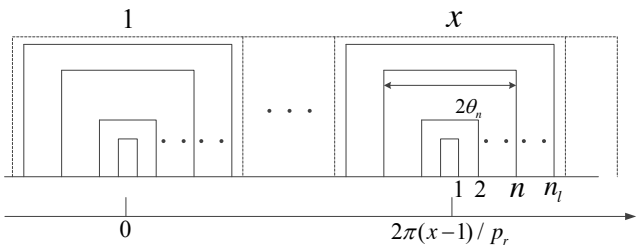

Figure 7.8 The configuration of the nested-loop rotor structure

$$\begin{aligned}\phi(t,n,x) &= Lr\int_{-\theta_n+(x-1)\frac{2\pi}{p_r}}^{\theta_n+(x-1)\frac{2\pi}{p_r}} B_s(\theta_r,t)\,d\theta_r \\ &= \sum_{k_s}^{\infty}\frac{2Lr}{k_s}\hat{B}_s^{(k_s)}\sin(k_s\theta_n)\cos\left[k_s\frac{2\pi(x-1)}{p_r}+(-\omega+k_s\Omega_m)t\right],\end{aligned} \tag{7.9}$$

in which L is the axial length of the machine and r is the radius of the air-gap. The induced rotor current is shown as (7.10) by assuming the impedance of an individual loop is Z_r.

$$i_r(t,x,n) = -\frac{1}{Z_r}\frac{d\phi}{dt} = \sum_{k_s}^{\infty}\frac{2Lr}{Z_r k_s}\hat{B}_s^{(k_s)}\sin(k_s\theta_n)(-\omega+k_s\Omega_m)\cdot\sin\left[k_s\frac{2\pi(x-1)}{p_r}+(-\omega+k_s\Omega_m)t\right]. \tag{7.10}$$

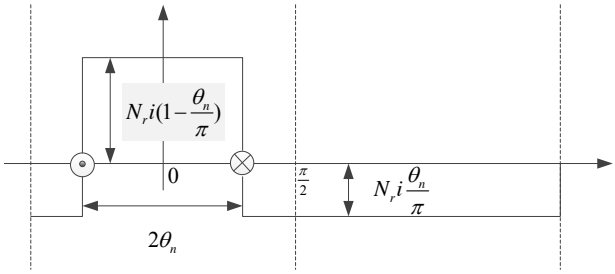

Figure 7.9 The MMF waveform due to the current in one short-circuit loop

Fig. 7.9 shows the MMF waveform produced by the rotor current in one short-circuit loop. Because the nested-loops are constructed with solid bars to maximize slot fill factor, the number of turns of a single loop N_r is equal to one. The induced rotor MMF can be expressed by the Fourier series as:

$$\mathscr{F}_r(\theta_r,t,x,n) = \sum_{k_r}^{\infty}\hat{\mathscr{F}}_r^{(k_r)}\cos\left[k_r(\theta_r-(x-1)\frac{2\pi}{p_r})\right], \tag{7.11}$$

in which k_r indicates the space-harmonic order, p_r is the number of nests which equals to (p_p+p_c) and $\hat{\mathscr{F}}_r$ is given by (7.12):

$$\begin{aligned}\hat{\mathscr{F}}_r^{(k_r)} &= \frac{2}{\pi}\left\{\int_{(x-1)\frac{2\pi}{p_r}}^{\theta_n+(x-1)\frac{2\pi}{p_r}}(1-\frac{\theta_n}{\pi})N_r i_r\cos\left[k_r(\theta_r-(x-1)\frac{2\pi}{p_r})\right]d\theta_r\right. \\ &\quad\left.+\int_{\theta_n+(x-1)\frac{2\pi}{p_r}}^{\pi+(x-1)\frac{2\pi}{p_r}}(-\frac{\theta_n}{\pi})N_r i_r\cos\left[k_r(\theta_r-(x-1)\frac{2\pi}{p_r})\right]d\theta_r\right\} \\ &= \sum_{k_s}^{\infty}\frac{4N_r Lr}{Z_r k_s k_r\pi}\hat{B}_s^{(k_s)}\sin(k_s\theta_n)(-\omega+k_s\Omega_m)\cdot\sin(k_r\theta_n)\sin\left[k_s\frac{2\pi(x-1)}{p_r}+(-\omega+k_s\Omega_m)t\right].\end{aligned} \tag{7.12}$$

The induced rotor magnetic field in the air-gap due to the PW (or the CW) can be formulated as (7.13).

$$\begin{aligned} B_r(\theta_r,t) = & \sum_{n=1}^{n_l}\sum_{x=1}^{p_r}\sum_{k_r}^{\infty}\sum_{k_s}^{\infty}\frac{2N_rLr\mu_0}{Z_rk_sk_r\pi k_Cg}\hat{B}_s^{(k_s)}\cdot\sin(k_s\theta_n)(-\omega+k_s\Omega_m)\sin(k_r\theta_n) \\ & \cdot\left\{\sin\left[(-\omega+k_s\Omega_m)t+k_r\theta_r+(k_s-k_r)(x-1)\frac{2\pi}{p_r}\right]\right. \\ & \left.+\sin\left[(-\omega+k_s\Omega_m)t-k_r\theta_r+(k_s+k_r)(x-1)\frac{2\pi}{p_r}\right]\right\}. \end{aligned} \tag{7.13}$$

The induced B_r will not equal to zero when k_r is equal to an element of (7.14).

$$k_r \in k_s \pm mp_r, \forall m \in \mathbb{Z}. \tag{7.14}$$

Similar to the stator side, the slotting space-harmonics k_r due to the stator slots and the rotor slots are an element of (7.15) and (7.16), respectively.

$$k_r \in k_r \pm mN_{ss}, \forall m \in \mathbb{Z}_0^+, \tag{7.15}$$

$$k_r \in k_r \pm mN_{rs}, \forall m \in \mathbb{Z}_0^+. \tag{7.16}$$

According to (7.2) and (7.13), we may define the number of effective turns for the stator winding and the rotor loop n as (7.17) and (7.18) [42]:

$$N_{se(k_s)} = \frac{4}{\pi}N_sk_{w(k_s)}, \tag{7.17}$$

$$N_{re,n(k_r)} = \frac{4}{\pi}N_r\sin(k_r\theta_n). \tag{7.18}$$

Fig. 7.10 displays the values of N_{se} and $N_{re,n}$ to provide a first expression of the winding distribution space-harmonics in the machine studied. The values of the PW and the CW are normalized to single turn per slot values obtained after dividing by $N_s/(pq)$. p is the number of pole-pair and q is the number of slots per pole per phase. Fig. 7.10 indicates that the dominant magnetic coupling happens between the main space-harmonic components ($k_s = p_p$ and $k_s = p_c$). Meanwhile, there is a coupling between some other stator and rotor space-harmonic components (e.g. 22^{nd}, 33^{rd}, 57^{th}, 58^{th}, 142^{nd} and 147^{th} etc. in Fig. 7.10). It can be expected that 142^{rd} and 147^{th} may play a bigger role when compared with the other harmonics. This is because these components are not only due to the rotor winding distribution, but also the slotting effect. In fact, the pole-pair combination of this prototype is relatively good since there are not too many high space-harmonics coupled between stator fields and rotor field.

Fig. 7.11 shows the N_{se} and $N_{re,n}$ of an early prototype with $p_p = 4$, $p_c = 2$, $N_{ss} = N_{rs} = 36$, which was developed by Cambridge University [41]. Compared with the Delft prototype, there are more rotor space-harmonics coupling with the stator windings which is undesirable. The detailed harmonic study of the Cambridge prototype can be found in [74].

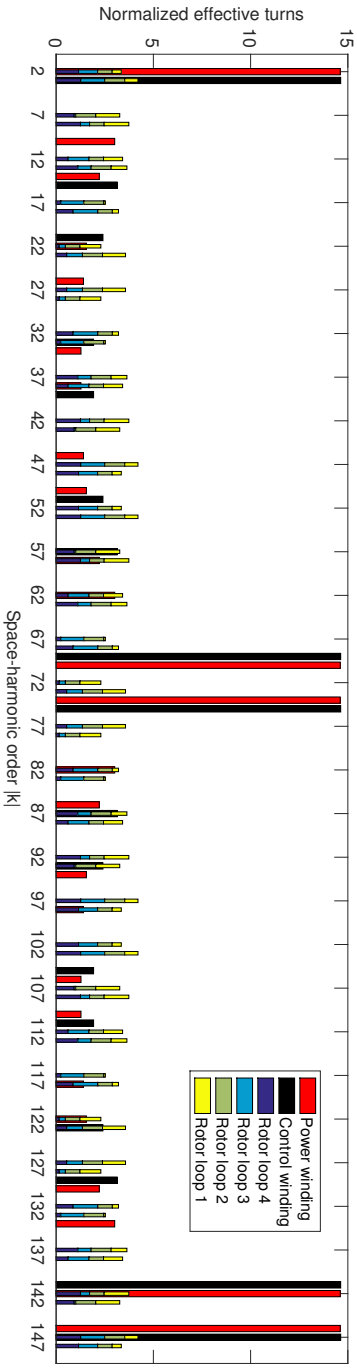

Figure 7.10 Normalized winding effective turns of Delft prototype

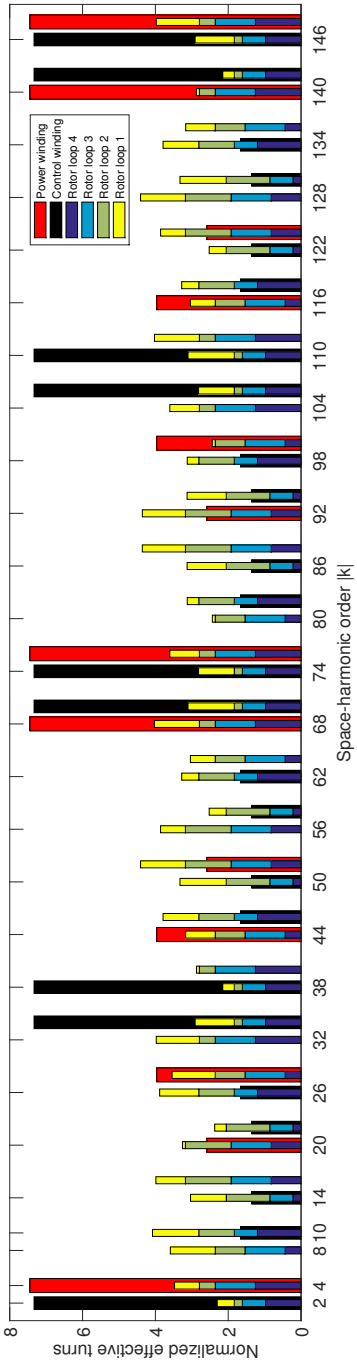

Figure 7.11 Normalized winding effective turns of Cambridge prototype

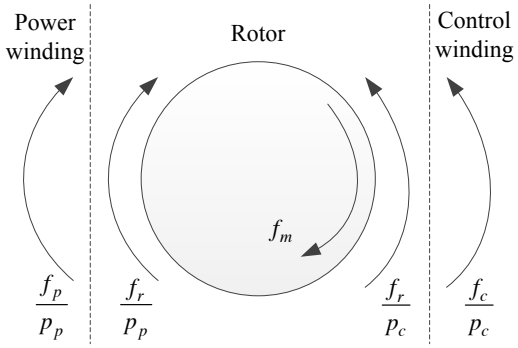

Figure 7.12 Rotating speed of fundamental magnetic fields in the brushless DFIM

7.4.2 Time-harmonics

According to Fig. 7.12, considering the rotor mechanical rotating frequency f_m, the frequencies of the rotor currents induced by the fundamental component of PW and CW are respectively:

$$f_{rp} = f_p - p_p f_m, \tag{7.19}$$

$$f_{rc} = f_c - p_c f_m. \tag{7.20}$$

This can be extended to any space-harmonic component k_s of stator magnetic field B_s. The frequency of the induced rotor current due to the k_s component is:

$$f_{re(k_s)} = f - k_s f_m, \forall k_s \in (k_p \cup k_c). \tag{7.21}$$

Table. 7.2 lists the time-harmonic frequencies of the rotor currents induced by different k_s components at rotating speed f_m = 8Hz when f_p = 50Hz and f_c = 10Hz in the synchronous operation mode.

Table 7.2 Induced rotor frequencies at 480rpm

$k_s = k_p$	2	-10	14	-22	62	-70	74	-142
$f_{rp(k_s)}$ Hz	34	130	-62	226	-446	610	-542	1186
$k_s = k_c$	-3	15	-21	33	-93	105	-111	213
$f_{rc(k_s)}$ Hz	34	-110	178	-254	754	-830	898	-1694
$k_s = k_p \pm mN_{ss}$	2+72		2-72		2+144		2-144	
$f_{re(k_s)}$ Hz	-542		610		-1118		1186	
$k_s = k_c \pm mN_{ss}$	-3+72		-3-72		-3+144		-3-144	
$f_{re(k_s)}$ Hz	-542		610		-1118		1186	

Each space-harmonic component k_r of rotor magnetic field B_r will also induce a time-harmonic component in the PW and the CW. The frequency of the induced component is:

$$f_{pe(k_r)} = f_{re(k_s)} + k_r f_m = f_p - (k_p - k_r) f_m, \forall k_r \in k_p, \tag{7.22}$$

$$f_{ce(k_r)} = f_{re(k_s)} + k_r f_m = f_c - (k_c - k_r) f_m, \forall k_r \in k_c. \tag{7.23}$$

Table. 7.3 summarizes some time-harmonic frequencies of voltage (and/or current) of PW and CW at rotating speed f_m = 8Hz when f_p = 50Hz and f_c = 10Hz in the synchronous operation mode. Some higher space-harmonics of the power winding field (e.g. -22nd, -142nd) may induce a rotor magnetic field with p_p pole-pairs, but rotating with an opposite direction with respect to the original PW p_p field. The induced stator frequencies due to these components are also given in Table. 7.3.

Table 7.3 Induced stator frequencies at 480rpm

Power winding	$f_{re(2)}$ = 34Hz				
k_r	2	2+4*5=22	2+28*5=142	-22+4*5=-2	-142+28*5=-2
$f_{pe(k_r)}$ Hz	50	210	1170	18	18
Control winding	$f_{re(-3)}$ = 34Hz				
$k_r \in k_c$	-3	-3-6*5=-33	-3+30*5=147	33-6*5=3	213-40*5=3
$f_{ce(k_r)}$ Hz	10	-230	1210	58	58

The above analysis is in the synchronous mode in which both stator windings are supplied. However, operating the brushless DFIM in the synchronous mode is not the only way to validate the harmonic analysis. Alternatively, it is easier to carry out the measurements in the simple induction mode. One stator winding is supplied while the other one is open-circuited. The induced voltage waveform of the stator winding which is open-circuited can be measured from the terminal. This voltage is induced by some certain space-harmonics of the rotor magnetic field. It actually means that the orders of these certain space-harmonics appear not only in the rotor field but also in the stator field. For instance, if the PW is supplied, the -3rd, 87th, 147th, etc. components of the induced rotor field will couple with the CW. The time-harmonic frequency of the induced CW voltage can be calculated as:

$$f_{ce(k_r)} = f_p - (k_p - k_r) f_m, \forall k_r \in k_c. \tag{7.24}$$

Similarly, if the CW is supplied and the PW is open-circuited, the 2nd, -58th, 142nd, etc. components of the induced rotor field will couple with the PW. The time-harmonic frequency of the induced PW voltage can be calculated as:

$$f_{pe(k_r)} = f_c - (k_c - k_r) f_m, \forall k_r \in k_p. \tag{7.25}$$

When the PW is supplied with 50Hz, the frequencies of the induced CW voltage at different rotating speeds can be calculated using (7.24) and given in Fig. 7.13. Fig. 7.14 shows the frequencies of the induced PW voltage at different speeds when the CW is supplied with 50Hz using (7.25).

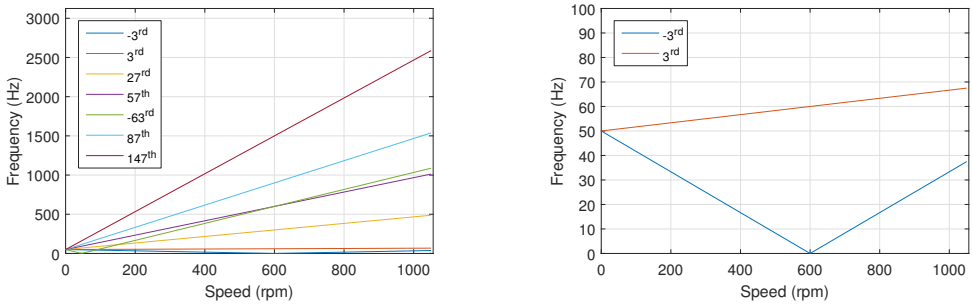

(a) All view **(b)** Enlarged view

Figure 7.13 Frequencies of induced CW voltage - analytical prediction

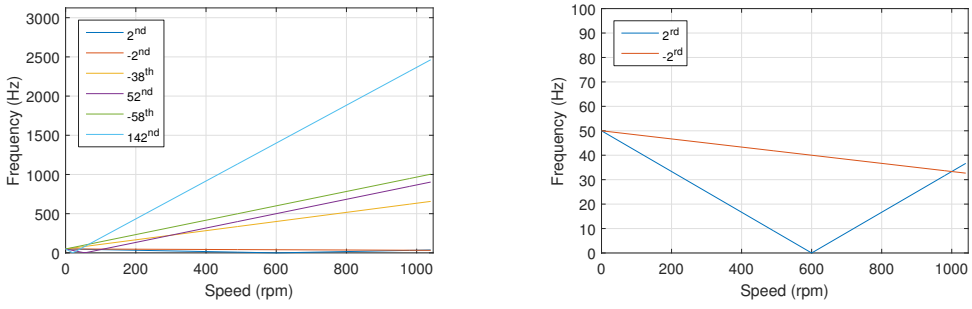

(a) All view **(b)** Enlarged view

Figure 7.14 Frequencies of induced PW voltage - analytical prediction

7.5 Results and discussions

7.5.1 Time-harmonics of CW voltages measured in the speed-up test

The short-time Fourier transform (STFT) can be applied to the CW voltage measured. The STFT is used to determine the sinusoidal frequency and phase content of local sections of a signal as it varies with time. A longer time signal is divide into shorter segments of equal length. The Fourier transform is applied to each shorter segment.

Fig. 7.15 presents the frequency spectrogram of the induced CW voltages with Rotor 1. The red dotted lines are drawn for clarity and for comparison with the analytical prediction. All of the space- and time-harmonics given in Fig. 7.13 are present in Fig. 7.15. Although there are some time-harmonics between 0 and 500Hz, their amplitude is so small that they are hardly visible. Fig. 7.15(b) gives an enlarged view to show the frequency of the fundamental component. At zero speed, the fundamental frequency of the induced CW voltage is 50Hz. The fundamental frequency goes down to zero at the natural synchronous speed (600rpm in this case). Then the frequency increases again when the speed goes up. Although the fundamental frequency is always positive, the phase sequence of the induced CW voltage changes when the speed goes above 600rpm. There is a component at 50Hz which is constant with respect to the speed. This is from the grid frequency.

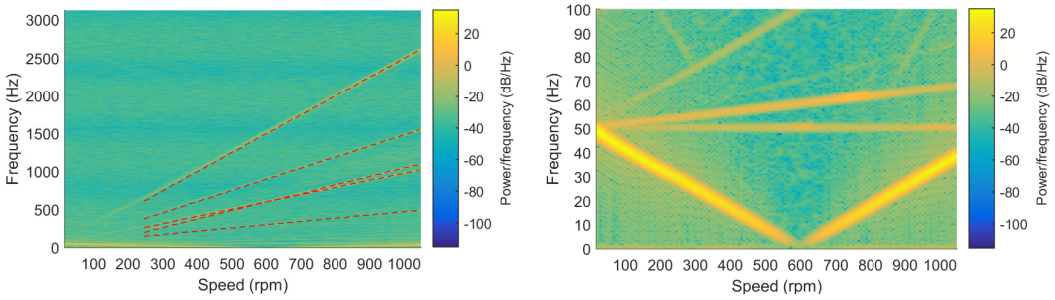

(a) All view **(b)** Enlarged view

Figure 7.15 Frequencies of CW voltage with Rotor 1 - measurement

Fig. 7.16 presents the frequency spectrogram of the induced CW voltages with rotor 2. It can be observed that the 147^{th} space-harmonic is almost invisible. It indicates that skewing rotor slots reduces the influence of this slotting space-harmonic. As mentioned before, rotor 2 has the highest concern of inter-bar currents. The inter-bar currents may change the distribution of the induced rotor magnetic field. It is hard to determine how big the influence is. However, it can be observed that lots of harmonic noises are present between 0 and 1000Hz. Fig. 7.16(b) indicates

that the fundamental frequency still agrees with the analytical expectation even if rotor 2 has significant inter-bar currents.

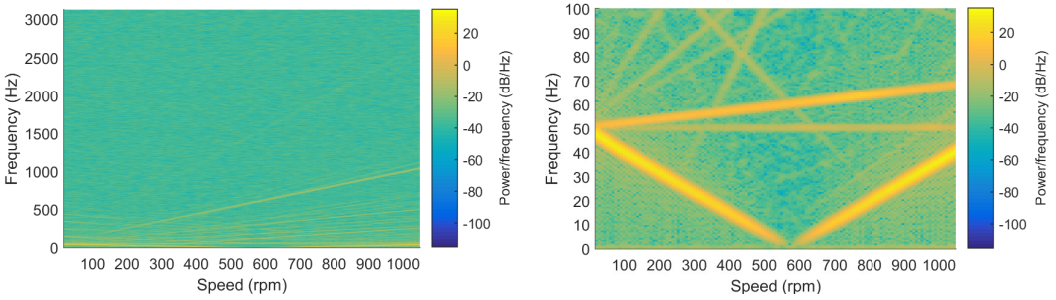

(a) All view **(b)** Enlarged view

Figure 7.16 Frequencies of CW voltage with Rotor 2 - measurement

Fig. 7.17 presents the frequency spectrogram of the induced CW voltages with rotor 3. Not only the space- and time-harmonics given in Fig. 7.13 are present, but also some additional space- and time-harmonics. Most of them are due to the inter-bar currents since rotor 3 also has a relatively big concern of inter-bar currents.

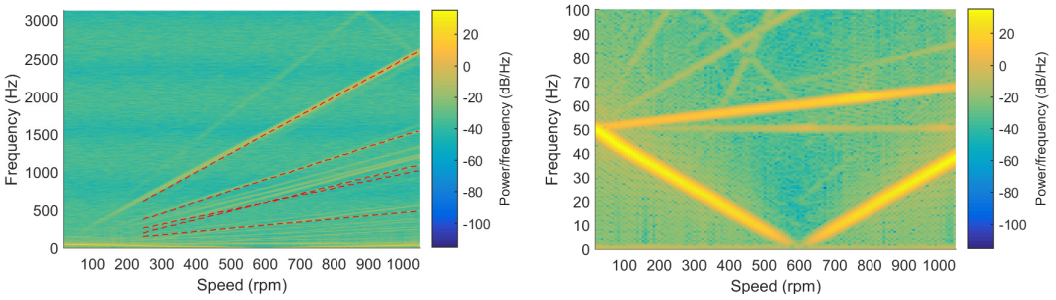

(a) All view **(b)** Enlarged view

Figure 7.17 Frequencies of CW voltage with Rotor 3 - measurement

Fig. 7.18 presents the frequency spectrogram of the induced CW voltages with rotor 4. Not all of the space- and time-harmonics given in Fig. 7.13 are visible. It means that skewing the rotor slots reduces the time-harmonics in the induced CW voltage.

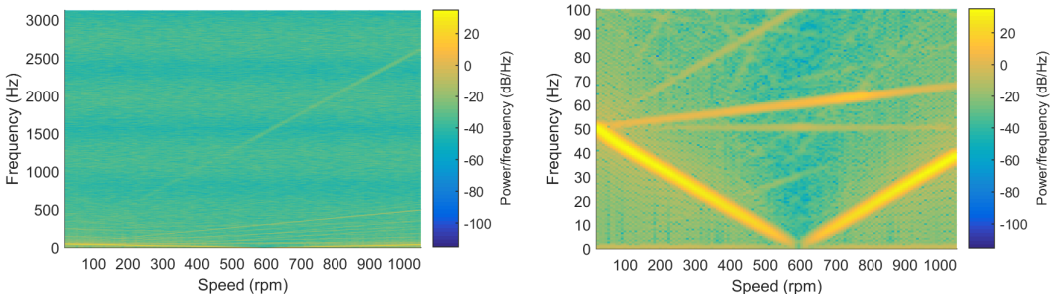

(a) All view **(b)** Enlarged view

Figure 7.18 Frequencies of CW voltage with Rotor 4 - measurement

7.5.2 Time-harmonics of PW voltages measured in the speed-up test

Figs. 7.19, 7.20, 7.21 and 7.22 give the frequency spectrogram of the induced PW voltages with rotors 1, 2, 3 and 4,respectively, when the CW is supplied. The explanation of some visible components can be referred to Figs. 7.14. The information derived from Fig. 7.19 to 7.22 is similar to the above section. Therefore, it is not necessary to discuss these figures one by one again.

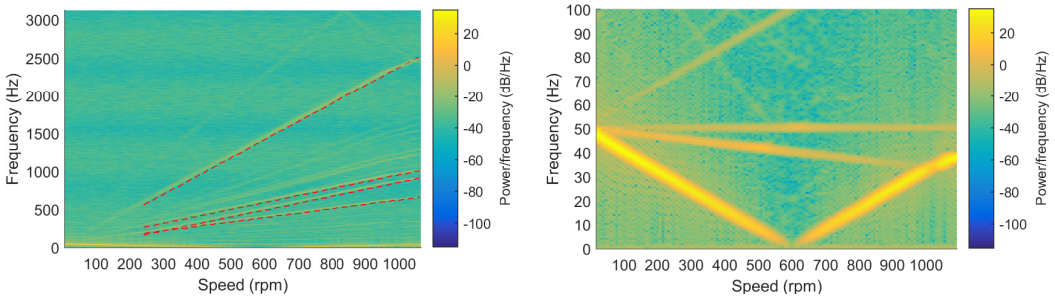

(a) All view **(b)** Enlarged view

Figure 7.19 Frequencies of PW voltage with Rotor 1 - measurement

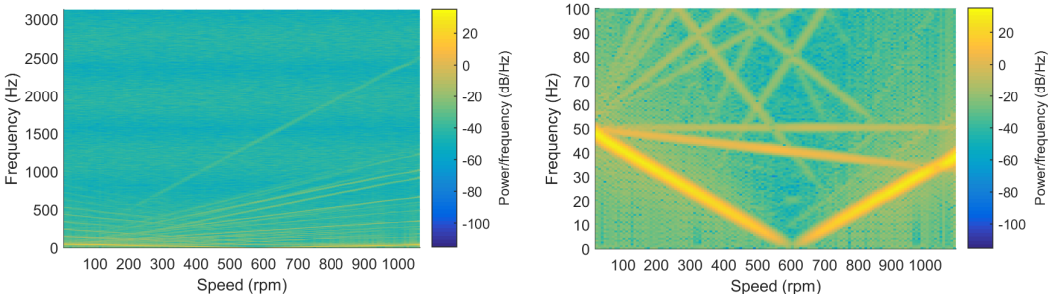

(a) All view **(b)** Enlarged view

Figure 7.20 Frequencies of PW voltage with Rotor 2 - measurement

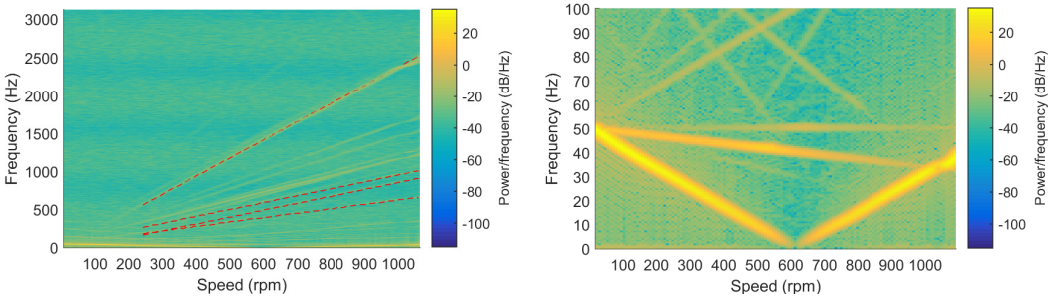

(a) All view **(b)** Enlarged view

Figure 7.21 Frequencies of PW voltage with Rotor 3 - measurement

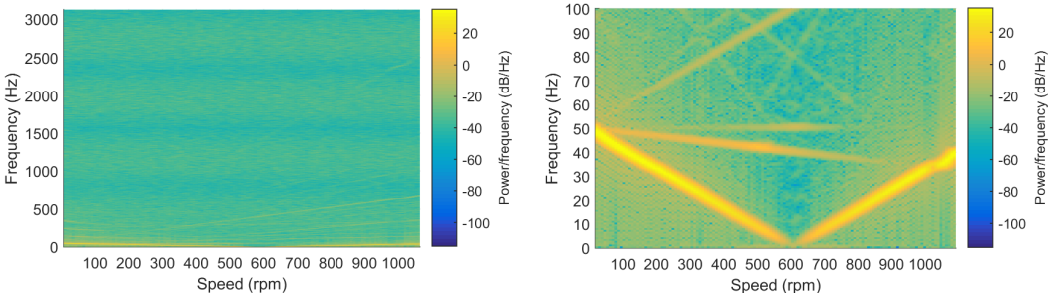

(a) All view **(b)** Enlarged view

Figure 7.22 Frequencies of PW voltage with Rotor 4 - measurement

7.5.3 Comparison of measurements and FE simulations at a fixed speed

This section gives a comparison of the measurements and FE simulations at 480rpm. Fig. 7.23 shows the stator voltages measured and calculated by the FE model. The agreement of the PW voltages happens to be good. The induced CW voltage predicted by the FE model is not close to the measurement since the 2D FE model does not take the inter-bar currents into account. Fig. 7.24 gives the time-FFT result of the induced CW voltages. Table 7.3 gives the analytical prediction of the induced CW frequencies at 480rpm. The predicted frequencies are present in the FE result and measurements. However, the amplitude calculated by the FE model is not close to the measurement. This is because the influence of the inter-bar currents is not taken into account in the FE simulation.

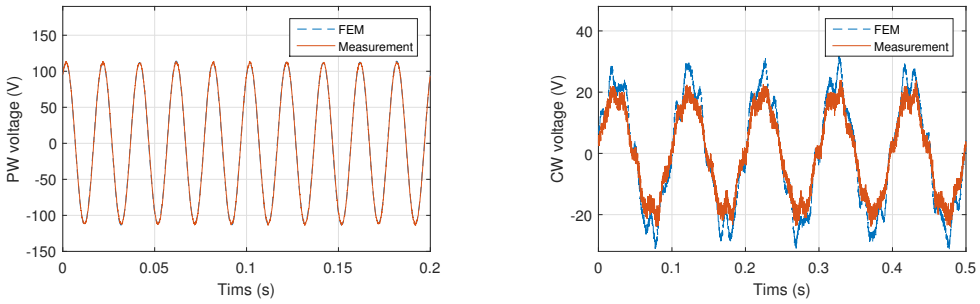

(a) Power winding **(b)** Control winding

Figure 7.23 Stator voltages at 480rpm - Rotor 1

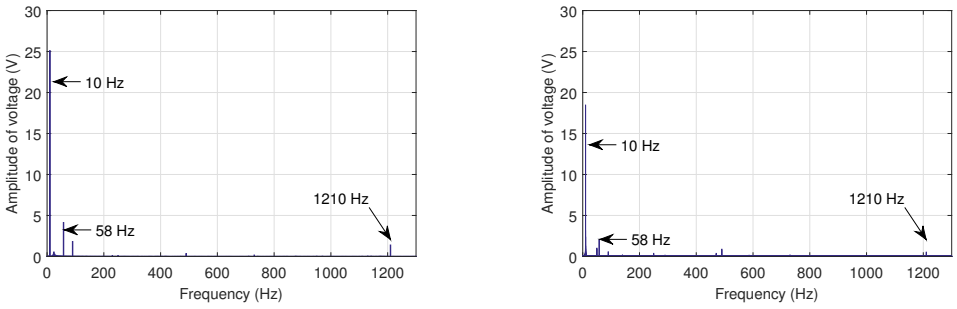

(a) FEM **(b)** Measurement

Figure 7.24 FFT of induced CW voltages - Rotor 1

Figs. 7.25 and 7.27 give the stator voltages with rotors 2 and 3, respectively. The FE results do not agree with the measurements. This can be expected because rotors 2 and 3 have a greater influence of the inter-bar currents. The voltages calculated by the FE models are higher than the measurements. This is because the input currents are higher which are shown in Fig. 7.5. Figs. 7.26 and 7.28 show the time-FFT results of the CW voltages given in Fig. 7.25(b) and 7.27(b), respectively. The frequencies agree with those give in Table 7.3. Some harmonic components with very small amplitudes appear in the FFT results. These are caused by the inter-bar currents.

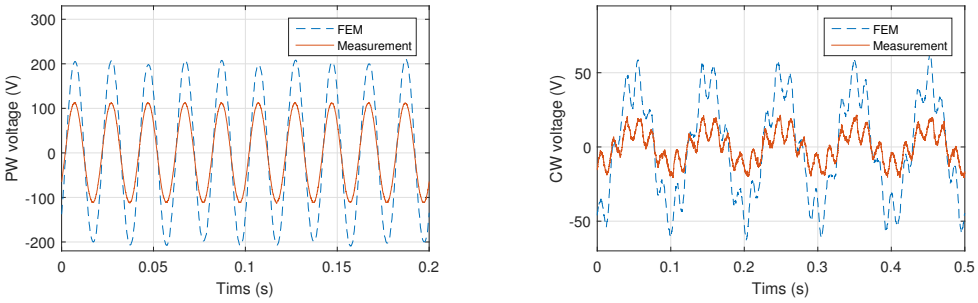

(a) Power winding **(b)** Control winding

Figure 7.25 Stator voltages at 480rpm - Rotor 2

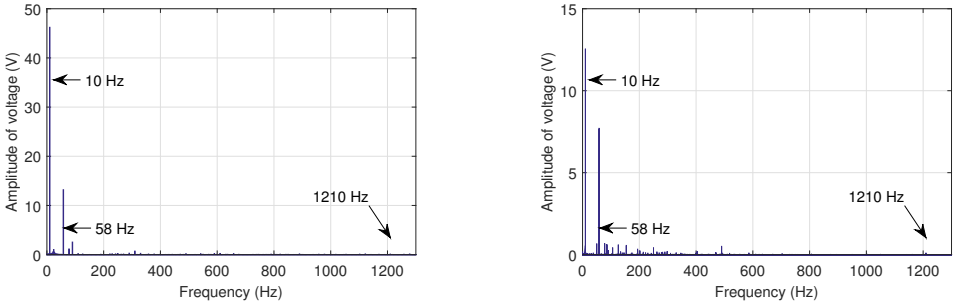

(a) FEM **(b)** Measurement

Figure 7.26 FFT of induced CW voltages - Rotor 2

Fig. 7.29 shows the stator voltages with Rotor 4 at 480rpm. As mentioned previously, the influence of the inter-bar currents is not so significant in this rotor. The difference between the FE simulations and the measurements is smaller than those with rotors 2 and 3. Moreover, the PW voltage calculated by the FE model is lower than the measurement which is opposite when compared

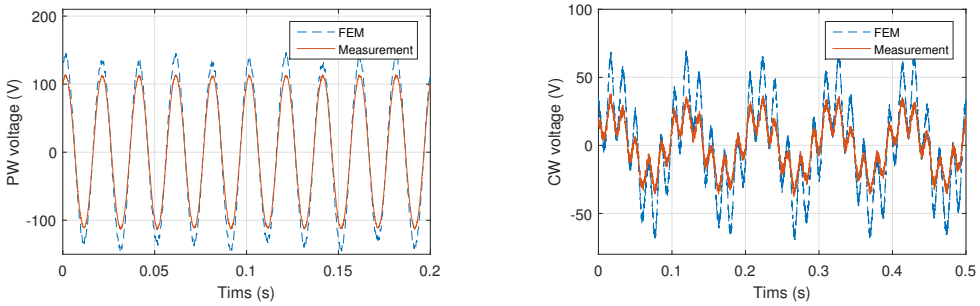

(a) Power winding **(b)** Control winding

Figure 7.27 Stator voltages at 480rpm - Rotor 3

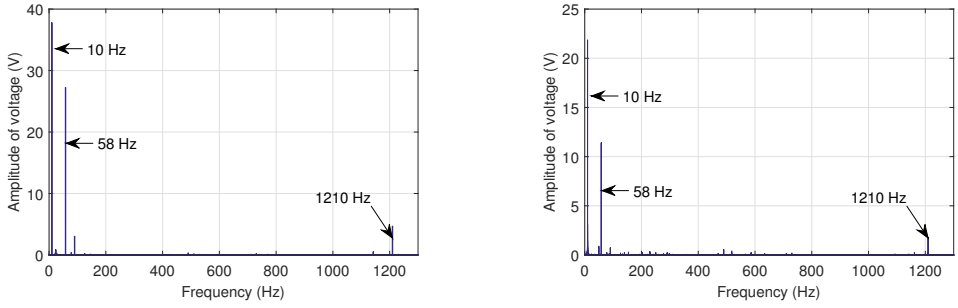

(a) FEM **(b)** Measurement

Figure 7.28 FFT of induced CW voltages - Rotor 3

with the situations with rotors 2 and 3. It means that the presence of the inter-bar currents leads to a lower input current in the case with rotor 4. At present, this has not yet been fully understood. Fig. 7.30 gives the time-FFT results of the induced CW voltages. The component with 58Hz is not visible in the FE result. This may be related to the cause which previously resulted in a lower input current.

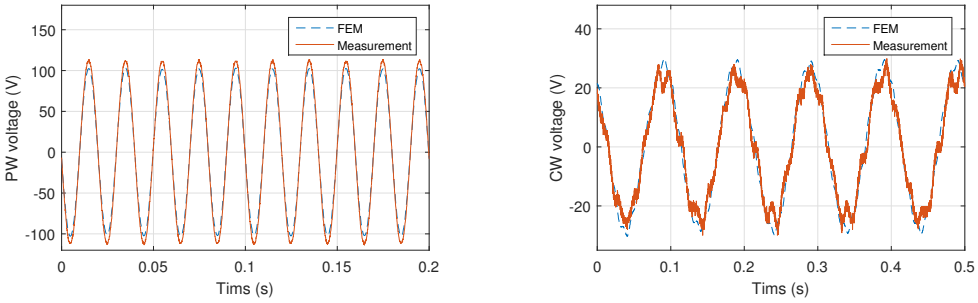

(a) Power winding **(b)** Control winding

Figure 7.29 Stator voltages at 480rpm - Rotor 4

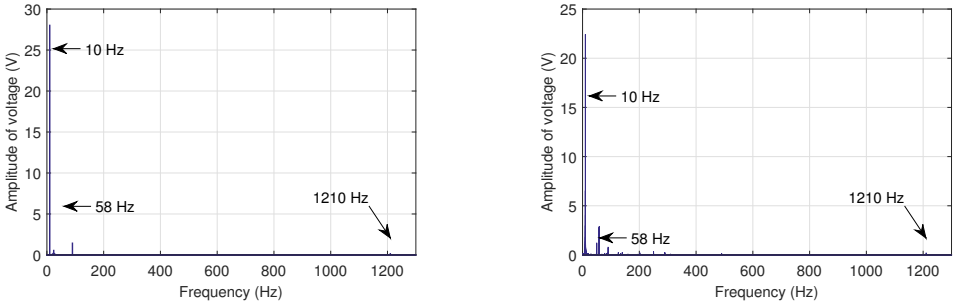

(a) FEM **(b)** Measurement

Figure 7.30 FFT of induced CW voltages - Rotor 4

Comparing the induced CW voltages with rotors 3 and 4, rotor 4 with skewed slots results in less time-harmonics than rotor 3. This can be because of the skewing which was the initial expectation. However, comparing the induced CW voltages with rotors 1 and 2, rotor 2 with skewed slots leads to much more time-harmonics than rotor 1. This means that the presence of the inter-bar currents has a significant influence on the space- and time-harmonics. The influence of the inter-bar currents can be so significant that the effects of skew are hardly observed.

Overall, the 2D FE model and the 2D multi-slice FE model do not give a good comparison with the measurements. This is because the unexpected influence of the inter-bars are not taken into account in 2D FE models.

7.5.4 Time-harmonics of rotor currents predicted by FEM at a fixed speed

The time-harmonics of the rotor currents are predicted analytically and given in Table 7.2. However, it is not straightforward to measure the rotor currents in the experiments. Therefore, FE results when the PW is supplied in simple induction mode at 480rpm are used to validate the time-harmonics of induced rotor currents. Since the inter-bar currents are not considered in the FE models, it does not make sense to look deeply into the amplitude of the rotor currents. However, it still makes some sense to look at the frequency components of the induced rotor currents.

Figs. 7.31, 7.33, 7.35 and 7.37 give the induced rotor currents of rotors 1, 2, 3 and 4, respectively. Figs. 7.32, 7.34, 7.36 and 7.38 show the corresponding time FFT analysis of the induced rotor currents. Table 7.2 has indicated that the fundamental component ($k_s = k_p = 2$) induces the fundamental rotor current with 34Hz at 480rpm. The other winding distribution space-harmonics of the PW field (e.g. $k_s = -10, -22, 62$) and the slotting space-harmonics (e.g. $k_s = 74, -70$) lead to induced rotor frequencies of 130, 226, -446, -542 and 610Hz at 480rpm, respectively. The negative sign represents the rotating direction and is not shown in the time-FFT results. All these frequencies are present in the FFT results of the induced rotor currents.

Rotors 2 and 4 with skewed slots leads to smoother rotor currents than rotors 1 and 3 which can be expected. However, rotor 3 with a larger loop span results in more time-harmonics in the rotor currents than rotor 1 which has a smaller loop span. This is not consistent with the expectation derived from Chapter 6. This is because rotor 3 is more affected by the inter-bar currents than rotor 1. The input currents measured with rotor 3 have more time-harmonics than rotor 1. Therefore, it is not strange that the induced rotor currents of rotor 3 have more time-harmonics in the FE results.

7.5.5 Influence of rotor skew

As mentioned previously, the presence of the inter-bar currents prevents observation of the influence of the rotor skew. However, it is worth presenting the comparison of the measurements to show the influence of the rotor skew.

Fig. 7.39 gives the induced CW voltages and the induced PW voltages with rotors 1 and 2 in the speed-up tests. In Fig. 7.39(a), starting from 0rpm, the induced voltage decreases gradually to 600rpm which is the natural synchronous speed of this brushless DFIM. At this speed, the frequency of the induced voltage is zero which can be observed from Figs. 7.15 to 7.22. Over 600rpm, the induced voltage increases as the speed increases. Fig. 7.39(b) shows the case in

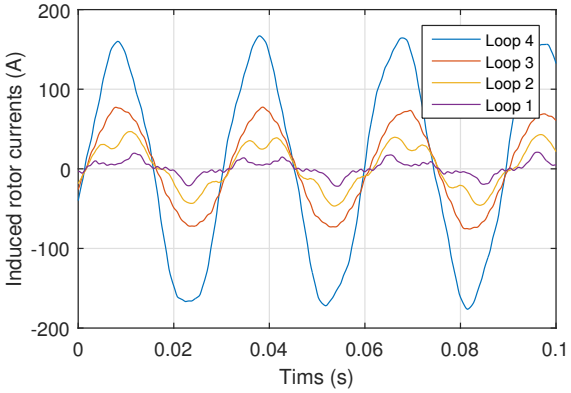

Figure 7.31 Induced rotor currents due to PW at 480rpm - Rotor 1

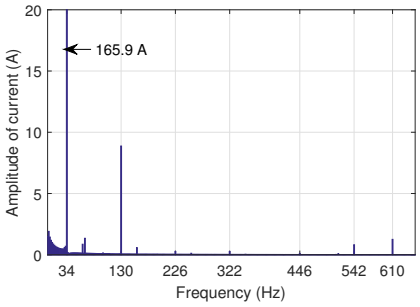

(a) Loop 4

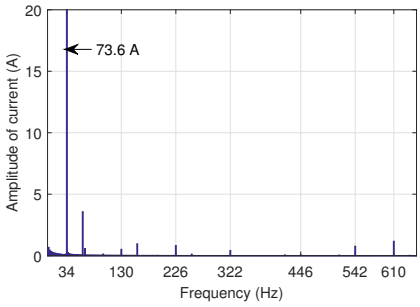

(b) Loop 3

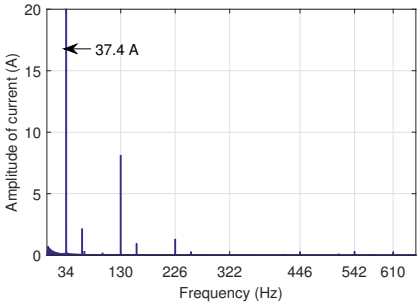

(c) Loop 2

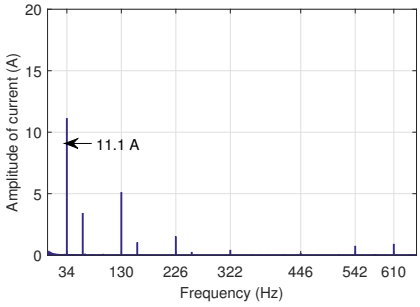

(d) Loop 1

Figure 7.32 FFT analysis of induced rotor currents of Fig. 7.31 - Rotor 1

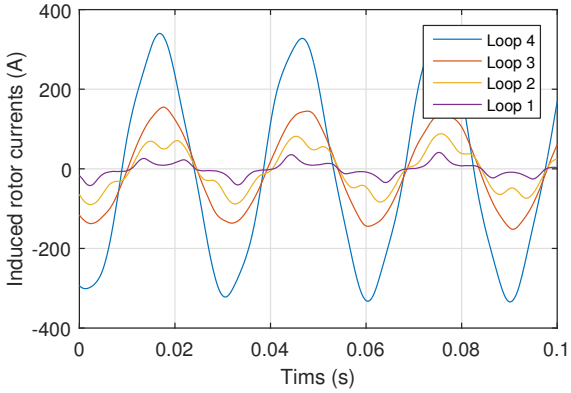

Figure 7.33 Induced rotor currents due to PW at 480rpm - Rotor 2

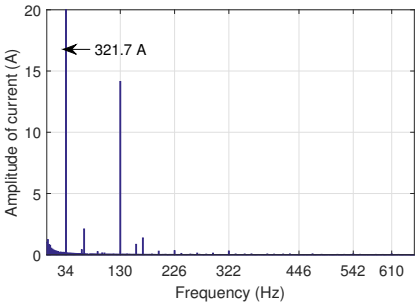

(a) Loop 4

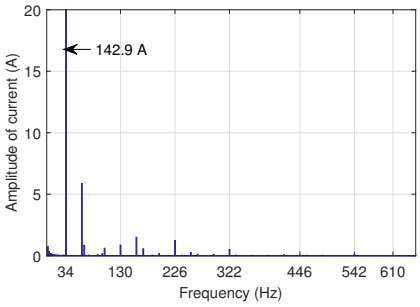

(b) Loop 3

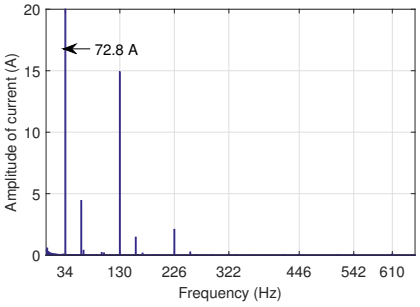

(c) Loop 2

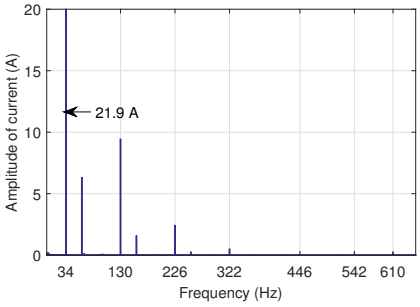

(d) Loop 1

Figure 7.34 FFT analysis of induced rotor currents of Fig. 7.33 - Rotor 2

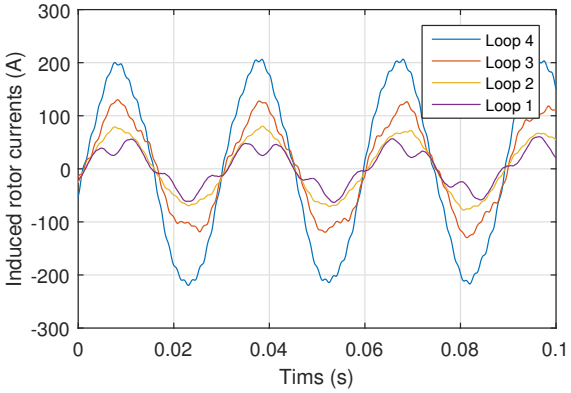

Figure 7.35 Induced rotor currents due to PW at 480rpm - Rotor 2

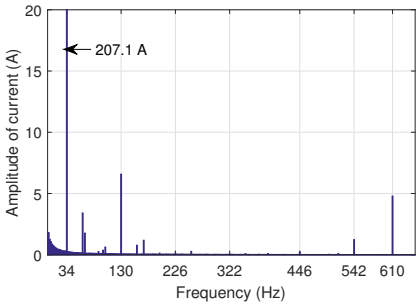

(a) Loop 4

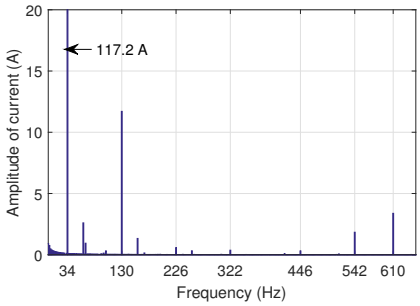

(b) Loop 3

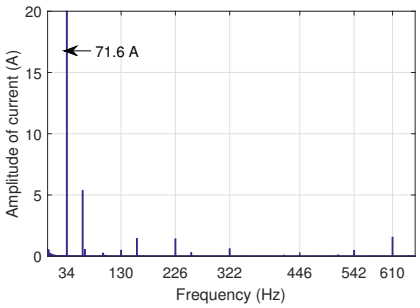

(c) Loop 2

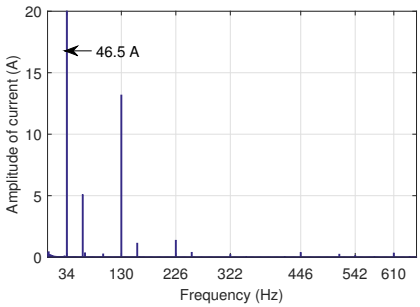

(d) Loop 1

Figure 7.36 FFT analysis of induced rotor currents of Fig. 7.35 - Rotor 3

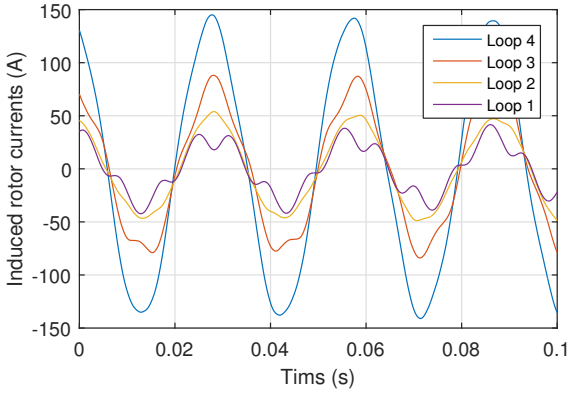

Figure 7.37 Induced rotor currents due to PW at 480rpm - Rotor 3

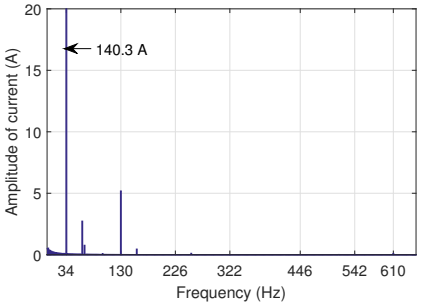

(a) Loop 4

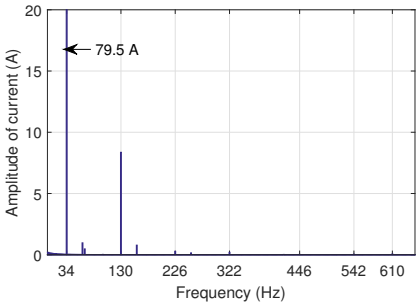

(b) Loop 3

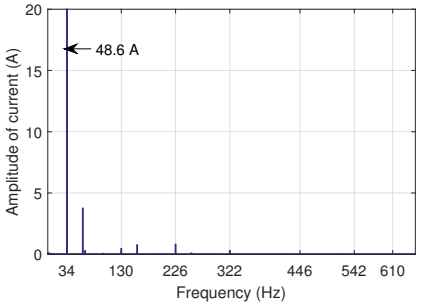

(c) Loop 2

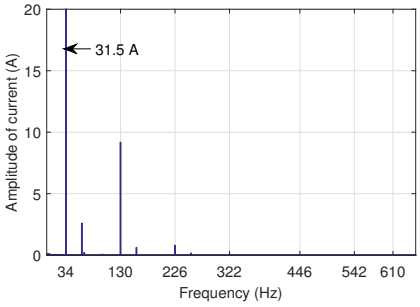

(d) Loop 1

Figure 7.38 FFT analysis of induced rotor currents of Fig. 7.37 - Rotor 4

which the CW is supplied and the PW is open-circuited. The induced PW voltage becomes very small at 1000rpm because the synchronous speed of the CW is 1000rpm in this case.

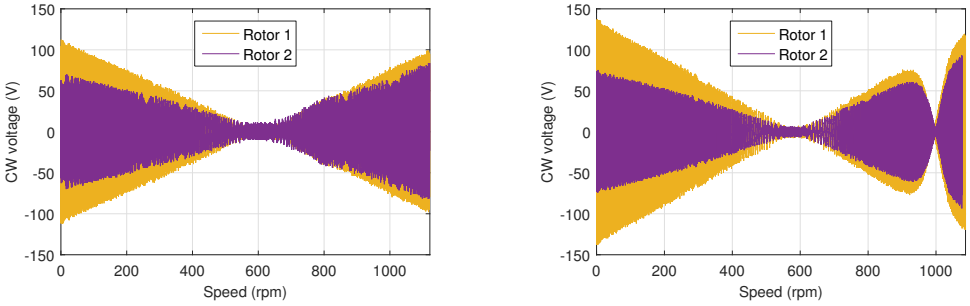

(a) Induced CW voltage **(b)** Induced PW voltage

Figure 7.39 Induced voltage with Rotor 1, 2 in speed-up test - measurement

Fig. 7.40 shows the amplitude of the fundamental induced voltages between the speed range from 400rpm to 720rpm. Rotor 2 with skewed slots leads to a lower induced voltage. The decrease is significant. The reason of this decrease is because of the significant inter-bar currents rather than the skewing.

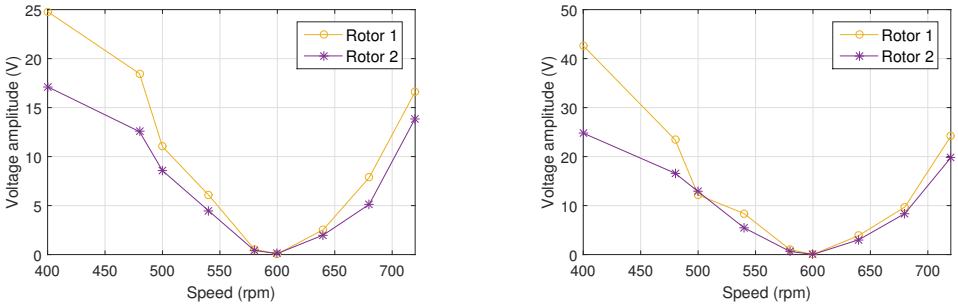

(a) Induced CW voltage **(b)** Induced PW voltage

Figure 7.40 Amplitude of the fundamental induced voltage with Rotor 1, 2 - measurement

Fig. 7.41 gives the THD of the induced voltages corresponding to Fig. 7.40. The THD can be

calculated by:

$$THD = \frac{\sqrt{\sum_{h=2}^{\infty} e_{p(c),h}^2}}{e_{p(c),1}} \times 100\%, \tag{7.26}$$

where $e_{p(c),h}$ is the amplitude of the h^{th} harmonic component of the induced PW (CW) voltage and $h = 1$ is the fundamental component. The amplitude of the fundamental voltage is almost zero at the natural synchronous speed (i.e. 600rpm in this case). Therefore, the THD value defined by (7.26) is extremely high at 600rpm. It does not make sense to show it in the figures. Overall, rotor 2 leads to a higher THD level than rotor 1. This does not agree with the expectation of applying skewed slots. The inter-bar currents in rotor 2 change the air-gap magnetic field and lead to more time-harmonics in the induced stator voltages.

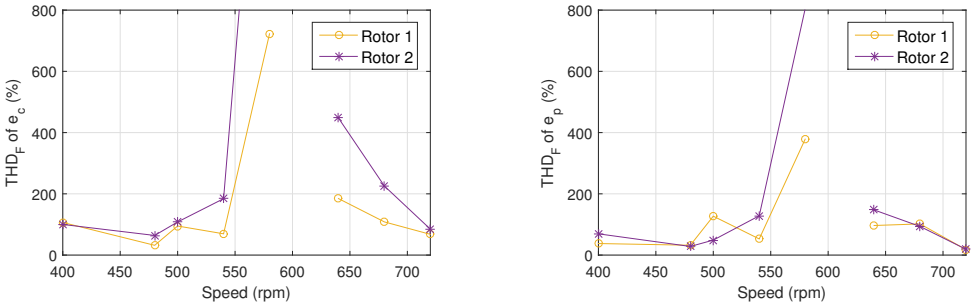

(a) Induced CW voltage **(b)** Induced PW voltage

Figure 7.41 THD of induced voltage with Rotor 1, 2 - measurement

Fig. 7.42 gives the induced CW voltages and the induced PW voltages with rotors 3 and 4 in the accelerating tests. The trend is similar to that in Fig. 7.39.

Fig. 7.43 shows the amplitude of the fundamental induced voltages for the speed range from 400rpm to 720rpm. Rotor 4 with skewed slots leads to an induced voltage which is approximately the same as rotor 3. This actually indicates that the effects of the rotor skew are hard to see due to the influence of the inter-bar currents.

Fig. 7.44 gives the THD of the induced voltages corresponding to Fig. 7.43. Rotor 4 with skewed slots leads to a lower THD level of the induced stator voltages. Although this is consistent with the initial expectation of applying skewed slots, it is difficult to quantify the influence of the inter-bar currents on the THD.

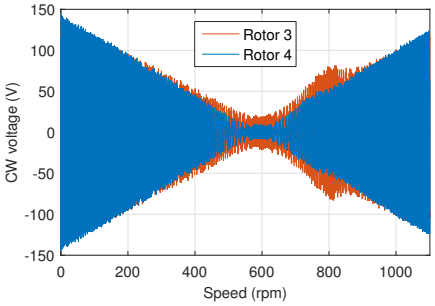

(a) Induced CW voltage

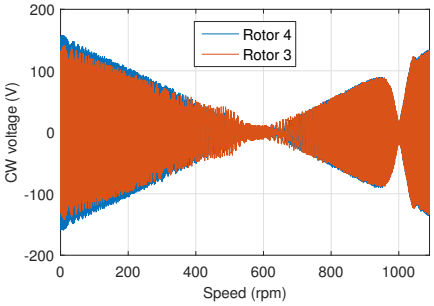

(b) Induced PW voltage

Figure 7.42 Induced voltage with Rotor 3, 4 in speed-up test - measurement

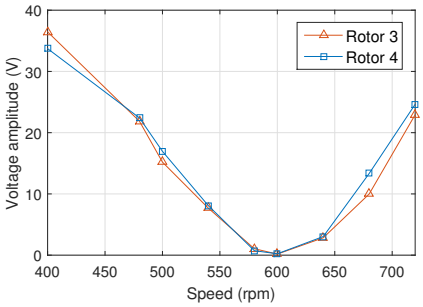

(a) Induced CW voltage

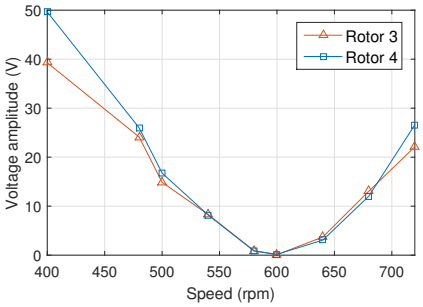

(b) Induced PW voltage

Figure 7.43 Amplitude of the fundamental induced voltage with Rotor 3, 4 - measurement

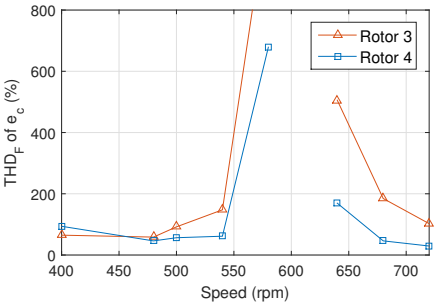

(a) Induced CW voltage

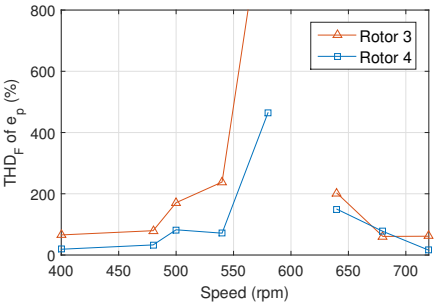

(b) Induced PW voltage

Figure 7.44 THD of induced voltage with Rotor 3, 4 - measurement

7.5.6 Influence of nested-loop configurations

Fig. 7.45 shows the induced CW voltage and the induced PW voltage with rotors 1 and 3 in the accelerating tests. The amplitude of the fundamental induced voltage for the speed range from 400rpm to 720rpm is shown in Fig. 7.46. Rotor 3 leads to a higher induced CW voltage in the first test while it results in a similar induced PW voltage in the second test. Overall, it seems that rotor 3 with a larger loop span leads to a stronger cross-coupling between the fundamental components. This agrees with the comparison of the torque load-angle characteristic shown in Fig. 6.8 (in Chapter 6) in which rotor 3 leads to a higher average torque than rotor 1.

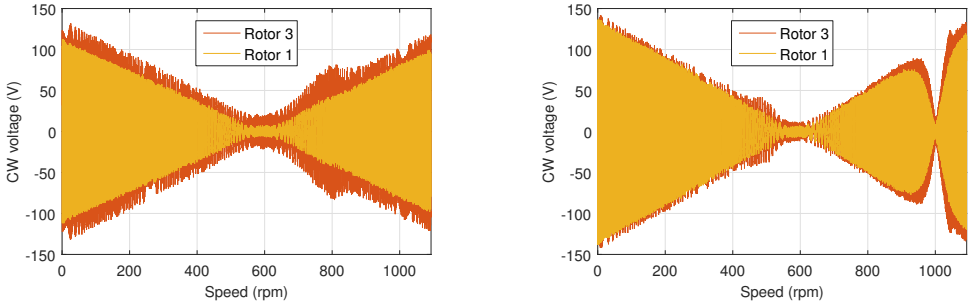

(a) Induced CW voltage **(b)** Induced PW voltage

Figure 7.45 Induced voltage with Rotor 1, 3 in speed-up test - measurement

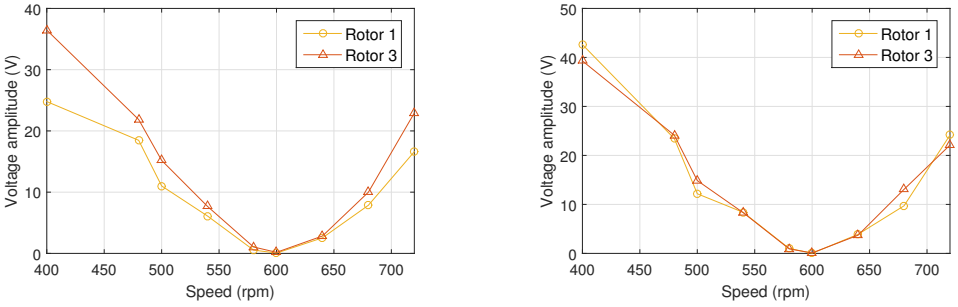

(a) Induced CW voltage **(b)** Induced PW voltage

Figure 7.46 Amplitude of the fundamental induced voltage with Rotor 1, 3 - measurement

As mentioned in Section 7.5.4, rotor 3 with a larger loop span results in more time-harmonics in the rotor currents calculated by the FE model. From the measurement point of view, rotor 3 leads

to higher THD values of the induced stator voltages than rotor 1 which has a smaller loop span. This is not consistent with the conclusion of Chapter 6. However, this can be explained by the fact that rotor 3 has more severe inter-bar currents.

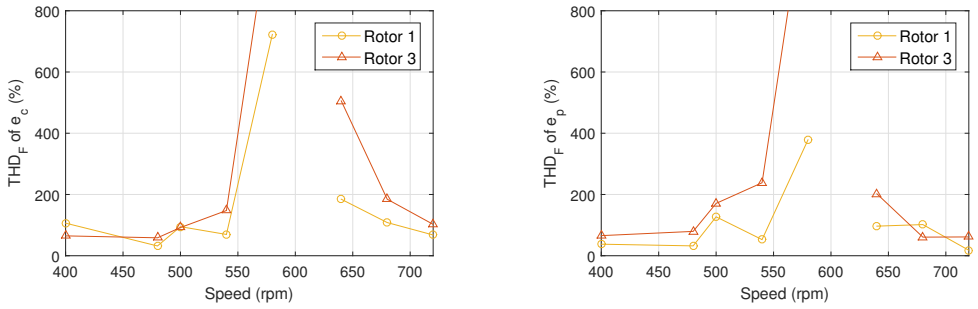

(a) Induced CW voltage **(b)** Induced PW voltage

Figure 7.47 THD of induced voltage with Rotor 1, 3 - measurement

Rotor 4 is less affected by the inter-bar currents. Therefore, it would be better to make a comparison between rotors 1 and 4 to show the influence of the nested-loop configurations. Fig. 7.48 shows the the induced CW voltage and the induced PW voltage with rotors 1 and 4 in the accelerating tests. The amplitude of the fundamental induced voltage for the speed range from 400rpm to 720rpm is shown in Fig. 7.49. Rotor 4 leads to higher induced voltages in both situations. This agrees with the conclusion derived in Chapter 6 that the rotor with a larger loop span results in a higher average torque.

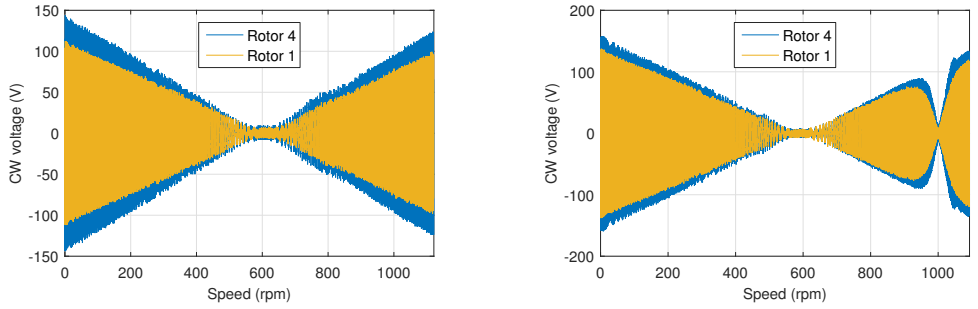

(a) Induced CW voltage **(b)** Induced PW voltage

Figure 7.48 Induced voltage with Rotor 1, 4 in speed-up test - measurement

Fig. 7.50 gives the THD of the induced voltages corresponding to Fig. 7.49. It seems that the

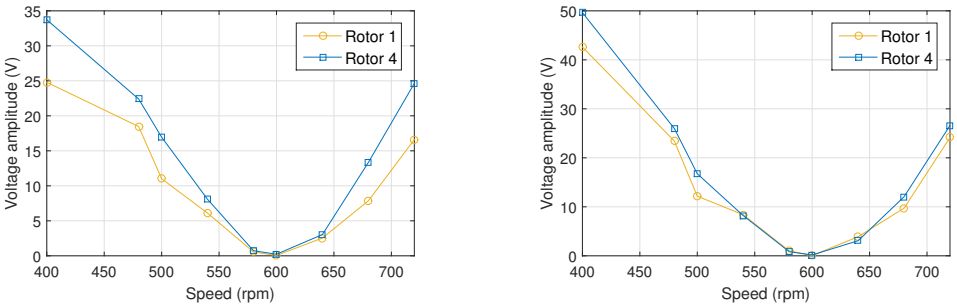

(a) Induced CW voltage **(b)** Induced PW voltage

Figure 7.49 Amplitude of the fundamental induced voltage with Rotor 1, 4 - measurement

nested-loop rotor with larger loop span leads to a slightly lower THD level of the stator voltages at most speed points. Seemly consistent with the conclusion of Chapter 6, the rotor with larger loop span leads to a lower THD level of the stator voltages. However, it is not straightforward to figure out whether the decrease of the THD value is due to the larger loop span or the skewed slots. Moreover, again, it is hard to quantify the influence of the inter-bar currents on the THD level.

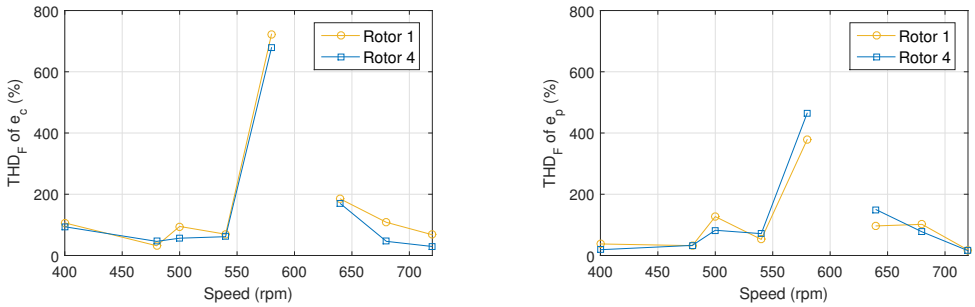

(a) Induced CW voltage **(b)** Induced PW voltage

Figure 7.50 THD of induced voltage with Rotor 1, 4 - measurement

7.6 Conclusion

This chapter presents an experimental study on a small-scale brushless DFIM prototype. Instead of operating the brushless DFIM in the synchronous mode, the simple induction mode is per-

formed for an indirect validation. The insulation between the rotor bars and the iron core was damaged during the manufacturing processing. This results in some inter-bar currents in the rotors. The inter-bar currents have an influence on the distribution of the rotor magnetic field which makes the validation not as good as expected. Moreover, the inter-bar currents increase the stator input currents when the same terminal voltages are supplied. The increase of the input currents is different with different rotors. Rotor 2 (with a small loop span and skewed slots) and rotor 3 (with a big loop span and non-skewed slots) have more severe problem of the inter-bar currents than rotor 1 (with a small loop span and non-skewed slots) and rotor 4 (with a big loop span and skewed slots).

The induced PW (and CW) voltage waveforms are measured at a accelerating range. The orders of the space- and time-harmonics predicted by the analytical derivation are validated by the frequency spectrogram of the induced PW (and CW) voltages measured. The induced CW voltage waveforms are measured a fixed rotating speed. The 2D FE model and the 2D multi-slice FE are then performed using the stator currents measured in the tests. The orders predicted analytically are present in the time-FFT results of the induced CW voltages measured and calculated by the FE models. However, the amplitudes of the space- and time-harmonics predicted by the FE models do not agree with the measurements since the inter-bar currents are not considered in the FE models. The inconsistency in rotors 2 and 3 is larger than that in rotors 1 and 4 as we expected that rotors 2 and 3 have more severe inter-bar currents. The 2D FE models are partially validated by the measurements.

The influence of the rotor skew is studied by comparing the induced voltages of the open-circuited winding with non-skewed and skewed rotors. For the rotors with a small loop span, rotor 2 with skewed slots leads to lower induced voltages and higher THD levels of the stator voltages than rotor 1 without skewed slots. This is not consistent with the expectation of applying skewed slots. However, it may be because rotor 2 has significant inter-bar currents. For the rotors with big loop span, rotor 4 with skewed slots leads to approximately the same induced voltages and a lower THD level compared with rotor 3 without skewed slots. This agrees with the expectation of applying skewed slots. However, it is difficult to quantify the influence of the inter-bar currents.

The influence of the nested-loop configurations is studied by comparing the induced voltages of the open-circuited winding of the rotors with small and big loop span. Rotor 3 with a big loop span leads to higher induced voltages than rotor 1 with a small loop span. This is consistent with the conclusion of Chapter 6. However, rotor 3 also results in a higher THD level of the stator voltages which is not consistent with the conclusion of Chapter 6. The reason for the higher THD level can be explained as rotor 3 has severe inter-bar currents. Then the induced voltages with rotor 4 are compared to rotor 1. Although rotor 4 has skewed rotor slots, it is expected that it will be less affected by the inter-bar currents. Rotor 4 leads to higher induced voltages because of the big loop span. Moreover, rotor 4 results in a slightly lower THD level of the stator voltages at most speed points compared with rotor 1. This seems to agree with the conclusion of Chapter 6 that, the rotor with a larger loop span leads to a lower THD level of the stator voltages. However, again, the influence of the rotor skew and the inter-bar currents on the THD level are hard to quantify based on the measurements.

CHAPTER 8

Analysis of Axial Flux Due to Skewed Slots Using 3D Magneto-Static FE Model

The aim of this chapter is to implement a 3D magneto-static FE model to study the influence of the axial flux due to skewed slots on the electromagnetic torque. Almost all of the FE models developed for brushless DFIMs in the literature, as well as in previous chapters of this thesis, are limited to two-dimensions. However, 3D FE models are useful for investigating some features such as skew effects, end effects and anisotropy of material properties and so on. The 3D FE model for the brushless DFIM is a large scale problem with millions of degrees of freedom (DoF). This is because the periodic boundary typically applied in normal electrical machines is not always valid for brushless DFIMs. This chapter applies two iterative solves, namely the Conjugate Gradients (CG) method and the Generalized Minimum Residual (GMRES) method, with Geometric multigrid preconditioning for dealing such a large scale problem. It shows both iterative solvers reduce the memory required significantly. From the memory required and the computing time points of view, the CG solver is better than the GMRES solver in this particular study. The axial flux due to skewed slots is estimated properly by the 3D magneto-static FE model presented. It shows that the axial flux has little influence on the electromagnetic torque meaning that the 2D multi-slice FE model is sufficient to capture the skew effects on the torque.

Most parts of this chapter have been published in

- F. M. Wani, X. Wang, D. Lahaye and H. Polinder, "3D FEM Computation of Axial Flux in a Brushless Doubly-Fed Induction Machine," in *IEEE Int. Magnetics Conf.*, Dublin, Ireland, Apr. 2017.

8.1 Introduction

With the development of computing power and numerical methods in recent years, finite element (FE) methods have been widely applied to the design and analysis of electrical machines. FE models have advantages of taking into account various complex effects in electrical machines such as nonlinear properties of the materials, eddy currents and effects due to complicated geometrical features and so on.

For the brushless doubly-fed induction machines (DFIMs), FE models have normally been employed for the validation of the analytical models [36, 42, 77, 78, 120]. Moreover, van der Blij *et al.* [104] have applied FE models to predict performance gaining more insight into the operating characteristics of the brushless DFIMs. Abdi *et al.* [83] have applied FE models to estimate the magnetic flux distribution in brushless DFIMs to optimize the design of the rotor back iron. In Chapter 4 and 5 of this thesis, FE models have been applied to investigate the effect of skew. These have also been applied to compare different nested-loop rotors in Chapter 6. Chapter 3 describes the building of a computationally efficient FE model based on magneto-static simulation.

However, all of these FE models are limited to two-dimensions. Therefore, some practical features such as end effects of eddy currents and end-windings, anisotropy of material properties, skewed slots, etc. are difficult or impossible to model using 2D FE models. For instance, Chapter 4 has applied a 2D multi-slice FE model to investigate the effects of skew which is essentially a 3D problem. In the 2D multi-slice FE model, induced rotor currents are assumed to flow in the axial direction even if the rotor slots are actually skewed over a certain pitch. The axial flux due to skewed slots is ignored based on that assumption. This raises a question about the influence of the axial flux after skewing the rotor slots. A 3D FE model can be a valuable tool to answer this question. Furthermore, 3D FE models would also be very useful to investigate other effects mentioned previously.

3D FE models have been applied to analyze and design electrical machines [121–124]. However, there are few papers know to us which are working on the 3D FE modeling for the brushless DFIMs. A small scale 3D FE model for a brushless DFIM with a few thousand degrees of freedom (DoF) has been developed by Thompson in [125]. However, the authors have indicated that their model had not achieved an accurate representation of the real machine due to the limitation of the computing resource. Actually, the authors have accessed one of the challenges for building a 3D FE model for a brushless DFIM. To most classic electrical machines, only a section of the full geometry with a periodic boundary is sufficient to represent the performance of the whole machine. However, it is not always straightforward to find out such a boundary in a brushless DFIM since two stator magnetic fields have different pole-pair numbers and different frequencies. For a large scale 3D problem with millions of DoFs, iterative solvers are normally applied to save the memory (RAM) required [126–128].

The aim of this chapter is to implement a 3D magneto-static FE model with iterative solvers. This will then be applied to study the influence of the axial flux due to skewed slots on the electromagnetic torque. This chapter starts with the detailed steps for building a 3D magneto-

static FE model in COMSOL Multiphysics. Then the estimation of the axial flux due to skewed slots using a 3D magneto-static FE model is given, followed by discussions. Finally, conclusions are drawn.

8.2 3D magneto-static finite element modeling

8.2.1 Assumptions

The following assumptions are made in the 3D FE magneto-static model:

1. Eddy currents are not taken into account. The magnetic filed produced by the eddy currents in the iron core is ignored, which is reasonable since the eddy currents are reduced significantly due to the lamination structure.
2. Skin effect and proximity effect are ignored. Current densities in the conductors are assumed to be uniform throughout the conductor domains. This is acceptable since the operating frequency is not very high in this study.
3. The unknown rotor currents are obtained from the 2D transient multi-slice FE model presented in Chapter 4. This might result in inaccurate rotor currents since the axial flux due to skewing was not considered in the multi-slice model. This will be further discussed in section 8.3.
4. Saturation is not taken into account.

These assumptions lead to some inaccuracy compared with the real physics. However, they help to simplify the 3D FE modeling in the starting stage.

8.2.2 Geometry

Table 8.1 gives the main specifications of the brushless DFIM studied in this chapter and Fig. 8.1 shows the configuration of the nested-loop rotor without skewing.

The geometry of the machine can be made by using a user interface of COMSOL Multiphysics or COMSOL LiveLink for MATLAB, or a combination. However, it is recommended to use script in COMSOL LiveLink for MATLAB in order to make the program more flexible.

In this chapter, to simplify the geometry, the end part of the machine is not modeled. A 2D cross-section of the brushless DFIM can be made in advance. The 3D geometry is achieved by extruding the stator and the rotor domains along the axial direction. Fig. 8.2 shows the 3D geometries for the stator and the skewed rotor. The air-gap domain is subsequently easily generated.

It is critical to be aware of the corners in the geometry of a 3D FE model solved using iterative methods. Sharp corners result in extremely slow or stalled convergence. Therefore, it is recommended to avoid sharp corners or edges. If there are any, additional steps need to taken to round

Table 8.1 Main Specifications of the Brushless DFIM Studied

Description	**Machine parameter**	**Value**
Axial length [mm]	L	240.0
Air-gap length [mm]	g	1.0
Stator outer radius [mm]	r_{so}	135.0
Stator inner radius [mm]	r_{si}	85.0
Rotor inner radius [mm]	r_{ri}	35.0
Number of phases	N_{ph}	3
Number of pole-pairs	p_p, p_c	2, 3
Rated frequency [Hz]	f_p, f_c	50, -10
Number of stator slots	N_{ss}	72
Number of rotor nests	p_r	5
Number of loops per nest	q_r	4
Loop span [rad]		π/25*[3 5 7 9]

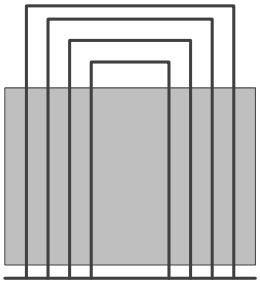

Figure 8.1 Nested-loop rotor structure

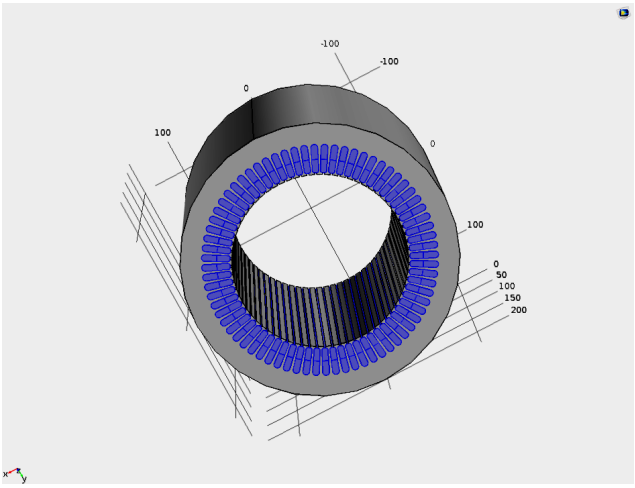

(a) Stator

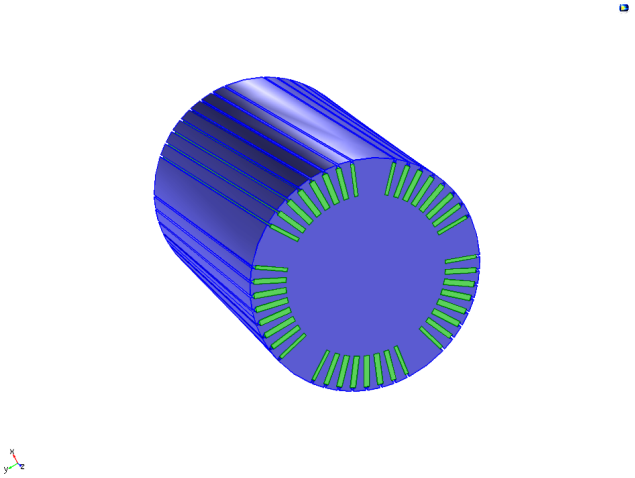

(b) Rotor with skewed slots

Figure 8.2 3D geometry of a brushless DFIM

them slightly. However, it is difficult to say to what extent the sharp corner should be rounded. As a rule of thumb, the solver can be interrupted once the convergence begins to stall. Then, it is useful to check the solution in the region around the corner. If the solution changes abruptly, it is necessary to round the corner slightly.

8.2.3 Material properties

Material properties have a big influence on the solutions. Generally, there are two main material properties needing to be set in an FE model.

Electric conductivity

Under the given set of assumptions, the electric conductivities are set as zero in all domains. The conductor material can be treated similarly to air while the current densities are assumed to be uniform. In addition, no eddy currents arise in the core domains which benefits speeding up of the calculations.

Magnetic permeability

For homogeneous and isotropic material domains (e.g. the conductor domain and the air-gap domain), it is easy to define the magnetic permeability as a scalar value. However, it is not straightforward to determine the permeabilities for the domains of the stator and the rotor core which are laminated in the axial direction. It is not realistic to model each individual laminated iron sheet from a computing time point of view. A magnetic permeability tensor is applied to take into account the laminated iron core [129, 130]. The relative permeability tensor for the laminated iron can be calculated as:

$$\mu_r = \begin{bmatrix} \mu_x & 0 & 0 \\ 0 & \mu_y & 0 \\ 0 & 0 & \mu_z \end{bmatrix}, \tag{8.1}$$

$$\mu_x = \mu_y = (\mu_{Fe} - 1)\kappa + 1, \tag{8.2}$$

$$\frac{1}{\mu_z} = \kappa\left(\frac{1}{\mu_{Fe}} - 1\right) + 1, \tag{8.3}$$

where κ is the stacking factor and μ_{Fe} is the relative permeability of iron material.

8.2.4 Governing electromagnetic field equation

The governing differential equation for all domains is given as (8.4) in which the displacement current is ignored.

$$\nabla \times H = J, \tag{8.4}$$

where J is the current density and H is the magnetic field intensity which has a relationship with magnetic flux density B as:

$$B = \mu_0 \mu_r H, \tag{8.5}$$

where μ_0 is the magnetic permeability of the vacuum and μ_r is the relative permeability of the material.

Magnetic vector potential formulation

Generally, (8.4) can be solved using magnetic vector potential A in all domains:

$$\nabla \times \left(\frac{1}{\mu} \nabla \times A \right) = J, \tag{8.6}$$

where A is a vector quantity and involves three unknowns in three directions.

Gauging vector potential

The only constraint on the magnetic vector potential A is that its curl must be equal to the magnetic flux density B. This is because of the divergence-free condition for B. However, the divergence of A is not determined. The fixing of $\nabla \cdot A$ is termed as *gauge fixing*. In magneto-static problems, Coulomb Gauge is widely used as [131]:

$$\nabla \cdot A = 0. \tag{8.7}$$

This condition is satisfied automatically in 2D problems, but not in 3D problems [132]. It is useful to ensure the uniqueness of the magnetic vector potential.

Magnetic scalar potential formulation

There is a rather simpler approach to solve (8.4) in a domain with zero current density by using the magnetic scalar potential V_m. The differential equation for such domain is written as:

$$-\nabla \cdot (\mu \nabla V_m) = 0. \tag{8.8}$$

Generally, the scalar formulation has advantages over the vector formulation because the information about the magnetic field is contained in a scalar number rather than a vector with three components. Therefore, it is much simpler and requires fewer computations to calculate the scalar potential than the vector potential. Additionally, if the scalar potential is applied to the air-gap domain, a moving boundary is allowed between the rotor and stator to be accounted for via interpolation [84]. However, a V_m formulation can only be used in a domain that is not only free of current but also simply connected.

Mixed potential formulation

It is possible to use both the vector and the scalar potential formulations in one model. Mixed potential formulations are mostly employed in 3D FE models to exploit the advantages of the scalar potential as mentioned previously.

For a magneto-static 3D FE model for brushless DFIMs, it can either formulate all domains using the vector potential or employ a mixed potential formulation.

8.2.5 Boundary conditions

Fig. 8.3 gives a representation of domains formulated using mixed potentials. Ω_A and Ω_{Vm} represent the vector and the scalar potential domains, respectively. It is mandatory to specify the appropriate boundary conditions for the computing domain Ω.

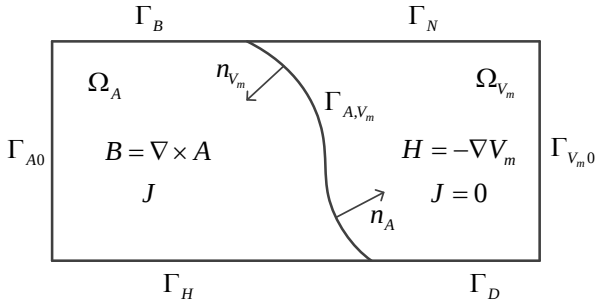

Figure 8.3 A representation for mixed potential formulations

A magnetic insulation boundary is applied to the external boundaries of the machine. For the vector potential domain, (8.9) is imposed at the boundary.

$$n \times A = 0, \quad on \ \Gamma_{A0}, \tag{8.9}$$

where n is the outward normal unit vector on Γ_{A0}. For the scalar potential domain, (8.10) is applied to the boundary.

$$n \cdot B = 0, \quad on \ \Gamma_{Vm0}, . \tag{8.10}$$

Suppose, the normal component of the magnetic flux density is known as:

$$B \cdot n = -b, \tag{8.11}$$

where b is the charge density of fictitious magnetic surface charges. For a vector potential domain, a Dirichlet boundary condition can be imposed as:

$$\nabla \cdot (n \times A) = b, \quad on \ \Gamma_B. \tag{8.12}$$

Suppose, the tangential component of the magnetic filed intensity is known as:

$$H \times n = K, \tag{8.13}$$

where K is the surface current density. For a vector potential domain, the Neumann boundary condition can be imposed as:

$$\left(\frac{1}{\mu}\nabla \times A\right) \times n = K, \quad on \ \Gamma_H. \tag{8.14}$$

Similarly, for a scalar potential domain, the Dirichlet and the Neumann boundary conditions are:

$$V_m = V_{m0}, \quad on \ \Gamma_D, \tag{8.15}$$

$$\nabla V_m \cdot n = \beta, \quad on \ \Gamma_N. \tag{8.16}$$

The tangential component of the magnetic field intensity and the normal component of the magnetic flux density need to be continuous for interface between Ω_A and Ω_{Vm}. This implies:

$$\left(\frac{1}{\mu}\nabla \times A\right) \times n_A - \nabla V_m \times n_{V_m} = 0, \tag{8.17}$$

$$(\nabla \times A) \cdot n_A - \mu \nabla V_m \cdot n_{V_m} = 0. \tag{8.18}$$

8.2.6 Meshing

The meshing in a 3D FE model is slightly more complicated compared with that in a 2D model. Firstly, the surface at one end of the machine is meshed. Then the mesh can be swept along the axial direction of the machine. In this case study, the default triangular and quad elements are applied to mesh the surface. This results in triangular prism and hexahedral elements after sweeping. Fig. 8.4 shows the sweep mesh for the brushless DFIM geometry. Only half of the mesh is shown for clarity while the model is actually solved for the entire geometry.

It is tricky to use the default sweep mesh for the brushless DFIM with skewed rotor slots. This is because the curve directions along which the meshes are swept in the stator and the rotor are different, shown in Fig. 8.5. A slightly distorted hexahedral element (shown in Fig. 8.6) is employed in the air-gap domain to overcome that problem.

There is no fixed rule to determine the number of mesh planes. However, it is necessary to take care of the number of mesh planes because the elements with a too high aspect ratio might result in stalled convergence or inaccurate results [133]. Typically, the number of mesh planes needs to be increased until the result does not have any appreciable change. However, more number of mesh planes will lead to more number of DoF or unknowns.

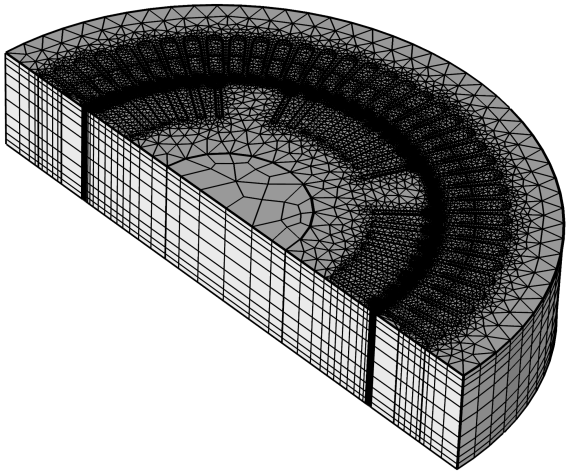

Figure 8.4 Sweep mesh for 3D geometry of a brushless DFIM

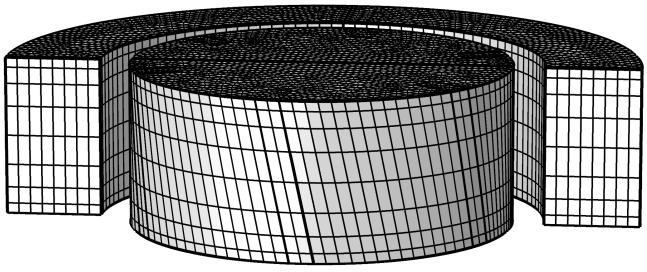

Figure 8.5 Sweep mesh in the rotor with skewed slots

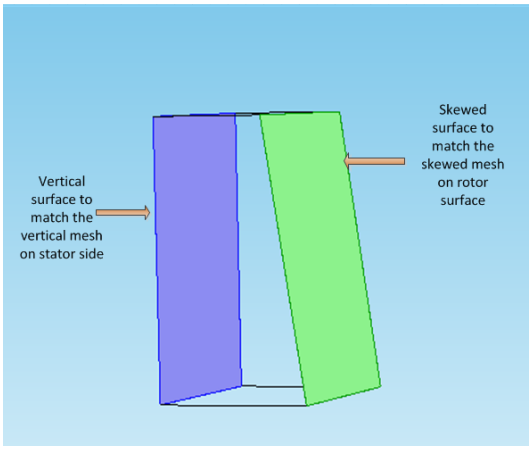

Figure 8.6 Intermediate hexahedral element in the air-gap for skewed rotor

8.2.7 Solvers

Solving partial differential equations (given in (8.6) and (8.8)) using the finite element method is to finally solve a system of linear equations. The steady state linear equations are generally in the following form:

$$S\hat{x} = f, \tag{8.19}$$

where S is a matrix with known coefficients, $\hat{x}$ is the unknown vector representing the nodal or edge unknowns and f is the known source vector. The unknowns in such equations are the DoF in the FE approximation.

(8.19) can be solved either by the direct solver or the iterative solver. The direct solver is normally applied to most 2D FE models and some 3D FE problems due to their robustness. However, it is not efficient as the size of the matrix increases. For a large scale problem, the direct solver needs large amounts of memory and lots of computing time. Therefore, two iterative solvers, namely the Conjugate Gradient (CG) method and the Generalized Minimum Residual (GMRES) method, are used in this chapter.

Preconditioning using multigrid method

Generally, preconditioning of the matrices is necessary to enhance the convergence of the iterative solvers before implementing the iterative methods. A better convergence can be achieved by the pre-multiplication of the matrix S with a preconditioning matrix which improves the spectral properties of the new matrix. It is not so effective to use, for example, the Jacobi, the symmetric Gauss-Seidel, the incomplete LU factorization and the incomplete Cholesky pre-conditioners to deal with very large matrices [134]. a multigrid method is developed precisely to deal with such

huge matrices. The objective of the multigrid method is to formulate an iterative solver whose convergence is somewhat independent of the grid size [134]. Moreover, the multigrid preconditioning can eliminate both low and high frequency errors by performing iterative procedures on coarser and finer meshes [135, 136].

Conjugate Gradients (CG) method

CG is essentially an advanced version of the Steepest gradient method which aims to minimize the following function:

$$F(x) = \frac{1}{2} x^T S x - x^T f, \tag{8.20}$$

where f and S are assumed to be positive definite and symmetric. The minimum value of $F(x)$ is achieved by setting $x = S^{-1} f$. Thus, minimizing F given by (8.20) and solving (8.19) are equivalent problems. F decreases most rapidly in the direction of the steepest descent given by the negative gradient:

$$-\nabla F(x) = f - Sx = r, \tag{8.21}$$

where r is called the residual.

In the CG method, the successive residuals are orthogonal to each other. Therefore, error eliminated at one iteration step is not reintroduced at another [131].

Generalized Minimum Residual (GMRES) method

The GMRES method is based on the minimization of the residual:

$$r = f - Sx. \tag{8.22}$$

The objective is given an initial guess $x^{(0)}$, to find an approximate solution, such that:

$$x^{(k)} \in x^{(0)} + M, \tag{8.23}$$

$$(f - Sx^{(k)}) \perp N, \tag{8.24}$$

where M and N are the expansion space and the projection space, respectively. Details of M and N can be found in [137].

The main problem with unlimited GMRES is that the k^{th} iteration involves all results calculated in the previous steps. Therefore, a more practical way for implementing GMRES is to use a restart strategy [137].

Comparison of solvers

As mentioned previously, the 3D magneto-static FE model for the brushless DFIM can either be modeled entirely by using the magnetic vector potential or by using a mixed potential formulation. The first situation leads to a symmetric and positive definite stiffness matrix S which makes the CG solver work in this case. Even though it results in a large number of DoFs by using the magnetic vector potential in all domains, the CG solver can reduce the memory (RAM) required significantly. The GMRES solver is applied in the second case using the mixed potential formulation.

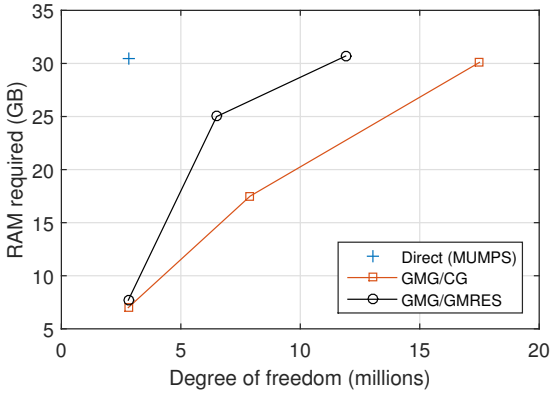

Figure 8.7 Comparison of memory (RAM) for direct and iterative solvers

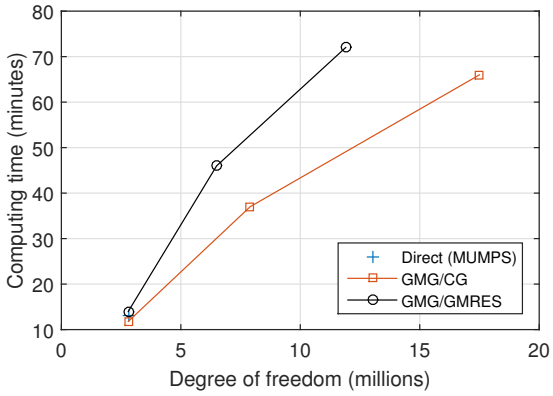

Figure 8.8 Comparison of computing time for direct and iterative solvers

Figs. 8.7 and 8.8 give the comparison of these two iterative solvers, as well as the direct solver. Fig. 8.7 indicates that the direct solver takes around 30GB memory to deal with 3 million DoFs while

the CG and the GMRES can manage around 18 million and 12 million, respectively. For a problem with around 3 million DoFs, the CG and GMRES only take around 8GB which can be performed on most personal computers. Fig. 8.8 gives the comparison of computing time using different solvers. It takes approximately the same time to deal with 3 million DoFs using different solvers. However, when the DoFs increase, the CG solver leads to a faster computation compared with the GMRES solver while the direct is already out of memory.

8.3 Simulation results and discussions

8.3.1 Axial flux

In order to show the usefulness of the 3D magneto-static FE model presented, the influence of the axial flux due to skewed slots which is ignored in the 2D multi-slice FE model is studied.

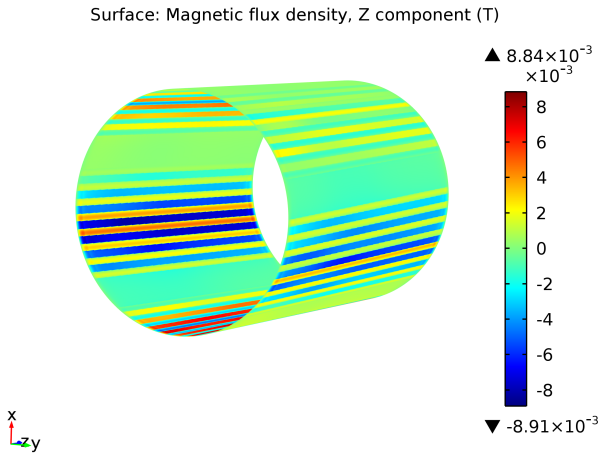

Figure 8.9 Axial component of the flux in the anisotropic rotor iron

Fig. 8.9 shows the 3D view of the axial component of the flux in the rotor. The rotor slots are skewed over one stator slot pitch. It can be seen that the magnitude of the axial component decreases slightly at the end part. This is because the axial flux changes direction and combines with the radial flux at the end. The axial flux adds to the radial flux at one side and subtracts from it at the other side.

There are two reasons for the difference of the rotor currents in the skewed case and the non-skewed case. The first one is due to the relative position shift between the stator and the rotor which has already been taken into account in the multi-slice model. The other one is the axial flux

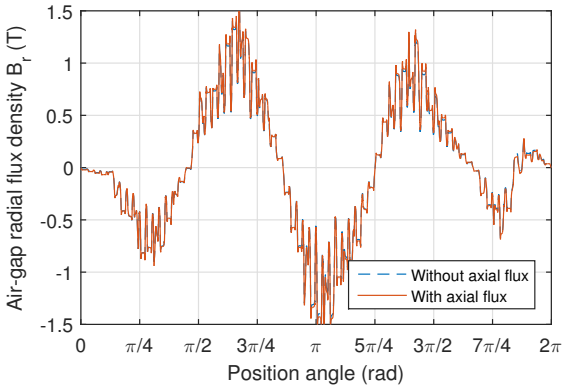

(a) at 1mm (left end)

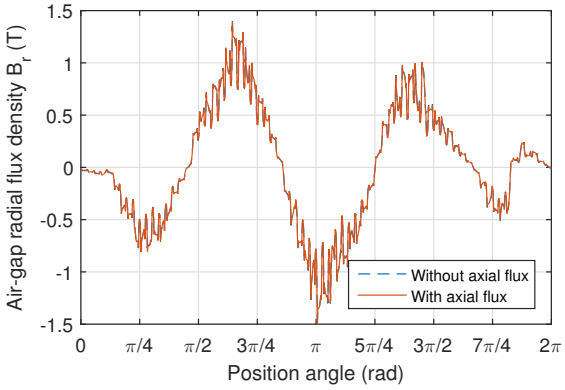

(b) at 120mm (middle)

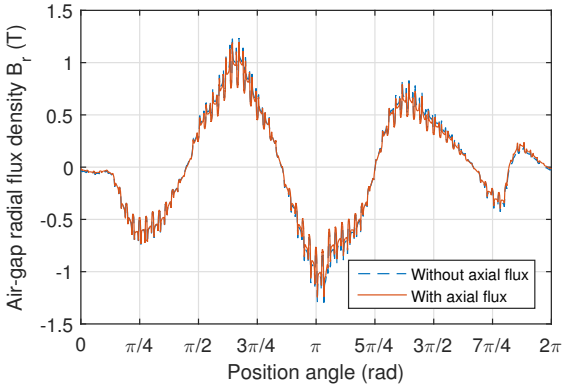

(c) at 239mm (right end)

Figure 8.10 Air-gap radial flux densities without and with axial flux

shown in Fig. 8.9. To evaluate the influence of the axial flux, another 3D magneto-static model is run by replacing the permeability tensor given by (8.1) with (8.25). By doing this, the axial flux is minimized.

$$\mu_r = \begin{bmatrix} \mu_x & 0 & 0 \\ 0 & \mu_y & 0 \\ 0 & 0 & 1 \end{bmatrix}. \tag{8.25}$$

Fig. 8.10 gives the air-gap radial flux densities at different positions along the axial direction. Firstly, it indicates that the axial flux adds to the radial flux at one side (left side in this case) and subtracts from it at the other side (right side in this case). Secondly, it shows the difference of the radial flux in the cases with and without the axial flux is very small. Then, it can be expected that the influence of the axial flux on the induced rotor currents is negligible.

8.3.2 Electromagnetic torque

Fig. 8.11 gives the electromagnetic torque with skewed slots calculated by the 2D multi-slice model and the 3D model presented. Considering the computing time cost, not all of the time moments in the 2D model are calculated in the 3D model. The torque values calculated by the 3D models are approximately 2-3% lower than those calculated by 2D multi-slice models. The influence of the axial flux on the electromagnetic torque is small enough to be ignored.

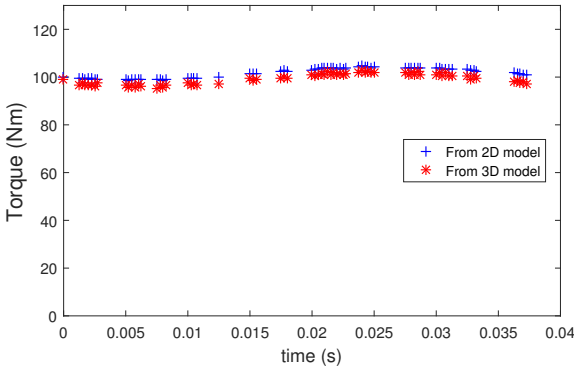

Figure 8.11 Electromagnetic torque with a rotor skewed over one stator slot pitch

8.4 Conclusion

This chapter implements a 3D magneto-static FE model for the brushless DFIM. There is not always a periodic boundary in the brushless DFIM since two stator windings have different pole-pair numbers and different frequencies (e.g. $p_p = 2, p_c = 3$ in this case study). The direct solver

hardly deals with such a 3D problem with millions of DoFs due to the limitation of memory. Iterative solvers with the Geometric multigrid preconditioning are applied to deal with this large scale 3D problem. The memory required is reduced significantly which makes it possible to deal with a very large scale 3D problem on a personal computer. In this particular study, the CG solver with geometric multigrid preconditioning gives a better performance than the GMRES solver from the memory required and the computing time points of view. The 3D magneto-static FE model is then applied to study the influence of the axial flux due to skewed slots which is ignored in the 2D multi-slice FE model in Chapter 4. The magnitude of the axial flux is much smaller than the radial flux due to the lamination structure. The results also indicate that the axial flux has little influence on the electromagnetic torque. Therefore, the 2D multi-slice FE model presented in Chapter 4 is sufficient for capturing the skew effects on the electromagnetic torque. However, the 3D magneto-static FE model presented in this chapter can be expected to be valuable when we look into the additional eddy current losses due to the axial flux and the end-windings in the future.

CHAPTER 9

Improved Design for a 3.2MW Brushless DFIM

The aim of this chapter is to apply the modeling methods and the design guidelines which have been presented in the previous chapters to optimize the design of a 3.2MW brushless doubly-fed induction machine (DFIM). The improved design does not start from nowhere, but is based on the case study machine initially designed by the University of Cambridge. The selections of the stator pole-pair combination and the nested-loop rotor construction are discussed. The initial design is optimized using the FE based multi-objective optimization tool. The objectives are to optimize both the active material costs and the efficiency of the brushless DFIM. Results show that the magnetic loading of the brushless DFIM is increased for a better design by using the FE based optimization tool. Two optimized designs are selected from the resulting Pareto optimal front and further compared with the initial design using the 2D transient FE model. Both optimized designs increase the efficiency and shear stress, and reduce both the torque ripple and the THD level of the stator voltages. However, the optimized designs result in a high electric loading which would be a challenge for cooling. Skewing the rotor slots of the improved design can further reduce the torque ripple and the THD level of the stator voltages at the expense of a lower average power, higher core losses and additional manufacturing costs.

Based on

- X. Wang, H. Polinder, D. Lahaye, and J. A. Ferreira, "FE Based Multi-Objective Optimization of a 3.2MW Brushless Doubly-Fed Induction Machine," in *IEEE Workshop on Electrical Machines Design, Control and Diagnosis (WEMDCD)*, Nottingham, UK, Apr. 2017.

9.1 Introduction

The brushless doubly-fed induction machine (DFIM) has great potential to be a variable-speed generator for wind turbine applications. However, the brushless DFIM has some disvantages such as higher manufacturing costs, slightly larger dimensions, and lower efficiency compared with the doubly-fed induction genrator (DFIG) with the same rating [60]. These shortcomings prevent the brushless DFIM being commercialized in wind turbine derive-train systems. Therefore, one open question is how to design and optimize the brushless DFIM to industrial levels. This question is related to the tools and the guidelines of the design and optimization.

For the tool of design and optimization, the electric equivalent circuit (EEC) model has been proven to be useful in analyzing and optimizing the brushless DFIM [63], [56]. The magnetic equivalent circuit (MEC) model has also been developed to provide reasonable accuracy and better results compared to EEC models [82]. The air-gap contains two main magnetic fields with different pole-pair numbers and different frequencies leading to a complicated magnetic field in the brushless DFIMs. It is not straightforward to take the saturation into account in the EEC and MEC models. These models are normally accurate in the case that the machine does not operate in the high saturation region. Therefore, the magnetic loading of the brushless DFIM designed using the EEC and MEC models is relatively low to prevent the brushless DFIM operating in the high saturation region. On the other hand, the two stator magnetic fields are added at some positions and subtracted at other positions. This results in local saturation in brushless DFIMs. It is interesting to then consider whether the brushless DFIMs designed by the EEC and the MEC models are too conservative. The finite element (FE) model has been widely applied to design and optimize the electrical machines. It has the advantages of considering detailed geometries and saturation. For the brushless DFIMs, it takes additional effort to make the EEC model consider the saturation [120]. The FE model is more attractive because it actually transfers the effort of modeling saturation from human to the computer. The transient FE model has been applied to analyze the brushless DFIM in [85, 104, 138]. Chapter 3 has developed a computationally efficient FE model to predict the steady-state performance of the brushless DFIMs. One candidate design can be evaluated within one or two minutes. This makes it possible to perform the FE-based multi-objective optimization for the brushless DFIMs on a personal workstation. The computationally efficient FE model has been successfully applied to design and optimize a small-scale prototype in Chapter 3. In this chapter, the computationally efficient FE model will be applied to optimize a 3.2MW brushless DFIM.

For the design guidelines, most of the research interests are related to the selection of the stator pole-pair combinations [139] and the design of the nested-loop rotors [65]. In Chapter 3, several different pole-pair combinations for a small-scale prototype have been studied to achieve the highest power and efficiency within a fixed stator frame size. Moreover, sixteen nested-loop rotor constructions for that prototype have been compared to derive the guidelines for a better rotor design in Chapter 6. Moreover, skewing the rotor slots is proposed to reduce the torque ripple and the total harmonic distortion (THD) of the stator voltages in Chapter 4 and 5. In this chapter, all the design guidelines derived from the previous chapters will be applied to a 3.2MW brushless

DFIM.

A complete cost-effective design needs to take into account not only the machine configurations (e.g. the pole-pair combinations of stator windings, the number of loops per nest, the distribution of loops, the skewed slots, etc.), but also the other components of the whole drive-train (e.g. the gearboxes, the PE converters, the mechanical support, etc.). Furthermore, it is also good to consider the cost-effective design within its whole operating range rather than only at the nominal operating point. However, it is not possible to cover all the design considerations of a 3.2MW brushless DFIM in one chapter. The aim of this chapter is to bring all the modeling methods and the design guidelines together to improve the design of a 3.2MW brushless DFIM. In this chapter, the improvement is defined in terms of the active material cost and the efficiency of the generator at nominal operating point. Therefore, according to this definition, an improved design means a design with lower active material cost, but higher efficiency.

This chapter starts with an introduction of the case study brushless DFIM. The selection of the stator pole-pair combinations and the design of nested-loop rotors are discussed based on the previous work. Next, the FE based multi-objective optimization for the 3.2MW brushless DFIM is illustrated. The detailed machine performance of the initial design and the optimized design is compared by performing 2D transient FE models. Subsequently, the 2D multi-slice FE model is performed for the optimized design to show the advantages by skewing the rotor slots over one stator slot pitch. Finally, conclusions are drawn.

9.2 Discussion on the initial design

In the Windrive project, the University of Cambridge has proposed a draft design for a 3.2MW brushless DFIM based on their design experience on 20kW [116] and 250kW [69] prototypes. Table 9.1 gives the specifications of the initial design. The initial design has been studied and analyzed in some of the previous chapters as a case study machine. The improved design in this chapter does not start from zero. It is an improved design based on the case study brushless DFIM. The pole-pair combination of the initial design is good based on our previous investigation while the nested-loop configuration can be slightly improved. The detailed explanations are as follows.

9.2.1 Stator pole-pair combinations

An optimization has been performed to study different pole-pair combinations for a small-scale prototype in Chapter 3. The pole-pair combination $p_p = 2, p_c = 3$ leads to the best performance in terms of efficiency and average torque for the small-scale prototype. Considering the magnetic coupling of space-harmonics apart from the fundamental components, less coupling between the stator and the rotor helps to reduce the torque ripple and increase the output power quality. Fig. 9.1 shows the normalized effective turns of the winding distribution space-harmonics. The detailed calculation of the winding effective turns can be found in Chapter 7. Fig. 9.1 indicates that

Table 9.1 Specifications of the case study brushless DFIM

Construction parameters		
Number of phases	N_{ph}	3
Number of pole-pairs	p_p, p_c	4, 6
Number of stator slots	N_{ss}	72
Stator slot fill factor		0.6
Number of rotor nests	N_{nest}	10
Number of loops per nest	q_r	4
Number of rotor slots	N_{rs}	80
Loop-span of individual loop [degree]		[7 5 3 1] × 36/8
Geometric parameters		
Axial length [m]	l_{stk}	1.60
Air-gap length [mm]	l_g	1.5
Stator outer radius [m]	r_{so}	0.83
Stator inner radius [m]	r_{si}	0.67
Rotor inner radius [m]	r_{ri}	0.58
Ratio stator (rotor) slot height / stator (rotor) height	$\alpha_{s,y}(\alpha_{r,y})$	0.5
Ratio stator (rotor) slot width / maximum possible slot width	$\alpha_{s,sw}(\alpha_{r,sw})$	0.5
Ratio stator (rotor) slot opening / slot width	$\alpha_{s,so}(\alpha_{r,so})$	0.3
Ratio stator slot heights for PW / CW	$\alpha_{s,pc}$	1
Stator (rotor) tooth tip height		1/16×tooth height
Operating specifications		
Nominal mechanical speed [Hz]	f_m	6
Rated power @ nominal speed [MW]	P	3.2
Power winding frequency [Hz]	f_p	50
Control winding frequency [Hz]	f_c	20 to -10
Slot current density [A/mm^2]	J	4

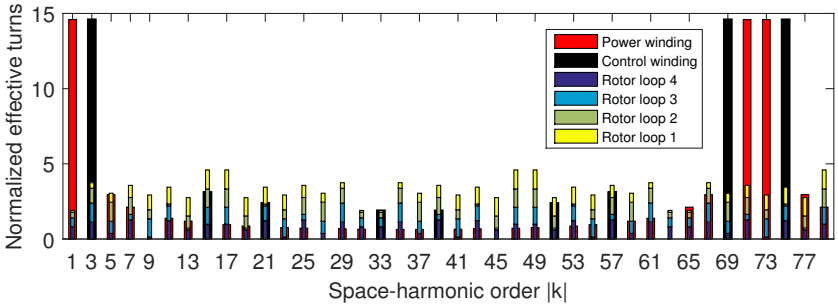

(a) $p_p = 1, p_c = 3$

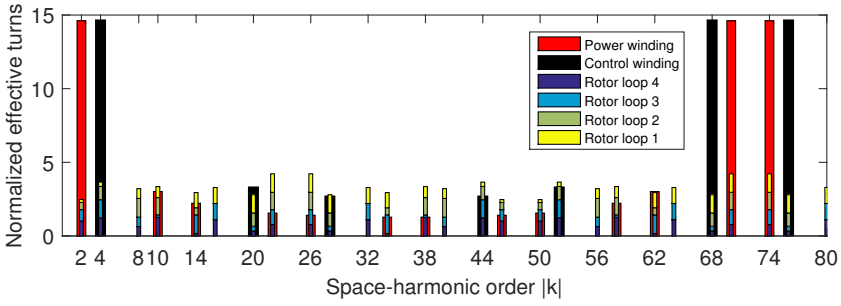

(b) $p_p = 2, p_c = 4$

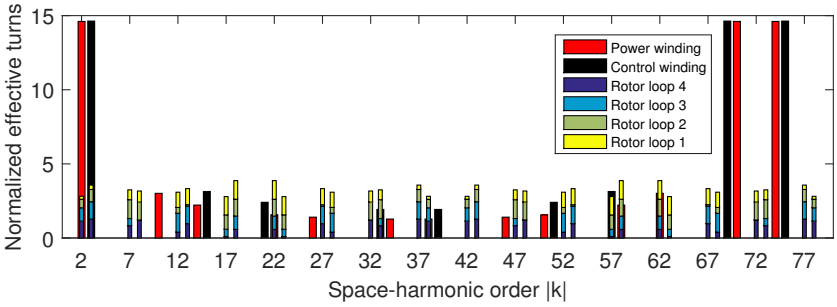

(c) $p_p = 2, p_c = 3$

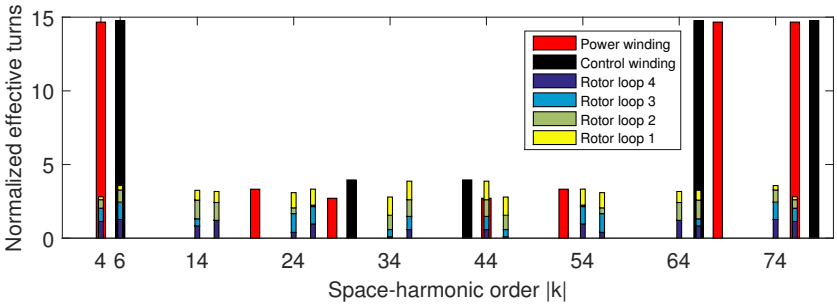

(d) $p_p = 4, p_c = 6$

Figure 9.1 Normalized winding effective turns

the pole-pair combination of $p_p = 2, p_c = 3$ leads to less coupling of the higher space-harmonics compared with the combination of $p_p = 1, p_c = 3$ and $p_p = 2, p_c = 4$. However, the combination of $p_p = 2, p_c = 3$ leads to the concern of unbalanced magnetic pull (UMP) which may be harmful to a large-scale wind generator [140]. Therefore, the pole-pair combination of $p_p = 4, p_c = 6$ is selected for the 3.2MW brushless DFIM. This combination results in less coupling between higher space-harmonics shown in Fig. 9.1(d) like the combination of $p_p = 2, p_c = 3$. This combination is consistent with the initial case study machine.

9.2.2 Nested-loop constructions

The previous study has indicated that making the loop span as big as possible and leaving out the loop with a small loop span lead to a better nested-loop rotor in Chapter 6. It can increase the average torque and the efficiency. Moreover, it can reduce the torque ripple and the total harmonic distortion (THD) of the stator voltages. Fig. 9.2(a) and (b) show the initial design and the improved design of the nested-loop rotor, respectively. The number of loops per nest is kept as four. These four loops are distributed evenly in the initial design. However, in the optimization, these four loops are actually the outer four loops of five evenly distributed loops while the most inner loop is left out.

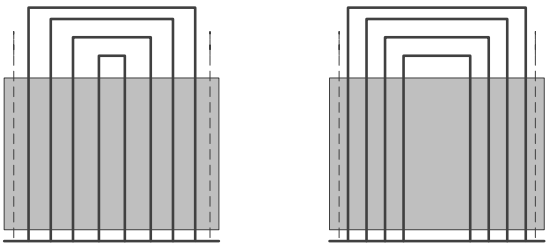

(a) Case study design **(b)** Improved design

Figure 9.2 Nested-loop rotor construction

9.3 FE based multi-objective optimization

9.3.1 Optimization procedure

The FE based multi-objective optimization follows the procedure shown in Fig. 9.3. Based on the input parameters, the machine geometry is built using a geometric model developed in MATLAB. Using a MATLAB - COMSOL interface, the machine geometry is loaded to the computationally efficient model given in Chapter 3. The machine performance can be then evaluated. The NSGA-II (non-dominated sorting genetic algorithm II) is applied to determine a Pareto optimal front of machine designs.

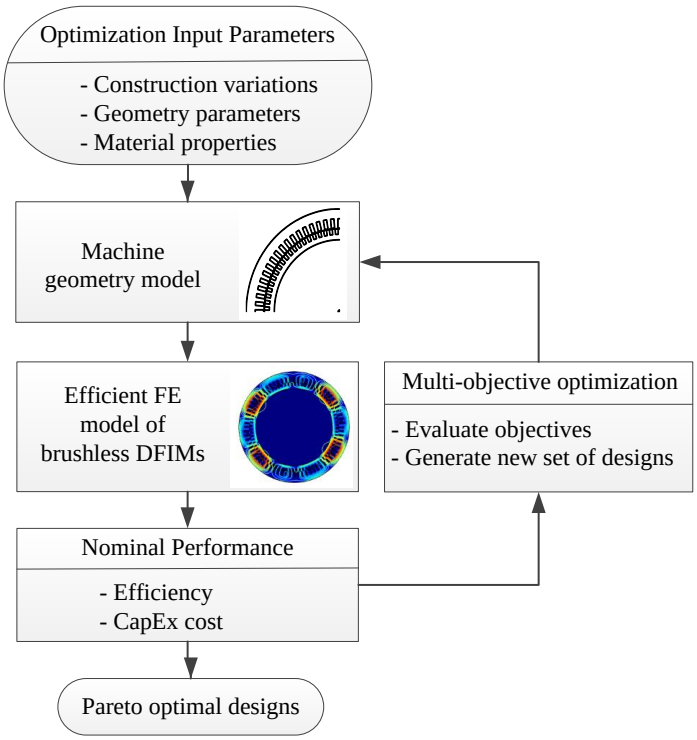

Figure 9.3 Optimization procedure of a brushless DFIM

9.3.2 Fixed specifications of the optimization

Table 9.2 provides an overview of the fixed specifications based on the case study machine.

Table 9.2 Fixed specifications of the brushless DFIM optimized

Construction parameters		
Number of phases	N_{ph}	3
Number of pole-pairs	p_p, p_c	4, 6
Number of stator slots	N_{ss}	72
Stator slot fill factor		0.6
Number of rotor nests	N_{nest}	10
Number of loops per nest	q_r	4
Number of rotor slots	N_{rs}	80
Loop-span of individual loop [degree]		[9 7 5 3] × 36/10
Geometric parameters		
Air-gap length [mm]	l_g	1.5
Stator outer radius [m]	r_{so}	0.83
Stator/rotor tooth tip height		1/16×tooth height
Operating specifications		
Nominal mechanical speed [Hz]	f_m	6
Rated power @ nominal speed [MW]	P	3.2
Power winding frequency [Hz]	f_p	50
Control winding frequency @ nominal speed [Hz]	f_c	-10
Slot current density [A/mm^2]	J	4
Material cost [141]		
Cost-price of copper [€/kg]	C_{Cu}	15
Cost-price of steel [€/kg]	C_{Fe}	3
Cost-price of aluminium [€/kg]	C_{Al}	5

9.3.3 Optimization objectives and variables

Table 9.3 gives the optimization variables and constraints. The vector of the optimization varibales id defined as:

$$\mathbf{V} = (r_{si}, r_{ri}, \alpha_{s,y}, \alpha_{s,sw}, \alpha_{s,so}, \alpha_{s,pc}, \alpha_{r,y}, \alpha_{r,sw}, \alpha_{r,so}). \tag{9.1}$$

The efficient FE model predicts the torque generated per unit length T (N·m/m) based on the fixed specifications and the variables $\mathbf{V}$. Then the machine axial length l_{stk} can be calculated as:

$$l_{stk} = \frac{P_{gen}}{2\pi f_m T}, \tag{9.2}$$

where p_{gen} is 3.2MW. The objectives are to optimize both the material cost of the brushless DFIM and the efficiency. The machine is optimized at its nominal operating point where the maximum torque is produced. The maximum torque is generated at the load-angle of ninty degree (electrical angle) [42]. The objective functions of this study are:

$$OF_1 = -C(\mathbf{V}, l_{stk}), \tag{9.3}$$

$$OF_2 = -\eta(\mathbf{V}, l_{stk}), \tag{9.4}$$

where C is the active material cost of the generator, η is the efficiency calculated by:

$$\eta = \frac{P_{gen}}{P_{gen} + P^s_{Core} + P^r_{Core} + P^s_{Cu} + P^r_{Cu}}, \tag{9.5}$$

where P^s_{Core} and P^r_{Core} are the stator and rotor core losses, P^s_{Cu} and P^r_{Cu} are the stator and rotor copper losses, respectively. The detailed calculation of the power and the losses can be found in Chapter 3. Table 9.4 gives an overview of the optimization setting.

Table 9.3 Geometric variables and constraints

Geometric variables			
	V	min	max
Stator inner radius [m]	r_{si}	$0.1 \cdot r_{so}$	$0.9 \cdot r_{so}$
Rotor inner radius [m]	r_{ri}	$0.1 \cdot r_{si}$	$0.9 \cdot r_{si}$
Ratio between stator slot height and stator height	$\alpha_{s,y}$	0.2	0.8
Ratio between stator slot width and maximum possible slot width	$\alpha_{s,sw}$	0.2	0.8
Ratio between stator slot opening and stator slot width	$\alpha_{s,so}$	0.2	0.8
Ratio between stator slot heights for PW and CW	$\alpha_{s,pc}$	0.25	4
Ratio between rotor slot height and rotor height	$\alpha_{r,y}$	0.2	0.8
Ratio between rotor slot width and maximum possible slot width	$\alpha_{r,sw}$	0.2	0.8
Ratio between rotor slot opening and rotor slot width	$\alpha_{r,so}$	0.2	0.8
Optimization constraints			
Stator tooth height ≤ 5· stator tooth width			
Rotor tooth height ≤ 5· rotor tooth width			
Axial length ≤ 4m			

Table 9.4 Optimization setting

Method		NSGA-II
Number of objectives	OF	2
Number of variables	**V**	9
Number of constraints		3
Number of population size	N	40
Number of generations	Gen	50
Calculation time for single generation		≈65min

9.3.4 Optimization results

The resulting Pareto optimal front is presented in Fig. 9.4. This figure displays the trade-off between the active material cost and the efficiency. It indicates that a more expensive design (a larger machine) will have a higher efficiency, which agrees with the general expectation. The initial design is also shown in Fig. 9.4. It clearly shows that the initial design is not optimal. The machine efficiency can be improved without increasing the material cost of the machine. A single optimized design is selected and will be used for the detailed comparison in the next section. The selected design is marked by the purple star in Fig. 9.4. At this power level, the efficiency of the DFIG and the PM generator approximaly achieves 97% and 98%, respectively. The brushless DFIM does not show any advantage as expected from the efficiency point of view. The optimization results of the stator slot current density of $3A/mm^2$ is added to Fig. 9.4. The lower current density leads to a more expensive design (a larger machine). However, the result indicates that the efficiency seems hardly to be improved over 96%. One optimized design marked by the green triangle is selected for the detailed comparison in the next section.

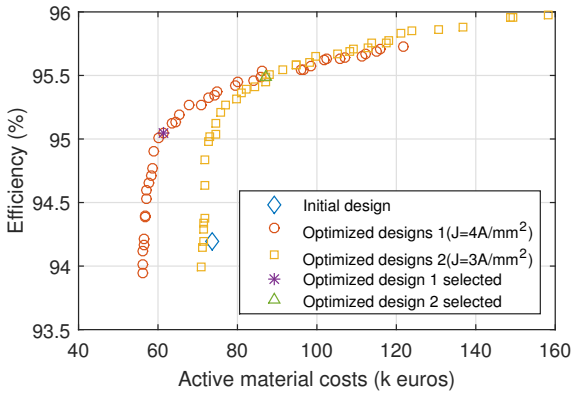

Figure 9.4 Optimization results of the 3.2MW brushless DFIM

9.4 Comparison and discussions

The magnetic loading in the brushless DFIM can be approximately defined as [61]:

$$B = \frac{2}{\pi}\sqrt{B_{p,max}^2 + B_{c,max}^2} \tag{9.6}$$

where $B_{p,max}$ and $B_{c,max}$ are the amplitudes of the flux densities of the p_p and p_c pole-pair fields, respectively. Fig. 9.5 shows the magnetic loading of the intial design and the optimized designs. It proves that the initial design is conservative. The magnetic loading is increased for a better design by using the FE based optimization tool.

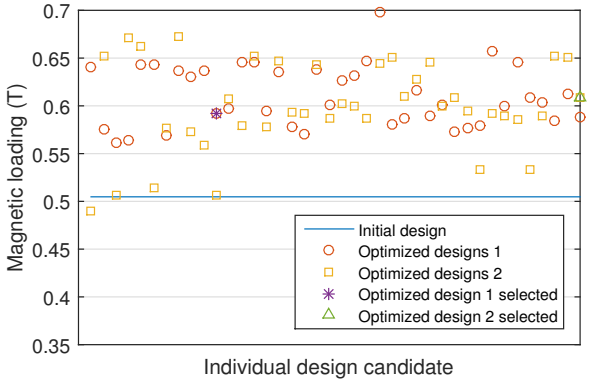

Figure 9.5 Magnetic loading

The geometric parameters of the selected optimized designs are given in Table 9.5. Fig. 9.6 shows the comparison of the geometry between the initial design and the optimized designs selected in Fig. 9.4. The 2D transient FE models are performed for the initial design and the optimized designs selected to accurately evaluate the detailed performance. The 2D multi-slice FE model is applied to evaluate the performance of the optimized designs if the rotor slots are skewed over one stator slot pitch.

Table 9.6 summaries the detailed performance and the active material cost of the initial design and the optimized designs. In the Pareto optimal front calculated by the computationally efficient model (shown in Fig. 9.4), the power and the efficiency of the optimized design 1 marked by the purple star are 3.2MW and 95.05%, respectively. The power and the efficiency are 3.25MW and 94.96% when the optimized design is evaluated using the full 2D transient FE model. Meanwhile, to the optimized design 2 marked by the green triangle, the power and the efficiency predicted by the efficient FE model are 3.2MW and 95.49%, respectively. The power and the efficiency are 3.19MW and 95.39% when it is evaluated by the transient FE model. This proves the accuracy of the computationally efficient model.

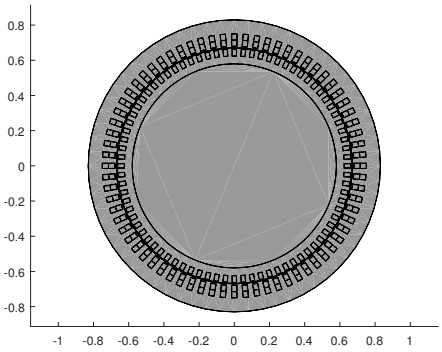

(a) Initial design

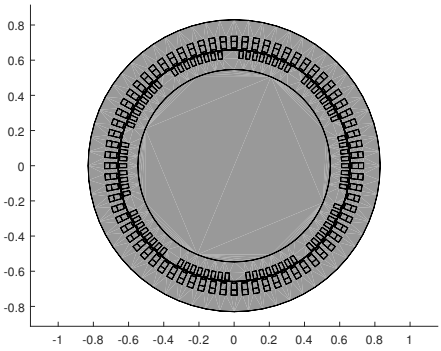

(b) Optimized design 1

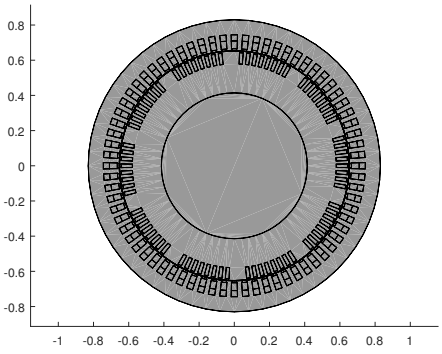

(c) Optimized design 2

Figure 9.6 Geometric comparison of the initial design and the selected optimized design

Table 9.5 Geometric parameters of the selected optimized design

Parameters		**Design 1**	**Design 2**
Axial length [m]	l_{stk}	1.208	1.3554
Stator inner radius [m]	r_{si}	0.659	0.654
Rotor inner radius [m]	r_{ri}	0.547	0.414
Ratio between stator slot height and stator height	$\alpha_{s,y}$	0.552	0.487
Ratio between stator slot width and maximum possible slot width	$\alpha_{s,sw}$	0.528	0.555
Ratio between stator slot opening and stator slot width	$\alpha_{s,so}$	0.616	0.739
Ratio between stator slot heights for PW and CW	$\alpha_{s,pc}$	0.766	0.783
Ratio between rotor slot height and rotor height	$\alpha_{r,y}$	0.576	0.693
Ratio between rotor slot width and maximum possible slot width	$\alpha_{r,sw}$	0.565	0.520
Ratio between rotor slot opening and rotor slot width	$\alpha_{r,so}$	0.581	0.769

Both optimized designs increase the efficiency. The design 1 reduces the active material cost while the design 2 increases the cost because the lower current density is applied. The optimized designs improve the shear stress compared with the initial design. However, the brushless DFIM does not show any advantage from the shear stress point of view compared with a PM generator. The shear stress of a PM generator leads to about 70kN/m^2 with the electric loading of 100kA/m. However, the initial and the optimized designs result in a high electric loading which would be a challenge to the cooling. This needs to be taken care in the further investigation.

The torque ripple of the optimized designs is much lower than that of the initial design which helps to reduce the noise and the vibrations of the brushless DFIM. Moreover, the THD of the stator voltages of the optimized designs is also lower than that of the initial design which leads to a better power quality. According to Table 9.6, the torque ripple and the THD level can be further reduced by skewing the rotor slots of the optimized design over one stator slot pitch. The material costs of the optimized design with a skewed rotor are almost the same as the optimized design in which the rotor is not skewed. However, the manufacturing costs is higher to build a skewed rotor. Moreover, a lower average power can be expected by applying skewed slots. The efficiency of the optimized design with a skewed rotor is almost the same as (or slightly higher than) that of the optimized design with a non-skewed rotor. In fact, it is not the real case since the additional core losses caused by the axial flux due to the skewed rotor bars are not taken into account in the 2D multi-slice FE model. Therefore, it can be expected that the efficiency will be reduced after skewing the rotor slots.

Table 9.6 Comparison of the initial design and the optimized designs

	Initial design	**Design 1**	**Design 1 with skew**	**Design 2**	**Design 2 with skew**
Average Torque [kN·m]	85.92	86.15	85.17	85.75	84.16
Power [MW]	3.24	3.25	3.21	3.19	3.17
Torque ripple [%]	32.06	14.05	7.04	15.78	8.34
THD of PW voltage [%]	30.42	19.02	17.05	15.69	13.79
THD of CW voltage [%]	152.59	87.75	77.80	69.66	58.91
Stator core losses [kW]	67.25	60.76	60.31	68.36	68.33
Rotor core losses [kW]	19.15	18.08	17.85	17.06	17.24
Stator copper losses [kW]	79.56	66.84	66.84	50.65	50.65
Rotor copper losses [kW]	33.84	26.55	24.16	18.42	15.97
Efficiency [%]	94.19	94.96	95.00	95.39	95.42
Steel cost [k€]	29.91	25.45	-	38.10	-
Copper cost [k€]	41.24	23.34	-	47.23	-
Aluminium cost [k€]	1.71	1.28	-	1.95	-
Total cost [k€]	72.85	61.38	-	87.28	-
Shear stress [kN/m^2]	19.09	26.25	25.93	23.59	23.44
Electric loading [kA/m]	95.89	119.75	119.75	85.68	85.68

9.5 Conclusion

This chapter shows the usefulness of the modeling methods and design guidelines which have been presented in the previous chapters. All of the modeling methods and design guidelines are brought together in this chapter to optimize the design of a 3.2MW brushless DFIM. It is not a new design, but an improved design based on the case study machine initially designed by using the analytical model. The selection of the pole-pair number and nested-loop rotor construction are briefly discussed. The combination of $p_p = 4, p_c = 6$ is selected. The rotor construction is designed to have a big loop span while the inner most loop is left out. Some geometric parameters of the initial design are then optimized using the FE based multi-objective optimization tool presented in Chapter 3. This tool optimizes both the active material cost and the efficiency of the brushless DFIM. The resulting Pareto optimal front indicates that the initial design is not optimal. The magnetic loading is increased for a better design by using the FE based optimization tool. Two individual optimized designs are selected for detailed comparison. Both optimized designs increase the efficiency and the shear stress while reducing the torque ripple and the THD level of the stator voltages. The torque ripple and the THD level can be further reduced by skewing the rotor slots of the improved designs over one stator slot pitch, although this may lead to a lower average power, higher core losses and additional manufacturing costs. The additional core losses due to the axial flux cannot be estimated by the 2D multi-slice FE model, which could be investigated in the future. However, the optimized designs result in a high electric loading which would be a challenge for cooling. Moreover, the results indicate that the brushless DFIM does not show advantages compared with normal DFIGs and PM generators from the efficiency and the shear stress points of view.

CHAPTER 10

Conclusions and Recommendations

The rapid increase of wind power in the power grid results in high grid connection requirements for wind turbines. Moreover, the reliability of wind turbines becomes more and more important, especially in offshore applications. One potential solution for these demands is the wind turbine drive-train based on the brushless doubly-fed induction machine (DFIM). This machine type has no brushes or slip-rings on the rotor side which provides an attractive alternative to the DFIM which is commonly employed in the current market. However, the brushless DFIM has not yet been commercialized. Therefore, the primary objective of this thesis focuses on 'modeling and design of brushless DFIM, to advance the development of this machine type for wind turbine applications'. Several aspects of modeling and design related to the brushless DFIM have been discussed in this thesis. The related conclusions are as follows.

Computationally efficient 2D FE model
The 2D FE model has advantages of taking the detailed geometric constructions and the saturation into account accurately without additional efforts on the modeling techniques. However, the transient FE model is rather time-consuming which makes it difficult to be combined with some optimization algorithms. A computationally efficient FE model is proposed to evaluate the average torque, losses and efficiency of the brushless DFIM. The calculation is based on the magneto-static FE solutions in which the induced rotor currents are calculated using the space-time relationship of the magnetic field in the rotor reference. One candidate design is evaluated within one to two minutes on a personal workstation. In general, the performance prediction of any electrical machine using FE simulation can be accelerated by considering the symmetry of the magnetic circuit and the periodicity of the electromagnetic field.

An efficient, flexible and accurate optimization approach is then developed by combining the computationally efficient FE model with the NSGA-II multi-objective optimization algorithm. The influence of the pole-pair combination and the number of loops per nest are briefly studied by using the developed approach. The results show that $p_p = 2, p_c = 3$ is a good pole-pair combination although it might suffer from the problem of unbalanced magnetic pull (UMP) in large scale wind generators. This also leads to a first impression that the case study machine

designed by University of Cambridge seems to have a good pole-pair combination of $p_p = 4, p_c = 6$. Moreover, the number of loops per nest has little influence on the average torque and the efficiency.

Analysis of the effects of skew using 2D multi-slice FE model
The brushless DFIM is expected to have more severe noise, vibrations and lower power quality compared with normal induction machines. This is because many undesired space-harmonics exist since the special rotor is designed to couple both stator windings. The 2D multi-slice FE model is applied to investigate whether skewing rotor slots is useful to overcome these drawbacks of brushless DFIMs. Slices with Gauss distribution are used to reduce the number of slices needed, as well as the computing time. The results indicate that skewing the rotor slots reduces the torque ripple significantly. However, skewing the rotor slots slightly reduces the time-harmonics in the stator voltages if the stator pole-pair combination is already good. Similarly to the normal induction machines, skewing a rotor slot over one stator slot pitch is a good choice in brushless DFIMs. However, the above benefits are at the expense of a slightly lower average torque, a lower efficiency and additional manufacturing costs.

FE post-processing for skew effects
Based on the study of the space- and time-harmonics in brushless DFIMs, a computationally efficient method is proposed to investigate the effects of skew at the initial design stage. The 2D-FFT is applied to the original magnetic field obtained from the 2D transient FE model. The well-known skew factors are appropriately applied to each component according to its space- and time-harmonic orders. The electromagnetic torque can be calculated using an effective magnetic field in which the effects of skew have been approximately considered. Therefore, the effects of skew on the electromagnetic torque at different skew angles can be predicted while the heavy FE computation does not need to be repeated. The results indicate that skewing the rotor slots over one stator slot pitch is a good choice to minimize the torque ripple in brushless DFIMs, which is consistent with the above conclusion. The method proposed and the 2D multi-slice FE model are validated with each other.

Comparison of nested-loop rotors
The rotor design is critical in brushless DFIMs because it is the key point to achieving cross-coupling between the two stator windings. To a certain extent, the quality of the rotor design determines the performance of the brushless DFIM. A nested-loop rotor is preferred over the reluctance rotor and the wound rotor, because it has the advantages of ruggedness, a lower impedance and a higher slot fill factor. To gain more design guidelines for nested-loop rotors, sixteen constructions are evaluated from four criteria. They are the torque load-angle characteristic, the torque ripple, the efficiency and the total harmonic distortion (THD) of the stator voltages. The number of loops per nest and their positions have a systematical influence on the torque load-angle characteristic and the efficiency, but do not have such a systematical effect on the torque ripple and the THD of the stator voltages. The contribution to the average torque made by an individual loop mostly depends on its loop span. Making the loop span bigger and leaving out the loop with a small loop span improves the torque load-angle characteristics and the efficiency, and reduces the THD level of the stator voltages.

Experimental study on a small-scale prototype
The brushless DFIM operates in synchronous mode for wind turbine applications. However, it is more straightforward to perform the simple induction mode for the experimental study. The complicated space- and time-harmonics, the influence of the rotor skew and the influence of the nested-loop configurations are studied and validated by carrying out measurements on a small-scale prototype with four different rotors. However, during the manufacturing processing, the insulation between the rotor bars and the iron core is damaged. The damage of the insulation results in the inter-bar currents in the rotor. The results indicate that the inter-bar currents have a significant influence on the amplitude and the distribution of the rotor magnetic field. The orders of the space- and time-harmonics predicted analytically are validated by the FE results and the measurements. However, the 2D FE model does not give an accurate prediction of the amplitude of the space- and time-harmonics compared with the measurement. This is because the inter-bar currents are not considered in the 2D FE model. The results show that skewing rotor slots over one stator slot pitch reduces the harmonic distortions of the stator voltages. Moreover, the results indicate that the nested-loop rotor with large loop span leads to a better cross-coupling between the two stator windings. The 2D FE model and the 2D multi-slice FE model can only be partially validated in the experimental study.

Analysis of axial flux using 3D magneto-static FE model
The 3D magneto-static FE model is applied to investigate the axial flux due to the skewed slots which is neglected in the 2D multi-slice FE model. Two iterative solvers, namely the Conjugate Gradients (CG) method and the Generalized Minimum Residual (GMRES) method, with Geometric multigrid preconditioning are applied to deal with this 3D FE model with millions of degrees of freedom (DoF). Both iterative solvers reduce the memory required significantly. The CG solver is better than the GMRES solver in this particular study from the memory required and the computing time points of view. The results indicate that the axial flux due to the skewed slots has little influence on the electromagnetic torque. It proves that the 2D multi-slice FE model is sufficient to capture the effects of skew on the torque.

Improved design for a 3.2MW brushless DFIM
All the modeling methods and the design guidelines are brought together to optimize the design of a 3.2MW brushless DFIM. It is not a new design starting from nothing. It is an optimized design based on a case study machine. The analysis in this thesis proves that the stator pole-pair combination of $p_p = 4, p_c = 6$ in the case study machine is a good choice compared with the combination of ($p_p = 1, p_c = 3$), ($p_p = 2, p_c = 3$) and ($p_p = 2, p_c = 4$). The number of loops per nest remains as four as with the case study machine. However, the loop span of each loop is increased. The case study machine is then optimized to minimize the active material cost and maximize the efficient of the machine in the cases with two stator slot current density (4 and 3A/mm^2). The results indicate that the magnetic loading is increased for a better design by using the FE based multi-objective optimization tool developed in this thesis. Two individual optimized designs are selected from the Pareto optimal front for detailed comparison. Both optimized designs increase the efficiency and the shear stress, and reduce the torque ripple and the THD level of the stator voltages. However, the optimized designs have a high electric loading which would be a challenge for cooling. The torque ripple and the THD level can be further reduced by skewing the rotor slots

over one stator slot pitch.

As a summary, the following conclusions are drawn for the modeling and design of the brushless DFIMs. The two stator magnetic fields in the brushless DFIMs are added at some positions and subtracted from some other positions. This special feature results in local saturation in the brushless DFIMs. It is reasonable to expect that the brushless DFIMs designed by normal analytical models are too conservative from the magnetic loading point of view. This thesis designs the brushless DFIMs by using FE models in which the local saturation is captured accurately. The results show that the design is improved from the active material cost and the efficiency of the machine points of view by increasing the magnetic loading of the brushless DFIMs. The efficiency of the 3.2MW brushless DFIM achieves around 95% to 95.5%. The efficiency seems hardly to be improved over 96% even if a larger machine with a lower stator slot current density (3A/mm^2) is used. At this power level, the efficiency of the doubly-fed induction generator (DFIG) and the permanent magnet (PM) generator approximately achieves 97% and 98%, respectively. The brushless DFIM does not show advantages from the efficiency point of view. For the shear stress, a PM generator leads to about 70kN/m^2 with an electric loading of 100kA/m. The shear stress of the optimized design is approximately three times smaller than the PM generator, although the shear stress has been improved compared with the initial design. The brushless DIFM also does not show advantages from the shear stress point of view. However, considering the additional advantages of maintenance and reliability, the brushless DFIMs may provide a feasible application for wind turbine drive-trains.

Contributions

The scientific contributions of this thesis can be summarized as follows:

- A computationally efficient 2D FE model has been developed for the brushless DFIM. By combining the efficient model with some optimization algorithms, it constitutes a fast, flexible and accurate design tool for the brushless DFIM. The multi-objective optimization tool combining the efficient FE model proposed and a generic algorithm (NSGA-II in this thesis) has been demonstrated to achieve an improved design for a 3.2MW brushless DFIM.

- The detailed effects of skew in the brushless DFIM have been investigated using the 2D multi-slice FE model. The optimized skew angle for minimizing the torque ripple is found. It proves that skewing the rotor slots over one stator slot pitch is an optimized choice which is consistent with the case in normal induction machines.

- A computationally efficient semi-numerical method has been developed to evaluate the effects of skew on the electromagnetic torque. The proposed method makes use of normal 2D FE results and applies the skew factors in the post-processing. The appropriate way to apply the skew factors is elaborated based on the analytical derivation of space- and time-harmonics.

- Some design guidelines for a better nested-loop rotor are derived based on the detailed comparison of sixteen nested-loop constructions. Making the loop span bigger and leaving out the loop with a small loop span increase the average torque and the efficiency. Moreover, this reduces the torque ripple and leads to a relatively low THD level of the stator voltages.
- A 3D magneto-static FE model using iterative solvers (CG and GMRES) with Geometric multigrid preconditioning has been implemented to investigate the axial flux due to the skewed slots. It proves that the 2D multi-slice model is sufficient to capture the effects of skew on the electromagnetic torque.
- The analysis of space- and time-harmonics and the influence of rotor configurations have been investigated by carrying out measurements on a small-scale prototype. It shows that the insulation between the rotor bar and the iron core is critical in brushless DFIMs. The experimental study also proves that skewing rotor slots reduces the THD level of the stator voltages (and/or currents). Moreover, the rotor with a larger loop span results in a better cross-coupling between the fundamental components of the stator magnetic fields.

Recommendations for future research

Although the modeling methods and the design guidelines proposed in this thesis have been successfully used to achieve an improved design for the brushless DFIM, further improvements are possible. The following recommendations are presented for further research studies:

- The optimized design of the 3.2MW brushless DFIM does not show advantages from the efficiency and the shear stress points of view compared with DFIGs and PM generators. This can be more or less expected in advance. However, it is not fair to the brushless DFIM if its advantages (e.g. higher reliability and better low voltage ride-through capability) are not evaluated quantitatively. Therefore, it makes sense to provide a more comprehensive evaluation of the brushless DFIM. This evaluation should include not only the capital cost but also the operating expenditure during the whole life-cycle. The energy yield is not estimated only at the rated condition but through the whole operating range. The downtime should also be taken into account in the calculation of the total energy yield. Moreover, the thermal model would be interesting to studied together with the electromagnetic model.
- This thesis only investigates the nested-loop rotors. However, it would be interesting to make a quantitative comparison between the nested-loop rotor constructions and the other rotor constructions (e.g. reluctance rotors and wound rotors) in terms of performance and manufacturing costs. Moreover, the FE based optimization tool developed in this thesis can ba applied to the other rotor constructions to study the upper limits of the efficiency and the shear stress.
- The insulation between the rotor bars and the iron core is damaged in the prototype. Therefore, it makes sense to confirm the conclusions derived in this thesis by carrying out measurements on well manufactured rotors.

- The additional core losses caused by the axial flux due to the skewed rotor slots are not taken into account in the 2D multi-slice FE model. However, it is really interesting to know how much the core losses will increase and the efficiency will decrease after skewing the rotor slots. This will be useful to determine whether skewing slots is cost-effective since this needs additional manufacturing costs.
- The end-part construction of the nested-loop rotor is not investigated in this thesis. It would be interesting to look into the influence of the end-part of the nested-loop rotor using the 3D magneto-static FE model developed in this thesis. Some guidelines can be derived for a better design of the end-part in the nested-loop rotor.

Bibliography

[1] "World energy resources," World Energy Council, Tech. Rep., 2013.

[2] "Global wind report - annual market update," Global Wind Energy Council, Tech. Rep., 2015.

[3] "Technology roadmap wind energy," International Energy Agency, Tech. Rep., 2013.

[4] "Global wind report - annual market update," Global Wind Energy Council, Tech. Rep., 2006.

[5] "Global wind report - annual market update," Global Wind Energy Council, Tech. Rep., 2007.

[6] "Global wind report - annual market update," Global Wind Energy Council, Tech. Rep., 2008.

[7] "Global wind report - annual market update," Global Wind Energy Council, Tech. Rep., 2009.

[8] "Global wind report - annual market update," Global Wind Energy Council, Tech. Rep., 2010.

[9] "Global wind report - annual market update," Global Wind Energy Council, Tech. Rep., 2011.

[10] "Global wind report - annual market update," Global Wind Energy Council, Tech. Rep., 2012.

[11] "Global wind report - annual market update," Global Wind Energy Council, Tech. Rep., 2013.

[12] "Global wind report - annual market update," Global Wind Energy Council, Tech. Rep., 2014.

[13] "Renewable energy technologies: cost analysis series," International Renewable Energy Agency, Tech. Rep., Jun. 2012.

[14] H. Polinder, J. A. Ferreira, B. B. Jensen, A. B. Abrahamsen, K. Atallah, and R. A. McMahon, "Trends in wind turbine generator systems," *Emerging and Selected Topics in Power Electronics, IEEE Journal of*, vol. 1, no. 3, pp. 174–185, Sept. 2013.

[15] U. Shipurkar, K. Ma, H. Polinder, F. Blaabjerg, and J. A. Ferreira, "A review of failure mechanisms in wind turbine generator systems," in *17the European Conference on Power Electronics and Applications (EPE'15 ECCE-Europe)*, Geneva, Switzerland, Sept. 2015.

[16] H. Li and Z. Chen, "Overview of different wind generator systems and their comparisons," *IET Renewable Power Generation*, vol. 2, no. 2, pp. 123–138, 2008.

[17] H. Polinder, "Overview of and trends in wind turbine generator systems," in *Power and Energy Society General Meeting, 2011 IEEE*, Jul. 2011, pp. 1–8.

[18] G. Bywaters, V. John, J. Lynch, P. Mattila, G. Norton, and J. Stowell, "Northern power systems WindPACT drive train alternative design study report," National Renewable Energy Laboratory, Tech. Rep., Oct. 2004.

[19] "IEA wind 2014 annual report," International Energy Agency, Tech. Rep., Aug. 2015.

[20] D.-j. Bang, "Design of transverse flux permanent magnet machines for large direct-drive wind turbines," Ph.D. dissertation, Delft University of Technology, 2010.

[21] T. Long, S. Shao, E. Abdi, R. A. McMahon, and S. Liu, "Asymmetrical low-voltage ride through of brushless doubly fed induction generators for the wind power generation," *IEEE Transactions on Energy Conversion*, vol. 28, no. 3, pp. 502–511, 2013.

[22] U. Shipurkar, T. D. Strous, H. Polinder, and J. A. Ferreira, "LVRT performance of brushless doubly fed induction machines - a comparison," in *2015 IEEE International Electric Machines & Drives Conference (IEMDC)*, Coeur d'Alene, USA, May 2015, pp. 362–368.

[23] A. R. W. Broadway and L. Burbridge, "Self-cascaded machine: a low-speed motor or high frequency brushless alternator," in *Proceedings, Institution of Electrical Engineers*, vol. 117, 1970.

[24] P. C. Roberts, "A study of brushless doubly-fed (induction) machines," Ph.D. dissertation, Cambridge University, 2005.

[25] S. Abdi, E. Abdi, A. Oraee, and A. McMahon, "Investigation of magnetic wedge effects in large-scale BDFMs," in *Renewable Power Generation Conference (RPG 2013), 2nd IET*, Sept. 2013, pp. 1–4.

[26] L. Xu and F. Wang, "Comparative study of magnetic coupling for a doubly fed brushless machine with reluctance and cage rotors," in *Industry Applications Conference, 1997. Thirty-Second IAS Annual Meeting, IAS '97., Conference Record of the 1997 IEEE*, vol. 1, Oct. 1997, pp. 326–332.

[27] F. Wang, F. Zhang, and L. Xu, "Parameter and performance comparison of doubly fed brushless machine with cage and reluctance rotors," *IEEE Transactions on Industry Applications*, vol. 38, no. 5, pp. 1237–1243, Sept./Oct. 2002.

[28] A. M. Knight, R. E. Betz, W. K. Song, and D. G. Dorrell, "Brushless doubly-fed reluctance machine rotor design," in *2012 IEEE Energy Conversion Congress and Exposition (ECCE)*, Sept. 2012, pp. 2308–2315.

[29] A. M. Knight, R. E. Betz, and D. G. Dorrell, "Design and analysis of brushless doubly fed reluctance machines," *IEEE Transactions on Industry Applications*, vol. 49, no. 1, pp. 50–58, Jan./Feb. 2013.

[30] H. Liu and L. Xu, "Design and performance analysis of a doubly excited brushless machine for wind power generator application," in *The 2nd International Symposium on Power Electronics for Distributed Generation Systems*, Hefei, China, Jun. 2010, pp. 579–601.

[31] S. Kunte, M. P. Bhawalkar, N. Gopalakrishnan, and Y. P. Nerkar, "Design and analysis of brushless doubly fed reluctance machine suitable for wind generation applications," in *Electrical Machines and Systems (ICEMS), 2015 18th International Conference on*, Pattaya City, Thailand, Oct. 2015, pp. 2082–2088.

[32] R. McMahon, P. Tavner, E. Abdi, P. Malliband, and D. Barker, "Characterising rotors for brushless doubly-fed machines (BDFM)," in *Electrical Machines (ICEM), 2010 XIX International Conference on*, Roma, Italy, Sept. 2010, pp. 1–6.

[33] ——, "Characterising brushless doubly fed machine rotors," *IET Electric Power Applications*, vol. 7, no. 7, pp. 535–543, 2013.

[34] Y. Guo, X. Wang, J. G. Zhu, and H. Lu, "Development of a wound rotor brushless doubly fed machine based on slot mmf harmonics," in *Industry Applications Society Annual Meeting, 2008. IAS '08. IEEE*, Oct. 2008, pp. 1–5.

[35] F. Xiong and X. Wang, "Development of a multi-pitch unequal-turn-coil wound rotor for the brushless doubly-fed generator," in *Electrical Machines and Systems (ICEMS), 2013 International Conference on*, Oct. 2013, pp. 668–671.

[36] ——, "Design of a low-harmonic-content wound rotor for the brushless doubly fed generator," *IEEE Transactions on Energy Conversion*, vol. 29, no. 1, pp. 158–168, Mar. 2014.

[37] ——, "Design and performance analysis of a brushless doubly-fed machine for stand-alone ship shaft generator systems," in *Electrical and Control Engineering (ICECE), 2011 International Conference on*, Sept. 2011, pp. 2114–2117.

[38] S. Williamson and M. S. Boger, "Impact of inter-bar currents on the performance of the brushless doubly fed motor," *IEEE Transactions on Industry Applications*, vol. 35, no. 2, pp. 453–460, Mar./Apr. 1999.

[39] B. Koch, R. Spee, and B. Clever, "A comparison of stack preparation methods for bar insulation in diecast rotors," in *Industry Applications Conference, 1997. Thirty-Second IAS Annual Meeting, IAS '97., Conference Record of the 1997 IEEE*, vol. 1, Oct. 1997, pp. 182–187.

[40] P. C. Robert, R. A. McMahon, P. J. Tavner, J. M. Maciejowski, T. J. Flack, and X. Wang, "Performance of rotors in a brushless doubly-fed induction machine (BDFM)," in *Electrical Machines (ICEM), 2004 International Conference on*, Cracow, Poland, 2004.

[41] P. J. Tavner, R. A. McMahon, P. C. Robert, E. Abdi-Jalebi, X. Wang, M. Jagiela, and T. Chick, "Rotor design & performance for a BDFM," in *Electrical Machines (ICEM), 2006 International Conference on*, Chania, Crete, Greece, 2006.

[42] T. D. Strous, X. Wang, H. Polinder, and J. A. Ferreira, "Brushless doubly-fed induction machines: magnetic field analysis," *IEEE Transactions on Magnetics*, vol. 52, no. 11, 2016.

[43] A. K. Wallace, R. Spee, and H. K. Lauw, "Dynamic modeling of brushless doubly-fed machines," in *Industry Applications Society Annual Meeting, 1989., Conference Record of the 1989 IEEE*, Oct. 1989, pp. 329–334 vol.1.

[44] R. Spee, A. K. Wallace, and H. K. Lauw, "Performance simulation of brushless doubly-fed adjustable speed drives," in *Industry Applications Society Annual Meeting, 1989., Conference Record of the 1989 IEEE*, Oct. 1989, pp. 738–743 vol.1.

[45] R. Li, A. Wallace, and R. Spee, "Dunamic simulation of brushless doubly-fed machines," *IEEE Transactions on Energy Conversion*, vol. 6, no. 3, pp. 445–452, Sept. 1991.

[46] R. Li, A. Wallace, R. Spee, and Y. Wang, "Two-axis model development of cage-rotor brushless doubly-fed machines," *IEEE Transactions on Energy Conversion*, vol. 6, no. 3, pp. 453–460, Sept. 1991.

[47] M. S. Boger, A. K. Wallace, R. Spee, and R. Li, "General pole number model of the brushless doubly-fed machine," *IEEE Transactions on Industry Applications*, vol. 31, no. 5, pp. 1022–1028, Sept./Oct. 1995.

[48] S. Williamson, A. C. Ferreira, and A. K. Wallace, "Generalised theory of the brushless doubly-fed machine. i. analysis," *IEE Proceedings - Electric Power Applications*, vol. 144, no. 2, pp. 111–122, Mar. 1997.

[49] S. Williamson and A. C. Ferreira, "Generalised theory of the brushless doubly-fed machine. 2. model verification and performance," *IEE Proceedings - Electric Power Applications*, vol. 144, no. 2, pp. 123–129, Mar. 1997.

[50] Z. Wu and O. Ojo, "Coupled-circuit-model simulation and airgap-field calculation of a dual-stator-winding induction machine," *Electric Power Applications, IEE Proceedings -*, vol. 153, no. 3, pp. 387–400, May 2006.

[51] R. Li, R. Spee, A. K. Wallace, and G. C. Alexander, "Synchronous drive performance of brushless doubly-fed motors," *IEEE Transactions on Industry Applications*, vol. 30, no. 4, pp. 963–970, Jul./Aug. 1994.

[52] P. C. Roberts, T. Long, R. A. Mcmahon, S. Shao, E. Abdi, and J. M. Maciejowski, "Dynamic modelling of the brushless doubly fed machine," *IET Electric Power Applications*, vol. 7, no. 7, pp. 544–556, 2013.

[53] M. N. Hashemnia and F. Tahami, "Dynamic modeling and simulation of brushless doubly fed induction machine in consideration of core loss," in *IECON 2012 - 38th Annual Conference on IEEE Industrial Electronics Society*, Montreal, QC, Canada, Oct. 2012, pp. 1753–1757.

[54] M. N. Hashemnia, F. Tahami, P. Tavner, and S. Tohidi, "Steady-state analysis and performance of a brushless doubly fed machine accounting for core loss," *IET Electric Power Applications*, vol. 7, no. 3, pp. 170–178, 2013.

[55] Y.-H. Chang, Y.-T. Li, I.-H. Lin, and M.-F. Hsieh, "A design approach integrating the magnetic circuit and electric circuit models for BDFIM," in *Electrical Machines and Systems (ICEMS), 2014 17th International Conference on*, Hangzhou, China, Oct. 2014, pp. 1685–1690.

[56] H. Gorginpour, H. Oraee, and R. A. McMahon, "Electromagnetic-thermal design optimization of the brushless doubly fed induction generator," *IEEE Transactions on Industrial Electronics*, vol. 61, no. 4, pp. 1710–1721, Apr. 2014.

[57] S. Tohidi, "Analysis and simplified modelling of brushless doubly-fed induction machine in synchronous mode of operation," *IET Electric Power Applications*, vol. 10, no. 2, pp. 110–116, 2016.

[58] P. C. Roberts, R. A. McMahon, P. J. Tavner, J. M. Maciejowski, and T. J. Flack, "Equivalent circuit for the brushless doubly fed machine (BDFM) including parameter estimation and experimental verification," *IEE Proceedings - Electric Power Applications*, vol. 152, no. 4, pp. 933–942, 2005.

[59] A. Ramchandran and G. Alexander, "Frequency-domain parameter estimation for the brushless doubly-fed machine," in *Conf. Rec. Power Conversion Conf.*, 1993, pp. 346–351.

[60] R. A. McMahon, X. Wan, E. Abdi-Jalebi, P. J. Tavner, P. C. Roberts, and M. Jagiela, "The BDFM as a generator in wind turbines," in *Power Electronics and Motion Control Conference, 2006. EPE-PEMC 2006. 12th International*, Aug.-Sept. 2006, pp. 1859–1865.

[61] R. A. McMahon, P. C. Roberts, X. Wang, and P. J. Tavner, "Performance of BDFM as generator and motor," *Electric Power Applications, IEE Proceedings* -, vol. 153, no. 2, pp. 289–299, Mar. 2006.

[62] E. Abdi, W. Xiaoyan, S. Shiyi, R. McMahon, and P. Tavner, "Performance characterisation of brushless doubly-fed generator," in *Industry Applications Society Annual Meeting, 2008. IAS '08. IEEE*, Oct. 2008, pp. 1–6.

[63] X. Wang, P. C. Roberts, and R. A. McMahon, "Optimisation of BDFM stator design using an equivalent circuit model and a search method," in *Power Electronics, Machines and Drives, 2006. The 3rd IET International Conference on*, Apr. 2006, pp. 606–610.

[64] X. Wang, R. A. McMahon, and P. J. Tavner, "Design of the brushless doubly-fed (induction) machine," in *Electric Machines & Drives Conference, 2007. IEMDC '07. IEEE International*, vol. 2, May 2007, pp. 1508–1513.

[65] H. Gorginpour, B. Jandaghi, and H. Oraee, "A novel rotor configuration for brushless doubly-fed induction generators," *IET Electric Power Applications*, vol. 7, no. 2, pp. 106–115, 2013.

[66] A. Oraee, E. Abdi, S. Abdi, R. McMahon, and P. J. Tavner, "Effects of rotor winding structure on the BDFM equivalent circuit parameters," *IEEE Transactions on Energy Conversion*, vol. 30, no. 4, pp. 1660–1669, Dec. 2015.

[67] X. Wang, P. C. Roberts, and R. A. McMahon, "Studies of inverter ratings of BDFM adjustable speed drive or generator systems," in *Power Electronics and Drives Systems, 2005. PEDS 2005. International Conference on*, vol. 1, 2005, pp. 337–342.

[68] S. Abdi, E. Abdi, A. Oraee, and R. McMahon, "Equivalent circuit parameters for large brushless doubly fed machines (BDFMs)," *IEEE Transactions on Energy Conversion*, vol. 29, no. 3, pp. 706–715, Sept. 2014.

[69] E. Abdi, R. Mcmahon, P. Malliband, S. Shao, M. E. Mathekga, P. Tavner, S. Abdi, A. Oraee, T. Long, and M. Tatlow, "Performance analysis and testing of a 250 kW medium-speed brushless doubly-fed induction generator," *IET Renewable Power Generation*, vol. 7, no. 6, pp. 631–638, 2013.

[70] E. Abdi, M. R. Tatlow, R. A. McMahon, and P. J. Tavner, "Design and performance analysis of a 6 MW medium-speed brushless DFIG," in *Renewable Power Generation Conference (RPG 2013), 2nd IET*, Sept. 2013, pp. 1–4.

[71] R. McMahon, P. Roberts, M. Tatlow, E. Abdi, A. Broekhof, and S. Abdi, "Rotor parameter determination for the brushless doubly fed (induction) machine," *IET Electric Power Applications*, vol. 9, no. 8, pp. 549–555, 2015.

[72] T. D. Strous, N. H. v. d. Blij, H. Polinder, and J. A. Ferreira, "Brushless doubly-fed induction machines: Magnetic field modelling," in *Electrical Machines (ICEM), 2014 International Conference on*, Berlin, Germany, Sept. 2014, pp. 2702–2708.

[73] F. Blazquez, C. Veganzones, D. Ramirez, and C. Platero, "Characterization of the rotor magnetic field in a brushless doubly-fed induction machine," *IEEE Transactions on Energy Conversion*, vol. 24, no. 3, pp. 599–607, Sept. 2009.

[74] T. D. Strous, X. Wang, H. Polinder, and J. A. Ferreira, "Evaluating harmonic distortions in brushless doubly-fed induction machines," *IEEE Transactions on Magnetics*, vol. 53, no. 1, 2017.

[75] H. Gorginpour, B. Jandaghi, M. A. Saket, A. Oraee, and H. Oraee, "Magnetic field harmonic analysis in brushless doubly fed machine," in *Energetics (IYCE), Proceedings of the 2011 3rd International Youth Conference on*, Jul. 2011, pp. 1–7.

[76] H. Gorginpour, B. Jandaghi, and H. Oraee, "Time and space harmonics in brushless doubly-fed machine," in *Electrical Engineering (ICEE), 2011 19th Iranian Conference on*, May 2011, pp. 1–6.

[77] J. Chen and W. Zhang, "Harmonics in brushless doubly fed induction generator for torque ripple analysis and modeling," *IEEE Transactions on Magnetics*, vol. 50, no. 11, pp. 1–4, Nov. 2014.

[78] T. D. Strous, X. Wang, H. Polinder, and J. A. B. Ferreira, "Brushless doubly-fed induction machines: Torque ripple," in *2015 IEEE International Electric Machines & Drives Conference (IEMDC)*, Coeur d'Alene, USA, May 2015, pp. 1145–1151.

[79] T. Logan, R. Mcmahon, and K. Seffen, "Noise and vibration in brushless doubly fed machine and brushless doubly fed reluctance machine," *IET Electric Power Applications*, vol. 8, no. 2, pp. 50–59, 2014.

[80] M. F. Hsieh, I. H. Lin, Y. C. Hsu, and R. A. McMahon, "Design of brushless doubly-fed machines based on magnetic circuit modeling," *IEEE Transactions on Magnetics*, vol. 48, no. 11, pp. 3017–3020, Nov. 2012.

[81] M. F. Hsieh, I. H. Lin, and D. Dorrell, "Magnetic circuit modeling of brushless doubly-fed machines with induction and reluctance rotors," *IEEE Transactions on Magnetics*, vol. 49, no. 5, pp. 2359–2362, May 2013.

[82] H. Gorginpour, H. Oraee, and R. A. McMahon, "A novel modeling approach for design studies of brushless doubly fed induction generator based on magnetic equivalent circuit," *IEEE Transactions on Energy Conversion*, vol. 28, no. 4, pp. 902–912, Dec. 2013.

[83] S. Abdi, E. Abdi, A. Oraee, and R. McMahon, "Optimization of magnetic circuit for brushless doubly fed machines," *IEEE Transactions on Energy Conversion*, vol. 30, no. 4, pp. 1611–1620, Dec. 2015.

[84] M. van der Geest, "Design and modeling of high performance permanent magnet synchronous machines," Ph.D. dissertation, Delft University of Technology, 2015.

[85] A. C. Ferreira and S. Williamson, "Time-stepping finite-element analysis of brushless doubly fed machine taking iron loss and saturation into account," *IEEE Transactions on Industry Applications*, vol. 35, no. 3, pp. 583–588, May/June 1999.

[86] A. M. Oliveira, P. Kuo-Peng, N. Sadowski, F. Runcos, R. Carlson, and P. Dular, "Finite-element analysis of a double-winding induction motor with a special rotor bars topology," *IEEE Transactions on Magnetics*, vol. 40, no. 2, pp. 770–773, Mar. 2004.

[87] Q. Zhang and H. Liu, "Comparative study of brushless doubly fed machine with different rotor structures used in wind power generation system," in *2010 Asia-Pacific Power and Energy Engineering Conference*, Chengdu, China, Mar. 2010, pp. 1–4.

[88] L. Jia and X. Wang, "Design a wound rotor brushless doubly-fed generator based on tooth harmonic principles and finite element analysis," in *Electrical Machines and Systems (ICEMS), 2014 17th International Conference on*, Hangzhou, China, Oct. 2014, pp. 1233–1239.

[89] H. Gorginpour, B. Jandaghi, A. Oraee, M. A. Saket, M. Ahmadian, and H. Oraee, "Reduction of the torque ripple in brushless doubly-fed machine," in *Energetics (IYCE), Proceedings of the 2011 3rd International Youth Conference on*, Leiria, Potugal, Jul. 2011, pp. 1–7.

[90] K. Hameyer and R. Belmans, *Numerical Modelling and Design of Electrical Machines and Devices*. WIT Press, 1999.

[91] M. A. Jabbar, P. Hla Nu, L. Zhejie, and B. Chao, "Modeling and numerical simulation of a brushless permanent-magnet DC motor in dynamic conditions by time-stepping technique," *IEEE Transactions on Industry Applications*, vol. 40, no. 3, pp. 763–770, May/Jun. 2004.

[92] J. Pyrhonen, T. Jokinen, and V. Hrabovcova, *Design of Rotating Electrical Machines*. John Wiley & Sons, Ltd, 2008.

[93] J. Donea, A. Huerta, J. Ponthot, and A. Rodríguze-Ferran, "Arbitrary Lagrangian-Eulerian methods," *Encyclopedia of computational mechanics*, 2004.

[94] D. Hutton, *Fundamentals of Finite Element Analysis*. McGraw-Hill, 2004.

[95] W. Hundsdorfer and J. Verwer, *Numerical Solution of Time-Dependent Advaction-Diffusion-Reaction Equations*. Springer, 2003.

[96] M. Popescu, D. M. Ionel, T. J. E. Miller, S. J. Dellinger, and M. I. McGilp, "Improved finite element computations of torque in brushless permanent magnet motors," *Electric Power Applications, IEE Proceedings -*, vol. 152, no. 2, pp. 271–276, 2005.

[97] M. Popescu, "Prediction of the electromagnetic torque in synchronous machines through maxwell stress harmonic filter (HFT) method," *Electrical Engineering*, 2006.

[98] D. Fang, "An improved iron loss estimation for permanent magnet brushless machines," *IEEE Transactions on Energy Conversion*, vol. 14, no. 4, pp. 1391–1395, Dec. 1999.

[99] J. Reinert, A. Brockmeyer, and R. W. A. A. De Doncker, "Calculation of losses in ferro- and ferrimagnetic materials based on the modified steinmetz equation," *IEEE Transactions on Industry Applications*, vol. 37, no. 4, pp. 1055–1061, Jul./Aug. 2001.

[100] D. M. Ionel, M. Popescu, S. J. Dellinger, T. J. E. Miller, R. J. Heideman, and M. I. McGilp, "On the variation with flux and frequency of the core loss coefficients in electrical machines," *IEEE Transactions on Industry Applications*, vol. 42, no. 3, pp. 658–667, May/Jun. 2006.

[101] H. Gorginpour, H. Oraee, and E. Abdi, "Calculation of core and stray load losses in brushless doubly fed induction generators," *IEEE Transactions on Industrial Electronics*, vol. 61, no. 7, pp. 3167–3177, Jul. 2014.

[102] G. Y. Sizov, D. M. Ionel, and N. A. O. Demerdash, "Modeling and parametric design of permanent-magnet AC machines using computationally efficient finite-element analysis," *IEEE Transactions on Industrial Electronics*, vol. 59, no. 6, pp. 2403–2413, Jun 2012.

[103] D. M. Ionel and M. Popescu, "Ultrafast finite-element analysis of brushless PM machines based on space-time transformations," *IEEE Transactions on Industry Applications*, vol. 47, no. 2, pp. 744–753, Mar./Apr. 2011.

[104] N. H. v. d. Blij, T. D. Strous, X. Wang, and H. Polinder, "A novel analytical approach and finite element modelling of a BDFIM," in *Electrical Machines (ICEM), 2014 International Conference on*, Berlin, Germany, Sept. 2014, pp. 346–352.

[105] K. Deb, A. Pratap, S. Agarwal, and T. Meyarivan, "A fast and elitist multiobjective genetic algorithm: NSGA-II," *IEEE Transactions on Evolutionary Computation*, vol. 6, no. 2, pp. 182–197, Apr. 2002.

[106] Y. Kawase, T. Yamaguchi, T. Zhipeng, N. Toida, N. Minoshima, and K. Hashimoto, "Effects of skew angle of rotor in squirrel-cage induction motor on torque and loss characteristics," *IEEE Transactions on Magnetics*, vol. 45, no. 3, pp. 1700–1703, Mar. 2009.

[107] S. L. Ho and W. N. Fu, "A comprehensive approach to the solution of direct-coupled multislice model of skewed rotor induction motors using time-stepping eddy-current finite element method," *IEEE Transactions on Magnetics*, vol. 33, no. 3, pp. 2265–2273, May 1997.

[108] D. G. Dorrell, A. M. Knight, and R. E. Betz, "Issues with the design of brushless doubly-fed reluctance machines: Unbalanced magnetic pull, skew and iron losses," in *2011 IEEE International Electric Machines & Drives Conference (IEMDC)*, May 2011, pp. 663–668.

[109] J. J. C. Gyselinck, L. Vandevelde, and J. A. A. Melkebeek, "Multi-slice fe modeling of electrical machines with skewed slots-the skew discretization error," *IEEE Transactions on Magnetics*, vol. 37, no. 5, pp. 3233–3237, Sept. 2001.

[110] D. Zwillinger, *Standard Mathematical Tables and Formulae*. CRC Press, 2003.

[111] M. Kamermans, "Gaussian quadrature weights and abscissae," Jun. 2011. [Online]. Available: https://pomax.github.io/bezierinfo/legendre-gauss.html

[112] G. Y. Sizov, P. Zhang, D. M. Ionel, N. A. O. Demerdash, I. P. Brown, A. O. Smith, and M. G. Solveson, "Modeling and analysis of effects of skew on torque ripple and stator tooth forces in permanent magnet ac machines," in *Energy Conversion Congress and Exposition (ECCE), 2012 IEEE*, Sept. 2012, pp. 3055–3061.

[113] B. Weilharter, O. Biro, S. Rainer, and A. Stermecki, "Computation of rotating force waves in skewed induction machines using multi-slice models," *IEEE Transactions on Magnetics*, vol. 47, no. 5, May 2011.

[114] M. Mohr, O. Biro, A. Stermecki, and F. Diwoky, "A finite element-based circuit model approach for skewed electrical machines," *IEEE Transactions on Magnetics*, vol. 50, no. 2, pp. 837–840, Feb. 2014.

[115] C. M. Spargo, B. C. Mecrow, and J. D. Widmer, "Computationally efficient skew effect calculation in electric machines utilising harmonic maxwellian stress decomposition," in *Electrical Machines (ICEM), 2014 International Conference on*, Sept. 2014, pp. 1044–1049.

[116] T. Logan, J. Warrington, S. Shiyi, and R. McMahon, "Practical deployment of the brushless doubly-fed machine in a medium scale wind turbine," in *Power Electronics and Drive Systems, 2009. PEDS 2009. International Conference on*, Nov. 2009, pp. 470–475.

[117] J. F. Gieras, C. Wang, and J. C. Lai, *Noise of Polyphase Electric Motors*. CRC Press, 2005.

[118] X. Wang, T. D. Strous, D. Lahaye, H. Polinder, and J. A. Ferreira, "Finite element modeling of brushless doubly-fed induction machine based on magneto-static simulation," in *2015 IEEE International Electric Machines & Drives Conference (IEMDC)*, Coeur d'Alene, USA, May 2015, pp. 315–321.

[119] ——, "Effects of rotor skew on the performance of brushless doubly-fed induction machine," in *2015 IEEE International Electric Machines & Drives Conference (IEMDC)*, Coeur d'Alene, USA, May 2015, pp. 260–265.

[120] T. D. Strous, X. Wang, H. Polinder, and J. A. Ferreira, "Saturation in brushless doubly-fed induction machines," in *Power Electronics, Machines and Drives (PEMD), IET International Conference on*, 2016.

[121] S. Baserrah and B. Orlik, "Eddy current investigation study for a non-conventional flux concentrated permanent magnet transverse flux machine using finite element method via 3d transient approach," in *2011 IEEE International Electric Machine & Drives Conference (IEMDC)*, May 2011.

[122] Z. Q. Zhu and Z. Azar, "Influence of end-effect and cross-coupling on torque-speed characteristics of switched flux permanent magnet machines," in *Power Electronics and ECCE Asia (ICPE & ECCE), 2011 IEEE 8th International Conference on*, 2011, pp. 145–152.

[123] B. Funieru and A. Binder, "3d numerical calculation method of electrical machines with time efficient air gap coupling and stabilized torque and force calculation," in *Electrical Machines (ICEM), 2014 International Conference on*, Sept. 2014, pp. 954–960.

[124] X. Ge, Z. Q. Zhu, G. Kemp, D. Moule, and C. Williams, "Optimal step-skew methods for cogging torque reduction accounting for 3-dimensional effect of interior permanent magnet machines," *IEEE Transactions on Energy Conversion*, 2016.

[125] B. E. Thompson, "Three-dimensional finite element design procedure for the brushless doubly fed machine," Master's thesis, Oregon State University, 1995.

[126] K. Bathe, *Finite Element Procedures*. Prentice Hall, 1996.

[127] C. Chen and O. Biro, "Geometric multigrid with plane smoothing for thin elements in 3-d magnetic fields calculation," *IEEE Transactions on Magnetics*, vol. 48, no. 2, pp. 443–446, Feb. 2012.

[128] W. Frei, "Solutions to linear systems of equations: direct and iterative solvers," Nov. 2013. [Online]. Available: https://www.comsol.com/blogs/solutions-linear-systems-equations-direct-iterative-solvers/

[129] C. Carpenter, "Theory of flux penetration into laminated iron and associated losses," in *Electrical Engineers, Proceedings of the Institution of*, vol. 124, no. 7, 1977, pp. 659–664.

[130] V. C. Silva, G. Meunier, and A. Foggia, "A 3D finite-element computation of eddy currents and losses in laminated iron cores allowing for electric and magnetic anisotropy," *IEEE Transactions on Magnetics*, vol. 31, no. 3, pp. 2139–2141, 1995.

[131] P. P. Silvester and R. L. Ferrari, *Finite elements for electrical engineers*. Cambridge University Press, 1996.

[132] M. Kuczmann, *Potential Formulations in Magnetics Applying the Finite Element Method*. Lecture notes, Laboratory of Electromagnetic Fields, Szechenyi Istvan University, 2009.

[133] V. N. Kaliakin, *Introduction to Approximate Solution Techniques, Numerical Modeling, and Finite Element Methods*. Marcel Dekker AG, 2002.

[134] Y. Zhu and A. C. Cangellaris, *Multigrid Finite Element Methods for Electromagnetic Field Modeling*. John Wilye & Sons, 2006.

[135] J. Ystrom, "Fast solver for complex problems," Feb. 2007. [Online]. Available: http://machinedesign.com/archive/fast-solvers-complex-problems

[136] V. Marra, "On solvers: Multigrid methods," Feb. 2013. [Online]. Available: https://www.comsol.com/blogs/on-solvers-multigrid-methods/

[137] G. H. Golub and C. F. Van Loan, *Matrix computations*. The Johns Hopkins University Press, 1996.

[138] X. Wang, D. Liu, H. Polinder, D. Lahaye, and J. A. Ferreira, "Comparison of nested-loop rotors in brushless doubly-fed induction machines," in *The 19th International Conference on Electrical Machines and Systems (ICEMS 2016)*, Chiba, Japan, Nov. 2016.

[139] M. S. Boger, A. K. Wallace, and R. Spee, "Investigation of appropriate pole number combinations for brushless doubly fed machines applied to pump drives," *IEEE Transactions on Industry Applications*, vol. 32, no. 1, pp. 189–194, Jan./Feb. 1996.

[140] S. Abdi, E. Abdi, and R. McMahon, "A study of unbalanced magnetic pull in brushless doubly fed machines," *IEEE Transactions on Energy Conversion*, vol. 30, no. 3, pp. 1218–1227, Sept. 2015.

[141] H. Polinder, F. F. A. van der Pijl, G. J. de Vilder, and P. J. Tavner, "Comparison of direct-drive and geared generator concepts for wind turbines," *IEEE Transactions on Energy Conversion*, vol. 21, no. 3, pp. 725–733, Sept. 2006.

Acknowledgements

This thesis is the result of four years of research performed in the Department of Electrical Sustainable Energy at Delft University of Technology (TU Delft). Doing a PhD research was a challenging journey. Fortunately, some people gave me lots of support and help during the past four years. Here, I would like to take the opportunity to thank those people.

First of all, I want to thank my daily supervisor and co-promotor, Dr. Domenico Lahaye for his continuous guidance and fruitful discussions about finite-element computation. You always read each of my reports, manuscripts and emails timely and carefully. You are so enthusiastic and always there when I need any help. I am deeply grateful to you.

Secondly, I want to thank my another daily supervisor and co-promotor, Dr. Henk Polinder for his valuable discussions about electrical machines. You give me a great amount of freedom to do my research. And you always encourage me to do the research independently. Four years are too short to learn more about the electrical machines from you.

Similarly, I want to thank my promotor Prof. Braham Ferreira. You gave me the opportunity to pursue my doctoral degree in TU Delft. Thank you for your supporting and attention on my work.

It is really nice to join the Windrive project team playing with the brushless DFIM. Teamwork makes me learn a lot from my teammates. Therefore, I would like to thank Tim Strous, Faisal M. Wani, Nils van der Blij, Udai Shipurkar, Zhi Xu for their discussions on the research work.

Next, I want to thank my colleagues from the EPP and DCE&S groups for their interesting talking during the coffee break. I also want to thank the lab managers, Harrie Olsthoorn, Bart Roodenburg, Joris Koeners, for supporting my experiments.

I also want to thank my friends, Peng Lu, Hui Jiang, Dong Liu, Kewei Huang, Wenbo Wang, Wandong Wang, Jianning Dong. Doing the PhD research would not be so funny without you.

Especially, I want to thank my previous supervisor during my bachelor and master studies, Prof. Xiaobin Zhang, for his support when I decided to pursue my doctoral degree abroad.

Last but not least, I want to thank my parents and parents-in-law for their continued support. 感谢父母对我的关爱和教育，谢谢你们尽最大的努力给予我最好的教育环境，感谢岳父母对我们小家庭无私的爱和付出，特别感谢你们不远万里来荷兰为我的顺利毕业做坚实的后盾，我定不会辜负你们的厚望。 I would like to thank especially my beloved wife, Jiehuan Tang, for her love and accompany. I am lucky to have you in my life. Thank you for bringing me such a lovely daughter. Thank you my dear daughter, Heguo Wang, for bringing so much happiness to my life. Wish you grow up smoothly, healthily and happily.

Xuezhou Wang
January 2017, Delft

List of publications

Journal Publications

- **Xuezhou Wang**, T. D. Strous, D. Lahaye, H. Polinder, J. A. Ferreira, *Computationally Efficient Calculation of Skew Effects in Brushless Doubly-Fed Induction Machines*, IET Electric Power Applications, vol.11, no.3, 2017.
- **Xuezhou Wang**, T. D. Strous, D. Lahaye, H. Polinder, J. A. Ferreira, *Modeling and Optimization of Brushless Doubly-Fed Induction Machines Using Computationally Effcient Finite-Element Analysis*, IEEE Trans. on Industry Applications, vol.52, no.6, 2016.
- T. D. Strous, **Xuezhou Wang**, H. Polinder, J. A. Ferreira, *Evaluating Harmonic Distortions in Brushless Doubly-Fed Induction Machines*, IEEE Trans. on Magnetics, vol.53, no.1, 2017.
- T. D. Strous, **Xuezhou Wang**, H. Polinder, J. A. Ferreira, *Brushless Doubly-Fed Induction Machines: Magnetic-Field Analysis*, IEEE Trans. on Magnetics, vol.52, no.11, 2016.

Conference Proceedings

- **Xuezhou Wang**, H. Polinder, D. Lahaye, J. A. Ferreira, *FE Based Multi-Objective Optimization of a 3.2MW Brushless Doubly-Fed Induction Machine*, IEEE Workshop on Electrical Machines Design, Control and Diagnosis (WEMDCD'2017), Apr. 20-21, 2017, Nottingham, UK.
- **Xuezhou Wang**, Dong Liu, H. Polinder, D. Lahaye, J. A. Ferreira, *Comparison of Nested-Loop Rotors in Brushless Doubly-Fed Induction Machines*, Electrical Machines and Systems (ICEMS), the 19$^{\text{th}}$ International Conference on, Nov. 13-16, 2016, Chiba, Japan.
- **Xuezhou Wang**, Dong Liu, D. Lahaye, H. Polinder, J. A. Ferreira, *Finite Element Analysis and Experimental Validation of Eddy Current Losses in Permanent Magnet Machines with Fractional-Slot Concentrated Windings*, Electrical Machines and Systems (ICEMS), the 19$^{\text{th}}$ International Conference on, Nov. 13-16, 2016, Chiba, Japan.
- **Xuezhou Wang**, T. D. Strous, D. Lahaye, H. Polinder, J. A. Ferreira, *A Finite Element Post-Processing for Skew Effects in Brushless Doubly-Fed Induction Machines*, Electrical Machines (ICEM), 2016 International Conference on, pp. 34-40, Sept. 4-7, 2016, Lausanne, Switzerland.
- **Xuezhou Wang**, T. D. Strous, D. Lahaye, H. Polinder, J. A. Ferreira, *Harmonics Study of Nested-Loop Rotors in Brushless Doubly-Fed Induction Machines*, Electrical Machines (ICEM), 2016 International Conference on, pp. 373-379, Sept. 4-7, 2016, Lausanne, Switzerland.
- **Xuezhou Wang**, T. D. Strous, D. Lahaye, H. Polinder, J. A. Ferreira, *Finite Element Modeling of Brushless Doubly-Fed Induction Machine Based on Magneto-Static Simulation*, Electric Machines & Drives Conference (IEMDC), 2015 IEEE International on, pp.315-321, May 10-13, 2015, Coeur d'Alene, USA.
- **Xuezhou Wang**, T. D. Strous, D. Lahaye, H. Polinder, J. A. Ferreira, *Effects of Rotor Skew on the Performance of Brushless Doubly-Fed Induction Machine*, Electric Machines & Drives Conference (IEMDC), 2015 IEEE International on, pp.260-265, May 10-13, 2015, Coeur d'Alene, USA.
- **Xuezhou Wang**, Dong Liu, D. Lahaye, H. Polinder, J. A. Ferreira, *Transient 3D Finite Element Analysis of Motional Eddy Current Losses in Concentrated Winding Permanent Magnet Machines*, Electromagnetic Field Computation (CEFC), 16$^{\text{th}}$ Biennial IEEE Conference on, May 25-28, 2014, Annecy, France.

- F. M. Wani, **Xuezhou Wang**, D. Lahaye and H. Polinder, *3D FEM Computation of Axial Flux in a Brushless Doubly-Fed Induction Machine*, IEEE International Magnetics Conference, INTERMAG Europe 2017, Apr. 24-28. 2017, Dublin, Ireland.
- T. D. Strous, **Xuezhou Wang**, H. Polinder, J. A. Ferreira, *Saturation in Brushless Doubly-Fed Induction Machines*, Power Electronic, Machines and Drives (PEMD), the 8th IET International Conference on, Apr. 19-21, 2016, Glasgow, UK.
- T. D. Strous, **Xuezhou Wang**, H. Polinder, J. A. Ferreira, *Finite Element Based Multi-Objective Optimization of a Brushless Doubly-Fed Induction Machine*, Electric Machines & Drives Conference (IEMDC), 2015 IEEE International on, pp.1689-1694, May 10-13, 2015, Coeur d'Alene, USA.
- T. D. Strous, **Xuezhou Wang**, H. Polinder, J. A. Ferreira, *Brushless Doubly-Fed Induction Machines: Torque Ripple*, Electric Machines & Drives Conference (IEMDC), 2015 IEEE International on, pp.1145-1151, May 10-13, 2015, Coeur d'Alene, USA.
- N. H. van der Blij, T. D. Strous, **Xuezhou Wang**, H. Polinder, *A Novel Analytical Approach and Finite Element Modelling of a BDFIM*, Electrical Machines (ICEM), 2014 International Conference on, pp. 346-352, Sept. 2-5, 2014, Berlin, Germany.
- Dong Liu, H. Polinder, A. B. Abrahamsen, **Xuezhou Wang**, J. A. Ferreira, *Comparison of Superconducting Generators and Permanent Magnet Generators for 10-MW Direct-Drive Wind Turbines*, Electrical Machines and Systems (ICEMS), the 19th International Conference on, pp. , Nov. 13-16, 2016, Chiba, Japan.
- Dong Liu, H. Polinder, **Xuezhou Wang**, J. A. Ferreira, *Evaluating the Cost of Energy of a 10 MW Direct-Drive Wind Turbine with Superconducting Generators*, Electrical Machines (ICEM), 2016 International Conference on, pp. 320-326, Sept. 4-7, 2016, Lausanne, Switzerland.

Biography

Xuezhou Wang was born in Jiangsu, China, in 1988. He received the BSc degree in Electrical Engineering and Automation from Northwestern Polytechnical University (NWPU), Xi'an, China, in 2010. He obtained the MSc degree in Power Electronics and Electrical Drive from NWPU in 2013. After that, he pursued the PhD degree in the department of Electrical Sustainable Energy at the Delft University of Technology, Delft, the Netherlands.

His main research interests include efficient finite element modeling of electrical machines, design and multi-objective optimization of those machines.